

**ON THE HIGH FIDELITY SIMULATION OF CHEMICAL
EXPLOSIONS AND THEIR INTERACTION WITH
SOLID PARTICLE CLOUDS**

A Thesis
Presented to
The Academic Faculty

by

Kaushik Balakrishnan

In Partial Fulfillment
of the Requirements for the Degree
Doctor of Philosophy in the
School of Aerospace Engineering

Georgia Institute of Technology
August 2010

**ON THE HIGH FIDELITY SIMULATION OF CHEMICAL
EXPLOSIONS AND THEIR INTERACTION WITH
SOLID PARTICLE CLOUDS**

Approved by:

Prof. Suresh Menon, Committee Chair
School of Aerospace Engineering
Georgia Institute of Technology

Prof. Stephen Ruffin
School of Aerospace Engineering
Georgia Institute of Technology

Prof. Mitchell Walker
School of Aerospace Engineering
Georgia Institute of Technology

Prof. Jeff Jagoda
School of Aerospace Engineering
Georgia Institute of Technology

Prof. Naresh Thadhani
School of Materials Science and
Engineering
Georgia Institute of Technology

Dr. Douglas Nance
Air Force Research Laboratory
Eglin Air Force Base

Date Approved: 4 June 2010

Dedicated to the human spirit of curiosity for the unknown, the desire for knowledge, and the pursuit of exploration—innate, veritable characteristics that have guided our species from a nomadic primate to a space-faring adventurer.

ACKNOWLEDGEMENTS

I hereby express my deep and sincere gratitude to my doctoral dissertation adviser, Prof. Suresh Menon, for his encouragement, guidance, and willingness to always set me on the right path during the undertaking of my graduate research. He has been a source of constant inspiration, and has taught me that discipline and dedication are vital to succeed at research. I am honored and privileged to have worked under his guidance. Furthermore, I extend my thanks to the other elite members of the thesis Committee: Prof. Jeff Jagoda, Prof. Steve Ruffin, Prof. Mitchell Walker and Prof. Naresh Thadhani, for evaluating this work and for their constructive criticisms. A special thanks to Dr. Douglas V. Nance of the Eglin Air Force Base, for sharing with me his knowledge on the behavior of explosives, for supplying the initial conditions used in this study, and for his constant interest, encouragement and support of my research effort. In addition, his line-by-line review of this dissertation and useful suggestions, have been very instrumental to its successful completion.

I appreciate the support from the sponsors of this research effort, the Office of Naval Research (ONR) and the Air Force Research Laboratory (Eglin Air Force Base). In addition, I thank the Department of Defense (DoD) Major Shared Resources Centers (MSRC) at the Naval Oceanographic Office (NAVO), Army Research Laboratory (ARL) and the Maui High Performance Computing Center (MHPCC) for providing the High Performance Computing (HPC) resources, without which this research undertaking may not have been possible. Furthermore, I thank the American working class and the Government for allowing foreigners like myself to pursue higher education in their esteemed institutions.

I extend my thanks to members of the Computational Combustion Laboratory

(CCL): Franklin, Satoshi, Ayse, Srikant, Jung, Miguel, Orcun, Sumit, Matthieu, Faisal, Alpha and Leandro, for the stimulating discussions I have had with them on various topics that include fluid mechanics, gas dynamics, combustion, computational fluid dynamics, etc., without which I probably may not have been able to complete this dissertation. Furthermore, I acknowledge the constant encouragement received over the years from my friends: Ravishekar, Ganesh, Dipa, Varun, Abhishek, Susheel, Ramraj and Nischint.

Last, but not the least, I thank my parents, on whose constant encouragement and love I have relied throughout my life in the pursuit of my dreams. This thanks also extends to my sister, Mahima, and to Balaji.

TABLE OF CONTENTS

DEDICATION	iii
ACKNOWLEDGEMENTS	iv
LIST OF TABLES	x
LIST OF FIGURES	xi
NOMENCLATURE	xix
SUMMARY	xxvi
I INTRODUCTION AND REVIEW	1
1.1 Introduction	1
1.1.1 On the physics of explosions	3
1.1.2 Simulation challenges	5
1.2 Literature Review	11
1.2.1 Two-phase modeling	11
1.2.2 Homogeneous explosives	14
1.2.3 Heterogeneous explosives	17
1.2.4 Rayleigh-Taylor and Richtmyer-Meshkov instabilities	20
1.2.5 Aluminum combustion in high-speed flow	23
1.3 Thesis Outline	25
II RESEARCH OBJECTIVES	27
III MATHEMATICAL FORMULATION	32
3.1 Gas (Eulerian) Phase	33
3.1.1 The Navier-Stokes equations	33
3.1.2 Non-conservative/“nozzling” terms	36
3.1.3 Equations of state	36
3.1.4 Governing equations for LES	42
3.1.5 Combustion modeling	49

3.2	Solid (Lagrangian) Phase	50
3.2.1	Solid phase governing equations	51
3.2.2	Inter-phase coupling terms	57
IV	COMPUTATIONAL METHODS	59
4.1	Finite Volume Scheme	61
4.2	MacCormack Time Integration	62
4.3	Central Scheme Flux Computation	64
4.4	Upwind Scheme Flux Computation	66
4.4.1	MUSCL interpolation scheme	68
4.4.2	The HLL and HLLC approximate Riemann solvers	71
4.5	Hybrid Approach	82
4.6	Discrete Equations Method (DEM)	83
4.6.1	Formulation	83
4.6.2	Interface closure	90
4.6.3	Non-Cartesian grids	93
4.6.4	Summary of DEM	99
4.7	Initial Detonation Profile (GISPA Method)	101
4.8	Other Computational Issues	101
4.8.1	Generalized grids	101
4.8.2	Boundary conditions	104
4.8.3	4 th order Runge-Kutta integration for particle phase	106
4.8.4	Interpolation of gas phase variables to particle location	108
V	VALIDATION STUDIES	111
5.1	Validation of the Gas Phase Solver	112
5.1.1	Explosion from a pressurized sphere	112
5.1.2	Sedov's point explosion problem	114
5.1.3	Blast wave from a homogeneous explosive	115
5.2	Validation of the Solid Phase Solver	116

5.2.1	Particle dispersion in a shock tube	116
5.2.2	Shock propagation through dust-gas suspension	117
5.2.3	Shock propagation through dense gas-particle mixture	119
5.2.4	Shock induced dispersion of acrylic plastic clouds	120
5.3	Summary	122
VI	HOMOGENEOUS EXPLOSIVE CHARGES	123
6.1	Homogeneous Explosions into Air	125
6.1.1	One-dimensional effects only	126
6.1.2	Three-dimensional effects included	131
6.1.3	Effect of initial perturbations	141
6.2	Homogeneous Explosions into Dilute Aluminum Particle Clouds	145
6.2.1	Perturbation growth and particle dispersion	147
6.2.2	Large particle regime	151
6.2.3	Small particle regime	164
6.2.4	Theoretical hydrodynamic considerations	187
VII	HETEROGENEOUS EXPLOSIVE CHARGES	194
7.1	One-Dimensional Effects Only	195
7.1.1	Detonation in a heterogeneous explosive	195
7.1.2	Impulsive loading	201
7.1.3	Parametric studies	208
7.2	Three-Dimensional Effects Included	217
7.2.1	Mixing layer characteristics	220
7.2.2	Some parametric studies	231
7.2.3	Concluding remarks	237
7.3	Aluminized Explosive Charges	238
7.3.1	Effect of particle size	241
7.3.2	Effect of volume fraction	243
7.3.3	Effect of burn time	246

VIII CONCLUSIONS AND RECOMMENDATIONS	249
8.1 Conclusions	249
8.2 Recommendations for Future Work	253
APPENDIX A PARTICLE DRAG LAWS AND NUSSELT NUMBER COR- RELATIONS	256
APPENDIX B INITIAL DETONATION PROFILE (GISPA METHOD) .	259
REFERENCES	265

LIST OF TABLES

1	Conservative flux at cell interface $i - 1/2$	87
2	Non-Conservative flux at cell interface $i - 1/2$	89
3	Properties of the three explosives considered	126
4	Overpressure scaling for the three explosives	129
5	Empirical scaling law for explosives	130
6	Scaled impulse for TNT without (1D) and with (3D) mixing	141
7	Scaling laws for the mixing layer (δ_{ML}/r_o) and particle cloud (δ_{cloud}/r_o) widths.	180
8	Detonation programming validation data for nitromethane: P_{CJ} - CJ pressure, u_{CJ} - CJ velocity, D - detonation velocity	261

LIST OF FIGURES

1	Wave diagram of the flow field in the post-detonation phase of a high explosive charge.	5
2	Non-spherical fireballs from chemical explosions.	5
3	Photographic image of a heterogeneous explosion from [214].	18
4	Photographic image of heterogeneous explosions showing hydrodynamic instabilities in a fireball [74].	19
5	A typical finite volume computational cell.	62
6	Schematic of a typical control volume showing the flux vectors and cell face areas.	65
7	Schematic of a typical Godunov scheme representation of flow variables.	67
8	Schematic of a typical Godunov scheme representation of flow variables with MUSCL reconstruction.	71
9	(x, t) diagram of an approximate Riemann problem evolution with two characteristic waves.	73
10	(x, t) diagram of an approximate Riemann problem evolution with three characteristic waves.	76
11	Volume fraction field representation in DEM. The schematic shows how a discrete particle field can be represented as a piecewise continuous volume fraction variable for flux computation.	84
12	When to compute conservative and non-conservative fluxes for cell (i, j, k) . The arrow denotes the direction the interface has to move to have a non-zero gas flux entering or leaving the middle cell. The white regions denote the space available for the gas; the grey regions denote the space occupied by the solid particles.	99
13	Explosion from a pressurized sphere. Experimental data from [33]; Attenuation law from [3].	113
14	Explosion from a high pressure source. The line denotes the current simulation results; the circles denote the numerical results of [201].	113
15	Blast wave trajectory (a) and overpressure (b) profiles for the Sedov point explosion problem. The circles denote the simulation results and the lines denote curve-fits.	115

16	Blast wave trajectory (a) and overpressure (b) profiles for a 11.8 cm dia. Nitromethane charge. Lines denote the simulation results and circles denote the experimental data from Zhang et al. [214].	116
17	Evolution of particle trajectory (left axis) and velocity (right axis) with time. The experimental data is from [54].	117
18	Planar shock wave attenuation in dust-gas suspension. The experimental data is from [187]; the attenuation law is from [2]; the other study is from [41].	118
19	Pressure traces upstream and downstream of a dense particle bed subjected to a shock wave. The experimental data is from [173].	120
20	Dispersion of acrylic plastic clouds of initial volume fractions (i) 0.1% and (ii) 3% by a Mach 2.8 shock. The experimental data is from [30].	121
21	Blast wave from a Nitromethane charge (a) trajectory; (b) overpressure. Experimental data from [214]. The numbers denote the number of grid points used for the one-dimensional grid. Real: real gas assumption; Thermally perfect: thermally perfect gas assumption. . . .	125
22	Blast wave from charges containing the same volume of the high explosive (a) primary and secondary shock trajectories; (b) overpressure. DoD (1998) [53].	127
23	Scaled impulse as a function of the scaled radius for NM, TNT and HMX.	128
24	Comparison of a 14.02 ton TNT charge with the scaling law.	131
25	Comparison of one-dimensional and three-dimensional approaches (a) pressure trace; (b) pressure contour.	132
26	Iso-surface of N_2 mass fraction to illustrate the growth of the mixing layer with time.	134
27	Inner and outer boundaries of the mixing layer for the TNT charge. .	135
28	Iso-surface of N_2 mass fraction at 3.2 msec for the random initialization based on Gaussian and Laplace distributions.	136
29	Natural logarithm of density contours at (a) 2.25 msec; (b) 2.72 msec.	137
30	Normalized mass of CO , C and CO_2 variation with time.	139
31	Pressure traces at the 0.9 m radial location for the TNT charge. . . .	140
32	Mixing layer growth at 0.4 msec ((a) & (b)) and 3.5 msec ((c) & (d)) for the low ((a) & (c)) and high ((b) & (d)) intensity initial perturbations. Shown here are the CO isosurface contours shaded with the density. .	142

33	Outer and inner boundaries of the mixing layer with low and high intensity initial perturbations.	144
34	Pressure traces at the 0.9 m radial location for the TNT charge with low and high intensity initial perturbations.	144
35	Radius-time diagram of the one-dimensional post-detonation flow-field. Note: this is a schematic only.	148
36	CO isosurface shaded with $\log(\rho)$ at times (a) ~ 0.3 msec; (b) ~ 3.8 msec. Particles are not shown for better clarity.	151
37	The interaction of solid particles with the mixing layer and their subsequent dispersion at times (a) 0.11 msec; (b) 0.4 msec.	152
38	Effect of particle size on the pressure field behind the blast wave. . .	154
39	Dependence of mixing and afterburn on particle size: (a) mixing layer boundaries; (b) $C(S)$ mass fractions remaining.	155
40	Interaction of the hydrodynamic structures with the primary blast wave: density contours at time instants (a) 0.11 msec; (b) 0.16 msec; (c) 0.22 msec; (d) 0.3 msec; (e) 0.4 msec and (f) 0.58 msec. Note that the figures are shown in different scale for better clarity.	158
41	Effect of initial mass loading ratio on the pressure field behind the blast wave.	159
42	Dependence of mixing layer boundaries on the initial mass loading ratio: (a) outer boundary; (b) inner boundary. The plain lines correspond to $\eta=1$; the lines with circles correspond to $\eta = 0.25$	160
43	Dependence of afterburn on the initial mass loading ratio: $C(S)$ mass fraction remaining.	160
44	Effect of initial extent of particle distribution on the pressure field behind the blast wave.	161
45	Dependence of mixing layer boundaries on the initial extent of particle distribution: (a) outer boundary; (b) inner boundary.	162
46	Dependence of afterburn on the initial extent of particle distribution: $C(S)$ mass fraction remaining.	162
47	Solid aluminum mass remaining with time.	163
48	Grid independence study: (a) inner and outer boundaries of the mixing layer; (b) mass fractions of $C(S)$ and CO remaining; (c) normalized mass of solid aluminum remaining.	165

49	Rayleigh-Taylor hydrodynamic structures in the mixing layer: (a) bubbles; (b) spikes. Shown here are the iso-surfaces of the CO mass fraction, colored by the local gas density.	166
50	Interaction of the particle cloud with the hydrodynamic structures at $t/t_o \sim 35$: (a) CO_2 mass fraction; (b) $\log(\omega)$ contours and particle locations.	167
51	Clustering of particle cloud at times t/t_o (a) 20; (b) 35; (c) 50; (d) 90; (e) 560. The scales of the figures have been adjusted for better clarity.	168
52	Effect of η on clustering of particle cloud ($\eta=2$): times t/t_o (a) 20; (b) 35; (c) 50; (d) 90; (e) 560. The scales of the figures have been adjusted for better clarity.	170
53	Effect of η on the average local gas velocity seen by the particles for particle group (a) $C60$; (b) $C80$	171
54	Effect of particle size on clustering of particle cloud ($r_p=10 \mu\text{m}$; initial cloud distribution: 5.9-12 cm; $\eta=1$): times t/t_o (a) 20; (b) 35; (c) 50; (d) 90; (e) 560. The scales of the figures have been adjusted for better clarity.	174
55	Effect of initial cloud width on the average local gas velocity seen by the particles for particle group (a) $C60$; (b) $C80$	175
56	Growth of the mixing layer: (a) outer and inner boundaries of the mixing layer; (b) mixing layer width (δ_{ML}). Both variables are normalized with the initial charge radius, r_o	176
57	Different phases in the dispersion of the particle cloud: (a) leading and trailing edges of the particle cloud; (b) cloud width. The phases are denoted by (1) engulfment phase; (2) hydrodynamic instability-interaction phase; (3) first vortex-free dispersion phase; (4) reshock phase; and (5) second vortex-free dispersion phase.	178
58	Carbon mass remaining with time, normalized with the initial charge mass.	181
59	Rate of carbon mass remaining with time.	182
60	Degree of mixedness (DM): (a) effect of η ; (b) effect of r_p and initial cloud width.	184
61	Boundaries of region of aluminum oxides ($AlO, Al_2O_3(L)$): (a) inner boundary; (b) outer boundary. Radius r is normalized with the initial charge radius, r_o	185

62	Preferential combustion of aluminum particles: particle temperature ((a) & (b)) and radius ((c) & (d)) at times $t/t_o \sim 25$ ((a) & (c)) and $t/t_o \sim 120$ ((b) & (d)). Temperature is in <i>Kelvin</i> , and radius is in <i>m</i> . The scales of the figures have been adjusted for better clarity.	187
63	Bubble analysis from the 3D simulation for $\eta=1$, $r_p=5 \mu\text{m}$ and the initial particle cloud extending from $r=5.9-8.68 \text{ cm}$: (a) L ; (b) $\ln(\rho)$ contours at $t/t_o \sim 130$ and (c) L/h . The circles in (a)&(c) denote the 3D simulation results.	190
64	Bubble similarity from the 3D simulation for $\eta=2$, $r_p=5 \mu\text{m}$ and the initial particle cloud extending from $r=5.9-8.68 \text{ cm}$	192
65	Bubble amplitudes obtained from the BD model for the case corresponding to $\eta=1$, $r_p=5 \mu\text{m}$ and initial cloud extending from $r=5.9-8.68 \text{ cm}$. The circles denote the 3D simulation results.	193
66	Detonation of a 11.8 cm diameter Nitromethane charge with a dense loading of steel particles: (a) trajectory and (b) shock overpressure. The experimental data is obtained from [214].	197
67	Flow topography at (a) 0.38 msec and (b) 0.98 msec. The legend denotes the pressure field in Pa.	198
68	Average acceleration/deceleration due to viscous drag, pressure drag (gas pressure gradient) and inter-particle collision/contact.	200
69	Wave diagram comparing the primary and secondary shock trajectories for homogeneous (NM) and heterogeneous (NM/Fe) charges containing the same amount of high explosive.	201
70	Pressure (a) and momentum flux (b & c) profiles for NM and NM/Fe charges at 0.9 m (a & b) and 1.55 m (a & c).	202
71	Flow field behind the blast wave: (a) average particle velocity and (b) average local gas velocity for different groups of particles. The diamond symbols indicate the times at which half the number of particles belonging to the corresponding group have penetrated the shock front.	203
72	Impulsive loading of a heterogeneous explosive: (a) total impulse and its components and (b) comparison between NM and NM/Fe charges. In (a), the line with the circles represents the ratio between the solid and gas momentum impulses and corresponds to the right y -scale; in (b), the line with the circles represents the ratio of the total impulses due to NM/Fe and NM and corresponds to the right y -scale.	205
73	Transient impulse and its components for a heterogeneous explosive at radial locations: (a) 0.5 m and (b) 2.25 m.	207

74	Effect of collision model: shock and particle front trajectories for different collision/contact model coefficients (P_s) (the results for the 0 MPa case are nearly coincident with the 100 MPa case, and thus the former is not clearly visible).	208
75	Effect of collision model on the (a) solid momentum flux and (b) total impulse.	210
76	Effect of particle size on the primary blast wave and particle front trajectories. Experimental data is from [214]; experimental particle front for the 275 μm size not available in [214].	212
77	Effect of particle size on the solid momentum flux profiles at 0.9 m.	213
78	Effect of particle size: (a) total impulse; (b) components of total impulse expressed as a percentage of the total. The arrows in (b) denote the left or right y -scale to which each curve corresponds.	214
79	Effect of gas pressure gradient on the solid momentum flux at the 0.9 m location.	216
80	Effect of initial volume fraction: (a) blast wave and particle front trajectories; (b) total impulse. In (b), the ratio of the total impulse values computed at $\alpha_{p,initial}=0.3$ and $\alpha_{p,initial}=0.62$ is represented by the curve annotated with circles.	217
81	Grid independence. Profiles at 4 msec: (a) rms of velocity profiles (blue: u_r , red: u_θ , green: u_ϕ); (b) resolved turbulent KE.	219
82	Mixing layer profiles shown at different times: (a) 0.13 msec, (b) 0.58 msec, (c) 1.52 msec, and (d) 4.02 msec.	220
83	(a) Y_{CO_2} ; (b) Temperature (K); (c) Y_{CO} contours in the mixing layer at 4 msec. In order to illustrate the structure of the mixing layer, the solid particles are not shown.	222
84	Mixing layer mean ((a) & (b)) and rms ((c) & (d)) velocity profiles shown at 2.2 msec ((a) & (c)) and 4 msec ((b) & (d)).	223
85	Y_{CO} profiles in the mixing layer normalized with the initial CO mass fraction in the detonation products, Y_{CO}^i : (a) mean; (b) rms.	224
86	Turbulent kinetic energy profiles: (a) resolved; (b) sub-grid.	225
87	Flame dynamics in the mixing layer: Temperature (K) and $\dot{\omega}_{CO}$ ($\log(\exp(-2)-\dot{\omega}_{CO})$) profiles at times (a) 1.42 msec; (b) 2.21 msec; (c) 4.02 msec. Temperature on the left and $\log(\exp(-2) - \dot{\omega}_{CO})$ on the right.	229
88	CO mass fraction gradient in the mixing layer at times (a) 0.22 msec; (b) 1.04 msec; (c) 1.62 msec; (d) 4.02 msec. The quantity $\log(\exp(-2)+ \nabla Y_{CO})$ is presented.	230

89	Comparison of homogeneous (NM) and heterogeneous (NM/Fe) explosives at 4 msec: (a) rms of velocity profiles (blue: u_r , red: u_θ , green: u_ϕ); (b) rms of Y_{CO} ; (c) resolved and sub-grid turbulent KE.	232
90	Comparison of the homogeneous (NM) and heterogeneous (NM/Fe) explosive charges containing the same amount of the high explosive: (a) mixing layer boundaries; (b) mixing layer width (δ). For the curve-fit expressions in (b), t is computed in msec.	233
91	Comparison of $463\mu\text{m}$ and $925\mu\text{m}$ particle sizes at 4 msec: (a) rms of velocity profiles (blue: u_r , red: u_θ , green: u_ϕ); (b) rms of Y_{CO} ; (c) resolved and sub-grid turbulent KE.	235
92	Comparison of the $463\mu\text{m}$ and $925\mu\text{m}$ particle sizes: (a) mixing layer boundaries; (b) mixing layer width (δ).	236
93	Aluminized explosive charges ($r_p = 2.5 \mu\text{m}$; 40 % initial solid volume fraction): gas temperature (in K) and particle locations at (a) 0.1 msec, (b) 0.215 msec; (c) particle radius in μm at 0.215 msec (only leading particles shown).	240
94	Effect of particle size on aluminized explosive charges: (a) normalized mass of solid Al remaining; (b) particle front trajectory; (c) average particle temperature; (d) average particle velocity.	241
95	Effect of particle size on afterburn effects of aluminized explosive charges: (a) mass fraction of C(S) remaining; and (b) fire-ball radius.	243
96	Effect of initial solid volume fraction on aluminized explosive charges containing $r_p = 5 \mu\text{m}$ particles: (a) mass of solid Al remaining; (b) particle front trajectory; (c) average particle temperature; (d) average particle velocity.	244
97	Effect of initial solid volume fraction on the afterburn effects of aluminized explosive charges containing $r_p = 5 \mu\text{m}$ particles: (a) mass fraction of C(S) remaining; (b) fire-ball radius.	245
98	Effect of initial solid volume fraction on aluminized explosive charges containing $r_p = 2.5 \mu\text{m}$ particles: (a) mass of solid Al remaining; (b) particle front trajectory; (c) average particle temperature; (d) average particle velocity.	246
99	Effect of initial solid volume fraction on the afterburn effects of aluminized explosive charges containing $r_p = 2.5 \mu\text{m}$ particles: (a) mass fraction of C(S) remaining; (b) fire-ball radius.	247
100	Effect of burn time on aluminized explosive charges: (a) mass of solid Al remaining; (b) particle front trajectory; (c) average particle temperature; (d) average particle velocity; (e) fire-ball radius.	248

101	Detonation wave profile (a) pressure (non-dimensional) and (b) velocity (non-dimensional) for the calorically perfect gas equation of state. . .	261
102	Initial profiles for the homogeneous 11.8 cm dia NM/TNT/HMX charges: (a) pressure; (b) velocity.	262
103	Initialization for the detonation simulations involving homogeneous (NM) and heterogeneous (NM/Fe) explosive charges: (a) pressure and (b) velocity.	263

NOMENCLATURE

Roman Symbols

a	Speed of sound
A	(i) Surface area; (ii) Atwood number
$A_{c,i}$	i -direction acceleration due to inter-particle collision/contact
\tilde{A}	Post-shock modified Atwood number
Bi	Biot number
c	Speed of sound
C	Bubble drag coefficient
C_a	Added mass coefficient
C_D	Drag coefficient
C_p	Specific heat at constant pressure per unit mass
C_v	Specific heat at constant volume per unit mass
C_ϵ	Sub-grid model constant
C_ν	Sub-grid model constant
\tilde{C}	Modified drag coefficient for bubbles
d_p	Particle diameter
dA	Differential surface area
dV	Differential control volume
D	Detonation velocity
D_k	k -th species diffusion coefficient
e	Internal energy per unit mass
E	Total energy per unit mass
F	(i) Conservative flux vector; (ii) x -direction flux vector
$F1$	Non-conservative flux vector
\dot{F}_p	Inter-phase momentum transfer

g	Acceleration driving the perturbation
G	y -direction flux vector
h	Bubble amplitude
h_k	Specific enthalpy of k -th species
H	(i) Total enthalpy per unit mass; (ii) z -direction flux vector
i, j, k	Computational grid indices
I	Impulse
k^{sgs}	Subgrid kinetic energy
L	Bubble transverse scale
Le	Lewis number
L_o	Flow length scale
L_v	Latent heat of vaporization
m	Mode number
m_p	Solid particle mass
MW_k	Molecular weight of the k -th species
n	Direction cosines
Nu	Nusselt number
p	Pressure
Pr	Prandtl number
P_s	Collision model constant
q_j	Heat flux vector
Q	(i) Conservative variable vector; (ii) Detonation energy release
\dot{Q}_p	Inter-phase heat transfer
r	(i) Radius; (ii) Spherical coordinate variable
r_i	Instantaneous interface radius
R	Mixture average gas constant
Re	Reynolds number

R_u	Universal gas constant
S	(i) Source term vector; (ii) Riemann solver wave speed
Sc	Schmidt number
St	Stokes number
S_{ij}	Strain rate tensor
$\dot{S}_{p,k}$	Inter-phase species mass fraction transfer for the k -th species
t	Time
t_b	Burn time
T	Temperature
u	x -direction velocity
u_i	Cartesian velocity tensor component
u_{inst}	Instability velocity
U	Vector of flow variables
U_o	Flow velocity scale
v	y -direction velocity
Vol	Control volume
$V_{j,k}$	j -direction diffusive velocity
w	z -direction velocity
\dot{W}_p	Inter-phase work transfer
x, y, z	Cartesian coordinate directions
Y_k	k -th species mass fraction
$Y_{i,k}^{sgs}$	Sub-grid convective k -th species flux

Greek Symbols

α	Volume fraction
α_{cs}	Volume fraction at close packing

β	Collision model constant
γ	Ratio of specific heats
δ_{ij}	Kronecker delta
$\Delta_x, \Delta_y, \Delta_z$	Local grid dimension in x , y or z
ϵ	Emissivity
ζ	Computational grid variable corresponding to k index
η	(i) Computational grid variable corresponding to j index; (ii) Particle mass loading ratio
η^*	Post-shock density ratio
θ	Spherical coordinate variable
$\theta_{i,k}^{sgs}$	Sub-grid diffusive species flux
κ	Thermal conductivity
λ	(i) Bulk viscosity; (ii) DEM indicator function; (iii) Bubble wavelength; (iv) Reaction progress variable
μ	Gas viscosity
ν_t	Eddy viscosity
ξ	Computational grid variable corresponding to i index
ρ	Density
$\dot{\rho}_p$	Inter-phase mass transfer
σ	Stefan-Boltzman constant
σ_i^{sgs}	Sub-grid viscous work
τ_{ij}	Viscous stress tensor
τ_{ij}^{sgs}	Subgrid stress tensor
ϕ	Spherical coordinate variable
χ	Scaled distance
ω	Radial velocity gradient evaluated at the instantaneous interface
$\dot{\omega}_k$	k -th species reaction rate

Subscripts

g	Gas
p	Particle
0	Reference quantity
i, j, k	Cartesian tensor indices
t	Turbulent quantity

Superscripts

n	Time step index
sgs	Subgrid scale
$*$	Interface quantity

Other Symbols

∂	Partial derivative
∇	Gradient operator
$\nabla \cdot$	Divergence operation
\sum	Summation
$\langle \phi \rangle$	Ensemble averaging of ϕ
$\tilde{\phi}$	Resolved scale of ϕ
ϕ''	Unresolved scale of ϕ
$\bar{\phi}$	Filtered value of ϕ
$[\lambda]$	Jump in the indicator function (used in DEM)

Abbreviations

<i>CFD</i>	Computational Fluid Dynamics
<i>CFL</i>	Courant-Friedrichs-Levy
<i>CJ</i>	Chapman-Jouguet
<i>DDT</i>	Deflagration-to-Detonation Transition
<i>DEM</i>	Discrete Equations Method
<i>DM</i>	Degree of Mixedness
<i>DNS</i>	Direct Numerical Simulation
<i>EE DEM</i>	Eulerian-Eulerian Discrete Equations Method
<i>EL DEM</i>	Eulerian-Lagrangian Discrete Equations Method
<i>EOS</i>	Equation of State
<i>GISPA</i>	Gas-Interpolated-solid-Stewart-Prasad-Asay
<i>HLL</i>	Harten-Lax-van Leer
<i>HLLC</i>	Harten-Lax-van Leer-Contact
<i>HLLD</i>	Harten-Lax-van Leer-Einfeldt
<i>HMX</i>	High Melting Explosive
<i>JWL</i>	Jones-Wilkins-Lee
<i>LDKM</i>	Localized Dynamic <i>k</i> -equation Model
<i>LE</i>	Leading Edge
<i>LES</i>	Large-Eddy Simulation
<i>ML</i>	Mixing Layer
<i>MUSCL</i>	Monotone Upstream centered Schemes for Conservation Laws
<i>NM</i>	Nitromethane
<i>PPM</i>	Piecewise Parabolic Method
<i>PS</i>	Primary Shock
<i>RANS</i>	Reynolds Averaged Navier-Stokes
<i>RDX</i>	Research Department Explosive

<i>RMI</i>	Richtmyer-Meshkov Instability
<i>RTI</i>	Rayleigh-Taylor Instability
<i>rms</i>	Root Mean Square, Variance
<i>SDF</i>	Shock Dispersed Fuel
<i>SS</i>	Secondary Shock
<i>TE</i>	Trailing Edge
<i>TNT</i>	Tri-Nitro Toluene
<i>WENO</i>	Weighted Essentially Non-Oscillatory

SUMMARY

The flow field behind chemical explosions in multiphase environments is investigated using a robust, state-of-the-art simulation strategy that accounts for the thermodynamics, gas dynamics and fluid mechanics of relevance to the problem. Focus is laid on the investigation of blast wave propagation, growth of hydrodynamic instabilities behind explosive blasts, the mixing aspects behind explosions, the effects of afterburn and its quantification, and the role played by solid particles in these phenomena. In particular, the confluence and interplay of these different physical phenomena are explored from a fundamental perspective, and applied to the problem of chemical explosions.

A solid phase solver suited for the study of high-speed, two-phase flows has been developed and validated. This solver accounts for the inter-phase mass, momentum and energy transfer through empirical laws, and ensures two-way coupling between the two phases, viz. solid particles and gas. For dense flow fields, i.e., when the solid volume fraction becomes non-negligible ($\sim 60\%$), the finite volume method with a Godunov type shock-capturing scheme requires modifications to account for volume fraction gradients during the computation of cell interface gas fluxes. To this end, the simulation methodology is extended with the formulation of an Eulerian gas, Lagrangian solid approach, thereby ensuring that the so developed two-phase simulation strategy can be applied for both flow conditions, dilute and dense alike. Moreover, under dense loading conditions the solid particles inevitably collide, which is accounted for in the current research effort with the use of an empirical collision/contact model

from literature. Furthermore, the post-detonation flow field consists of gases under extreme temperature and pressure conditions, necessitating the use of real gas equations of state in the multiphase model. This overall simulation strategy is then extended to the investigation of chemical explosions in multiphase environments, with emphasis on the study of hydrodynamic instability growth, mixing, afterburn effects ensuing from the process, particle ignition and combustion (if reactive), dispersion, and their interaction with the vortices in the mixing layer.

The problems of chemical explosions into air as well as dilute aluminum particle clouds are investigated, and hydrodynamic instabilities such as Rayleigh-Taylor and Richtmyer-Meshkov are observed in the post-detonation regime. These instabilities inevitably give rise to a mixing layer where the inner detonation products mix with the outer air and afterburn. The growth of these hydrodynamic instabilities, and the amount of mixing and afterburn are investigated for a suite of identified parameters. The particles in the ambient cloud, when present, are observed to pick up significant amounts of momentum and heat from the gas, and thereafter disperse, ignite and burn. Small particles which have response time scales comparable to the fluid mechanic time scales in the mixing layer, are observed to cluster as they traverse the mixing layer, which leads to their preferential ignition/combustion. Overall, this study demonstrates that three-dimensional effects such as hydrodynamic instabilities are crucial for the analysis of explosions in multiphase environments.

Building on the above accomplishments, the post-detonation behavior of heterogeneous explosives is addressed by using three parts to the investigation. In the first part, only one-dimensional effects are considered, with the goal to assess the presently developed dense two-phase formulation. The total deliverable impulsive loading from heterogeneous explosive charges containing inert steel particles is estimated for a suite of operating parameters and compared, and it is demonstrated that heterogeneous explosive charges deliver a higher near-field impulse than homogeneous explosive charges

containing the same mass of the high explosive. In the second part, three-dimensional effects such as hydrodynamic instabilities are accounted for, with the focus on characterizing the mixing layer ensuing from the detonation of heterogeneous explosive charges containing inert steel particles. It is shown that particles introduce significant amounts of hydrodynamic instabilities in the mixing layer, resulting in additional physical phenomena that play a prominent role in the flow features. In particular, the fluctuation intensities, fireball size and growth rates are augmented for heterogeneous explosions *vis-à-vis* homogeneous explosions, thereby demonstrating that solid particles enhance the perturbation intensities in the flow.

In the third part of the investigation of heterogeneous explosions, dense, aluminized explosions are considered, and the particles are observed to burn in two phases, with an initial quenching due to the rarefaction wave, and a final quenching outside the fireball. Due to faster response time scales, smaller particles are observed to heat and accelerate more during early times, and also cool and decelerate more at late times, compared to counterpart larger particle sizes. Furthermore, the average particle velocities at late times are observed to be independent of the initial solid volume fraction in the explosive charge, as the particles eventually reach an equilibrium with the local gas. These studies have provided some crucial insights to the flow physics of dense, aluminized explosives.

Overall, a wide range of physical phenomena has been studied in relation to hydrodynamic instabilities in multiphase chemical explosions, on mixing and afterburn effects, on particle ignition and burning (when reactive), and particle dispersion characteristics due to explosions. In addition, these investigations also demonstrate the efficacy of the presently developed two-phase formulation to study dense, two-phase, high-speed, reacting flows—a problem still in its infancy.

CHAPTER I

INTRODUCTION AND REVIEW

1.1 Introduction

One of the earliest use of explosive material was in the form of Gunpowder, and was invented, documented, and used in ancient China by the military forces of the time in rockets, guns and cannons. Later, the technology of explosives spread to other parts of the world, and with further research, developed from low-yield explosives to high explosives with enhanced destructive power. High explosives have been in use for many centuries and have also found applications outside the military. Civilian applications of explosives include commercial blasting for construction or mining, fire-fighting (especially in the petroleum industry), metal welding and forming, etc. Many different types of explosives are in use with different strengths and signatures, and these characteristics determine their application. A proper understanding of the physics that govern their behavior is essential to the research and development of the next generation of explosives with tailored performance characteristics. Experimental studies are often expensive and hazardous, and data collection can be cumbersome due to the very high temperatures and pressures in the flow field. In addition, the post-detonation flow field is inevitably sensitive to hydrodynamic instabilities involving a wide range of time and length scales, all of which cannot be measured. Computational simulations can therefore play a vital role in investigating the governing physics, provided efficient and state-of-the-art simulation tools are used.

Solid particles are widely used along with explosives, as they augment the impulsive loading delivered. The mechanism of impulse augmentation from explosives due to solid particles can be classified into two kinds: (1) impulse augmentation due to

bombardment and (2) impulse augmentation due to afterburn. In the former, the particles pick up momentum from the gas very early, and by virtue of their inertia, retain most of their momentum for a longer time. Upon bombardment with a structure, the contribution to the total impulse is due to both the gas and the solid particles. Since solid particles have a higher inertia than the gas, enhanced deliverable impulse on the structure can be made available due to direct particle bombardment. On the other hand, for impulse augmentation of the second kind, chemically reactive solid particles are added to explosive charges. These particles acquire heat from the explosion and may melt, ignite and/or burn, releasing additional energy into the multiphase flow field.

Naturally, heavy and large inert solid particles such as steel, tungsten and lead are ideal candidates for impulse augmentation due to direct bombardment as they have high inertia and can therefore retain most of their momentum for a longer time and space. For the use of solid particles of the second kind with explosives, chemically-reactive particles such as aluminum, magnesium and zirconium are ideal candidates. Obviously, these particles have to be small in size so that they can easily pick up heat from the gas and subsequently ignite. For both the first and the second kind, the solid particles may be present inside the charge or encapsulated in an outside shell. The advantages and disadvantages of using solid particles within the charge *vis-á-vis* outside are still not well understood, and further investigations are warranted. To this end, this study assesses these different explosive-solid particle configurations from a fundamental perspective.

Upon explosive dispersal, solid particles initially pick up momentum and heat from the gas. The early forces on the particles are primarily due to viscous drag, pressure drag, and inter-particle collisions (if dense), all of these forces have varying magnitudes that change with time. The viscous drag coefficient is generally higher under dense loading conditions, as the gas flow around a spherical particle will be

affected by the presence of other particles in the close vicinity. After particles pick up significant amounts of momentum, they are set into motion, and by virtue of their higher inertia than the gas, preserve a significant enough amount of their momentum. Furthermore, at early times, heat transfer—both convective as well as radiative—can also be significant depending on the particle size, and can raise the particle temperature. If particles are reactive (for instance aluminum), they may reach an ignition temperature, after which they can burn. Much later, as the particles disperse outward due to the explosion, large particles may even catch-up with the leading blast wave and can overtake it. Aerodynamic drag may slow down the particles, thereby reversing the momentum transfer between the two phases in relation to that at earlier times. In addition, at later times, the local gas may also be cooler than the particles, thereby reversing the flow of heat transfer between the two phases as well. It is of interest to quantify the effects of the inter-phase momentum and heat transfer at different stages of the explosive dispersal, and this study also investigates these inter-phase coupling aspects.

The primary focus of this study, *inter alia*, is on characterizing the growth of hydrodynamic instabilities, mixing and afterburn effects involved in chemical explosions, and the role played by solid particles to the same. In addition, also of interest are the particle burning (if reactive) and dispersion aspects due to explosions, and their interaction with the ensuing hydrodynamic instabilities.

1.1.1 On the physics of explosions

The basic premise of a chemical explosion from a high explosive is as follows: when a condensed explosive charge is detonated, a detonation wave propagates through the unreacted explosive material. The detonation wave is essentially a reactive shock wave, and in the thickness of this wave, the unreacted explosive is converted into detonation product gases and soot. As this detonation wave reaches the outer surface

of the explosive charge, a blast wave propagates outward, and a rarefaction wave inwards, forcing an outward acceleration of the detonation product gases. A schematic representation is presented in Fig. 1. The contact surface between the detonation products and the shock compressed air is swept outward by the exploding detonation product gases. Due to the high density gradient, the contact surface is hydrodynamically unstable to perturbations, and a slight distortion of the equilibrium between the heavy and the light fluids on either side can grow, resulting in Rayleigh-Taylor [192] instabilities.

At the same time, the inward moving rarefaction wave may also over-expand the flow and result in the formation of a secondary shock [34]. The secondary shock is initially weak, and is swept outward by the detonation product gases. During this time, the secondary shock strengthens, and subsequently implodes inward [34]. When the secondary shock reflects from the origin, it propagates outward and interacts with the Rayleigh-Taylor structures, giving rise to further growth of these hydrodynamic instabilities, this time in the form of Richtmyer-Meshkov instabilities [169]. Such hydrodynamic instabilities inevitably result in a non-spherically symmetric fireball, as is evidenced by experimental photography shown in Fig. 2. During this interaction, a second rarefaction wave can also be generated moving inward. This rarefaction wave, like its predecessor, can also over-expand the flow, giving rise to a tertiary shock. This process of subsequent shock formation repeats until most of the energy of the detonation product gases is expended as kinetic energy of the outward flow [34].

The scale of the instability growth is critical to the mixing process between the detonation products and the shock-compressed air. If the initial surface of the charge is rough, the initial instabilities start to grow from the scale of the surface roughness. On the other hand, if the initial charge surface is hydrodynamically smooth, the instabilities start to grow from molecular scales at a rate predicted by the linear stability theory [38]. In both scenarios, the instabilities grow to macroscopic scales

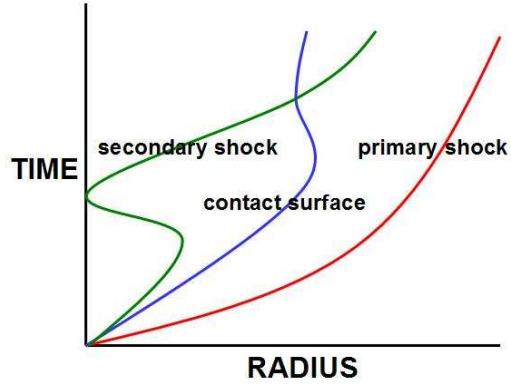


Figure 1: Wave diagram of the flow field in the post-detonation phase of a high explosive charge.



Figure 2: Non-spherical fireballs from chemical explosions.

and form a turbulent mixing layer. The resulting inevitable mixing between the core detonation products and the outer air results in afterburn, which occurs at a rate controlled by turbulent mixing, rather than by molecular diffusion [120]. The role of these hydrodynamic instabilities is significant, as it dictates the amount of mixing and afterburn, which are crucial for carbon-rich explosives such as TNT.

1.1.2 Simulation challenges

Numerical simulation of both homogeneous and heterogeneous explosives involves several complex physical phenomena that have to be captured in order to successfully predict their behavior. These complex phenomena include, but are not limited to,

the Deflagration to Detonation Transition (DDT) [68] in an explosive charge, blast wave propagation and subsequent decay, shock-particle interaction, particle-particle collision, inter-phase momentum and energy transfer, growth of hydrodynamic instabilities, afterburn and the concomitant energy release, particle ignition and burning (if reactive), particle clustering effects (for small particles), and impact material behavior to shock and particle cloud bombardment. These various physical phenomena must be properly accounted for in order to make accurate computations.

Computational studies offer promise and leverage in the elucidation of the physics that governs the blast characteristics and mixing behind explosions. Many computational methodologies rely on the finite volume scheme, where the simulation domain is broken down into a series of finite volumes [7, 129, 191, 194]. Using the conservation laws, flux vectors are calculated at each cell face. In turn, these vectors are used to compute volume averaged properties in each cell. The methodology employed to compute the fluxes decides the overall accuracy of the simulation strategy, and is often problem dependent. For instance, when the flow field involves strong discontinuities such as shock waves and contact surfaces, a shock-capturing scheme such as MUSCL (Monotone Upstream-centered Schemes for Conservation Laws) [200] or WENO (Weighted Essentially Non-Oscillatory) [132], or higher order Godunov schemes such as PPM (Piecewise Parabolic Method) [47] are required, along with a Riemann solver to compute the fluxes at the cell boundaries [194]. For smooth flow regions such as shear layers, on the other hand, a central scheme is required, as shock-capturing schemes are dissipative by nature. This necessitates the use of a hybrid approach that computes fluxes based on a shock-capturing or higher order Godunov scheme in sharp regions, and a central scheme in smoother regions [78, 79]. Furthermore, for time accuracy of the simulations, a predictor-corrector [138] or Runge-Kutta type integration are common and widely used in Computational Fluid Dynamic (CFD) codes [7, 129]. Thus, simulation strategies need to incorporate appropriate

schemes to compute the fluxes, for this inevitably decides the overall accuracy of the computed results.

Another challenge of the current investigation pertains to the presence of two phases, viz. gas and solid particles, and both are generally governed by different physics; in addition, both phases also interact. This necessitates the use of governing equations for each phase to also account for the existence and interaction of the other phase. While the gas phase is generally solved by means of an Eulerian approach with the assumption of continuum validity, the dispersed phase (solid or liquid, as the case may be) can be solved either by an Eulerian approach similar to the gas, or by a Lagrangian approach [51]. In the former, also termed Eulerian-Eulerian (EE), continuum is assumed to govern the behavior also of the dispersed phase; this is not the case in the latter, also termed Eulerian-Lagrangian (EL), in which the particle trajectories are determined explicitly due to the tracking of individual particles (or groups of particles).

Both EE and EL approaches have been used in past studies to investigate fluid-particle problems, and both approaches have their own advantages and disadvantages. The EE approach allows no restrictions on the number of particles that can be considered for a simulation, since individual particles are not tracked but only their number density is evaluated. However, the EE approach suffers from its inability to predict individual particle trajectories. The EL approach, on the other hand, tracks individual particles (or groups of particles), thereby enabling the estimation of particle trajectories. However, the major drawback of the EL approach is that the total number of particles (or groups) that can be accounted is restricted by available computational memory. For instance, the computation of a 1 m radius cloud comprising of 10 μm radius particles with a volume fraction of 1% will require 10,000,000,000,000 particles—each of which cannot be tracked with present day computing power. Many engineering applications involving two-phase flows usually require sufficiently large

number of particles to be tracked, which can be achieved—to some extent—using the concept of a parcel [51, 160, 186]. Here, a parcel represents a group of particles with the same particle position vectors, velocity vectors, radius and temperature. The number of particles assigned to each parcel is chosen based on available computational memory and the desired particle concentration/loading. It must, however, be ensured that the computational accuracy is not compromised when too many particles are assigned per parcel. Due to the aforesaid advantages of the EL approach, the current study employs this simulation strategy.

Heterogeneous explosions involve solid particles in the dense regime [75]. By dense, it is referred to the flow-field being characterized by significantly large amounts of solid particles, thereby rendering the total volume to not be exclusively available to any one phase, gas or solid. Due to this non-negligible volumes occupied by the two phases, additional modifications have to be included in the simulation strategy. To better illustrate this discussion, the gas phase Navier-Stokes equations, applicable in dense two-phase flows in the absence of body forces are summarized as [1, 11, 40, 44, 106]:

$$\begin{aligned}
\frac{\partial}{\partial t} \begin{bmatrix} \alpha_g \rho_g \\ \alpha_g \rho_g u_{g,i} \\ \alpha_g \rho_g E_g \\ \alpha_g \rho_g Y_{g,k} \end{bmatrix} + \frac{\partial}{\partial x_j} \begin{bmatrix} \alpha_g \rho_g u_{g,j} \\ \alpha_g \rho_g u_{g,i} u_{g,j} + \alpha_g p_g \delta_{ij} - \alpha_g \tau_{g,ij} \\ \alpha_g (\rho_g E_g + p_g) u_{g,j} - \alpha_g u_{g,i} \tau_{g,ji} + \alpha_g q_{g,j} \\ \alpha_g \rho_g Y_{g,k} (u_{g,j} + V_{g,j,k}) \end{bmatrix} = \\
\begin{bmatrix} 0 \\ p^* \frac{\partial \alpha_g}{\partial x_j} \delta_{ij} - \tau_{ij}^* \frac{\partial \alpha_g}{\partial x_j} \\ p^* u_j^* \frac{\partial \alpha_g}{\partial x_j} - u_i^* \tau_{ij}^* \frac{\partial \alpha_g}{\partial x_j} \\ \dot{\omega}_k \end{bmatrix} + \begin{bmatrix} \dot{\rho}_p, \\ \dot{F}_{p,i}, \\ \dot{Q}_p + \dot{W}_p, \\ \dot{S}_{p,k}. \end{bmatrix} \quad (1)
\end{aligned}$$

The above equations and the flow variables will be described in detail in Chapter 3. As evident, the governing equations are in a non-conservative form, where conservative form refers to the representation of these equations in the form:

$$\frac{\partial Q}{\partial t} + \frac{\partial F}{\partial x_j} = S, \quad (2)$$

and non-conservative form corresponds to

$$\frac{\partial Q}{\partial t} + \frac{\partial F}{\partial x_j} = F1 \frac{\partial \alpha_g}{\partial x_j} + S. \quad (3)$$

The non-conservative terms, also referred to as “nozzling terms” [1], inhibit the use of a Hugoniot-type Riemann solver [194] directly. These terms have to be integrated at cell interfaces which encounter volume fraction discontinuities. Furthermore, another challenge with dense two phase flows pertains to the closure used for the pressure and velocity at the interface, which has to be appropriately evaluated. In addition, suitable models have to be used to account for the presence of inter-particle collisions and contact, which will be significant for dense flow fields. These aspects are taken into account in the present simulation strategy, and it is ensured that their efficacy is not compromised when applied in conjunction with the other numerical developments.

The problem currently under study involves high density gradients across the contact surface, which inevitably leads to a Rayleigh-Taylor Instability (RTI) [192]. A RTI is a hydrodynamic instability that occurs when an interface separating high and low density fluids is accelerated, with small perturbations growing into larger scale structures. Although RTI have been studied in the past by numerous researchers, their application to a chemical explosion is still in its infancy. Explosive charges are generally not “hydrodynamically smooth,” resulting in perturbations on the contact surface/interface at the onset of detonation. Even if the surface of the explosive charge is smooth, perturbations still exist at the molecular scales. In both scenarios, these perturbations inevitably grow into a RTI. At the later stages of an explosion, a secondary shock [34] propagates outward and interacts with the hydrodynamic structures, across which density gradients still exist. This impulsive acceleration of a density interface is termed as a Richtmyer-Meshkov Instability (RMI) [169], and grows

at different rates *vis-à-vis* a RTI. Such hydrodynamic instabilities are encountered in various engineering applications such as Scramjets [78] and explosions [74, 120, 121], as well as natural phenomena such as supernovae explosions [151, 152]. These instabilities will also be described in more detail later as they are of direct relevance to the current problem of interest. In addition, particles can also interact with these hydrodynamic instabilities, thereby giving rise to different dispersion characteristics, and will also be investigated in this study.

The flow field behind explosions inevitably transitions to turbulence after the aforementioned hydrodynamic instabilities break down, cascading kinetic energy from larger to smaller scales. Moreover, when solid particles are present in an explosion, they often introduce perturbations that augment turbulence in the flow. Thus, during the later stages of explosions, a range of time and length scales exist, which pose a great computational challenge. One approach to solve for fluid turbulence is by Direct Numerical Simulation (DNS), where all scales are resolved. However, present day computational resources do not permit the resolution of most engineering problems, thereby necessitating the use of other simulation strategies. To this end, often only the large scales are resolved in simulations, and appropriate models are used to account for the effect of the small scales (also termed as sub-grid scales) on the large scales. Generally, universality of the small scales—first envisioned by Kolmogorov in 1941 [115, 116]—is exploited to formulate the sub-grid model. This separation of scales enables robust CFD simulations of many engineering problems, and offers a useful tool for the design and development of various practical systems in aerospace, mechanical, chemical, civil and petrochemical industries. Both incompressible as well as compressible turbulence have been studied in the past, and often require different modeling approaches. To permit the resolution of the relevant scales, the current formulation employs a one-equation sub-grid kinetic equation to model the small scales, the mathematical form will be elaborated upon later.

1.2 *Literature Review*

In this section, some of the past work on pertinent physics and computational approaches that are of direct relevance to the current research effort are presented.

1.2.1 Two-phase modeling

Research on two-phase modeling has been undertaken extensively in the past, and detailed discussions of early research works can be identified by the review papers of Gokhale & Krier [89] and Drew [59]. Two approaches are common in the modeling of two-phase flows as aforementioned: Eulerian-Eulerian and Eulerian-Lagrangian. In this section, the Eulerian-Eulerian modeling approach is reviewed first, followed by the Eulerian-Lagrangian approach.

One of the very popular numerical studies of two-phase granular flows was undertaken by Baer & Nunziato [11], where Deflagration to Detonation Transition (DDT) in granular explosives such as HMX was studied employing a two-fluid Eulerian-Eulerian model. The presence of non-conservative terms (discussed earlier in this chapter) in the governing equations was identified, and closures were required for interface velocity and pressure. This two-phase model, despite some minor weaknesses, forms the basis for many two-phase approaches to come in the later years. In particular, issues related to interface closures, treatment of non-conservative terms, handling of equations of state for mixtures, etc., have been widely addressed in the coming years with this model as the baseline. For instance, the non-conservative terms were treated like source terms in [20, 106], and were neglected in [91]—both these approaches have no physical justification. In the former ([20, 106]), the treatment of these terms as source terms negates their proper evaluation at volume fraction discontinuities; in the latter ([91]), pressure forces at volume fraction discontinuities will inhibit a dense multi-phase system at rest to continue to remain at rest. In another approach, Sainsaulieu [174] introduces additional viscous effects to regularise the solution, and estimate the

solution under the limit of a viscosity parameter tending to zero. The mathematical treatment of the non-conservative term may have a significant impact on the solution [101], thereby emphasizing that this term should be accurately computed.

A step aimed to address two-phase modeling issues was undertaken by Saurel & Abgrall [175], focusing on micro-scale motion by accounting for relaxation parameters for pressure and velocity. Building on this achievement, the same research group extended the approach to the Discrete Equations Method (DEM) [1], in which the system of equations are discretely solved for both phases and then averaged. Stated in these terms, volume fraction discontinuities are allowed at inter-cell interfaces, where the fluxes are evaluated as a summation of multiple combinations of pure-fluids on either side. This approach permits the use of pure fluid equations of state (EOS) for each fluid, unlike the use of a mixture EOS in previous approaches. Later, the authors extended the study to heterogeneous detonation [44] and to evaporating fronts [125]. A description of using different interface pressure closures in the DEM was recently addressed [154].

Several other closely-related formulations also exist in literature from the same DEM originators, and have been applied to a wide variety of two-fluid problems such as cavitating flows and shocks in multiphase mixtures [176, 177, 179]. Recently, another research group independently developed an Eulerian-Eulerian approach very similar in mathematical form to the DEM, and successfully applied it to the study of shock-interface problems [39, 40]. All these approaches offer different simulation strategies for multiphase flow problems, and have different advantages and disadvantages.

Eulerian-Lagrangian approaches have also been employed in the past to model two-phase flows, in which the gas phase is treated to obey Eulerian continuum laws, and the discrete phase (solid particles or liquid droplets) is solved using a Lagrangian tracking approach. Andrews & O'Rourke [8] and Snider et al. [185] presented a

multiphase particle-in-cell (MP-PIC) method for particulate flows accounting for full coupling between the carrier and the dispersed phases. An inter-particle stress model was developed to empirically compute the force due to inter-particle interactions, which prevents the particle volume fraction from exceeding the close packing limit. A mapping procedure was used in these studies to obtain particle properties to and from an Eulerian grid. Later, Snider [186] extended the approach to the study of gravity-dominated sedimentation of particles, two-phase Rayleigh-Taylor instability under gravity, and gas-particle jets, thereby demonstrating the two-phase numerical approach for a range of problems, albeit in the low-speed regime. The same simulation strategy was then employed by Patankar & Joseph [160] and applied to study bubbling fluidized beds and gravity-dominated sedimentation under different conditions. These references have demonstrated the efficacy and challenges involved in Eulerian-Lagrangian modeling of two-phase flows.

The physics and mathematics of multiphase flows has also been elaborately discussed in the books by Gidaspow [81] and Crowe et al. [51]. The mathematics and computation of multicomponent flows is also comprehensively detailed in the book by Drew & Passman [60], with primary applications to bubbly liquids and particle-fluid mixtures, albeit in the low-speed regime. They derived the two-phase equations using ensemble averaging, and also discuss closure for dispersed flows from a fundamental perspective. Their exposition in terms of ensemble averaging was new, and forms the averaging procedure in many two-phase methods developed henceforth, including the Discrete Equations Method (DEM) [1, 44]. The choice of applying an appropriate method is problem dependent, thereby also emphasizing that the scope for the development of more robust two-phase methodologies still exists.

1.2.2 Homogeneous explosives

Several studies have been carried out in the past to study blast waves from homogeneous explosives, and based on available experimental data, scaling laws for blast wave decay and impulse have been reported in the past [12]. The earliest scaling law of Hopkinson (1915) [12] suggested that blast waves from two different charges of different mass, but of the same explosive, would have the same strength at the same scaled distance. This scaled distance (units: $mKg^{-1/3}$) is given by $r/W^{1/3}$, where r denotes the distance from the explosive in m , and W is the mass of the explosive in the charge in Kg . This scaling law forms the basis of many scaling laws proposed for explosives in the later years. For example, the Sachs scaling law (1944) [12] is a modification of the Hopkinson law to account for atmospheric conditions, and the scaled distance is given by $rp_o^{1/3}/E^{1/3}$, where p_o is the ambient pressure in *bar*, and E is the detonation energy from the charge in *Joules*. This scaling law assumes that air behaves as a perfect gas, and that the effects of viscosity and gravity are negligible [12]. Experiments of chemical explosions have been carried out for decades, and pressures and impulses have been consolidated by Kingery & Bulmash [113] and Kinney & Graham [114], both of which are widely used by the research community for comparisons. Another widely used scaling is the TNT equivalence, which has been reported for a few commercial blasting explosives [55, 69, 206]. However, recent experimental studies [93] on gram-range explosive charges has shown that a single TNT equivalence value is insufficient to represent the overall explosive strength. Thus, several such scaling laws and parameters exist to characterize the behavior of explosives, assuming one-dimensional post-detonation behavior of the explosion.

Numerical studies on blast effects from explosives have also been undertaken. Brode [34] undertook one of the first numerical studies of an explosive charge (TNT) using a one-dimensional assumption and presented overpressure impulse. This study was the first to show the presence of secondary and tertiary shocks in an explosion.

Another study focusing on bursting spheres was carried out by Vanderstraeten et al. [201], and they proposed an empirical model to estimate the peak overpressure as a function of the energy scaled distance. They also presented an empirical expression for the explosive efficiency as a function of the contact surface velocity. A general discussion of the phenomena involved in the estimation of blast loading from three explosive scenarios, i.e., from atomic weapons, conventional high explosives, and unconfined vapor cloud explosions on above-ground structures was reported by Beshara [28]. In this study, loading was characterized from dynamic pressure and reflected overpressure. A comparison of several scaling laws proposed for TNT has been reported [32] with simple curve-fit expressions for the blast wave parameters. In another one-dimensional study, the afterburn energy release was parametrically assumed [6] and it was postulated that the total energy release of explosions in closed chambers is a function only of the end-state quasi-static pressure. Recently, the blast effects were assessed from the simulation of explosions in a variety of city-like configurations [46], and compared to experimental observations. The role of multiple wave interactions was identified, thereby emphasizing that the presence of structures alters the blast characteristics of explosions compared to free-explosions.

All the above noted studies were based on a one-dimensional assumption of the blast effects from explosive charges. However, viewing photographic images of chemical explosions (Fig. 2), it is evident that three-dimensional effects such as hydrodynamic instabilities and turbulence are prominent; in particular, the fireball is non-spherically symmetric. The growth of instabilities in the contact surface of an explosive fireball was first reported by Anisimov & Zeldovich [9, 10]. They identified two limiting cases, i.e., when the length scale of the instability is much less than the distance between the primary and secondary shock (they refer to it as free Rayleigh-Taylor turbulence), and when the scale of the instability is of the same order. They

identified that the position of the secondary shock decides the spatial scale of the initial Taylor modes, and hence, the rate of mixing between the detonation products and the shock-compressed air. Kuhl et al. [120, 121], in a series of papers, performed a numerical investigation of the growth of hydrodynamic instabilities in explosives and its significance to the afterburn of the detonation products, using an adaptive mesh refinement (AMR) technique. Four different regimes/phases were identified by the authors: (i) blast wave, (ii) implosion, (iii) re-shock, and (iv) asymptotic mixing [120]. The study reported that while the mean kinetic energy decays rapidly, the fluctuating component asymptotes to a constant value at late times, thereby highlighting the turbulent nature of the mixing region. Baroclinic torque effect (misaligned pressure and density gradients) was observed to cause vorticity in the mixing region, which decays at late times. In [121], the authors reported that most ($\sim 90\%$) of the afterburn of the detonation products occurs in the asymptotic mixing phase, due to the merging of vortex rings and the accompanying wrinkling of the exothermic surface.

Recently, different kinds of explosions, viz. blast from pressure vessel rupture, blast from explosive evaporation of superheated liquids, fuel-air explosive blast and high-explosive blasts, were studied [27] with the goal to assess the “BLAST” software. Although this study demonstrates the differences in the physics involved for the different types of explosions, the effects of hydrodynamic instabilities—critical to the problem of explosions—was not addressed to detail. The current research effort will address these three-dimensional effects, the role of solid particles, mixing, and afterburn behind chemical explosions, etc., and characterize and quantify the same in order to provide valuable physical insights to the problem.

1.2.3 Heterogeneous explosives

Heterogeneous explosives are formed when solid metal particles are added to a charge of a high explosive. Although the fundamental understanding of the physics of heterogeneous explosives is still in its infancy, both experimental and numerical investigations of heterogeneous explosives have been undertaken and provide some valuable insights. The detonation of a heterogeneous explosive charge is characterized by a detonation velocity deficit in comparison with a homogeneous charge, as observed in experiments undertaken by Lee et al. [126], due to the associated momentum and energy transfer. Lanovets et al. [122] performed a numerical study based on a two-fluid approach and reported that for a certain range of particle size and density, the solid particles can catch-up with the shock front and overtake it. Milne [153] developed a mesoscale model to study detonation of a nitromethane charge with inert particles using a simple one step Arrhenius kinetics, and explained the increase in detonation failure diameter with particle size for small inert particles. A one-dimensional model of the steady-state detonation of a heterogeneous explosive with reactive particles was developed by Gonor et al. [90], and applied to study RDX charges comprising of aluminum particles. It was reported that ultra-dispersed aluminum particles ($0.1 \mu\text{m}$) burn completely in the RDX reaction zone, but $5 \mu\text{m}$ -sized aluminum particles do not. Furthermore, the authors also concluded that the reduction in mass fraction of the gaseous component of the detonation products is an important factor that affects the decrease in detonation velocity.

Later, Zhang et al. [214] carried out experimental and numerical studies to obtain the shock front and the particle cloud trajectory for a nitromethane charge containing steel particles. They found that for spherical and cylindrical charges, the possibility of the solid particles overtaking the shock front exists, but is highly unlikely for planar charges due to their lower attenuation rates. They also noted that the distance required for the large particles to overtake the shock front strongly depends on the

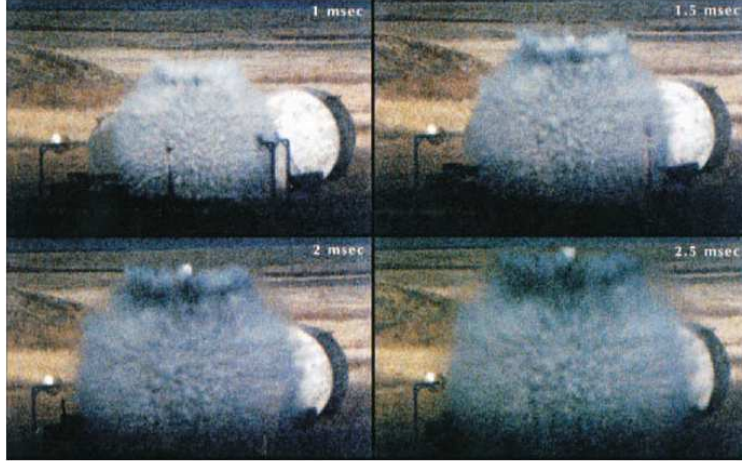


Figure 3: Photographic image of a heterogeneous explosion from [214].

charge size and material density, but weakly on the solid volume fraction. Photographic images of particle dispersal due to explosion are shown in Fig. 3 at different times, and indicate that for the large particle size considered ($463 \mu\text{m}$ steel), the exploding particle cloud is spherically symmetric. In addition, they also concluded that a particle size limit exists, above which the distance required for the particles to penetrate the shock front is less sensitive to the particle size, and below which, the distance required depends on particle size. In another study, Zhang et al. [215] reported that the momentum transfer from an explosive to the solid particles during the particle crossing of the detonation front is insignificant for heavy-metal and significant for light-metal particles. These studies provide valuable insights on the physics of detonation interactions with solid particle clouds.

Some joint experimental and numerical efforts have also been undertaken to evaluate impulsive loading from a heterogeneous charge comprising of a high explosive and inert/reacting solid particles. Frost et al. [72] investigated the critical conditions required for the ignition of metal particles in heterogeneous explosive charges, and later, presented the blast wave pressure and impulse for heterogeneous charges containing spherical magnesium particles and a liquid explosive such as Nitromethane, varying



Figure 4: Photographic image of heterogeneous explosions showing hydrodynamic instabilities in a fireball [74].

both the particle size and charge diameter [73]. Then, the same research group [74] presented some photographic images of explosions from heterogeneous charges, clearly showing hydrodynamic instabilities, and some of these are displayed in Fig. 4. Later, Frost et al. [75] carried out a combined experimental and numerical study focusing on particle momentum and impulse effects of a nitromethane charge with steel particles. They showed that the integrated particle momentum flux is larger than the gas momentum flux by a factor of about 3-4 in the near field, and the impulsive load on a near-field structure was increased by a factor of 2 for a heterogeneous charge, when compared to a homogeneous charge.

Massoni et al. [141] proposed a reactive model for aluminized explosive charges in spherical coordinates. They combined an ALE method and a detonation tracking technique, and matched blast wave parameters with experiments for aluminized explosive charges. Ripley et al. [171] numerically obtained velocity and temperature transmission factors, defined as the ratio of velocity and temperature, respectively, of particle to the gas as the detonation wave crosses the particle in a heterogeneous explosive. They identified three different regimes of interest, i.e., when the particle size is much smaller, comparable to, and much larger than the reaction zone thickness. Although these studies have provided valuable insights to the problem of heterogeneous explosions, additional insights are required to characterize the physics of the

flow field, in particular to the dependence of the impulsive loading on particle size, growth of hydrodynamic instabilities from heterogeneous explosions, the associated mixing and afterburn aspects, etc., and these areas will be focused in the current research.

1.2.4 Rayleigh-Taylor and Richtmyer-Meshkov instabilities

Hydrodynamic instabilities have been studied in the past extensively—theoretically, experimentally and numerically. Despite this, several interesting physics still remains unexplored. For the study of explosions, both Rayleigh-Taylor Instability (RTI) as well as Richtmyer-Meshkov Instability (RMI) are of relevance as aforementioned, and some of the major research efforts in the past aimed to understand these are hereby discussed. The science of RTI started with the seminal work of Taylor [192], who investigated the growth of instabilities on accelerated liquid surfaces. Later, Layzer [124] applied perturbation theory to obtain analytic expressions for the rise of multiple bubbles in a vertical column subjected to an accelerating field and derived Bessel functions based solutions. The theory of perturbation growth can be best identified with the pioneering work of Chandrasekhar [38], which forms the foundation for most of the later theoretical works in the field. Studies have shown that RTI grows as “bubbles” of lighter fluid “rising” into the heavier fluid, and “spikes” of heavier fluid “falling” into the lighter fluid. Furthermore, “bubble competition” is a well established feature of multi-mode hydrodynamic instabilities. Here, contiguous bubbles interact with each other, with larger bubbles overtaking smaller bubbles and engulfing them completely, leading to amalgamation of bubbles. Consequently, larger length scales appear with time.

Experimental studies of Rayleigh-Taylor instabilities have been carried out by Read & Youngs [167, 168], focusing on the turbulent mixing ensuing from RTI. At the same time, Youngs [211] undertook two-dimensional numerical simulations by

adding perturbations to a fluid interface, and demonstrated that RTI grows linearly at early times, soon transitioning into a non-linear growth that eventually leads to a loss of memory of the initial conditions. One of the early detail reviews on RTI was presented by Sharp [183]. With advances in computing power, more elaborate numerical studies on RTI have been undertaken in the later years. A front-tracking approach was used to numerically study RTI [86, 87], and runaway growth of bubbles was also reported to occur under certain conditions. A different approach was introduced by Alon et al. [5], who used a statistical model for predicting RTI bubble growth and demonstrated scale-invariance and runaway growth regimes; later, the same group applied a potential flow model [97] to investigate the same problem. DNS studies of three-dimensional RTI was undertaken [48] and it was shown that the growth rates and the amount of mixing are sensitive to the initial conditions, and that the height of the mixing zone, rather than time, was postulated to be a suitable parameter for scaling the turbulent statistics. In another study, a self-similar scaling law for fluid mixing in the compressible regime of RTI was established [80], and it was demonstrated that compressible effects enhance the amount of mixing. The same research group then assessed grid and sub-grid effects to validate turbulent mixing for RTI simulations [127], with emphasis on physical mass diffusion, thereby illustrating grid requirements for large scale simulations of RTI. Very recently, Youngs & Williams [212] have undertaken numerical simulations to quantify turbulent mixing in spherical implosions using a spherical sector grid, with particular focus on kinetic energy dissipation in the mixing layer.

The study of RTI driven by a blast wave is of significance to supernovae explosions, and forms the basis for a series of papers by Miles and co-workers [149, 150, 151, 152] at the Lawrence Livermore National Laboratory. The authors focused on the effect of initial conditions on the late time behavior of multi-mode RTI driven by blast waves, and speculated that quasi-self-similar growth of Rayleigh-Taylor structures is

possible at late times, thereby opening up more discussions on the physics of RTIs from explosions. These authors used a bubble merger model as well as a buoyancy-drag model, and complement their results with numerical simulations. In summary, RTI is encountered in various engineering problems and natural phenomena, and their characterization and understanding requires more detailed analysis. To this end, the further advance of computing power will enable more understanding of the same.

The Richtmyer-Meshkov Instability (RMI), closely related to RTI, was first identified theoretically by Richtmyer [169] and experimentally by Meshkov [146]. The primary difference between RTI and RMI is that the latter involves an impulsive acceleration, unlike the former. Perhaps the earliest numerical simulation of RMI was undertaken by Meyer & Blewett [148], using a two-dimensional Lagrangian inviscid hydrocode, and they obtained good agreement with Richtmyer's formula. To complement the theoretical developments, experiments have also been undertaken. Vetter & Sturtevant [202] reported flow visualization experiments of RMI in an air-SF₆ combination, and it was shown that whereas the thin membrane that forms the initial surface plays a significant influence on the initial growth of the interface, the growth rates measured after the first reflected shock are independent of the same. To circumvent membrane effects, another research group [105] employed a novel membraneless shock tube where the light and heavy fluids flow from opposite directions of a vertical shock tube, and obtained good agreement with Richtmyer's theory. A research group based in Israel have also studied the RTI and RMI using theoretical, numerical and experimental approaches [107, 128, 158, 170, 189], and emphasized on the significance of bubble competition in the RMI growth behavior. Both classical as well as re-shocked RMI were considered, and it was shown in [128] that the late time mixing zone loses memory of the initial perturbations, and depends strongly on the strength of the re-shock.

Large-Eddy Simulations (LES) of RMI with re-shock have also been undertaken

recently [98, 123, 198], demonstrating that sub-grid modeling can capture the small scales associated with the problem. In addition, the RMI has also been investigated in cylindrical [133, 134, 135, 219] and spherical geometries [147], demonstrating that the problem involves multiple combinations. For instance, the converging geometry RMI can be both explosive as well as implosive, and both heavy-light as well as light-heavy combinations [135, 219]. A comprehensive review of RMI was presented by Brouillette [35] in 2002, although significant numerical developments have also been undertaken since then. Despite all these detail studies, the application of RMI to engineering problems still poses several challenges, and offers an interesting avenue for future research. In the current study, both RTI and RMI are encountered, and will be illustrated in more detail later.

1.2.5 Aluminum combustion in high-speed flow

Aluminum particles are used in a wide variety of engineering applications for their high energy release (~ 50 MJ/Kg). In particular, aluminum particles are added to solid propellants and explosives so as to augment the total energy release for propulsion or blast applications. The burning characteristics of aluminum particles have been studied both experimentally and numerically for several decades. It is well known that aluminum particles exist with a metal oxide shell, and that ignition would not occur until this shell is melted. After this melting, the inner pure aluminum is exposed to heat and oxidizer, and can sustain burning. During the 1960s *space race* between the former Soviet Union and the United States, the significance of aluminum addition to propellants and explosives was realized, resulting in research on its burning characteristics. Early Soviet research on aluminum can be identified by [23, 71, 164], and counterpart American research by the pioneering works of Glassman and co-workers [36, 84, 85]. A good review of aluminum combustion research was summarized by Beckstead [21], and a burn time correlation was obtained using experimental data

from past research. However, significant amounts of scatter exists in the burn time plot owing to the different kinds of aluminum particle ignition considered in the experiments, viz. propellant, gas burner, laser, flash and shock ignited.

Aluminum combustion applied to other high-speed phenomena including explosions have also been researched. In France, Veyssiere & Khasainov [108, 109, 203, 204] have studied detonations in aluminum air mixtures experimentally and have postulated models for aluminum burning applicable for detonation conditions. Shock tube experiments in Russia on aluminum combustion have been undertaken by Boiko and co-workers [29, 30, 31] and they have also reported aluminum combustion models applicable under shock tube conditions. In addition, they also investigated the possibility of initiating the ignition of aluminum powders in air using combustible liquids such as diesel and alcohol nitrate. Recently, several numerical studies have been undertaken in Russia focusing on aluminum combustion for both shock tube applications [65, 110] as well as detonations [66, 67]. At the same time, a Japanese group also undertook numerical studies focusing on shock and detonation studies involving aluminum particles [24, 25, 26].

Combustion of an aluminum particle can occur in two regimes: (i) diffusive and (ii) kinetic [205]. The diffusive regime has been extensively studied by the research community, with an established correlation provided by Beckstead [21, 22] widely used. However, recent shock tube experimental data of small aluminum particles [18] show that particle diameters below $10\ \mu\text{m}$ exhibit transition from the diffusive regime to the kinetic regime, particularly under high-speed conditions. Furthermore, they also reported the dependence of the aluminum burning time on the oxidizer used, on the percentage of oxidizer in the ambient gas, and the pressure dependence of the burning time. Later, the same group undertook more shock tube studies of small aluminum particles in the $3\text{--}11\ \mu\text{m}$ dia. range and obtained burn time correlations [136, 137] dependent on pressure, particle size and oxidizer concentration.

Even experiments conducted by another research group [184, 196] suggest deviations from the classical diffusive regime for small particle sizes. An experimental study undertaken by Zhang et al. [217] investigated the effect of initial pressure on the detonation of aluminum-air mixtures, and showed that the classical diffusion theories fail to address the high pressure effects observed. Since aluminum is widely used in explosives, it is also of interest to study the combustion characteristics when aluminum is exposed to detonation products.

The interaction of aluminum particles with the products of detonation of condensed high explosives such as HMX and RDX was experimentally studied by Gilev & Anisichkin [82] by measuring the electrical conductivity of mixtures, and the amount of reacted aluminum and the oxide-layer thickness were estimated. In another recent study, Tanguay et al. [190] undertook an experimental/numerical study of aluminum particle combustion of size 2-100 μm in high-speed hydrogen-oxygen detonation products, and reported that aluminum combustion conforms to the kinetic regime in detonation-like conditions. Despite several decades of research interest on aluminum combustion under high-speed conditions, its dispersion characteristics due to explosive dispersal has not been elaborately addressed in literature. In particular, the interaction of aluminum particles with hydrodynamic instabilities under high-speed conditions has not been studied to detail in the past. To shed light along these lines, the ignition, combustion and dispersion aspects of aluminum particle clouds due to chemical explosions will be addressed in the current study.

1.3 Thesis Outline

This thesis is organized as follows: the research objectives are detailed in Chapter 2. This is followed by a presentation of the mathematical formulation of the governing equations for both the gas phase and solid particles in Chapter 3. Details of the computational method employed for solving the governing equations are discussed in

Chapter 4. Some relevant validation studies are presented in Chapter 5 to demonstrate the efficacy of the simulation strategy. Then the results obtained from this research effort are presented: homogeneous explosive charges into ambient air and into dilute particle clouds in Chapter 6; heterogeneous explosive charges in Chapter 7. Finally, the conclusions drawn from this study and some recommendations for future extensions are discussed in Chapter 8.

CHAPTER II

RESEARCH OBJECTIVES

The primary goal of this research effort is to investigate the problem of chemical explosions and their interaction with solid particle clouds, focusing on the various thermo-fluid mechanic phenomena such as perturbation growth, hydrodynamic instabilities, inter-phase interactions, particle dispersion and ignition, dense particle effects, combustion/afterburn effects, etc. The flow field can be dilute or dense in terms of the volume occupied by the solid particles; both these regimes are of interest and will be investigated. In addition, from a numerical standpoint, particle-gas interactions in the form of mass, momentum and energy transfer will have to be handled, ensuring two-way coupling. For dense flow scenarios, blockage effects have to be accounted for, since the total volume is not exclusively available to any one single phase. Moreover, under dense loading, particle-particle collision/contact forces have to be taken into account.

The primary interest of this research effort is to apply the simulation approach to investigate the post-detonation characteristics of homogeneous explosives into air as well as into dilute aluminum particle clouds. Building on this, the simulation strategy will be extended to the study of heterogeneous explosives, i.e., explosive charges consisting of a mass of metal particles. The complex physics involved in the problem of interest poses several challenges that have to be identified and investigated. In addition, the computational approaches need to be tested and verified before their employment to investigate the problem of interest. The individual objectives that need to be addressed in order to achieve these goals are proposed:

1 Ascertain the physics involved in homogeneous explosions into ambient air

Explosions from homogeneous explosive charges will be considered, and the fundamental physics of the flow field will be studied. Three different high explosive charges, viz. Nitromethane (NM), Trinitrotoluene (TNT) and High Melting Explosive (HMX) will be considered, and the gas dynamics of explosions from these explosives will be compared. The problem under study involves explosives—whose detonation product gases do not behave like an ideal/perfect gas—necessitating the use of real gas models. To this end, the Jones-Wilkins-Lee (JWL) [220] and the Noble-Abel [104] equations of state are identified and will be incorporated in the hydrocode to obtain thermodynamic closure. Based on the simulation results for these explosives, scaling laws for the blast wave overpressure and impulsive loading will be obtained, which can serve as a benchmark for future comparisons. Furthermore, for carbon rich explosives such as TNT, the afterburn energy release is to also be taken into account, and this inevitably depends on the role played by hydrodynamic instabilities such as Rayleigh-Taylor and Richtmyer-Meshkov. The amount of mixing in the fireball is dependent on the growth of these instabilities, and in turn decides the amount of afterburn energy release. To gain fundamental insights into the physics of mixing and hydrodynamic instabilities in the explosive fireball, these aspects will be investigated.

2 Ascertain the physics involved in homogeneous explosions into dilute aluminum clouds

Homogeneous explosions into reactive aluminum particle clouds will be investigated, focusing on the role played by the particles to the gas dynamics and afterburn in the mixing layer. A new solver that can track solid particles discretely is to be incorporated into the simulation hydrocode, modeled along the lines of the existing liquid phase solver. This solver will use the appropriate mass, momentum and energy transfer laws to model the interaction between the two phases, and will also employ two-way coupling [51]. Several validation studies from literature will be identified, and used as a means for validating the implemented models in the hydrocode.

With the validation tests completed, the investigation will extend into the study of chemical explosions into dilute aluminum particle clouds, with focus on particle dispersion, ignition, and afterburn. The role played by ambient particle clouds on the amount of mixing and afterburn in the ensuing mixing layer, and the growth of hydrodynamic instabilities will be quantified, thereby characterizing the combustion and gas dynamic phenomena of relevance in the mixing layer. In addition, the dispersion of particles upon their interaction with the hydrodynamic instabilities in the mixing layer will be addressed, with the goal to elucidate the underlying physics of two-phase explosions. These studies will shed light on the physics of particle cloud motion, ignition, burning, and the interaction of particle clouds with hydrodynamic instabilities when subjected to explosive dispersal.

3 Investigate the physics of heterogeneous explosive charges containing inert steel particles

Heterogeneous explosive charges are inherently dense in nature, i.e., the two phases (solid particles and gas) occupy non-negligible volumes—necessitating

the use of a dense, two-phase approach. To this end, the Discrete Equations Method (DEM) [1, 44] will be extended to an Eulerian-gas, Lagrangian-solid formulation (denoted as EL DEM), and implemented in the solver. Furthermore, due to the dense nature of the problem, the collision/contact between particles has to be accounted for, and will be accomplished with the use of Snider's empirical collision model [186]. These numerical developments will be validated with pertinent problems from literature, before their application to the study of heterogeneous explosions.

The problem of heterogeneous explosions will be investigated for a range of operating parameters such as particle size, charge volume fraction, etc., with focus on the evaluation of the total deliverable impulsive loading from such charges. In particular, the individual contributions of the gas pressure, gas momentum and particle momentum to the total deliverable impulsive loading will be quantified. Furthermore, the contributions of viscous drag, gas pressure gradient and inter-particle collision forces will be determined to study the particle acceleration/deceleration at different stages of the explosion. The impulsive loading for the heterogeneous explosive charge will also be compared with counterpart homogeneous explosive charges. Overall, these investigations are aimed at understanding the efficacy of heterogeneous explosive charges for impulsive applications.

Building on this, the mixing layer ensuing from heterogeneous explosions will be quantified, with focus on the amount of mixing, afterburn, and perturbation/fluctuation intensities. The mixing layer ensuing from heterogeneous explosive charges will also be compared to the corresponding mixing layers from homogeneous explosions, thereby assessing the role played by the particles in the amount of mixing and afterburn in the mixing layer. The gas dynamics of the mixing layer for different particle sizes used in the heterogeneous explosive

will also be addressed. These studies will provide insights on the growth trends of hydrodynamic instabilities and quantification of the ensuing mixing in the post-detonation regime of heterogeneous explosions.

4 Investigate the physics of heterogeneous explosive charges containing reactive aluminum particles

Finally, high explosive charges containing a dense loading of aluminum particles will be investigated, with focus on estimating the particle burning and dispersion characteristics. The role of particle size and initial volume fraction in the charge on the heating, burning and dispersion of particle clouds will be examined and quantified. This investigative study will further the understanding on the behavior of aluminum particle dispersion, heating and combustion in explosions.

CHAPTER III

MATHEMATICAL FORMULATION

This chapter describes the governing equations and the related closure/empirical models for both the gas and solid phases. Under the assumption of continuum, the gas phase is computed using an Eulerian approach by solving the three-dimensional, compressible, unsteady, two-phase Navier-Stokes equations [1, 11, 44]. Stated in these terms, the equations of interest are comprised of the continuity, momentum, energy and multi-component species equations. In this chapter, the governing equations are described in detail, as well as their extension to a Large-Eddy Simulation (LES) formulation and the associated sub-grid closure models. In addition, the thermodynamic closure is explained with the consideration of both perfect gas as well as real gas equations of state. Finally, the combustion model used in this study and the multi-step chemical equations are presented.

For the dispersed phase, viz. solid particles, a Lagrangian tracking approach [51] is employed, and this chapter outlines the associated equations and the coupling involved between the two phases. Here, the particle kinematic equations, inter-particle collision model, particle heat and mass transfer equations are presented and explained. Empirical parameters are appropriately used to account for the various physical phenomena and discussed in this chapter.

The gas phase equations and closures are first presented, followed by the solid particle phase.

3.1 Gas (Eulerian) Phase

3.1.1 The Navier-Stokes equations

The gas phase Navier-Stokes equations, applicable for dense two-phase flows in the absence of body forces are summarized as [1, 11, 40, 44, 106]:

$$\frac{\partial}{\partial t} \begin{bmatrix} \alpha_g \rho_g \\ \alpha_g \rho_g u_{g,i} \\ \alpha_g \rho_g E_g \\ \alpha_g \rho_g Y_{g,k} \end{bmatrix} + \frac{\partial}{\partial x_j} \begin{bmatrix} \alpha_g \rho_g u_{g,j} \\ \alpha_g \rho_g u_{g,i} u_{g,j} + \alpha_g p_g \delta_{ij} - \alpha_g \tau_{g,ij} \\ \alpha_g (\rho_g E_g + p_g) u_{g,j} - \alpha_g u_{g,i} \tau_{g,ji} + \alpha_g q_{g,j} \\ \alpha_g \rho_g Y_{g,k} (u_{g,j} + V_{g,j,k}) \end{bmatrix} = \begin{bmatrix} 0 \\ p^* \frac{\partial \alpha_g}{\partial x_j} \delta_{ij} - \tau_{ij}^* \frac{\partial \alpha_g}{\partial x_j} \\ p^* u_j^* \frac{\partial \alpha_g}{\partial x_j} - u_i^* \tau_{ij}^* \frac{\partial \alpha_g}{\partial x_j} \\ \dot{\omega}_k \end{bmatrix} + \begin{bmatrix} \dot{\rho}_p \\ \dot{F}_{p,i} \\ \dot{Q}_p + \dot{W}_p \\ \dot{S}_{p,k} \end{bmatrix} \quad (4)$$

where α_g denotes the gas phase volume fraction, ρ_g the density, $u_{g,i}$ the i -th Cartesian component of velocity, E_g the total specific energy given by the sum of the internal (e_g) and kinetic energies, $e_g + \frac{1}{2} u_{g,i} u_{g,i}$, and $Y_{g,k}$ the mass fraction of the k -th species. The stress tensor is denoted by $\tau_{g,ij}$, the j -direction heat flux by $q_{g,j}$, the j -direction diffusion velocity by $V_{g,j,k}$, and the chemical production of the k -th species by $\dot{\omega}_k$. In a multi-component flow, the internal energy (e_g) is obtained as a sum of the contributions from all species:

$$e_g = \sum_{k=1}^{N_s} Y_{g,k} e_{g,k}, \quad (5)$$

where $e_{g,k}$ corresponds to the k -th species sensible energy, and N_s denotes the total number of species in the gas. The stress tensor, heat flux vector, and the species diffusion velocity are now defined.

- Definition of the stress tensor ($\tau_{g,ij}$)

The stress tensor in Eqn. (4) is obtained by assuming the fluid to be Newtonian, i.e., the stresses are proportional to the local rate of strain. This can be mathematically expressed as:

$$\tau_{g,ij} = \mu_g \left(\frac{\partial u_{g,i}}{\partial x_j} + \frac{\partial u_{g,j}}{\partial x_i} \right) + \lambda \frac{\partial u_{g,k}}{\partial x_k} \delta_{ij}, \quad (6)$$

where μ_g is the viscosity coefficient of the gas, assumed to be a function of temperature (T_g) only. For gases, the viscosity is an increasing function of temperature, and different models exist to describe this dependence [208]. Perhaps the most widely used model in literature is the Sutherland's law, in which the viscosity is given by:

$$\mu_g = \mu_0 \left(\frac{T_g}{T_0} \right)^{3/2} \frac{T_0 + S}{T_g + S}, \quad (7)$$

where μ_0 and T_0 are reference values and S is the Sutherland's constant. The viscosity dependence on temperature is sometimes given as a power-law function:

$$\mu_g = \mu_0 \left(\frac{T_g}{T_0} \right)^n, \quad (8)$$

where the exponent n depends on the fluid composition, but usually takes values close to 0.7 [208].

The other constant in Eqn. (6), λ , is the bulk viscosity [208]. Following Stokes' hypothesis, it is assumed that the stress tensor is traceless, so that the bulk viscosity is related to μ_g as $\lambda = -2/3 \mu_g$. With these definitions, the shear-stress tensor is given by

$$\tau_{g,ij} = 2\mu_g \left(S_{g,ij} - \frac{1}{3} S_{g,kk} \delta_{ij} \right), \quad (9)$$

where $S_{g,ij}$ is the rate of strain tensor:

$$S_{g,ij} = \frac{1}{2} \left(\frac{\partial u_{g,i}}{\partial x_j} + \frac{\partial u_{g,j}}{\partial x_i} \right). \quad (10)$$

- Definition of the heat flux vector ($q_{g,j}$)

The heat flux vector has contributions from the thermal conduction and from the flux of sensible enthalpy due to species diffusion. Fourier's law of thermal conduction is used to obtain the heat flux as a function of the local temperature gradient and gas thermal conductivity. Using this law, the expression for the heat flux vector is obtained as:

$$q_{g,j} = -\kappa_g \frac{\partial T_g}{\partial x_j} + \rho_g \sum_1^{N_s} Y_{g,k} h_{g,k} V_{g,j,k}, \quad (11)$$

where $h_{g,k}$ denotes the enthalpy of the k -th species, and κ_g is the thermal conductivity of the gas, assumed to be a function of temperature only. The Prandtl number (Pr) is used to obtain κ_g from μ_g , defined as

$$Pr = \frac{C_{p,g} \mu_g}{\kappa_g}, \quad (12)$$

and is assumed constant in the present study with a value of $Pr = 0.72$.

- Definition of the species diffusion velocities ($V_{g,j,k}$)

The species diffusion velocities, $V_{g,j,k}$, are modeled assuming Fickian diffusion, and obtained as

$$V_{g,j,k} = -\frac{D_{g,k}}{Y_{g,k}} \frac{\partial Y_{g,k}}{\partial x_j}. \quad (13)$$

Here, the diffusion coefficient $D_{g,k}$ depends on species k , and is obtained from a constant Lewis number (Le) assumption, given as

$$Le = \frac{\kappa_g}{\rho_g C_{p,g} D_{g,k}}. \quad (14)$$

In the current study, Le is assumed to be unity, i.e., $Le = 1$.

3.1.2 Non-conservative/“nozzling” terms

In Eqn. (4), p^* and u_i^* denote, respectively, the pressure and i -th component of velocity at the interface between the two phases. Also, τ_{ij}^* denotes the stress tensor at the multiphase interface. The $*$ superscript is used to emphasize that these terms are to be evaluated at multiphase-interfaces only. Note that these terms occur in Eqn. (4) multiplied with $\frac{\partial \alpha_g}{\partial x_j}$, indicating that they occur wherever a volume fraction gradient is prevalent, i.e., a multiphase interface. Furthermore, these terms occur in Eqn. (4) in a non-conservative form, thus they are generally termed as “non-conservative terms,” and play a critical role in dense multiphase-flows. They are also referred to as “nozzling terms,” by virtue of them being analogous to the equations that govern one-dimensional flow in a variable area nozzle [1, 44].

The nozzling terms were first identified in the seminal paper on two-phase flows by Baer & Nunziato [11] in the context of granular explosives, which forms the basis for many other research works to come in the later years. Some researchers have dropped these terms for simplicity [91], thus rendering the system of equations to be in conservative form. Others treat these terms as source terms [106]; there is, however, no justification to this. Appropriate closures have to be used for p^* and u_i^* ensuring mathematical consistency [1], and this will be revisited later in Chapter 4.

3.1.3 Equations of state

A thermodynamic closure is essential to solve the governing equations outlined in Eqn. (4) so as to arrive at a relation between the state variables, viz. p_g , ρ_g , e_g and T_g . This relation is referred to as the equation of state, or EOS for short. Although several EOS exist in literature, the appropriate choice is problem dependent, i.e., depends on the range of variation of the state variables themselves. Furthermore, the frozen speed of sound (a_g) also depends on the choice of the EOS used, where the term ‘frozen’ is used to emphasize that the speed of sound of the gas mixture is

computed assuming the chemical composition of the gases is frozen at the instant, i.e., the gas pressure can be represented as $p_g = p_g(\rho_g, e_g)$. Under this assumption, a_g can be obtained for any gas as [83]

$$a_g^2 = \left(\frac{\partial p_g}{\partial \rho_g} \right)_{e_g} + \frac{p_g}{\rho_g^2} \left(\frac{\partial p_g}{\partial e_g} \right)_{\rho_g}. \quad (15)$$

Thus, $\left(\frac{\partial p_g}{\partial \rho_g} \right)_{e_g}$ and $\left(\frac{\partial p_g}{\partial e_g} \right)_{\rho_g}$ have to be evaluated for the gas mixture to compute a_g .

The different EOS considered in the current study are now summarized along with their respective speeds of sounds:

- Perfect gas EOS

The perfect gas EOS is given by

$$p_g = \rho_g R_g T_g, \quad (16)$$

where R_g and T_g denote respectively, the gas constant and temperature of the gas. For a mixture of gases, the gas constant R_g is obtained from the mass-fractions of the individual species as

$$R_g = \mathcal{R}_u \sum_{k=1}^{N_s} \frac{Y_{g,k}}{MW_k}, \quad (17)$$

where MW_k is the molar weight of the k -th species. For this perfect gas EOS, it can be shown that the internal energy is a function of the temperature only, so that the k -th species sensible energy is expressed as

$$e_{g,k} = e_{g,k}^0 + \int_{T_0}^{T_g} C_{v,g,k}(T') dT', \quad (18)$$

where $C_{v,g,k}(T_g)$ is the specific heat at constant volume for the k -th species and $e_{g,k}^0$ is the reference energy evaluated at a reference temperature T_0 . The internal enthalpy

is defined as $h_g = e_g + p_g/\rho_g$. The sensible enthalpy of a given species k can then be written as

$$h_{g,k} = h_{g,k}^0 + \int_{T_0}^{T_g} C_{p,g,k}(T')dT', \quad (19)$$

where $C_{p,g,k}(T_g)$ is the specific heat at constant pressure for the k -th species and is related to $C_{v,g,k}(T_g)$ as

$$C_{p,g,k}(T_g) = C_{v,g,k}(T_g) + \frac{\mathcal{R}_u}{MW_k}. \quad (20)$$

If the specific heats are assumed independent of temperature, a calorically perfect gas is considered, and it is customary in this case to define the ratio of specific heats γ as

$$\gamma = \frac{C_{p,g}}{C_{v,g}}. \quad (21)$$

Here, the mixture specific heats, $C_{p,g}$ and $C_{v,g}$ are obtained as a summation over all the species

$$\begin{aligned} C_{p,g} &= \sum_{k=1}^{N_s} Y_{g,k} C_{p,g,k}; \\ C_{v,g} &= \sum_{k=1}^{N_s} Y_{g,k} C_{v,g,k}. \end{aligned} \quad (22)$$

The EOS is then fully defined with Eqn. (20) and (21). This closure is appropriate to fundamental studies or simulations of practical flows with low temperatures and/or flows with small temperature variations. However, when higher variations in the temperature field are expected, one must resort to the assumption of a thermally perfect gas, where the specific heats and γ are assumed to vary with temperature. A good reference for polynomial curve-fit expressions for specific heats as a function of temperature for various species can be obtained from [92]. For a perfect gas, $\frac{\partial p_g}{\partial e_g} = 0$, as $e_g = e_g(T_g)$. Thus, the frozen speed of sound (a_g) for a perfect gas is given by

$$a_g^2 = \gamma \frac{p_g}{\rho_g}. \quad (23)$$

- Jones-Wilkins-Lee (JWL) EOS

The problem under study is characterized by high pressures and densities, and thus the use of the perfect gas equation of state for the detonation products will not accurately predict the behavior of the flow-field. A real gas model that accounts for the dependence of the internal energy on both pressure and density is thus essential. To this end, explosives are modeled using a real gas assumption, typically of the form

$$p_g = p_g(e_g, \rho_g). \quad (24)$$

A Mie-Gruneisen EOS is generally used, where the pressure is given as

$$p_g = \mathfrak{S}(\rho_g) + \Omega \rho_g e_g, \quad (25)$$

where $\mathfrak{S}(\rho_g)$ is a function of ρ_g only, and Ω is a constant. Note that when $\mathfrak{S}(\rho_g) = 0$ and $\Omega = \gamma - 1$, the Mie-Gruneisen EOS reduces to the perfect gas EOS. Many EOS belong to the realm of Mie-Gruneisen EOS; one of the more widely used EOS in the context of explosives is the Jones-Wilkins-Lee (JWL) EOS for the detonation products [57, 220], summarized as

$$p_g(\rho_g, e_g) = A \left[1 - \frac{\omega \rho_g}{R_1 \rho_o} \right] \exp\left(-\frac{R_1 \rho_o}{\rho_g}\right) + B \left[1 - \frac{\omega \rho_g}{R_2 \rho_o} \right] \exp\left(-\frac{R_2 \rho_o}{\rho_g}\right) + \omega \rho_g (e_g - e_0), \quad (26)$$

where A , B , R_1 , R_2 , ρ_o and ω are constants for an explosive and e_0 denotes a reference internal energy. These constants for several explosives are documented [220]. The JWL equation of state is further simplified by using the constant specific heat at

constant volume ($C_{v,g}$) approach [50] to obtain a thermal form of the equation of state, i.e., $p_g = p_g(\rho_g, T_g)$, given as

$$p_g = A \exp\left(\frac{-R_1 \rho_o}{\rho_g}\right) + B \exp\left(\frac{-R_2 \rho_o}{\rho_g}\right) + \omega \rho_g C_{v,g} T_g. \quad (27)$$

The above thermal form can be different if $C_{p,g}$, on the other hand, is assumed constant and $C_{v,g}$ allowed to vary with other thermodynamic variables [50]. Note that this choice of using either constant $C_{v,g}$ or constant $C_{p,g}$ to arrive at a thermal form is purely *ad hoc*. In literature, constant $C_{v,g}$ assumption is more widely used, and is also employed in the current study. The JWL EOS constants are usually obtained by curve-fit of experimental data such that the three terms in the JWL EOS come into play at different density regimes, i.e., the first term at high densities, the second term at intermediate densities, and the last term at low densities. Thus, the JWL equation of state becomes asymptotic to the perfect gas equation of state at low densities.

The pressure derivatives are computed for the gas conforming to the JWL EOS as

$$\begin{aligned} \left(\frac{\partial p_g}{\partial \rho_g}\right)_{e_g} &= A \left[-\frac{\omega}{R_1 \rho_o} + \frac{R_1 \rho_o}{\rho_g^2} - \frac{\omega}{\rho_g} \right] \exp\left(-\frac{R_1 \rho_o}{\rho_g}\right) + \\ &\quad B \left[-\frac{\omega}{R_2 \rho_o} + \frac{R_2 \rho_o}{\rho_g^2} - \frac{\omega}{\rho_g} \right] \exp\left(-\frac{R_2 \rho_o}{\rho_g}\right) + \omega e_g; \\ \left(\frac{\partial p_g}{\partial e_g}\right)_{\rho_g} &= \omega \rho_g. \end{aligned} \quad (28)$$

Using these derivatives, the frozen speed of sound of the gas can be computed as

$$\begin{aligned} a_g^2 &= A \left[-\frac{\omega}{R_1 \rho_o} + \frac{R_1 \rho_o}{\rho_g^2} - \frac{\omega^2}{R_1 \rho_o} \right] \exp\left(-\frac{R_1 \rho_o}{\rho_g}\right) + \\ &\quad B \left[-\frac{\omega}{R_2 \rho_o} + \frac{R_2 \rho_o}{\rho_g^2} - \frac{\omega^2}{R_2 \rho_o} \right] \exp\left(-\frac{R_2 \rho_o}{\rho_g}\right) + \\ &\quad \omega (1 + \omega) e_g. \end{aligned} \quad (29)$$

- Van der Waals EOS

Another widely used real gas model is the Van der Waals EOS, which can be applied to the ambient air. This EOS is summarized as [99]

$$\left(p_g + \frac{a}{V_g^2}\right)(V_g - b) = R_g T_g, \quad (30)$$

where a and b are constants, and V_g denotes the volume of the gas. This EOS must be used only when $V_g - b > 0$, so as to preserve positivity. The pressure derivatives for a van der Waals gas are obtained as

$$\begin{aligned} \left(\frac{\partial p_g}{\partial \rho_g}\right)_{e_g} &= \frac{\gamma p_g V_g^2 + a}{V_g - b} - \frac{2a}{V_g}, \\ \left(\frac{\partial p_g}{\partial e_g}\right)_{\rho_g} &= 0, \end{aligned} \quad (31)$$

and the speed of sound is obtained as

$$a_g^2 = \frac{\gamma p_g V_g^2 + a}{V_g - b} - \frac{2a}{V_g}. \quad (32)$$

- Noble-Abel EOS

Another widely used equation of state to model explosives is the Noble-Abel equation of state [104], given by

$$p_g = \frac{\rho_g R_g T_g}{1 - A \rho_g}, \quad (33)$$

where A is an empirical constant which is determined from two criteria: (1) ensuring the term $1 - A \rho_g$ always remains positive; (2) from *a priori* knowledge of the blast wave overpressure. Furthermore, to obtain the enthalpy of the gas, the specific heat capacities ($C_{p,g}$) are used, and are assumed to vary with temperature by means of polynomial curve-fits [92].

The pressure derivatives for a gas conforming to the Noble-Abel EOS are given as

$$\begin{aligned}\left(\frac{\partial p_g}{\partial \rho_g}\right)_{e_g} &= \frac{p_g \gamma}{\rho_g (1 - A \rho_g)}; \\ \left(\frac{\partial p_g}{\partial e_g}\right)_{\rho_g} &= 0.\end{aligned}\tag{34}$$

Using these derivatives, the speed of sound for a Noble-Abel gas is obtained as

$$a_g^2 = \frac{\gamma R T_g}{(1 - A \rho_g)^2}.\tag{35}$$

Additional details about the Noble-Abel EOS can be found in [104].

3.1.4 Governing equations for LES

Turbulent fluid flows are characterized by a range of length and time scales, with the smallest scales not being easily resolved with presently available computational resources. Thus, in order to undertake a simulation strategy that accounts for all the scales of physical relevance, the Large Eddy Simulation (LES) strategy is widely used. Here, the large scales of the fluid flow are fully resolved, while models are employed to account for the effect of the unresolved scales (also termed as subgrid-scales or SGS) on the large, resolved scales. The separation of scales in high-Reynolds number turbulent flows, and the universality of the small scales, as first envisioned by Kolmogorov [115, 116], are widely accepted characteristics of turbulent flows, and forms the basis of LES formulation. A spatial filtering operation is performed on the Navier-Stokes equations to separate the large and small scales, following the procedures outlined elsewhere [63, 156]. Thus, any variable f can be represented as $f = \tilde{f} + f''$, where $\tilde{}$ and $''$ denote, respectively, the resolved scales and the unresolved sub-grid terms. Once this definition is exploited to separate the scales, the large geometry-dependent scales are explicitly solved, and the effect of the small scales on the large scales is modeled, assuming the small scales to be universal in behavior.

In this section, the spatial filter is applied to the Navier Stokes equations, and the Favre-filtered LES equations are presented [162, 165]; all subgrid unclosed terms are explicitly identified.

3.1.4.1 Spatial filtering and Favre averaging

The separation between large and small scales is obtained by applying a spatial filter to the governing equations. Let $G(\mathbf{x}, \mathbf{x}')$ denote the mathematical description of the filter Kernel used for this operation, where \mathbf{x} and \mathbf{x}' are position vectors. Then, variable f is filtered into \bar{f} as:

$$\bar{f}(\mathbf{x}, t) = \int_{\Omega} f(\mathbf{x}', t) G(\mathbf{x}, \mathbf{x}') d^3 \mathbf{x}', \quad (36)$$

where Ω represents the domain of simulation. A top-hat filter kernel is used in the present formulation, and G is the product of three one-dimensional filters:

$$G(\mathbf{x} - \mathbf{x}') = \prod_{i=1}^3 g_i(x_i - x'_i), \quad (37)$$

where x_i is the i -th computational coordinate, and g_i 's are one-dimensional top-hat filters, summarized as:

$$g_i(x_i - x'_i) = \begin{cases} \frac{1}{\Delta_i}, & |x_i - x'_i| < \frac{\Delta_i}{2} \\ 0, & \text{otherwise.} \end{cases} \quad (38)$$

Here, Δ_i denotes the local one-dimensional i -direction filter size, and Δ , the global filter size, obtained as $\Delta = (\Delta_x \Delta_y \Delta_z)^{1/3}$. Δ_x , Δ_y and Δ_z denote, respectively, the local grid dimensions in the x -, y - and z -directions.

The *Favre-filtered* variable \tilde{f} is defined as [162, 165]:

$$\tilde{f} = \frac{\overline{\rho_g f}}{\rho_g}, \quad (39)$$

where ρ_g is the local gas density. The so applied filter is spatial in character, rather than temporal as is for the Reynolds Averaged Navier Stokes (RANS) formulation. Note that in the RANS formulation, only the averaged equations are solved, and thus the instantaneous turbulence features cannot be studied. One of the primary differences between LES and RANS arises from the fact that $\widetilde{f''} \neq 0$ for LES, which is not the case for RANS.

3.1.4.2 Filtering the Navier-Stokes equations

The spatial filter described above can be reduced to a function of $\mathbf{x} - \mathbf{x}'$, the relative position in space, and can thus commute with both temporal and spatial partial derivatives. The application of the filter to the Navier-Stokes equations, Eqn. (4), is now presented, following the approach outlined by Oefelein [156], and are summarized as:

$$\frac{\partial \overline{\alpha_g \rho_g}}{\partial t} + \frac{\partial \overline{\alpha_g \rho_g \widetilde{u}_{g,i}}}{\partial x_i} = \widetilde{\dot{\rho}}_p, \quad (40)$$

$$\frac{\partial \overline{\alpha_g \rho_g \widetilde{u}_{g,i}}}{\partial t} + \frac{\partial}{\partial x_j} [\overline{\alpha_g \rho_g \widetilde{u}_{g,i} \widetilde{u}_{g,j}} + \overline{\alpha_g \overline{p}_g} \delta_{ij} + \overline{\alpha_g \tau_{g,ij}^{sgs}} - \overline{\alpha_g \tau_{g,ij}}] = \overline{p}_g \frac{\partial \overline{\alpha_g}}{\partial x_j} \delta_{ij} - \overline{\tau_{g,ij}} \frac{\partial \overline{\alpha_g}}{\partial x_j} + \widetilde{\dot{F}}_{p,i}, \quad (41)$$

$$\begin{aligned} \frac{\partial \overline{\alpha_g \rho_g \widetilde{E}_g}}{\partial t} + \frac{\partial}{\partial x_j} [\overline{\alpha_g \rho_g \widetilde{u}_{g,j} \widetilde{E}_g} + \widetilde{u}_{g,j} \overline{\alpha_g \overline{p}_g} + \overline{\alpha_g \overline{q}_{g,j}} - \widetilde{u}_{g,i} \overline{\alpha_g \tau_{g,ji}} + \overline{\alpha_g H_{g,j}^{sgs}} + \overline{\alpha_g \sigma_{g,j}^{sgs}}] = \\ \overline{p}_g \widetilde{u}_{g,j} \frac{\partial \overline{\alpha_g}}{\partial x_j} - \widetilde{u}_{g,i} \overline{\tau_{g,ij}} \frac{\partial \overline{\alpha_g}}{\partial x_j} + \widetilde{\dot{Q}}_p + \widetilde{\dot{W}}_p, \end{aligned} \quad (42)$$

$$\frac{\partial \overline{\alpha_g \rho_g \widetilde{Y}_{g,k}}}{\partial t} + \frac{\partial}{\partial x_i} [\overline{\alpha_g \rho_g} (\widetilde{Y}_{g,k} \widetilde{u}_{g,i} + \widetilde{Y}_{g,k} \widetilde{V}_{g,i,k}) + \overline{\alpha_g Y_{g,i,k}^{sgs}} + \overline{\alpha_g \theta_{g,i,k}^{sgs}}] = \overline{\alpha_g} \dot{\omega}_{g,k} + \widetilde{\dot{S}}_{p,k}, \quad (43)$$

for the continuity, momentum, energy and k -th species equations, respectively. The variable $\overline{\rho_g}$ denotes the filtered gas density, $\widetilde{u}_{g,i}$ is the resolved i -direction gas velocity,

\overline{p}_g is the filtered gas pressure, \widetilde{E}_g is the resolved total energy per unit mass, obtained as $\widetilde{E}_g = \widetilde{e}_g + \frac{1}{2}\widetilde{u}_{g,i}\widetilde{u}_{g,i} + k^{sgs}$, where \widetilde{e}_g denotes the resolved specific internal energy, and k^{sgs} denotes the sub-grid kinetic energy. The term $\overline{\tau}_{g,ji}$ represents the filtered viscous stress tensor, and $\overline{q}_{g,j}$, the filtered heat flux vector. The variable $\overline{\alpha}_g$ represents the filtered gas phase volume fraction, and is obtained by treating the gas phase volume fraction (α_g) as a passive scalar.

The filtered viscous stress tensor ($\overline{\tau}_{g,ji}$) and filtered heat flux vector ($\overline{q}_{g,j}$) are obtained as:

$$\begin{aligned}\overline{\tau}_{g,ij} &= \overline{\mu}_g \left(\frac{\partial \widetilde{u}_{g,i}}{\partial x_j} + \frac{\partial \widetilde{u}_{g,j}}{\partial x_i} \right) - \frac{2}{3}\overline{\mu}_g \left(\frac{\partial \widetilde{u}_{g,k}}{\partial x_k} \right) \delta_{ij}; \\ \overline{q}_{g,i} &= -\overline{\kappa}_g \frac{\partial \widetilde{T}_g}{\partial x_i} + \overline{\rho}_g \sum_{k=1}^{N_s} \widetilde{h}_{g,k} \widetilde{Y}_{g,k} \widetilde{V}_{g,i,k} + \sum_{k=1}^{N_s} \overline{q}_{g,i,k}^{sgs}.\end{aligned}\quad (44)$$

Here, \widetilde{T}_g denotes the resolved gas temperature, $\widetilde{Y}_{g,k}$ is the resolved mass-fraction of the k -th species, and $\overline{\mu}_g$ and $\overline{\kappa}_g$ denote, respectively, the gas viscosity and thermal conductivity based on the resolved gas temperature. Assuming Fickian diffusion, the resolved species diffusion velocity is obtained as:

$$\widetilde{V}_{g,i,k} = \left(-\overline{D}_{g,k} / \widetilde{Y}_{g,k} \right) \partial \widetilde{Y}_{g,k} / \partial x_i, \quad (45)$$

where $\overline{D}_{g,k}$ is the resolved diffusion coefficient of the k -th species. The filtered gas pressure, \overline{p}_g , is obtained from an appropriate equation of state, as aforementioned in this chapter. Filtering the equations of state will result in a sub-grid temperature-species correlation term, T^{sgs} [78, 144, 161], that may also have to be accounted for.

The unknowns from the above governing equations are identified as the following: $\overline{\alpha}_g$, $\overline{\rho}_g$, $\widetilde{u}_{g,i}$, \overline{p}_g , \widetilde{e}_g and $\widetilde{Y}_{g,k}$, and are solved for. The other terms in the governing equations are obtained either directly from these variables, or through modeling. In the above LES equations, the superscript sgs represents the sub-grid terms, and

appropriate closures are used to model them [78, 79, 144, 161]. These closure models are now discussed.

3.1.4.3 Closure model for the LES equations

All the subgrid-scale (SGS) terms, denoted with a *sgs* superscript, are unclosed and have to be modeled. These terms are first identified (note that the index k in the following equations is used to denote the k -th species, and when appears multiple times in the same expression, is not to be misconstrued as a tensor summation):

- sub-grid stress tensor

$$\tau_{g,ij}^{sgs} = \overline{\rho}_g \left(\widetilde{u_{g,i}u_{g,j}} - \widetilde{u_{g,i}}\widetilde{u_{g,j}} \right); \quad (46)$$

- sub-grid enthalpy flux

$$H_{g,i}^{sgs} = \overline{\rho}_g \left(\widetilde{E_g u_{g,i}} - \widetilde{E_g} \widetilde{u_{g,i}} \right) + \left(\overline{u_{g,i} p_g} - \widetilde{u_{g,i}} \overline{p_g} \right); \quad (47)$$

- sub-grid viscous work

$$\sigma_{g,i}^{sgs} = \left(\overline{u_{g,j} \tau_{g,ij}} - \widetilde{u_{g,j}} \overline{\tau_{g,ij}} \right); \quad (48)$$

- sub-grid convective species flux

$$Y_{g,i,k}^{sgs} = \overline{\rho}_g \left(\widetilde{u_{g,i} Y_{g,k}} - \widetilde{u_{g,i}} \widetilde{Y_{g,k}} \right); \quad (49)$$

- sub-grid diffusive species flux

$$\theta_{g,i,k}^{sgs} = \overline{\rho}_g \left(\widetilde{V_{g,i,k} Y_{g,k}} - \widetilde{V_{g,i,k}} \widetilde{Y_{g,k}} \right); \quad (50)$$

- sub-grid heat flux

$$q_{g,i,k}^{sgs} = \bar{\rho}_g \left(\widetilde{h_{g,k} Y_{g,k} V_{g,i,k}} - \tilde{h}_{g,k} \tilde{Y}_{g,k} \widetilde{V_{g,i,k}} \right); \quad (51)$$

- sub-grid temperature-species correlation

$$T^{sgs} = \left(\widetilde{Y_k T} - \tilde{Y}_k \tilde{T} \right). \quad (52)$$

To close the sub-grid stress tensor, $\tau_{g,ij}^{sgs}$, an eddy-viscosity type closure is adopted in this study:

$$\tau_{g,ij}^{sgs} = -2\bar{\rho}_g \nu_t \left(\widetilde{S_{g,ij}} - \frac{1}{3} \widetilde{S_{g,kk}} \delta_{ij} \right) + \frac{2}{3} k^{sgs} \delta_{ij}, \quad (53)$$

where the resolved strain-rate, $\widetilde{S_{g,ij}}$, is obtained as

$$\widetilde{S_{g,ij}} = \frac{1}{2} \left[\frac{\partial \widetilde{u_{g,i}}}{\partial x_j} + \frac{\partial \widetilde{u_{g,j}}}{\partial x_i} \right]. \quad (54)$$

The term k^{sgs} denotes the sub-grid kinetic energy. The sub-grid eddy viscosity (ν_t) is modeled as

$$\nu_t = C_\nu \sqrt{k^{sgs}} \Delta, \quad (55)$$

where Δ is the local filter width. To obtain the sub-grid kinetic energy (k^{sgs}), a one-equation sub-grid transport of k^{sgs} is solved as:

$$\frac{\partial}{\partial t} \bar{\alpha}_g \bar{\rho}_g k^{sgs} + \frac{\partial}{\partial x_i} (\bar{\alpha}_g \bar{\rho}_g \tilde{u}_{g,i} k^{sgs}) = -\bar{\alpha}_g \tau_{g,ij}^{sgs} \frac{\partial \tilde{u}_{g,i}}{\partial x_j} + \bar{\alpha}_g P_{k^{sgs}} - \bar{\alpha}_g D_{k^{sgs}}. \quad (56)$$

Here, $P_{k^{sgs}}$ and $D_{k^{sgs}}$ denote, respectively, the production and dissipation of k^{sgs} , and are obtained as:

$$P_{k^{sgs}} = \frac{\partial}{\partial x_i} \left(\overline{\rho}_g \nu_t \frac{\partial k^{sgs}}{\partial x_i} \right); D_{k^{sgs}} = C_\epsilon \overline{\rho}_g \frac{(k^{sgs})^{1.5}}{\Delta}. \quad (57)$$

The constants C_ν and C_ϵ are set values of 0.067 and 0.916, respectively [144]. However, they can also be obtained by using the Localized Dynamic k -Equation Model (LDKM) [111, 112, 145].

Next, the sub-grid total enthalpy, $H_{g,j}^{sgs}$, is modeled using the eddy viscosity and gradient diffusion assumption:

$$H_{g,i}^{sgs} = -\overline{\rho}_g \frac{\nu_t}{Pr_t} \frac{\partial \widetilde{H}_g}{\partial x_i}. \quad (58)$$

Here, \widetilde{H}_g is the filtered total enthalpy, given by $\widetilde{H}_g = \widetilde{h}_g + \frac{1}{2} \widetilde{u}_{g,i} \widetilde{u}_{g,i} + k^{sgs}$, where $\widetilde{h}_g = \sum_{k=1}^{N_s} \widetilde{h}_{g,k} \widetilde{Y}_{g,k}$. Pr_t is the turbulent Prandtl number; it can be dynamically computed, but is assumed unity in the present study.

The sub-grid convective species flux, $Y_{g,i,k}^{sgs}$, is modeled using the gradient diffusion assumption as well:

$$Y_{g,i,k}^{sgs} = -\frac{\overline{\rho}_g \nu_t}{Sc_t} \frac{\partial \widetilde{Y}_{g,k}}{\partial x_i}, \quad (59)$$

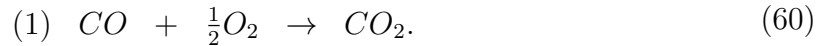
where Sc_t is the turbulent Schmidt number. It can also be dynamically computed; however, it is assumed unity for the present study. The other sub-grid terms, viz. $\sigma_{g,i}^{sgs}$, $\theta_{g,i,k}^{sgs}$, $q_{g,i,k}^{sgs}$ and T^{sgs} are neglected for the present study, as also done so in [77, 144].

In Eqns. (40)-(43), the terms $\widetilde{\rho}_p$, $\widetilde{F}_{p,i}$, \widetilde{Q}_p , \widetilde{W}_p and $\widetilde{S}_{p,k}$ denote, respectively, the source terms due to inter-phase interaction, which are obtained from the Lagrangian tracking of the solid particles, and will be discussed in Section 3.2. Again, the $\widetilde{}$ notation is used to emphasize that they are based on resolved gas-phase quantities, unlike their counterparts discussed earlier in the chapter for the Navier-Stokes equations solved directly.

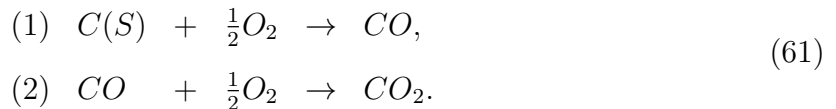
3.1.5 Combustion modeling

To close chemistry, the chemical reaction rate, ω_k , is assumed to be infinitely fast, i.e., the reaction rate is dictated by turbulent mixing, rather than by kinetics/temperature (this approximation is widely referred to as the “flame-sheet” approximation). This approach has been used in the past for modeling the post-detonation flow-field of explosives [120, 121, 181], especially because an Arrhenius-type reaction rate applicable for the gas phase chemical reactions under the very high pressures and temperatures encountered behind chemical explosions is not available in literature.

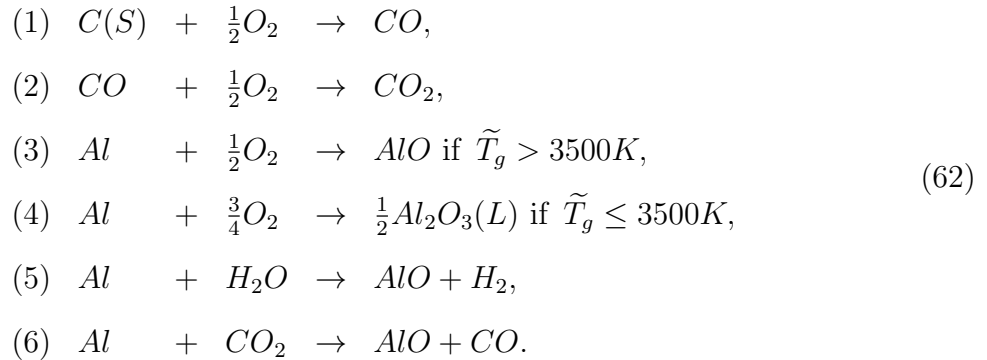
For simulations involving Nitromethane (NM) without aluminum particles, a one step chemistry is used assuming CO as the only species in the detonation products. Thus, the only chemical equation is:



For simulations involving Trinitrotoluene (TNT) without aluminum particles, a two step chemistry is used assuming $C(S)$ (soot) and CO as the only species in the detonation products. Thus, the two-step chemical equations are:



For simulations involving TNT as well as aluminum, a more detailed six-step chemistry is assumed and the following chemical equations (\tilde{T}_g : resolved gas temperature) are used:



The aerobic reactions are represented by the 3rd and 4th reactions, while the anaerobic by 5th and 6th; the terms ‘aerobic’ and ‘anaerobic’ here are based on the choice of the oxidizer: O_2 or otherwise [14].

Temperature dependent curve-fits for the specific heats, $C_p(\tilde{T}_g)$ for the species [92] are used in this study. Note that the species $C(S)$ and $Al_2O_3(L)$ exist in the condensed phase, and thus their respective condensed phase $C_p(\tilde{T}_g)$ curve-fits are used. A 700 K threshold gas temperature is assumed for chemistry to occur, as also assumed in [181]. This is done to ensure that combustion is inhibited in ‘cold’ regions of the flow, as defined by this threshold temperature. Furthermore, although $C(S)$ and $Al_2O_3(L)$ exist in the condensed phase, they are usually treated as a gaseous species for computations [181].

3.2 Solid (Lagrangian) Phase

Two approaches are common for modeling the dispersed phase, viz. solid particles: Eulerian and Lagrangian [51]. Whereas in the former continuum is assumed for the solid phase, the particles are discretely tracked in the latter approach. The Eulerian approach is better suited to compute the solid phase field when the number of particles involved is beyond computational memory availability. On the other hand, the Lagrangian approach is better suited to simulate flows that involve relatively fewer total number of solid particles, and also allows for the computation of individual

particle trajectories. Another advantage of discrete particle tracking is that it allows a better representation of particle boundary conditions and impact.

In the present study, Lagrangian particle tracking is used in order to enable the computation of particle trajectories. The particles are treated as points moving in free space, and are identified with a specific tag number. Thus, each tag is associated with a specific particle position vector $(x_{p,i})$, velocity vector $(u_{p,i})$, temperature (T_p) and radius (r_p) . The number of particles to be tracked can be very large under some scenarios, beyond available computational memory. In such cases, the concept of parcel is employed [160]. Here, a parcel represents a group of particles, each corresponding to the same position and velocity vectors, and temperature. The number of parcels is chosen based upon various factors such as computational cost and available memory, while the number of particles assigned to a parcel is chosen based upon the desired volume fraction/mass loading. The following sub-sections describe the particle phase governing equations.

3.2.1 Solid phase governing equations

3.2.1.1 Kinematics

Following [51], the particle position vector $(x_{p,i})$ is obtained from the velocity vector $(u_{p,i})$, which is obtained from Newton's law by accounting for all the forces acting on the particle. These equations are summarized below:

$$\frac{dx_{p,i}}{dt} = u_{p,i}, \quad (63)$$

$$m_p \frac{du_{p,i}}{dt} = \frac{\pi}{2} r_p^2 C_D \rho_g |u_{g,i} - u_{p,i}| (u_{g,i} - u_{p,i}) - \frac{4}{3} \pi r_p^3 \frac{\partial p_g}{\partial x_i} + m_p A_{c,i}, \quad (64)$$

where m_p is the particle mass, r_p is the particle radius, and $A_{c,i}$ is the i -component of net acceleration/deceleration on a particle due to inter-particle collisions [160, 186]. Furthermore, $u_{g,i}$ represents the gas velocity at the location of the particle. The terms

on the right side of Eqn. (64) represent the forces due to viscous drag, pressure drag and inter-particle collision. The viscous drag is generally the predominant term and many numerical studies in the past [41, 64, 65, 66, 67, 117, 118] consider only this term for modeling particle dispersion due to gas flow. The pressure drag term can be significant when strong shock waves are involved, and the inter-particle collision force comes into play for dense flow fields. Other forces such as Saffman lift, Magnus lift, Basset term and gravity [51] have been neglected based on an order of magnitude analysis. More details on these different forces can be found in Maxey & Riley [142].

The particle mass, m_p , is obtained as $4/3\pi r_p^3 \rho_p$, where ρ_p is the solid particle material density. Furthermore, C_D in Eqn. (64) represents the drag coefficient, and is usually expressed as an empirical function of Reynolds number, Mach number and solid volume fraction [51]. Several different drag laws have been proposed in literature, each being unique to a specific multiphase problem. To the best of our knowledge, no universally accepted drag law available in literature is applicable for all kinds of multiphase problems, e.g., dilute and dense particle fields or high and low speed flow. Thus, different drag laws will be used for different problems in this paper, depending on their regime of application. Appendix A summarizes some of the widely used particle drag laws in literature.

For LES framework, the $u_{g,i}$ in Eqn. (64) is to be replaced with $\widetilde{u}_{g,i} + u'_{g,i}$, where $\widetilde{u}_{g,i}$ is the resolved gas velocity, and $u'_{g,i}$ is an instantaneous velocity fluctuation computed from the sub-grid kinetic energy as $u'_{g,i} = \vartheta \sqrt{\frac{2}{3} k^{sgs}}$, where ϑ is an instantaneously computed random number between -1 and +1. In this procedure, any sub-grid fluctuation is assumed to be *locally isotropic*, and a sub-grid fluctuation velocity is evaluated based on this approximation. The resolved gas velocity as seen by the particle is then augmented by this sub-grid fluctuating velocity component to indirectly introduce the effect of sub-grid eddies on the particles. Such a procedure has also been used elsewhere [144].

3.2.1.2 *Inter-particle collision/contact model*

When the flow field is dilute, i.e., if the particle volume fraction is negligible, it is customary to neglect the inter-particle collision forces. On the other hand, for dense flows, i.e., when the solid volume fraction (α_p) is sufficiently high, contiguous particles tend to collide often, and thus necessitating the employment of an inter-particle collision model. One option is to use the Hard Sphere model [51], where a collision event (elastic or inelastic) is considered between particles close enough to each other. Here, momentum and energy equations are used to predict the final velocity vectors of the particles, using their respective masses, initial velocities and the coefficient of restitution. Although this model has been used in the context of shock-particle studies [117, 118], it is probably not suited for granular explosions like the problem under study, since inter-particle contact effects are not accounted for in this model. At high solid volume fractions (α_p), such as in the problem of granular explosions, two contiguous particles can stay in contact, compressing each other, ensuing in a continuous force of interaction. This contact force is not accounted for in the Hard Sphere model, in which only instantaneous collision forces are considered.

To account for contact effects, an empirical model where the inter-granular stress is empirically obtained from the solid volume fraction field (α_p) is useful. To this end, Snider's collision model [160, 186] is used in this research effort to compute the inter-particle collision acceleration/deceleration ($A_{c,i}$). This term arises due to the dynamic compaction of the flow-field in the vicinity of the solid particles under dense conditions. More details on the physics of dynamic compaction can be found elsewhere [11, 91]. For the collision/contact model used in this study (and in [160, 186]), the stress due to inter-particle collision is obtained as an empirical function of the solid volume fraction only, similar to the approaches used in [11, 91]. Other researchers have used an empirical model where the granular-stress is a function of both the solid volume fraction and solid material density [4, 106]. In the present study, the model

proposed by [160, 186] is chosen, as this is applicable for an Eulerian-Lagrangian formulation, unlike the others mentioned.

The stress due to inter-particle interaction is generally high when the particle cloud is dense, as the interactions between contiguous particles are more pronounced for denser clouds. As the particle cloud expands outwards, the cloud density decreases, thereby resulting in fewer inter-particle interactions. Subsequently, as the solid particles have significantly expanded outwards, the particle cloud tends to the dilute limit (in terms of solid volume fraction), and the inter-particle interaction becomes negligible. Hence, the inter-granular stress and forces are expected to monotonically vary with the solid volume fraction (α_p). In the collision/contact model used, the inter-particle force is obtained from the inter-particle stress (τ) given by [160, 186]

$$\tau = \frac{P_s \alpha_p^\beta}{\alpha_{cs} - \alpha_p}, \quad (65)$$

where P_s (units of pressure) and β are model coefficients, and α_{cs} is the solid volume fraction at close packing. The choice of the close packing limit (α_{cs}) may depend on the compressibilities of the solid particles as well as the loading involved. The geometrical close packing of spheres in a lattice arrangement is $\frac{\pi}{3\sqrt{2}} \approx 0.74048$, a result first shown by the German mathematician Carl Friedrich Gauss. However, Snider [186] and Patankar & Joseph [160] have assumed $\alpha_{cs} = 0.6$. Simulation of granular explosives such as HMX undertaken by Baer & Nunziato [11] report compaction volume fractions as high as 0.85. The choice of α_{cs} is rather problem dependent. The particle acceleration/deceleration due to inter-particle collision is obtained as a gradient of the inter-particle stress using the equation

$$A_{c,i} = -\frac{1}{\alpha_p \rho_p} \frac{\partial \tau}{\partial x_i}, \quad (66)$$

where ρ_p is the particle material density. In this inter-particle collision/contact model, the inter-particle stress and acceleration are assumed to be independent of particle

size and velocity, as also assumed in other models [4, 11, 91, 106].

3.2.1.3 Heat transfer

A common approximation in literature generally undertaken in the Lagrangian tracking approach of particles is the assumption of a uniform temperature within the particle [51]. This approximation is valid for small particles or when the thermal conductivity of the material of the particle is infinitely large. The Biot number (Bi) is critical to this approximation, and is defined as

$$Bi = \frac{hd_p}{k_p}, \quad (67)$$

where h is the convective heat transfer coefficient, d_p is the particle diameter, and k_p is the thermal conductivity of the material of the particle. When $Bi < 0.1$, the uniform temperature assumption within the particle is generally valid [51]. In the present study, k_p is assumed to be infinitely large, thereby tacitly assuming that uniform temperature within the particle is valid.

The heat transfer between the two phases is estimated assuming convection and radiation, and is used to obtain the particle temperature (T_p):

$$m_p C_p \frac{dT_p}{dt} = 2\pi r_p \kappa_g Nu (T_g - T_p) - \dot{m}_p L_v + 4\pi r_p^2 \epsilon \sigma (T_g^4 - T_p^4), \quad (68)$$

where C_p is the specific heat of the solid particle and κ_g is the thermal conductivity of the gas phase. Furthermore, T_g denotes the temperature of the gas evaluated at the location of the particle. The Nusselt number (Nu) is typically expressed as empirical functions of Reynolds number and Prandtl number in the literature; refer to Appendix A for an extensive list. The term L_v represents the latent heat of vaporization, and is well documented for many liquids and solids as an empirical function of temperature, usually in the form of polynomial curve-fits. For the LES formulation, T_g is to be replaced with the resolved gas temperature, \tilde{T}_g . The last term in Eqn. (68) represents

the Stefan-Boltzmann radiative heat transfer law, where ϵ denotes the emissivity and σ is the Stefan-Boltzmann constant ($\sigma = 5.6704 \times 10^{-8} Jsec^{-1}m^{-2}K^{-4}$).

The particle-particle collision model could, in theory, also play a role in the particle temperature equation. Particle collisions can cause velocity fluctuations, and this can give rise to the so called “granular temperature.” This granular temperature is due to shear in particle collisions, during which energy dissipation can occur due to inelastic collisions [51]. This effect is neglected in the current research effort.

3.2.1.4 Particle evaporation/pyrolysis

Liquid droplets evaporate when exposed to heat and solid particles pyrolyze and/or melt. Consequently, inter-phase mass transfer has to be accounted for in the governing equations. To this end, the mass transfer equation is given by the equation

$$\frac{dm_p}{dt} = -\dot{m}_p. \quad (69)$$

The term $\frac{dm_p}{dt}$ is computed as

$$\frac{dm_p}{dt} = 4\pi r_p^2 \rho_p \frac{dr_p}{dt}. \quad (70)$$

In order to predict droplet/particle mass transfer rates, it is very critical to accurately compute the last term of the above equation, i.e., $\frac{dr_p}{dt}$. Although steel can burn under some conditions, it is generally treated as non-reactive, and so $\frac{dr_p}{dt} = 0$ is assumed for steel particles. On the other hand, for aluminum particles, evaporation and/or reaction is assumed with the employment of the widely used empirical quasi-steady evaporation law following [14, 26, 108]:

$$\frac{dr_p}{dt} = -\frac{r_p}{t_b} \left(1 + 0.276\sqrt{Re} \right), \quad (71)$$

where t_b denotes the burning time; this term is critical to the accurate prediction of the evaporation rate of aluminum. In the above equation, Re denotes the Reynolds

number based on the slip velocity, i.e., the difference of particle and gas velocities. As mentioned in Section 1.2.5, two regimes of aluminum combustion exist: diffusion and kinetic [18, 136, 190], and appropriate burn times need to be used. For simplicity, the evaporation law as specified in Eqn. (71) is used, and the burn time data from two sources [137, 190] are employed in this study. Furthermore, the ignition temperature of the aluminum particles is assumed to be 1000 K [108, 203]. It is emphasized that when aluminum particles melt they can also agglomerate, which can change the overall burning characteristics; these aspects are considered to be beyond the scope of the current research effort.

3.2.2 Inter-phase coupling terms

The terms that appear on the right side of the governing equations, Eqns. (4), (40), (41), (42) and (43) represent the inter-phase interaction terms, and are now discussed. They represent the mass transfer, $\dot{\rho}_p$; i -th component momentum transfer, $\dot{F}_{p,i}$; heat transfer, \dot{Q}_p ; work transfer, \dot{W}_p ; and chemical production of k -th species, $\dot{S}_{p,k}$. Since the particle/parcel locations at every instant are precisely known, the local inter-phase interaction/coupling term can be obtained by volume averaging over all the particles/parcels in a finite volume (Vol), and are summarized as follows:

$$\dot{\rho}_p = \frac{1}{Vol} \sum_{n=1}^N n_{p,n} \dot{m}_{p,n}, \quad (72)$$

$$\begin{aligned} \dot{F}_{p,i} = \frac{1}{Vol} \sum_{n=1}^N n_{p,n} \left[\frac{\pi}{2} r_{p,n}^2 C_{D,n} \rho_{g,n} |u_{p,i,n} - u_{g,i,n}| (u_{p,i,n} - u_{g,i,n}) \right. \\ \left. + \frac{4}{3} \pi r_{p,n}^3 \frac{\partial p_{g,n}}{\partial x_i} + \dot{m}_{p,n} u_{p,i,n} \right], \end{aligned} \quad (73)$$

$$\dot{Q}_p = \frac{1}{Vol} \sum_{n=1}^N n_{p,n} [2\pi r_{p,n} \kappa_{g,n} Nu_n (T_{p,n} - T_{g,n}) + \dot{m}_{p,n} h_{v,n}], \quad (74)$$

$$\begin{aligned} \dot{W}_p = \frac{1}{Vol} \sum_{n=1}^N n_{p,n} \left[\frac{\pi}{2} r_{p,n}^2 C_{D,n} \rho_{g,n} |u_{p,i,n} - u_{g,i,n}| (u_{p,i,n} - u_{g,i,n}) u_{p,i,n} \right. \\ \left. + \frac{4}{3} \pi r_{p,n}^3 \frac{\partial p_{g,n}}{\partial x_i} u_{p,i,n} + \dot{m}_{p,n} \frac{1}{2} u_{p,i,n} u_{p,i,n} \right], \end{aligned} \quad (75)$$

$$\begin{aligned} \dot{S}_{p,k} &= \dot{\rho}_{p,i} \text{ for the evaporating/pyrolyzing species only;} \\ \dot{S}_{p,k} &= 0 \text{ for all other species.} \end{aligned} \quad (76)$$

Here, N is the total number of parcels in a finite volume cell and n_p is the number of particles per parcel. The term $h_{v,n}$ in Eqn. (74) denotes the enthalpy change due to mass transfer. The subscript n is used to denote the n -th particle; when used for a gas-phase variable, it represents the value of the gas-phase variable at the location of the n -th particle. In Eqn. (75), the terms that involve repetition of the index i are obtained as a summation over the three Cartesian directions.

CHAPTER IV

COMPUTATIONAL METHODS

In the preceding chapter, the gas and particle phase governing equations were summarized, along with their associated closure/empirical models. In this chapter, the computational methodology to solve these governing equations are described. Two approaches exist to solve the gas phase equations in Eulerian form: (i) the differential form/finite difference and (ii) the integral form/finite volume [191]. In the differential form, the simulation domain is discretized into several points (or nodes), at whose locations the variables of primary interest are solved by a finite difference approach. In the integral form, on the other hand, the simulation domain is divided into discrete finite volumes, and the variables of primary interest are obtained as a volume averaged quantity in each of these volumes by employing the integral form of the conservation laws. Very often, the finite volume approach is preferred over the finite difference due to two main reasons: (i) the tractability of the finite volume approach to handle complex geometrical domains, and (ii) the strict enforcement of mass, momentum and energy conservation due to the use of the governing equations in a conservative form. Due to these advantages, the integral form/finite volume approach is used in the present study.

The problem under investigation involves strong discontinuities such as shock waves and contact surfaces, as well as smooth flow regions such as shear layers. Traditional shock capturing schemes [194] are usually employed in literature to capture the discontinuities in the flow field. However, these schemes are more dissipative *vis-à-vis* central schemes [194], thereby rendering them not ideally suitable for solving the

relatively smoother shear/turbulent regions. Thus, a hybrid approach is of preponderant interest which captures both the strong discontinuities as well as the smooth regions [78]. To accurately predict the use of the shock capturing scheme in the high gradient regions, and the central scheme in smoother regions, it is customary to use a switch [78] based on the local flow conditions that identifies the regions suited for computation one way or the other. This study uses such a simulation strategy, and the mathematical procedure will be outlined in this chapter.

For dense, two-phase flow fields, the governing equations are not tractable to solution with conventional shock capturing approaches due to two main reasons: (i) the Riemann problem at cell interfaces involving a volume fraction gradient is not easy to employ due to the governing equations being in a non-conservative form; (ii) the use of a mixture equation of state introduces mathematical constraints [1, 44, 154]. To circumvent these deficiencies, the Discrete Equations Method (DEM) was introduced in [1] as a step aimed to address these issues. Here, the volume fraction variable is assumed to be piecewise continuous, resulting in volume fraction discontinuities at cell interfaces; this results in a combination of multiple pure fluid Riemann problems at cell interfaces. Later, this formulation was extended to study multiphase detonation waves [44] and evaporating liquid fronts [125]. Whereas the original DEM formulation treats both the gas and solid phases to be Eulerian (EE-DEM), the present research effort extends the formulation to an Eulerian-gas, Lagrangian-solid approach (EL-DEM). This currently developed EL-DEM formulation is first of its kind in literature, and is a useful contribution towards solving dense, two-phase, high-speed flow fields.

In this chapter, the finite volume scheme is explained, followed by descriptions of the MacCormack time integration, and the central, upwind and hybrid flux computations. Then, the Discrete Equations Method (DEM) is presented, followed by the method used to obtain the initial detonation profile. Finally, some crucial computational issues are addressed.

4.1 Finite Volume Scheme

The governing equations for the gas phase as described in Chapter 3 under dilute conditions are obtained with the assumption that $\alpha_g = 1$ and $\alpha_p = 0$. These equations can be represented in conservative form as:

$$\frac{\partial Q}{\partial t} + \frac{\partial F_x}{\partial x} + \frac{\partial F_y}{\partial y} + \frac{\partial F_z}{\partial z} = S, \quad (77)$$

where Q is the matrix of conserved state variables, $(\rho, \rho u, \rho v, \rho w, \rho E, \rho Y_k)^T$; F_x , F_y and F_z represent the fluxes in the x -, y - and z -directions, respectively, summarized below:

$$\begin{aligned} F_x &= (\rho u, \rho u^2 + p, \rho uv, \rho uw, \rho u(E + p), \rho u Y_k)^T, \\ F_y &= (\rho v, \rho uv, \rho v^2 + p, \rho vw, \rho v(E + p), \rho v Y_k)^T, \\ F_z &= (\rho w, \rho uw, \rho vw, \rho w^2 + p, \rho w(E + p), \rho w Y_k)^T, \end{aligned} \quad (78)$$

and S denotes the source terms. A finite volume approach is used in the current study with the governing equations integrated over a control volume Vol , bounded by a surface A (refer to Fig. 5), as follows:

$$\iiint_{Vol} \frac{\partial Q}{\partial t} dV + \iiint_{Vol} \left(\frac{\partial F_x}{\partial x} + \frac{\partial F_y}{\partial y} + \frac{\partial F_z}{\partial z} \right) dV = \iiint_{Vol} S dV. \quad (79)$$

Using Green's theorem, the above relation can be represented as [7, 191]

$$\frac{\partial Q}{\partial t} + \frac{1}{Vol} \oint_A (F_x n_x + F_y n_y + F_z n_z) dA = S, \quad (80)$$

where Q and S are averaged over the volume. The terms (n_x, n_y, n_z) are the normalized Cartesian components of the elemental surface normal vector.

In the structured framework adopted in the present study, any computational cell with coordinates (i, j, k) and hexahedral in shape (refer to Fig. 5) is bounded by 6

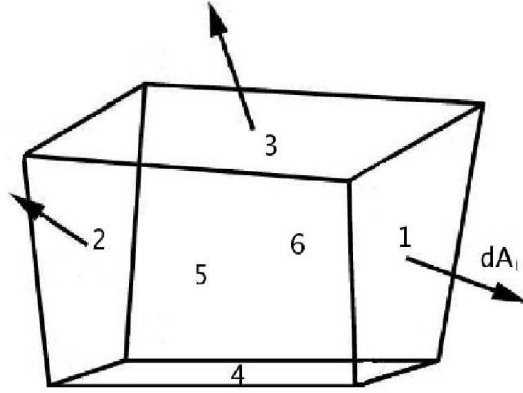


Figure 5: A typical finite volume computational cell.

interfaces $(A_l)_{l=1..6}$ located at $(i \pm 1/2, j, k)$, $(i, j \pm 1/2, k)$, and $(i, j, k \pm 1/2)$. Noting more generally, $F_l = F_x n_x + F_y n_y + F_z n_z$ as the corresponding fluxes evaluations, the increment in the cell-centered variable Q is computed as:

$$dQ = -\frac{dt}{Vol} \sum_{l=1}^6 (F_l A_l) + S dt. \quad (81)$$

Thus, the evaluation of the volume averaged conservative variable Q requires the computation of fluxes at the boundaries of the cell, whose mathematical form will be elaborated later in this Chapter.

4.2 *MacCormack Time Integration*

Two different time integration approaches have been used in literature: (i) explicit and (ii) implicit [7, 191]. When a direct computation by using the flow variables at a time t to evaluate the flow variables at time $t + \Delta t$ is undertaken, the approach is an explicit scheme; the integration procedure is straightforward to evaluate in mathematical form. On the other hand, in an implicit approach, the flow variables at time $t + \Delta t$ as well as at t are used to evaluate the parameters at time $t + \Delta t$, often requiring the inverting of very large size matrices—a cumbersome task by itself—or

an iterative option. For implicit schemes, the computational cost often outweighs the stability gains [191]; therefore, an explicit scheme is used in the present study primarily for its simplicity.

The time integration is performed using a two-stage MacCormack method [7, 191], first envisaged by MacCormack [138]. Here, the two steps are often called *predictor* and *corrector* steps, and their formulation is given by:

$$\begin{aligned} Q^{(\star)} &= Q^{(n)} + dQ^{(n)} && (\textit{Predictor}); \\ Q^{(n+1)} &= \frac{1}{2} [Q^{(n)} + Q^{(\star)} + dQ^{(\star)}] && (\textit{Corrector}). \end{aligned} \tag{82}$$

The terms $dQ^{(n)}$ and $dQ^{(\star)}$ denote the increments in state variables, obtained as in Eqn. (81) based on the variables $Q^{(n)}$ and $Q^{(\star)}$, respectively. These increments are computed as

$$\begin{aligned} dQ^{(n)} &= -\Delta t \left[\frac{1}{Vol} \sum_l (F_l^{(n)} A_l) - S^{(n)} \right], \\ dQ^{(\star)} &= -\Delta t \left[\frac{1}{Vol} \sum_l (F_l^{(\star)} A_l) - S^{(\star)} \right]. \end{aligned} \tag{83}$$

The variables denoted with a superscript (\star) are computed using the quantities at the *predictor* or intermediate time-step. Both the *predictor* and *corrector* time steps use Δt as the time step for the integration, and the $\frac{1}{2}$ factor in Eqn. (82) ensures that $Q^{(n+1)}$ represents the value of the variables at time $t + \Delta t$. Note that the notation n and $n + 1$ for time index corresponds to the respective values at times t and $t + \Delta t$, respectively.

One major restriction for explicit schemes is the choice of the time step, Δt . The maximum permissible Δt is restricted by numerical stability and accuracy requirements [7, 191], and is evaluated using the *Courant-Friedrichs-Levy* number, denoted *CFL* number [7, 191]. The maximum allowable time step, Δt , is estimated as

$$\Delta t = CFL \times \left(\frac{Vol/|dA|}{v_p} \right), \quad (84)$$

where CFL is generally less than unity, Vol represents the volume of the hexahedral cell, dA is the surface area of the cell, and v_p is the propagation velocity of *information*, or wave velocity. Essentially, Eqn. (84) implies that information cannot propagate in one time step a distance farther than a fraction of the volume-to-area ratio of the cell. More elaborate details on this time step determination, and the stability analysis can be found elsewhere [7, 191]. Overall, the MacCormack time integration approach results in an explicit methodology with second order time accuracy.

4.3 Central Scheme Flux Computation

As demonstrated in Section 4.1, a finite volume scheme computes volume averaged quantities, which is typically assigned as the value of information at the cell center. However, fluxes are evaluated at the cell interfaces/boundaries, whose computation requires information of variables at the cell interfaces. To this end, an interpolation scheme is required to enable the precise computation of information at the cell interfaces. The accuracy of this interpolation decides the overall spatial accuracy of the numerical interpolation scheme so employed.

A schematic of a typical control volume is shown in Fig. 6; a two-dimensional schematic is presented for illustration purposes only, and can be easily extended to a three-dimensional framework. Consider the control volume (i, j) , where i and j are indices used to represent, respectively, the x - and y -directions. One approach to compute the cell interface fluxes in Eqn. (83) was proposed by MacCormack [138], and considers the cell-centered primitive variables to compute the cell-face fluxes:

$$\begin{aligned} F_{i+\frac{1}{2}}^+ &= F_{i+1} = F(Q_{i+1}), \\ F_{i+\frac{1}{2}}^- &= F_i = F(Q_i), \end{aligned} \quad (85)$$

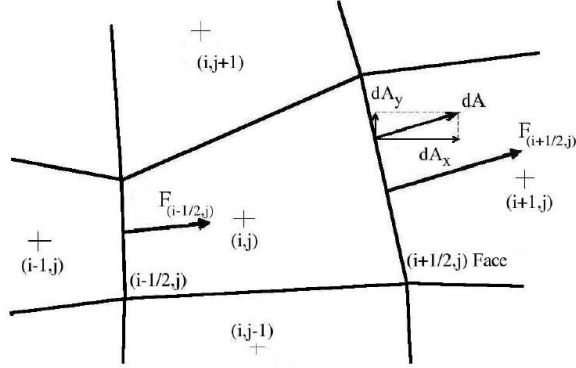


Figure 6: Schematic of a typical control volume showing the flux vectors and cell face areas.

where F_{i+1} and F_i are evaluated using cell-centered values. Note that the superscripts + and - are used to represent forward and backward differences, respectively [7, 191]. This approach, however, is only first order accurate.

To extend the original MacCormack approach to a higher order, Gottlieb and Turkel [139] proposed the following flux computation:

$$\begin{aligned} F_{i+\frac{1}{2}}^+ &= \frac{1}{6} (7F_{i+1} - F_{i+2}); \\ F_{i+\frac{1}{2}}^- &= \frac{1}{6} (7F_i - F_{i-1}), \end{aligned} \quad (86)$$

which is fourth order accurate in space. It is often desired to use higher order schemes to better resolve shear flows. Later, Nelson [155] conducted a stability analysis and showed that the scheme is third order accurate in space, and approaches fourth order as the CFL number tends to zero. The following scheme was then proposed by Nelson to compute fluxes:

$$\begin{aligned} F_{i+\frac{1}{2}}^+ &= \frac{1}{6} (2F_i + 5F_{i+1} - F_{i+2}); \\ F_{i+\frac{1}{2}}^- &= \frac{1}{6} (2F_{i+1} + 5F_i - F_{i-1}). \end{aligned} \quad (87)$$

More details of this approach can be found in [155]. Rather than extrapolating fluxes, the other option is to extrapolate the Q variables, and use these extrapolated variables to compute the cell interface fluxes, such as:

$$\begin{aligned}
Q_{i+\frac{1}{2}}^+ &= \frac{1}{6}(2Q_i + 5Q_{i+1} - Q_{i+2}); \\
Q_{i+\frac{1}{2}}^- &= \frac{1}{6}(2Q_{i+1} + 5Q_i - Q_{i-1}), \\
F_{i+\frac{1}{2}}^+ &= F(Q_{i+\frac{1}{2}}^+); \\
F_{i+\frac{1}{2}}^- &= F(Q_{i+\frac{1}{2}}^-).
\end{aligned} \tag{88}$$

The hydrocode used for the current research effort is equipped with these formulas for the use of the central scheme for flux computation. However, it is well known that central schemes fail to resolve strong discontinuities such as shocks and contact surfaces, requiring the use of upwind schemes [129, 194], i.e., schemes where information from only one side of a cell interface are used to evaluate the fluxes.

4.4 Upwind Scheme Flux Computation

When a central scheme is used to compute strong discontinuities such as shock waves or contact surfaces, it gives rise to oscillations owing to the use of information from both sides of the wave [194]. To circumvent this, the concept of upwinding is essential [100, 194]. In general, the term “upwind” applies to schemes in which the discretization depends on the direction of propagation of the wave. Usually, for a system of equations, there may be characteristic waves propagating in both directions, and so an upwind method must use information from both sides; but, use characteristic decomposition (via a Riemann solver) to select information from which direction is of preponderance. The origin of the upwinding technique can be traced back to Courant et al. [49] and this technique over the later years has developed into a variety of related approaches such as flux vector splitting, flux difference splitting, and other

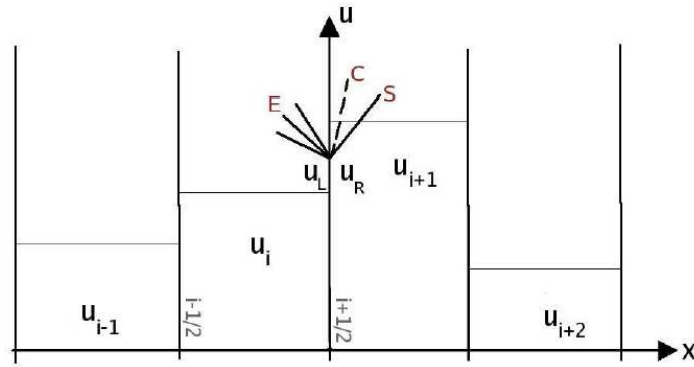


Figure 7: Schematic of a typical Godunov scheme representation of flow variables.

flux-controlling methods [129, 194].

The flux difference splitting, first proposed by Godunov [88], assumes that the flow variables are piecewise constant in each cell, thus giving rise to discontinuities in the flow variables at cell boundaries. This scheme has revolutionized Computational Fluid Dynamics, and offers a numerical solution procedure for compressible fluid flow. In the original Godunov scheme [88], the value of the primitive variables at cell centers are assumed to be piecewise constant within each cell, resulting in discontinuities in the flow variables at cell interfaces. Thus, Riemann problems—essentially, shock tube problems—exist at cell boundaries [129, 194], requiring the employment of a Riemann solver to compute the fluxes at cell interfaces. A schematic of a typical Godunov representation of flow variables is shown in Fig. 7.

In the Godunov scheme, as evident from Fig. 7, the left and right states of the flow variables at the cell interface, U_L and U_R , respectively, can be different, i.e., a Riemann problem, or a local shock-tube problem. The exact solution to such Riemann problems are generally comprised of a shock wave (denoted in the figure as S), a contact discontinuity (denoted C), and an expansion fan (denoted E). Stated in these terms, the flux components at the cell boundaries are then constructed deciding on the pattern of these waves/interfaces.

The Godunov scheme, although being robust in its representation of the flow variables, is however only first order accurate; a higher order extension is described below. The exact solution of the Riemann problem requires the resolution of a non-linear algebraic equation, leading to an iteration-type solution approach [129, 194]. This can be cumbersome to solve for, especially when applied for three-dimensional problems. To alleviate this difficulty, several approximate Riemann solvers have been developed; for instance, Roe [172], Harten et al. [94], and Osher [159]. In addition, several variants of these approximate Riemann solvers have also been reported in literature [194].

Higher order accuracy with a Godunov scheme can be achieved by replacing the piecewise constant approximation of the state variables to either a piecewise linear approach (MUSCL, [200]) or a piecewise parabolic extrapolation (PPM, [47]) of the flow variables. One deficiency, however, with such higher order approaches is the introduction of spurious numerical oscillations due to the use of large gradients used in the extrapolation of these variables from the cell centers to the cell interfaces. To correct these effects, often non-linear correction factors called “limiters” are used, first introduced by Van Leer [199]. Later, several limiters have been developed and are summarized in [129, 194]. More details on limiters will be addressed in the following sub-section. In the current study, the piecewise linear extrapolation of the flow variables is considered, and will now be elaborated.

4.4.1 MUSCL interpolation scheme

The piecewise linear extrapolation of flow variables is based on the Monotone Upstream-centered Schemes for Conservation Laws (MUSCL), first envisioned by Van Leer [200]. The left and right state variables (U) for a given interface are evaluated as:

$$\begin{aligned} U_{i+1/2}^L &= U_i + \frac{\epsilon(1-\xi_i)}{4} \left[(1 - \kappa) \Delta_{i-1/2}^+(U) + (1 + \kappa) \Delta_{i+1/2}^-(U) \right]; \\ U_{i+1/2}^R &= U_{i+1} - \frac{\epsilon(1-\xi_{i+1})}{4} \left[(1 + \kappa) \Delta_{i+1/2}^+(U) + (1 - \kappa) \Delta_{i+3/2}^-(U) \right]. \end{aligned} \quad (89)$$

Here, first order piecewise constant extrapolation is used if $\epsilon = 0$, and higher order is obtained for $\epsilon = 1$. The coefficient ξ_i is computed from a flattening operation [47]. The order of the interpolation scheme is decided by the value for κ ; whereas for $\kappa = 1/3$, third order spatial accuracy is obtained, all other values lead to a second order interpolation [194]. A central differencing scheme is obtained with the use of $\kappa = 1$, while a pure upwind interpolation results with $\kappa = -1$.

As aforementioned, limiters are used in conjunction with the interpolation procedure to ensure monotonicity. Here, for instance, to interpolate $\Delta_{i-1/2}^\pm(U)$, the following differencing is employed:

$$\begin{aligned}\Delta_{i+1/2}(U) &= U_{i+1} - U_i, \\ \Delta_{i+1/2}^+(U) &= \Delta_{i+1/2}(U)\phi(r_{i+1/2}^+); & r_{i+1/2}^+ &= \frac{\Delta_{i+3/2}(U)}{\Delta_{i+1/2}(U)}, \\ \Delta_{i+1/2}^-(U) &= \Delta_{i+1/2}(U)\phi(r_{i+1/2}^-); & r_{i+1/2}^- &= \frac{\Delta_{i-1/2}(U)}{\Delta_{i+1/2}(U)},\end{aligned}\quad (90)$$

where ϕ is the limiter. The interpolation procedure is summarized as:

$$\begin{aligned}U_{i+1/2}^L &= U_i + \frac{\epsilon(1-\xi_i)}{4} \left[(1-\kappa)\phi(r_{i-1/2}^+)(U_i - U_{i-1}) + (1+\kappa)\phi(r_{i+1/2}^-)(U_{i+1} - U_i) \right], \\ U_{i+1/2}^R &= U_{i+1} - \frac{\epsilon(1-\xi_{i+1})}{4} \left[(1-\kappa)\phi(r_{i+3/2}^-)(U_{i+2} - U_{i+1}) + (1+\kappa)\phi(r_{i+1/2}^+)(U_{i+1} - U_i) \right].\end{aligned}\quad (91)$$

Noting that $r_{i-1/2}^+ = 1/r_{i+1/2}^-$, the overall procedure can be re-arranged as:

$$\begin{aligned}U_{i+1/2}^L &= U_i + \frac{\epsilon(1-\xi_i)}{4} \left[(1-\kappa)\phi(r_{i-1/2}^+) + (1+\kappa)\phi\left(\frac{1}{r_{i-1/2}^-}\right)r_{i-1/2}^+ \right] (U_i - U_{i-1}), \\ U_{i+1/2}^R &= U_{i+1} - \frac{\epsilon(1-\xi_{i+1})}{4} \left[(1-\kappa)\phi(r_{i+3/2}^-) + (1+\kappa)\phi\left(\frac{1}{r_{i+3/2}^-}\right)r_{i+3/2}^- \right] (U_{i+2} - U_{i+1}).\end{aligned}\quad (92)$$

Several limiters have been developed by the research community and used [129, 194], some of which are summarized here:

- Minmod Limiter

$$\phi_{mm}(r) = \max [0, \min(r, 1)]; \quad (93)$$

- Superbee Limiter

$$\phi_{sb}(r) = \max [0, \min(2r, 1), \min(r, 2)]; \quad (94)$$

- Monotonized Central Limiter

$$\phi_{mc}(r) = \max \left[0, \min(2r, 2, \frac{1+r}{2}) \right]; \quad (95)$$

- Van Leer Limiter

$$\phi_{vl}(r) = \frac{|r| + r}{1 + r}; \quad (96)$$

- Van Albada Limiter

$$\phi_{va}(r) = \frac{r^2 + r}{1 + r^2}. \quad (97)$$

These limiters satisfy a symmetry condition, i.e., the forward and backward gradients are treated in a similar fashion; this condition can be summarized as:

$$\frac{\phi(r)}{r} = \phi\left(\frac{1}{r}\right). \quad (98)$$

For a symmetric limiter, the relation expressed in Eqn. (92) is simplified to:

$$\begin{aligned} U_{i+1/2}^L &= U_i + \frac{\epsilon(1-\xi_i)}{2} \phi(r_{i-1/2}^+) (U_i - U_{i-1}), \\ U_{i+1/2}^R &= U_{i+1} - \frac{\epsilon(1-\xi_{i+1})}{2} \phi(r_{i+3/2}^-) (U_{i+2} - U_{i+1}), \end{aligned} \quad (99)$$

showing that for symmetric limiters the dependence on κ is lost. Consequently, the order of the reconstruction depends on the local variations of the interpolated variable and on the choice of the limiter used for the interpolation. Overall, this procedure results in a second order spatial accuracy [194]. With the MUSCL reconstruction approach, the flow variables can be schematically represented as shown in Fig. 8. More details on limiters can be found elsewhere [129, 194].

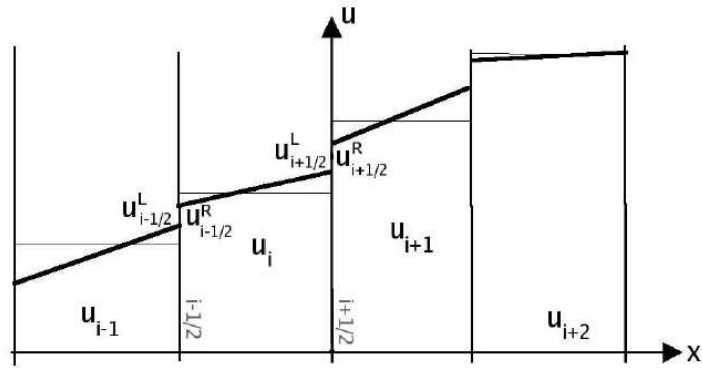


Figure 8: Schematic of a typical Godunov scheme representation of flow variables with MUSCL reconstruction.

The MUSCL interpolation procedure outlined here, used in conjunction with an appropriate limiter, ensures that the primitive variables are extrapolated from the cell centers to the cell boundaries/interfaces. Note that discontinuities exist at cell interfaces, i.e., the left and right fluid states are usually different at cell interfaces. To compute the fluxes across these discontinuities, it is customary to use an appropriate Riemann solver. The next sub-section describes some Riemann solvers widely used in literature.

4.4.2 The HLL and HLLC approximate Riemann solvers

The HLL approximate Riemann solver was first developed by Harten, Lax and van Leer [94], and hence the name HLL, by expressing a hyperbolic system of conservation laws in integral form. An interface separated by two constant states (denoted usually as *left* and *right*) is assumed to give rise to two waves from the characteristics evolution of the system, separating into 3 constant-property regions. The knowledge of the jump relation through the waves and their wave-speeds permits the obtention of a closed form expression for the intermediate states, and from it the associated fluxes can be evaluated.

The 2-waves formulation for the resolution of the Euler equations (with wave-speeds expressions given by Einfeldt and co-workers [61, 62], thus referred to as HLLE) has been widely used in literature. The HLLE Riemann solver has proven itself well in its capture of shocks and rarefactions, but appears as very dissipative for contact discontinuities [194]. Later, Toro [195] proposed a correction to the original solver, with the inclusion of the missing contact wave (thus called HLLC), whose wave-speed was estimated by an approximation of the particle velocity in the intermediate region. The formulation is closed by solving the associated jump conditions across all the waves obtained from the exact Riemann solver for the Euler equations. Recently, another modification to this Riemann solver family uses a combination of the HLLE and HLLC solvers in order to reduce the instabilities associated to contact-resolving solvers [78]. This proposed hybrid Riemann solver approach has demonstrated success in shock-turbulence problems [79], and is of interest in the current study.

In this section, the derivation of the 2-waves formulation of the original HLL method is first presented, followed by its HLLC extension. The choice of wavespeeds is critical to the use of the HLLE and HLLC Riemann solvers [17], and is also discussed here.

4.4.2.1 *The 2-waves HLL Riemann Solver*

In the derivation of the HLL Riemann solver, the initial one-dimensional discontinuity is assumed to give rise to 2 waves: a left-moving wave with speed S^L , and a right-moving wave with speed S^R ; a typical (x, t) diagram is illustrated in Fig. 9. Following [194], the integral form of the Euler equations can be expressed as

$$\oint [U dx - F(U) dt] = 0, \tag{100}$$

where U and $F(U)$ are represented as:

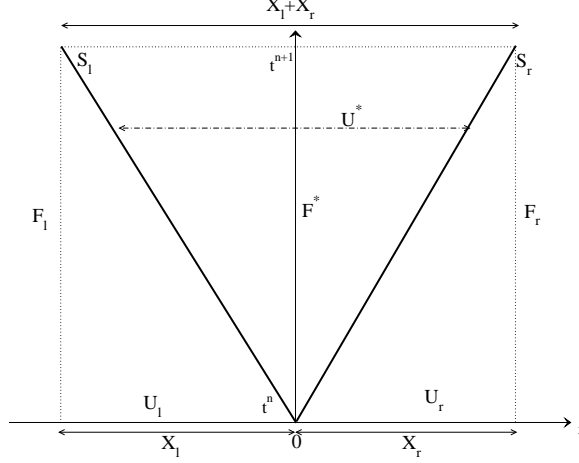


Figure 9: (x, t) diagram of an approximate Riemann problem evolution with two characteristic waves.

$$U = \begin{bmatrix} \rho \\ \rho u \\ \rho v \\ \rho w \\ \rho E \\ \rho k^{sgs} \\ \rho Y_k \end{bmatrix} ; \quad F = \begin{bmatrix} \rho q \\ \rho u q + p n_x \\ \rho v q + p n_y \\ \rho w q + p n_z \\ (\rho E + p) q \\ \rho k^{sgs} q \\ \rho Y_k q \end{bmatrix} . \quad (101)$$

Here, $q = \vec{V} \cdot \vec{n} = un_x + vn_y + wn_z$, is the interface normal velocity amplitude, also referred to as the contravariant velocity. Note that only the gas phase is assumed here for the sake of illustration, and so the subscript g is dropped. The local time step is denoted as T , where $T = t^{n+1} - t^n > 0$. Note that $S^L < S^R$ always. Three scenarios exist: (i) $S^L > 0$, (ii) $S^R < 0$, and (iii) $S^L \leq 0 \leq S^R$. The first scenario, i.e., when $S^L > 0$, corresponds to a supersonic flow from left to right. Under this condition, the S^L wave propagates to the right side of the interface (see Fig. 9), and the flux at $x = 0$, F^* , is then given by $F(U^L)$. Similarly, for the second scenario, i.e., if $S^R < 0$, the flow is supersonic from right to left, and F^* is given by $F(U^R)$.

The third scenario, i.e., when $S^L \leq 0 \leq S^R$, requires more computation. From Fig. 9, the lengths X_l and X_r can be expressed as $X_l = -TS^L$ and $X_r = TS^R$, respectively. Using the integral form of the Euler equations on the system in Fig. 9 results in the following:

$$\begin{aligned} \int_0^{-X_l} U(x, 0) dx - \int_0^T F(U(X_l, t)) dt + \int_{X_l}^{X_r} U(x, T) dx \\ - \int_T^0 F(U(X_r, t)) dt + \int_{X_r}^0 U(x, 0) dx = 0. \end{aligned} \quad (102)$$

With the assumption of piecewise constant variables and fluxes, the above relation can be re-written as:

$$U^L.(S^L T) - F^L.(T) + U^*.(S^R - S^L)T - F^R.(-T) + U^R.(-S^R T) = 0, \quad (103)$$

which can be rearranged as:

$$U^* = \frac{F^L - S^L U^L - (F^R - S^R U^R)}{S^R - S^L}. \quad (104)$$

It is directly implied from this expression that once U^L and U^R are obtained from MUSCL reconstruction, and with information on the wave-speeds (S^L and S^R), the variables in the intermediate \star -region are completely defined. Applying the integral relation across a given k -wave, $k = L/R$, results in the Rankine-Hugoniot relations, summarized below:

$$\begin{aligned} F^* &= F^L + S^L (U^* - U^L), \\ F^* &= F^R + S^R (U^* - U^R). \end{aligned} \quad (105)$$

U^* can be eliminated from the two expressions in Eqn. (105) to obtain F^* , given by:

$$F^* = \frac{S^R F^L - S^L F^R + S^L S^R (U^R - U^L)}{S^R - S^L}. \quad (106)$$

Combining the three scenarios, the flux evaluated at the $i + 1/2$ interface from the 2-waves HLL Riemann solver can be expressed as:

$$F_{i+1/2}^{HLL E} = \begin{cases} F^L & \text{if } 0 \leq S^L; \\ F^* & \text{if } S^L \leq 0 \leq S^R; \\ F^R & \text{if } S^R \leq 0. \end{cases} \quad (107)$$

The only other requirement for closing the HLL E Riemann solver is an estimate for the wave-speeds (S^L and S^R). Several wave-speed estimates can be found in the literature [52, 61, 62, 194], giving rise to schemes corresponding to different robustness and dissipation. Einfeldt [61] proposed the following wave-speeds:

$$S^L = \min [q^L - c^L, \check{q} - \check{c}]; \quad S^R = \max [q^R + c^R, \check{q} + \check{c}], \quad (108)$$

where \check{q} refers to the Roe-averaged [172] contravariant velocity, and c is the speed of sound. The Roe-averaged variables are obtained as:

$$\check{U} = \begin{bmatrix} \check{\rho} \\ \check{u} \\ \check{v} \\ \check{w} \\ \check{H} \\ \check{k}^{sgs} \\ \check{Y}_k \end{bmatrix} = \frac{1}{\sqrt{\rho^L} + \sqrt{\rho^R}} \left(\sqrt{\rho^L} \begin{bmatrix} \sqrt{\rho^L \rho^R} \\ u^L \\ v^L \\ w^L \\ H^L \\ k^{sgs L} \\ Y_{k,l} \end{bmatrix} + \sqrt{\rho^R} \begin{bmatrix} \sqrt{\rho^L \rho^R} \\ u^R \\ v^R \\ w^R \\ H^R \\ k^{sgs R} \\ Y_{k,r} \end{bmatrix} \right). \quad (109)$$

More details on wave-speeds and their application to the Riemann solver can be found elsewhere [17, 129, 194].

Although the HLL E has proven to be robust and accurate for hypersonic calculations and shock capturing purposes, it suffers from the drawback of smearing of

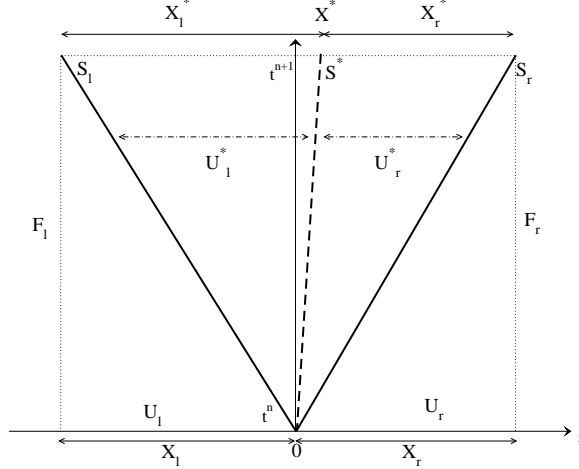


Figure 10: (x, t) diagram of an approximate Riemann problem evolution with three characteristic waves.

contact discontinuities, shear waves, etc. To alleviate this deficiency, Toro [195] extended this approach by including the middle contact wave in the Riemann problem and the derivation of the flux computation. This extended Riemann solver is referred to in literature as HLLC (C standing for Contact), and its derivation is now presented.

4.4.2.2 HLLC approximate Riemann solver

In the derivation of the HLLC solver, it is assumed that a given interface separating two states gives rise to three waves, of speed S^L for the left moving wave, S^R for the right moving wave, and S^* for the contact wave. A schematic representation is presented in Fig. 10. Here, S^L separates U^L from U^{L^*} ; S^* separates U^{L^*} and U^{R^*} ; and S^R separates U^{R^*} and U^R . The interfaces separating the different states are assumed to be thin, which is justified for both shocks and contact discontinuities, but is only an approximation in the case of rarefactions.

Let T denote the local time step, where $T = t^{n+1} - t^n > 0$. Note that $S^L < S^* < S^R$ always. Similar to the HLL solver, three scenarios exist: (i) $S^L > 0$, (ii) $S^R < 0$, and (iii) $S^L \leq 0 \leq S^R$. The first scenario, i.e., when $S^L > 0$, corresponds to the case of a supersonic flow from left to right, and the flux at $x = 0$ is given by $F(U^L)$. For

the second scenario, i.e., when $S^R < 0$, the flux is given by $F(U^R)$.

The third scenario, i.e., when $S^L \leq 0 \leq S^R$, the flux evaluation is more complicated. From Fig. 10, the lengths X_l and X_r can be expressed as $X_l = -TS^L$ and $X_r = TS^R$, respectively, and $X^{L\star} = T(S^\star - S^L)$; $X_r^\star = T(S^R - S^\star)$. The Euler equations in integral form (Eqn. 100), when applied to the system represented in Fig. 10, results in the following relation:

$$\begin{aligned} & \int_0^{-X_l} U(x, 0) dx - \int_0^T F(U(X_l, t)) dt + \int_{-X_l}^{X^\star} U(x, T) dx \\ & + \int_{X^\star}^{X_r} U(x, T) dx - \int_T^0 F(U(X_r, t)) dt + \int_{X_r}^0 U(x, 0) dx = 0. \end{aligned} \quad (110)$$

As before, assuming piecewise constant variables and fluxes, the above relation can be re-written as:

$$\begin{aligned} & U^L \cdot (S^L T) - F^L \cdot (T) + U^{L\star} \cdot ((S^\star - S^L) T) \\ & + U^{R\star} \cdot ((S^R - S^\star) T) - F^R \cdot (-T) + U^R \cdot (-S^R T) = 0. \end{aligned} \quad (111)$$

Re-arranging this results in:

$$(S^\star - S^L) U^{L\star} + (S^R - S^\star) U^{R\star} = F^L - S^L U^L - (F^R - S^R U^R), \quad (112)$$

which is a relation between the left and right \star -variables, and is often referred to as the consistency condition. Note that with the assumption $U^{L\star} = U^{R\star}$, the consistency condition of the HLL solver (Eqn. 104) is recovered.

As before, the integral applied around a control volume surrounding a given k -wave, $k = L/R$, (refer to Fig. 10) results in:

$$U^k \cdot (S^k T) - F^k \cdot (T) - U^{k\star} \cdot (-S^k T) + F^{k\star} \cdot (T) = 0. \quad (113)$$

The corresponding Rankine-Hugoniot relations across the k -wave are recovered, and are summarized as:

$$\begin{aligned}
F^{L\star} &= F^L + S^L (U^{L\star} - U^L); \\
F^{R\star} &= F^R + S^R (U^{R\star} - U^R).
\end{aligned}
\tag{114}$$

Furthermore, the Rankine-Hugoniot relation across the \star -wave are summarized as:

$$F^{L\star} = F^{R\star} + S^\star (U^{L\star} - U^{R\star}). \tag{115}$$

The system of equations described here contain four unknowns ($F^{L\star}$, $F^{R\star}$, $U^{L\star}$, and $U^{R\star}$), and four relations are available, Eqns. (112), (114) and (115). However, this system is not linearly independent, and requires a further assumption in order to be amenable to solution.

Toro [195] closed the system of equations with the assumption that the intermediate wave is a contact discontinuity, i.e., continuity of pressure and velocity hold across this intermediate wave. In addition, the propagation speed of this intermediate wave is then assumed identical to the particle velocity in the \star -region, and passive scalars are continuous. These assumptions are summarized as:

$$(\vec{V}^{L\star} \cdot \vec{n} = q^{L\star}) = (\vec{V}^{R\star} \cdot \vec{n} = q^{R\star}) = S^\star; p^{L\star} = p^{R\star}; \phi^{L\star} = \phi^L; \phi^{R\star} = \phi^R, \tag{116}$$

where ϕ is any passive scalar advected by the fluid ($\phi = k^{sgs}, Y_k, \dots$).

With the above assumptions, the first four entries of the vector equation in Eqn. (112) can be written as:

$$\begin{aligned}
& (S^* - S^L) \underbrace{\begin{bmatrix} \rho^{L^*} \\ \rho^{L^*} u^{L^*} \\ \rho^{L^*} v^{L^*} \\ \rho^{L^*} w^{L^*} \end{bmatrix}}_{U^{L^*}} + (S^R - S^*) \underbrace{\begin{bmatrix} \rho^{R^*} \\ \rho^{R^*} u^{R^*} \\ \rho^{R^*} v^{R^*} \\ \rho^{R^*} w^{R^*} \end{bmatrix}}_{U^{R^*}} = S^R \underbrace{\begin{bmatrix} \rho^R \\ \rho^R u^R \\ \rho^R v^R \\ \rho^R w^R \end{bmatrix}}_{U^R} - S^L \underbrace{\begin{bmatrix} \rho^L \\ \rho^L u^L \\ \rho^L v^L \\ \rho^L w^L \end{bmatrix}}_{U^L} + \\
& \underbrace{\begin{bmatrix} \rho^L q^L \\ \rho^L q^L u^L + p^L n_x \\ \rho^L q^L v^L + p^L n_y \\ \rho^L q^L w^L + p^L n_z \end{bmatrix}}_{F^L} - \underbrace{\begin{bmatrix} \rho^R q^R \\ \rho^R q^R u^R + p^R n_x \\ \rho^R q^R v^R + p^R n_y \\ \rho^R q^R w^R + p^R n_z \end{bmatrix}}_{F^R}.
\end{aligned} \tag{117}$$

Using Toro's assumption, $q^{k^*} = S^*$ for both $k = L/R$. Projecting the vectorial momentum equation on the directional unit vector gives, along with the first relation, results in the following set of two equations:

$$\begin{aligned}
& \rho^{L^*}(S^* - S^L) + \rho^{R^*}(S^R - S^*) = \rho^R(S^R - q^R) - \rho^L(S^L - q^L), \\
& \underbrace{\left[\rho^{L^*}(S^* - S^L) + \rho^{R^*}(S^R - S^*) \right]}_{S^*} = p^L - p^R + \rho^R q^R (S^R - q^R) - \rho^L q^L (S^L - q^L).
\end{aligned} \tag{118}$$

The under-braced term of the second equation above can be replaced by the right-hand side of the first equation above to yield an expression for the speed of the intermediate contact wave:

$$S^* = \frac{p^R - p^L + \rho^L q^L (S^L - q^L) - \rho^R q^R (S^R - q^R)}{\rho^L (S^L - q^L) - \rho^R (S^R - q^R)}. \tag{119}$$

Now, Eqn. (114) is closed and the expressions for all \star -variables are obtained. Thus, the first four relations, i.e., for continuity and three momentum equations are:

$$\underbrace{\begin{bmatrix} \rho^{k\star} S^\star \\ \rho^{k\star} S^\star u^{k\star} + p^{k\star} n_x \\ \rho^{k\star} S^\star v^{k\star} + p^{k\star} n_y \\ \rho^{k\star} S^\star w^{k\star} + p^{k\star} n_z \end{bmatrix}}_{F^{k\star}} = \underbrace{\begin{bmatrix} \rho^k q^k \\ \rho^k q^k u^k + p^k n_x \\ \rho^k q^k v^k + p^k n_y \\ \rho^k q^k w^k + p^k n_z \end{bmatrix}}_{F^k} + S^k \left(\underbrace{\begin{bmatrix} \rho^{k\star} \\ \rho^{k\star} u^{k\star} \\ \rho^{k\star} v^{k\star} \\ \rho^{k\star} w^{k\star} \end{bmatrix}}_{U^{k\star}} - \underbrace{\begin{bmatrix} \rho^k \\ \rho^k u^k \\ \rho^k v^k \\ \rho^k w^k \end{bmatrix}}_{U^k} \right). \quad (120)$$

The first relation leads directly to an expression for the density in the \star region:

$$\rho^{k\star} = \rho^k \frac{S^k - q^k}{S^k - S^\star}. \quad (121)$$

Multiplying the second relation by n_x , the third by n_y and the last by n_z , and then adding the three relations, and using the expression for $\rho^{k\star}$ given in Eqn. (121) yields:

$$p^{k\star} = p^k + \rho^k (q^k - S^k)(q^k - S^\star). \quad (122)$$

This relation expressed in Eqn. (122) is valid for both $k = L/R$, and satisfies the pressure equality, $p^{L\star} = p^{R\star}$. Now, define β^k , α^k and ω^k as:

$$\beta^k = \frac{S^\star - q^k}{S^k - S^\star}; \alpha^k = \beta^k + 1; \omega^k = -\beta^k (q^k - S^k). \quad (123)$$

The state vectors $U^{k\star}$ can then be expressed as:

$$U^{k\star} = \alpha^k U^k + \begin{bmatrix} 0 \\ \rho^k \omega^k n_x \\ \rho^k \omega^k n_y \\ \rho^k \omega^k n_z \\ \frac{p^\star S^\star - p^k q^k}{(S^k - S^\star)} \\ 0 \\ 0 \end{bmatrix}. \quad (124)$$

Using these relations and the evaluation of the wave-speeds, the description of all states in the Riemann problem under consideration is closed, thereby enabling the obtention of the fluxes at the $i + 1/2$ interface. The general expression for these fluxes is given by:

$$F_{i+1/2}^{HLLC} = \begin{cases} F^L & \text{if } 0 \leq S^L; \\ F^{L^*} = F^L + S^L(U^{L^*} - U^L) & \text{if } S^L \leq 0 \leq S^*; \\ F^{R^*} = F^R + S^R(U^{R^*} - U^R) & \text{if } S^* \leq 0 \leq S^R; \\ F^R & \text{if } S^R \leq 0. \end{cases} \quad (125)$$

Thus, the HLLC Riemann solver is completely defined, and requires only estimates for the wave-speeds (S^L and S^R). The estimates detailed in Eqn. (108) for the HLLE solver are used also for the HLLC solver to evaluate S^L and S^R , whereas S^* is defined through Eqn. (119).

4.4.2.3 A hybrid Riemann solver - HLLC/E

Solvers that incorporate a 3-wave structure are known to suffer from instabilities in shock regions. The odd-even decoupling and carbuncle [131, 166] phenomena can lead to oscillations in the post-shock regions, which results in the deformation of shock fronts. Since the HLLC solver incorporates a 3-wave structure, it suffers from this deficiency; on the other hand, the HLLE solver incorporates only 2-waves, and therefore is free from such numerical artifacts. To overcome the odd-even decoupling and carbuncle problems, Quirk [166] proposed to switch to a non-contact-preserving solver like HLLE within shocks thickness. It was however found that the instabilities arise from the use of contact-preserving solvers in the directions transverse to the shock front. Recently, Genin & Menon [78, 79] developed a hybrid Riemann solver that combines the HLLC and HLLE. Here, the hybrid Riemann solver returns the flux evaluation of the HLLC by default, but reverts to the HLLE fluxes if a shock is detected in the direction transverse to the direction of computation. This hybrid

approach significantly alleviates these numerical deficiencies, and has proven to be a robust solver, as demonstrated in [78, 79].

4.5 *Hybrid Approach*

The aforementioned central scheme flux computation (Section 4.3) is preferred in smooth regions such as shear layers, and the just mentioned MUSCL shock capturing approach with either HLL, or HLLC, or HLLC/E Riemann solver (Section 4.4) is required to accurately capture discontinuities. In order to undertake a procedure that accounts for both simulation strategies, it is essential to use a hybrid approach that combines both schemes. This section describes such a hybrid methodology.

In literature, several studies have been reported that incorporate a combination of different schemes, whose choice is decided by a blending parameter. This parameter, inevitably, should depend on the local flow conditions, so as to dynamically decide the choice of the scheme to be appropriately used. For instance, Harten & Zwas [95] suggested a blending parameter based on the velocity difference of adjacent cells across a boundary. Another switching procedure compares the magnitude of the second derivative of a given variable Q to its first derivative in the computational space [76, 78, 79]:

$$S_l \approx \frac{\partial^2 Q / \partial \xi^2}{\partial Q / \partial \xi} = \frac{|Q_{l+1} - 2Q_l + Q_{l-1}|}{|Q_{l+1} - Q_l| + |Q_l - Q_{l-1}|}, \quad (126)$$

where Q is any flow variable of interest (typically ρ or p), l is the computational index for any direction ($l = i, j, k$). The variable S_l is referred to as the “smoothness parameter.” To prevent switching due to numerical noise, the above parameter is set to zero if either the numerator or the denominator in Eqn. (126) divided by Q_l is less than 0.01 [78]. In case the smoothness parameter (S_l) exceeds some threshold (typically 0.5), the upwind scheme is used in order to compute the fluxes at the cell boundary.

Fryxell & Menon [76] applied this technique to combine the Piecewise Parabolic Method (PPM) [47] and a MacCormack-based central scheme [138]. They applied this to Richtmyer-Meshkov instabilities in multi-dimensions and showed that the approach was able to capture growth of small perturbations leading to a noticeable effect on the flow field. Recently, Genin & Menon [78, 79] extended the above concept to LES, and successfully investigated shock-turbulence interactions in sonic jets.

4.6 Discrete Equations Method (DEM)

4.6.1 Formulation

The problem of heterogeneous explosions involves the presence of a dense cloud of solid particles where finite volumes are occupied by both phases, thereby necessitating the use of a dense multiphase model. Here, blockage effects are to be accounted for, i.e., when both phases occupy non-negligible volumes, each phase partially blocks the flow of the other phase. Furthermore, the “nozzling terms” [1, 11] are critical to dense multiphase models and have to be appropriately evaluated. To this end, the Discrete Equations Method (DEM) [1, 44, 125] is used in the present study—a robust multiphase method well suited for multiphase flows involving shocks and solid particles. The basic idea behind the method starts with the representation of the volume fraction field as piecewise continuous, typical in any Godunov scheme. This is shown in Fig. 11 for three cells containing different number of particles, and therefore different volume fractions, before applying the MUSCL reconstruction, i.e., first order representation.

Following the methodology outlined in [1, 44], the DEM approach in 3 dimensions is derived, although it was originally proposed in 2 dimensions. First, the approach applicable for a Cartesian grid is derived, and later extended to non-Cartesian grids. While the original DEM proposed by Abgrall & Saurel [1] is Eulerian for both the carrier and dispersed phases, the current research effort involves the extension of the

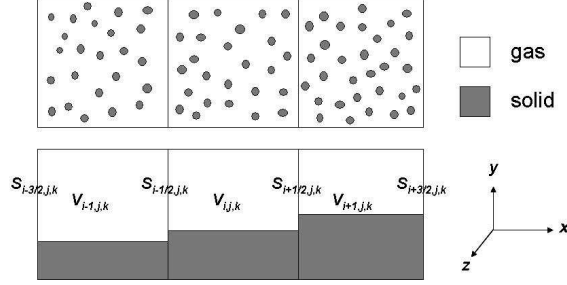


Figure 11: Volume fraction field representation in DEM. The schematic shows how a discrete particle field can be represented as a piecewise continuous volume fraction variable for flux computation.

Eulerian-Eulerian (EE) DEM to an Eulerian-Lagrangian (EL) formulation. In the present formulation, since the exact distribution of particles in space is known at every time instant due to the Lagrangian tracking of the particles, a separate volume fraction equation as used in the EE DEM is not needed. The solid volume fraction, α_p , is obtained by volume averaging each finite volume cell; the gas volume fraction field is then obtained as $\alpha_g = 1 - \alpha_p$. In addition, the EL DEM differs from [1, 44] in the sense that the DEM approach is used to only compute the gas-phase fluxes, as the solid-phase is solved for by means of Lagrangian tracking. Moreover, the solid phase is treated to be incompressible in the EL DEM unlike its counterpart EE DEM. The gas-phase governing equations at the microscopic scale in 3D can be summarized as:

$$\frac{\partial W}{\partial t} + \frac{\partial F}{\partial x} + \frac{\partial G}{\partial y} + \frac{\partial H}{\partial z} = 0, \quad (127)$$

where

$$\begin{aligned} W &= (\rho_g, \rho_g u_g, \rho_g v_g, \rho_g w_g, \rho_g E_g, \rho_g Y_k)^T, \\ F &= (\rho_g u_g, \rho_g u_g^2 + p_g, \rho_g u_g v_g, \rho_g u_g w_g, (\rho_g E_g + p_g) u_g, \rho_g u_g Y_k)^T, \\ G &= (\rho_g v_g, \rho_g u_g v_g, \rho_g v_g^2 + p_g, \rho_g v_g w_g, (\rho_g E_g + p_g) v_g, \rho_g v_g Y_k)^T, \\ H &= (\rho_g w_g, \rho_g u_g w_g, \rho_g v_g w_g, \rho_g w_g^2 + p_g, (\rho_g E_g + p_g) w_g, \rho_g w_g Y_k)^T, \end{aligned} \quad (128)$$

for the continuity, x -momentum, y -momentum, z -momentum, energy and k -th species equations, respectively.

Define an indicator function, λ , that takes the value 1 in regions of gas, and 0 otherwise. Following [44], this function obeys the equation

$$\frac{\partial \lambda}{\partial t} + u^* \frac{\partial \lambda}{\partial x} + v^* \frac{\partial \lambda}{\partial y} + w^* \frac{\partial \lambda}{\partial z} = 0, \quad (129)$$

where u^* , v^* and w^* denote, respectively, the local interface velocities in the x -, y - and z -directions. This equation vanishes for points within either of the phases, and is non-vanishing only at points located at multiphase interfaces. Combining these equations by integrating in time and space, results in the following for a cell C_{ijk} :

$$\begin{aligned} & \int_0^{\Delta t} \int_{C_{ijk}} \left(\frac{\partial(\lambda W)}{\partial t} + \frac{\partial(\lambda F)}{\partial x} + \frac{\partial(\lambda G)}{\partial y} + \frac{\partial(\lambda H)}{\partial z} \right) dV dt \\ &= \int_0^{\Delta t} \int_{C_{ijk}} \left((F - u^* W) \frac{\partial \lambda}{\partial x} + (G - v^* W) \frac{\partial \lambda}{\partial y} + (H - w^* W) \frac{\partial \lambda}{\partial z} \right) dV dt, \end{aligned} \quad (130)$$

where $dV = dx dy dz$. In the above equation, the left-hand side denotes the conservative fluxes, and the right-hand side denotes the non-conservative fluxes. The non-conservative terms arise only at multiphase interfaces and are obtained from the uniform interface velocity assumption, and will be (for a Cartesian grid)

$$\begin{aligned} F - u^* W &= (0, p^*, 0, 0, p^* u^*, 0)^T, \\ G - v^* W &= (0, 0, p^*, 0, p^* v^*, 0)^T, \\ H - w^* W &= (0, 0, 0, p^*, p^* w^*, 0)^T. \end{aligned} \quad (131)$$

The above expression is strictly valid only when no inter-phase mass transfer is involved. When mass transfer is to be accounted for, the procedure outlined in [125] is better suited.

The different types of integrals from Eqn. (130) that need to be evaluated are:

$$\begin{aligned}
I_1 &= \int_0^{\Delta t} \int_{C_{ijk}} \frac{\partial(\lambda W)}{\partial t} dV dt, \\
I_2 &= \int_0^{\Delta t} \int_{C_{ijk}} \frac{\partial(\lambda F)}{\partial x} dV dt, \\
I_3 &= \int_0^{\Delta t} \int_{C_{ijk}} (F - u^* W) \frac{\partial \lambda}{\partial x} dV dt,
\end{aligned} \tag{132}$$

for the temporal term, x -direction conservative and non-conservative fluxes, respectively, and similar expressions for fluxes in the y - and z -directions. For the remainder of the formulation, we present these expressions only for the x -direction fluxes, with the expressions being similar in mathematical form for the y - and z -directions. Following the approach outlined in [44], these integrals can be approximated as

$$I_1 = \int_{C_{ijk}} ((\lambda W)^{n+1} - (\lambda W)^n) dV = \left((\lambda W)_{ijk}^{n+1} - (\lambda W)_{ijk}^n \right) \Delta x \Delta y \Delta z, \tag{133}$$

for the temporal term and

$$\begin{aligned}
I_2 &= \int_0^{\Delta t} \int_{z_{k-1/2}}^{z_{k+1/2}} \int_{y_{j-1/2}}^{y_{j+1/2}} \int_{x_{i-1/2}}^{x_{i+1/2}} \frac{\partial(\lambda F)}{\partial x} dV dt = \\
&\int_0^{\Delta t} \int_{z_{k-1/2}}^{z_{k+1/2}} \int_{y_{j-1/2}}^{y_{j+1/2}} \left((\lambda F)_{i+1/2} - (\lambda F)_{i-1/2} \right) dS dt,
\end{aligned} \tag{134}$$

for the x -direction conservative flux, where $dS = dydz$. To compute I_2 , the flux is obtained as a surface average. Observing Fig. 11, it is deduced that the inter-cell interface at $i + 1/2$ and $i - 1/2$ can be constructed as a series of smaller interfaces, i.e., three out of four different possible scenarios, viz. gas-gas ($g - g$), gas-solid ($g - s$), solid-gas ($s - g$) and solid-solid ($s - s$), where ‘gas-solid’ refers to a state of gas on the left and solid on the right. This is made possible due to the piecewise representation of the volume fraction field. The total gas flux passing through the surface area at $i + 1/2$ or $i - 1/2$ is obtained as a summation over each of these smaller interfaces.

For instance, at $i - 1/2$, the total flux integrated from $j - 1/2$ to $j + 1/2$ and $k - 1/2$ to $k + 1/2$ is obtained as follows

$$\int_{z_{k-1/2}}^{z_{k+1/2}} \int_{y_{j-1/2}}^{y_{j+1/2}} (\lambda F)_{i-1/2} dS = \lambda^*_{i-1/2} F^*_{i-1/2} (g - g) S_{g-g} + \lambda^*_{i-1/2} F^*_{i-1/2} (g - s) S_{g-s} + \lambda^*_{i-1/2} F^*_{i-1/2} (s - g) S_{s-g} + \lambda^*_{i-1/2} F^*_{i-1/2} (s - s) S_{s-s}, \quad (135)$$

where the subscripts g and s denote the gas and solid, respectively. The ‘*’ superscript is introduced to denote interface quantities. Here, λ^* denotes the indicator function, which is obtained from the sign of the interface velocity (u^*); the interface surface areas S_{g-g} , S_{g-s} , etc. are obtained using the gas volume fraction. These expressions are summarized in Table 1 for the cell interface at $i - 1/2$, where S denotes the inter-cell area, α is the gas volume fraction, and u^* is the interface velocity. Note that the first row of Table 1 corresponds to the gas phase on either sides of the interface, and therefore the indicator function is unity as gas flux always has to flow through the interface; the last row of Table 1 corresponds to the solid phase on both sides of the interface, and therefore the indicator function is zero as no gas flux can flow through the interface.

Table 1: Conservative flux at cell interface $i - 1/2$

Contact type	Contact surface	Indicator function, λ
gas–gas	$S \min(\alpha_{i-1}, \alpha_i)$	1
gas–solid	$S \max(\alpha_{i-1} - \alpha_i, 0)$	1 if $u^* \geq 0$; 0 otherwise
solid–gas	$S \max(\alpha_i - \alpha_{i-1}, 0)$	1 if $u^* < 0$; 0 otherwise
solid–solid	$S \min(1 - \alpha_{i-1}, 1 - \alpha_i)$	0

At gas-solid contacts, the indicator function is based on the sign of the interface velocity, which decides whether the flux of gas is permissible through the local interface. For conservative fluxes, the gas flux can be flowing either inside or outside the cell, depending on the sign of the interface velocity. When the multiphase interface is blocking the flow of gas, the indicator function is zero. Note that the conservative

flux consists of the convective and the pressure fluxes; since they are together computed from the Riemann solver, the sign of the interface velocity decides whether or not both fluxes have to be computed. The underlying reason behind the splitting of the cell interfaces into different pairs in the flux computation with the DEM is that the Riemann problem is different when gas exists on both sides of the interface, as opposed to gas on one side and solid on the other. If a pressure wave approaches an interface, part of the momentum and energy is reflected and part of it transmitted; the exact amounts that are reflected and transmitted will be different when the interface consists of gas on either side, or gas on one side and solid on the other. This is due to different compressibilities of the two phases under consideration, and thus the splitting of cell interfaces into a combination of different Riemann problems, as first proposed in the EE DEM [1], is essential to accurately use the appropriate Riemann solver in the evaluation of the total flux crossing the cell interface.

The same approach for flux computation is used at the location $i + 1/2$. The y - and z -direction conservative fluxes are similar in form to I_2 and are thus not shown here for brevity. To obtain the non-conservative flux I_3 , the following expression is used:

$$\begin{aligned}
I_3 = & \int_0^{\Delta t} \int_{z_{k-1/2}}^{z_{k+1/2}} \int_{y_{j-1/2}}^{y_{j+1/2}} \left[(F - u^*W)_{i-1/2}[\lambda]_{i-1/2} + (F - u^*W)_{i+1/2}[\lambda]_{i+1/2} \right] dSdt \\
& + \int_0^{\Delta t} \int_{z_{k-1/2}}^{z_{k+1/2}} \int_{y_{j-1/2}}^{y_{j+1/2}} (F - u^*W)_i[\lambda]_i dSdt, \tag{136}
\end{aligned}$$

where the subscripts $i - 1/2$ and $i + 1/2$ denote the multiphase interfaces at the cell boundary, and i denotes the internal interfaces; the boundary and internal terms are evaluated separately. Following the approach outlined in [44], the non-conservative term at $i - 1/2$ is evaluated as

Table 2: Non-Conservative flux at cell interface $i - 1/2$

Contact type	Contact surface	Jump in indicator function, $[\lambda]$
gas–gas	$S \min(\alpha_{i-1}, \alpha_i)$	0
gas–solid	$S \max(\alpha_{i-1} - \alpha_i, 0)$	-1 if $u^* \geq 0$; 0 otherwise
solid–gas	$S \max(\alpha_i - \alpha_{i-1}, 0)$	1 if $u^* \geq 0$; 0 otherwise
solid–solid	$S \min(1 - \alpha_{i-1}, 1 - \alpha_i)$	0

$$\int_{z_{k-1/2}}^{z_{k+1/2}} \int_{y_{j-1/2}}^{y_{j+1/2}} (F - u^*W)_{i-1/2} [\lambda]_{i-1/2} dS = [\lambda^*]_{i-1/2} (F^* - u^*W^*)_{i-1/2} (s - g) S_{s-g} + [\lambda^*]_{i-1/2} (F^* - u^*W^*)_{i-1/2} (g - s) S_{g-s}. \quad (137)$$

In the above expression, $[\lambda^*]$ represents the jump in the indicator function, and is summarized in Table 2 at the cell interface $i - 1/2$. The same approach is used to compute the non-conservative term at $i + 1/2$. Note that at the cell interface $i - 1/2$, the non-conservative flux will have to be computed for the cell i only if the multiphase interface velocity (u^*) is positive; otherwise, it has to be computed for the cell $i - 1$. Furthermore, the non-conservative flux will be computed at the interface $i + 1/2$ for the cell i only if the interface velocity is negative; otherwise it will be computed for cell $i + 1$. These terms in the y - and z -directions are similar in form to I_3 and are thus not shown here for brevity.

To compute I_3 , the only term that remains to be addressed is the last integral in Eqn. (136), which corresponds to internal interfaces—these terms represent the relaxation/coupling terms. The significance of the relaxation terms are that when the two phases are not in mechanical or thermal equilibrium, the relaxation terms tend to drive the flow-field such that the two phases tend toward equilibrium, albeit with finite time scales. In the EE DEM, the non-conservative fluxes at the internal interfaces (relaxation terms) were computed by using the Riemann solver and summing up over all the internal interfaces [44]. The present EL DEM formulation, however, differs from the EE DEM in the sense that viscous effects are also considered, i.e., the total

drag (viscous + pressure) and heat transfer, for which empirical correlations (Section 3.2) are used. In doing so, spherical particles can also be accounted inside the finite volume, unlike the original EE DEM, which was formulated for square particles [44] only. One similarity between the evaluation of these terms between the EE DEM and the EL DEM is that they are obtained as a summation over all the particles present in a given cell.

4.6.2 Interface closure

Since the flux estimation in DEM involves knowledge of the interface velocity precisely (refer to Tables 1 & 2), only contact surface based Riemann solvers, such as the HLLC and the Roe scheme [194] can be used; in the current study, the HLLC Riemann solver is used for flux estimation with the DEM. While the inter-cell flux is obtained in the conventional way (see Section 4.4.2) at gas-gas contacts, for the gas-solid contacts a half-Riemann problem [178] is solved, due to the incompressible solid assumption. A half-Riemann problem is a condition when the shock or rarefaction propagates only on one side of the inter-cell interface, i.e., the side of the gas. Since the solid particles are incompressible, the interface velocity at gas-solid contacts is equated to the mass-weighted average velocity of all the solid particles in the cell corresponding to the side of the solid, given as

$$u_i^* = \frac{\sum_{n=1}^N m_{p,n} u_{p,i,n}}{\sum_{n=1}^N m_{p,n}}. \quad (138)$$

This is obtained from the assumption that continuity in velocity exists near gas-solid contacts. The conservative and non-conservative fluxes at multiphase contacts are computed using this solid particle velocity based interface velocity. When all the particles in a cell have the same mass, the interface velocity is the arithmetic average of all the solid particle velocities. Although only mono-disperse particle distributions are investigated in this study, the current formulation can be easily extended to handle

a varying particle size distribution. This is made possible by using an appropriate particle mass (dependent on size) for each particle in a cell in the mass-weighting computation of u_i^* (Eqn. 138).

For the non-conservative flux computation, both interface pressure and velocity needs to be known, as can be perceived from Eqn. (131). The interface velocity computation (Eqn. 138) has been demonstrated; now the interface pressure computation is presented. The interface pressure (p^*) is obtained accordingly, depending on a compression or rarefaction at the two-phase interface. Comparing the velocities of the gas and solid particles, it can be deduced whether any interface corresponds to a state of compression or rarefaction. For compression, the interface pressure is obtained using shock and Rankine-Hugoniot relations; for rarefaction, isentropic relations and Riemann invariants are used. These equations are now discussed.

For a compression, the equations are obtained from Toro [193]. Consider the case of a right traveling shock wave and an incompressible solid on the left. Let subscript ‘ r ’ correspond to the right state and superscript ‘ $*$ ’ the interface. The steady shock relations for a right travelling shock give:

$$M_r^2 = \frac{\rho_{g,r} (p^* - p_{g,r}) D_r}{D_r - 1}, \quad (139)$$

where M_r is defined as:

$$M_r = \frac{p^* - p_{g,r}}{u^* - u_{g,r}} \quad (140)$$

and D_r is the density ratio $\rho^*/\rho_{g,r}$ across the shock. The Rankine-Hugoniot relation is given by:

$$e^* - e_{g,r} = \frac{1}{2} \left(\frac{p_{g,r}}{\rho_{g,r}} \right) \frac{(H_r + 1) (D_r - 1)}{D_r}, \quad (141)$$

where H_r is the pressure ratio $p^*/p_{g,r}$ across the shock. Using the equation of state for the ‘ $*$ ’ and ‘ r ’ states, the variables e^* and $e_{g,r}$ in the above equation can be replaced

by a function of the corresponding state pressure and density. This gives rise to two equations in two variables (p^* and ρ^*), which are solved numerically. Similar expressions can be obtained for a left travelling shock wave with the incompressible solid on the right.

For a rarefaction, on the other hand, the isentropic relation and Riemann invariant are applied across the ‘*’ and left or right gas state, as the case may be. The isentropic relation applicable for the JWL equation of state is given by [220] as follows:

$$p_g = A \exp\left(\frac{-R_1 \rho_o}{\rho_g}\right) + B \exp\left(\frac{-R_2 \rho_o}{\rho_g}\right) + C \left(\frac{\rho_o}{\rho_g}\right)^{-(1+\omega)}. \quad (142)$$

The Riemann invariant for a left moving rarefaction, applicable for a generic equation of state is given by:

$$u_g + \int \frac{a_g}{\rho_g} d\rho_g = \text{constant}, \quad (143)$$

where a_g denotes the speed of sound in the gas. For a right moving rarefaction, the ‘+’ is replaced by ‘-’. The above two equations are applied for the ‘*’ and left or right state, as the case may be, thus giving rise to two equations in two unknowns (p^* and ρ^*). These are numerically solved to obtain p^* and ρ^* . For a perfect gas, the above equations simplify to close-form expressions for p^* and ρ^* , thereby simplifying their numerical implementation. Thus, two equations are solved numerically to obtain two variables, i.e., interface pressure and density, with the interface velocity known. Once the interface variables have been computed, the conservative and non-conservative fluxes can be evaluated following the DEM approach. Another approach to obtain the interface pressure, more simpler in nature, is the use of an acoustic analogy [44]. For a multiphase interface with gas to the left and solid to the right, the acoustic analogy gives the expression for the interface pressure (assuming incompressible solid):

$$p^* = p_l - \rho_l c_l (u_l - u^*), \quad (144)$$

where the variable c denotes the speed of sound, and the subscript l denotes the left gas state. On the other hand, the corresponding acoustic analogy expression for a multiphase interface with gas to the right and solid to the left will be:

$$p^* = p_r + \rho_r c_r (u_r - u^*), \quad (145)$$

where the subscript r denotes the right gas state. Very recently, the effect of using different interface pressure closures in the EE DEM was addressed [154].

4.6.3 Non-Cartesian grids

The DEM formulation presented thus far is applicable only for a Cartesian grid; modifications involved to extend the formulation to non-Cartesian grids are now discussed. The integral form of the finite volume representation presented in Eqn. (130) is generic for any grid. The flux integrals presented in Eqn. (132) are the same also for non-Cartesian grids; however, their evaluation requires alterations when applied to non-Cartesian grids. The temporal term, i.e., I_1 in Eqn. (132), will be

$$I_1 = \int_{C_{ijk}} ((\lambda W)^{n+1} - (\lambda W)^n) dV = \left((\lambda W)_{ijk}^{n+1} - (\lambda W)_{ijk}^n \right) \Delta V, \quad (146)$$

where ΔV denotes the volume of the cell (i, j, k) under consideration. In order to compute the conservative flux integral I_2 in Eqn. (132), the mathematical form of Eqn. (134) is retained. As before, the cell interface is broken into a series of Riemann problems with pure fluid on either side, as identified by Eqn. (135). The next step in the approach involves modifications for non-Cartesian grids. To evaluate Eqn. (135), the terms to be determined are $\lambda^*_{i-1/2}$, $F^*_{i-1/2}(g-g)$, S_{g-g} , $F^*_{i-1/2}(g-s)$, S_{g-s} , $F^*_{i-1/2}(s-g)$, S_{s-g} , $F^*_{i-1/2}(s-s)$ and S_{s-s} .

To determine the above variables, the rules presented in Table 1 are used, with a modification to the definition of the interface velocity at gas-solid contacts when

a non-Cartesian grid is under consideration. Here, the interface velocity at gas-solid contacts is obtained using the direction cosines (n_i) of the outward normal to the non-Cartesian interface under consideration, as done earlier for the gas-gas Riemann problem in Section 4.4.2. For non-Cartesian grids, the interface velocity is the contravariant velocity, q^* , and is obtained at the gas-solid contact as $q^* = u_i^* n_i$, where n_i denotes the direction cosines of the outward normal at the interface. This is analogous to obtaining the left and right velocities in the pure-gas (single phase) Riemann solver, in which the direction cosines of the outward normal are used to estimate the interface velocity using the left and right velocity components (as done in Section 4.4.2). The interface velocity at gas-solid contacts is then obtained as

$$q^* = u_p n_x + v_p n_y + w_p n_z, \quad (147)$$

where u_p , v_p and w_p denote, respectively, the x , y and z components of the solid particle velocity obtained from mass-weighted averaging (Eqn. 138). Table 1 is used with q^* instead of u^* , in order to extend the same approach to non-Cartesian grids as well. In particular, the terms $\lambda^*_{i-1/2}$, S_{g-g} , S_{g-s} , S_{s-g} , and S_{s-s} are evaluated using Table 1, with the just defined q^* for gas-solid contacts. In order to evaluate Eqn. (135) for non-Cartesian grids, the fluxes $F^*_{i-1/2}(g-g)$, $F^*_{i-1/2}(g-s)$, $F^*_{i-1/2}(s-g)$ and $F^*_{i-1/2}(s-s)$ must also be computed taking into account the direction cosines. The flux $F^*_{i-1/2}(g-g)$ is computed as before (Section 4.4.2), since this involves a Riemann problem with pure gas states on either side of the interface. In addition, $F^*_{i-1/2}(s-s) = 0$, as this corresponds to the solid phase on either side, which is of no interest with respect to the gas flux evaluation. As before, $F^*_{i-1/2}(g-s)$ and $F^*_{i-1/2}(s-g)$ are evaluated at the respective multiphase interfaces by solving a half-Riemann problem, whose modifications for a non-Cartesian grid are now discussed.

A half-Riemann problem at a gas-solid contact can be treated to be equivalent to a full-Riemann problem with the solid state replaced with a modified ‘ghost’ gas

state with the same pressure and density as the side of the gas, but with the negative of the velocity augmented with twice the solid velocity. To illustrate this, consider a half-Riemann problem corresponding to a gas on the left (l) and solid on the right (r). Define $u_{g,l}$, $v_{g,l}$, $w_{g,l}$, $p_{g,l}$ and $\rho_{g,l}$ to denote the x , y and z components of velocity, pressure and density, respectively, of the gas on the left; $u_{p,r}$, $v_{p,r}$ and $w_{p,r}$ to denote the three velocity components of the solid on the right. It is now demonstrated that the modified full Riemann problem with this ghost gas state to replace the solid can recover the same interface velocity as the original gas-solid half-Riemann problem. Replace the solid state on the right with a ghost gas state with $u_{g,r}$, $v_{g,r}$, $w_{g,r}$, $p_{g,r}$ and $\rho_{g,r}$ to denote the x , y and z components of velocity, pressure and density, respectively, of the ghost gas on the right. Impose the following constraints to this ghost gas state on the right:

$$\begin{aligned}
u_{g,r} &= -u_{g,l} + 2q^*n_x, \\
v_{g,r} &= -v_{g,l} + 2q^*n_y, \\
w_{g,r} &= -w_{g,l} + 2q^*n_z, \\
p_{g,r} &= p_{g,l}, \\
\rho_{g,r} &= \rho_{g,l}.
\end{aligned} \tag{148}$$

Following Toro [194], the following wave speed (S_l , S_r) estimates are used for the HLLC Riemann solver

$$S_l = q_l - c_l; S_r = q_r + c_r, \tag{149}$$

where q_l and q_r are obtained as

$$q_l = u_{g,l}n_x + v_{g,l}n_y + w_{g,l}n_z; q_r = u_{g,r}n_x + v_{g,r}n_y + w_{g,r}n_z, \tag{150}$$

and c_l and c_r denote, respectively, the speeds of sound in the left and right states. Note that since $p_{g,r} = p_{g,l}$ and $\rho_{g,r} = \rho_{g,l}$, it directly follows that $c_r = c_l$. Using Eqn. (148), it can be easily shown that $q_r = -q_l + 2q^*$. Substituting the left gas state and the modified right ghost gas state into the HLLC interface velocity equation (Eqn. (119)) results in:

$$S^* = \frac{p_{g,r} - p_{g,l} + \rho_{g,l}q_l(S_l - q_l) - \rho_{g,r}q_r(S_r - q_r)}{\rho_{g,l}(S_l - q_l) - \rho_{g,r}(S_r - q_r)}, \quad (151)$$

which can be expressed as:

$$S^* = \frac{p_{g,l} - p_{g,l} + \rho_{g,l}q_l(S_l - q_l) - \rho_{g,l}(-q_l + 2q^*)c_l}{\rho_{g,l}(S_l - q_l) - \rho_{g,l}c_l}, \quad (152)$$

and simplifies to

$$S^* = \frac{\rho_{g,l}q_l(-c_l) - \rho_{g,l}(-q_l + 2q^*)c_l}{\rho_{g,l}(-c_l) - \rho_{g,l}c_l}, \quad (153)$$

and, on re-arranging, results to

$$S^* = q^*. \quad (154)$$

Note that this result can also be obtained for the other possible half-Riemann problem, i.e., when the gas is to the right and solid to the left. Thus, at gas-solid contacts, replacing the solid with the specified ghost gas state, the half-Riemann problem can be made analogous to the full-Riemann problem with the ghost gas state. This is a very useful result, as it directly implies that a modified gas-gas Riemann problem for which a solution exists even with non-Cartesian grids (as detailed in Section 4.4.2), can be constructed in lieu of a gas-solid or solid-gas half-Riemann problem in order to evaluate the conservative flux integrals. Hence, the conservative fluxes at gas-solid interfaces, viz. $F^*_{i-1/2}(g - s)$ and $F^*_{i-1/2}(s - g)$, can be evaluated using the same procedure as outlined in Section 4.4.2, by appropriately modifying the local Riemann

problem to that of an equivalent gas-gas system. In particular, Eqn. (125) can be applied to evaluate the conservative fluxes even at gas-solid contacts ($F^*_{i-1/2}(g-s)$, $F^*_{i-1/2}(s-g)$), as this multiphase Riemann problem has been simplified to a pure gas Riemann problem with the use of the modified ghost gas state as defined in Eqn. (148). Thus, even I_2 in Eqn. (132) can be computed for non-Cartesian grids, by appropriately computing the fluxes at the gas-gas, gas-solid and solid-gas states as just demonstrated. In order to complete the evaluation of Eqn. (132), the only other integral that remains to be extended to non-Cartesian grids is I_3 , i.e., the non-conservative flux.

For the non-conservative flux computation in non-Cartesian grids, the evaluation of I_3 in Eqn. (132) is not trivial as the integrand is in a non-conservative form. However, in this formulation this term is computed only at the cell boundaries, i.e., not in the interior, which simplifies the computation. Recall that I_3 involves two sub-integrals, one computed at the boundary, and the other at the interior of cells [1, 44]. Whereas the integration at the boundary interfaces represents the non-conservative/“nozzling” terms, the integration at the interior interfaces corresponds to the source/relaxation terms, which are obtained as a summation in the current approach (Section 3.2.2). The interface pressure and interface velocity are used to compute the non-conservative fluxes at the cell boundaries. For a grid not aligned along the Cartesian axes, the non-conservative fluxes are obtained as p^*n_x , p^*n_y and p^*n_z , respectively for the x -, y - and z -momentum equations, following [39].

For the energy equation, the corresponding non-conservative flux will be the pressure work, and is given as p^*q^* , where, as mentioned before, q^* is obtained as $q^* = u_p n_x + v_p n_y + w_p n_z$. This is analogous to the consideration of three surface areas Sn_x , Sn_y and Sn_z at an inter-cell interface whose surface area is S , aligned along x -, y - and z -directions, respectively. The non-conservative fluxes are computed at each of these three interfaces, multiplied by the appropriate surface areas and the

jump in the indicator functions (see Table 2), and then included in the finite volume methodology. This term, which is I_3 in Eqn. (132) evaluated at the boundary, will be:

$$\begin{bmatrix} 0 \\ p^* n_x \\ p^* n_y \\ p^* n_z \\ p^* q^* \\ 0 \end{bmatrix} [\lambda] (S\Delta\alpha), \quad (155)$$

in three-dimensions for the continuity, x -, y -, and z -momentum, energy and k -th species equations, respectively. The rules for obtaining $[\lambda]$ and $(S\Delta\alpha)$ are summarized in Table 2. Note that q^* as defined in Eqn. (147) must be used instead of u^* in Table 2 for non-Cartesian grids. Furthermore, from Table 2, $[\lambda] = +1$ or -1 decides whether the flux is entering or leaving the cell. Thus, I_3 in Eqn. (132) can be evaluated for non-Cartesian grids as well. The computation strategy demonstrated here for non-Cartesian grids in the x -direction can be extended to the evaluation of the fluxes also in the y and z directions as well, and whose mathematical form is not presented here for brevity.

In summary, the DEM formulation for a generic grid is represented by Eqn. (130) in three-dimensions, which involves three kinds of integrals, viz. I_1 , I_2 and I_3 , as presented in Eqn. (132). For non-Cartesian grids, I_1 is evaluated using Eqn. (146); I_2 using Eqn. (135) and following the rules outlined in Table 1, but with an appropriate choice of the local Riemann problem; and I_3 is solved using Eqn. (155) and following the rules outlined in Table 2. For using Tables 1 and 2, q^* from Eqn. (147) is to be used in place of u^* for non-Cartesian grids. With these modifications in place, the DEM formulation is amenable to computation even with non-Cartesian grids.

4.6.4 Summary of DEM

To summarize this formulation, Fig. 12 shows the volume fraction representation across three contiguous cells. The arrows denote the direction to which the interface has to move so that the gas-phase flux needs to be computed for the middle cell. Note that MUSCL reconstruction is applied for the gas volume fraction, α_g , to obtain a higher order of accuracy. For interfaces with gas on either side, the conservative flux is non-zero for any direction of the movement of the interface. For interfaces with gas on one side, and solid on the other, the conservative flux is non-zero if and only if the interface moves in a direction such that the flow of gas is permissible (either entering or leaving the cell). Furthermore, the non-conservative fluxes are non-zero if and only if the gas-solid contact moves in a direction such that the cell-interface is not blocked. Note that the arrow directions shown for the non-conservative flux in Fig. 12 are applicable only for cell (i,j,k) ; if the arrows are reversed for the non-conservative flux computation shown in Fig. 12, these terms will not be accounted for cell (i,j,k) , but will be considered for the other cells $(i-1,j,k)$ or $(i+1,j,k)$, as the case may be. The rules outlined in Table 1 are used for computing the conservative fluxes, and those in Table 2 to compute the non-conservative fluxes.

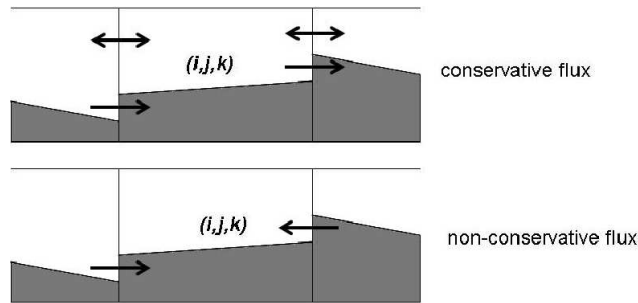


Figure 12: When to compute conservative and non-conservative fluxes for cell (i,j,k) . The arrow denotes the direction the interface has to move to have a non-zero gas flux entering or leaving the middle cell. The white regions denote the space available for the gas; the grey regions denote the space occupied by the solid particles.

The DEM approach is used to compute the fluxes in all the three directions, i.e., x ,

y and z . To compute the fluxes in y , the cells aligned along the y directions, i.e., $(i, j-1, k)$, (i, j, k) and $(i, j+1, k)$ are considered and the piecewise linear representation of the volume fraction field (using MUSCL) is constructed along the y -direction this time. The same methodology mentioned hitherto is used this time to compute the fluxes in the y -direction; similarly for the fluxes in the z -direction. Thus, the piecewise linear representation of the volume fraction field is so constructed, depending on whether the flux computation is along x -, y - or z -direction.

Due to the presence of a volume fraction gradient within the cell (due to MUSCL reconstruction), an additional term has to be included in the finite volume formulation [1]. This term arises in the computation of the non-conservative flux for the second-order scheme due to the presence of a volume fraction gradient within the cell. This term (in x -direction) is computed using the gas volume fractions to the immediate left of the $i+1/2$ interface and to the right of the $i-1/2$ interface, which are obtained from MUSCL reconstruction. The origin of this term and its precise mathematical form are well explained in [154], and not detailed here for brevity.

The major advantage of the EL DEM over the EE DEM is that the treatment of the dispersed phase to not be in continuum, enables the precise estimation of particle trajectories. However, the EL DEM suffers a major drawback over its counterpart. The EL DEM will not be applicable to multiphase problems where $\alpha_p \rightarrow 1$, since this would violate continuum assumption required for flux computation and equation of state usage. Thus, the EL DEM is not suited for multiphase simulations such as liquid jet breakup, under water explosions, shock bombardment into compressible materials, etc. For these problems, the EE DEM is better suited. Problems involving α_p less than, say 0.7, such as the problem under investigation, and the problem of detonation propagation through a dense cloud of solid particles are well suited for study with the EL DEM. In Chapter 7, the efficacy of the EL DEM to simulate dense, multiphase, high-speed flows will be demonstrated for initial solid volume fractions (α_p) as high

as $\sim 60\%$.

4.7 Initial Detonation Profile (GISPA Method)

The initial detonation profiles are obtained based on a one-dimensional simulation employing the Gas-Interpolated-solid-Stewart-Prasad-Asay (GISPA) method for the detonation process [209]. This method permits time-accurate simulation of detonation from the time of the initial shock through the completion of the explosive burn. The GISPA method is robust, as emphasized by its ability to capture the reaction zone as well as the Von Neumann spike [209]. In the GISPA method, the Euler equations are solved in a one-dimensional radial coordinate system using the progress variable approach [210]. Since the current study also includes solid particles, the original GISPA method has been extended to a multiphase problem, along with appropriate reaction rates and equations of state for the condensed explosive and the detonation product gases.

The GISPA method is described in elaborate detail in Appendix B, including the governing equations, validation studies, and the detonation profiles for homogeneous as well as heterogeneous explosive charges—these profiles will be used as initial conditions for the simulations considered in the current study.

4.8 Other Computational Issues

4.8.1 Generalized grids

Many a time, the simulation grids are not aligned along the Cartesian directions, resulting in meshes that are skewed and/or stretched with non-orthogonal computational cells. This introduces modifications to the solution procedure. The geometrical grid represented by the co-ordinate system (x, y, z) is usually transformed to a so-called computational grid represented with the co-ordinate system (ξ, η, ζ) . This mapping is undertaken so as to enable the computation of spatial derivatives of flow variables, which would not be straightforward in the geometrical grid when skewed

meshes are involved. The computational grid is treated as a structured row and column distribution of the co-ordinate system (ξ, η, ζ) , thereby enabling the computation of spatial derivatives of flow variables with ease, provided the mapping procedure is undertaken with care.

Stated in these terms, the second order derivative of any variable ϕ with respect to x is given by:

$$\frac{\partial \phi}{\partial x} = \frac{\partial \xi}{\partial x} \frac{\partial \phi}{\partial \xi} + \frac{\partial \eta}{\partial x} \frac{\partial \phi}{\partial \eta} + \frac{\partial \zeta}{\partial x} \frac{\partial \phi}{\partial \zeta}, \quad (156)$$

where the derivatives of ϕ with respect to ξ , η and ζ are evaluated as:

$$\begin{aligned} \frac{\partial \phi}{\partial \xi} &= \phi(i+1, j, k) - \phi(i-1, j, k), \\ \frac{\partial \phi}{\partial \eta} &= \phi(i, j+1, k) - \phi(i, j-1, k), \\ \frac{\partial \phi}{\partial \zeta} &= \phi(i, j, k+1) - \phi(i, j, k-1). \end{aligned} \quad (157)$$

Note that $\Delta\xi = \Delta\eta = \Delta\zeta=1$. The derivatives of the set (x, y, z) with respect to the set (ξ, η, ζ) can be summarized as:

$$\begin{aligned}
\frac{\partial x}{\partial \xi} &= \frac{x(i+1, j, k) - x(i-1, j, k)}{2}, \\
\frac{\partial x}{\partial \eta} &= \frac{x(i, j+1, k) - x(i, j-1, k)}{2}, \\
\frac{\partial x}{\partial \zeta} &= \frac{x(i, j, k+1) - x(i, j, k-1)}{2}, \\
\frac{\partial y}{\partial \xi} &= \frac{y(i+1, j, k) - y(i-1, j, k)}{2}, \\
\frac{\partial y}{\partial \eta} &= \frac{y(i, j+1, k) - y(i, j-1, k)}{2}, \\
\frac{\partial y}{\partial \zeta} &= \frac{y(i, j, k+1) - y(i, j, k-1)}{2}, \\
\frac{\partial z}{\partial \xi} &= \frac{z(i+1, j, k) - z(i-1, j, k)}{2}, \\
\frac{\partial z}{\partial \eta} &= \frac{z(i, j+1, k) - z(i, j-1, k)}{2}, \\
\frac{\partial z}{\partial \zeta} &= \frac{z(i, j, k+1) - z(i, j, k-1)}{2}.
\end{aligned} \tag{158}$$

The spatial derivatives can be obtained by applying chain rule:

$$\begin{bmatrix} \frac{\partial x}{\partial \xi} & \frac{\partial x}{\partial \eta} & \frac{\partial x}{\partial \zeta} \\ \frac{\partial y}{\partial \xi} & \frac{\partial y}{\partial \eta} & \frac{\partial y}{\partial \zeta} \\ \frac{\partial z}{\partial \xi} & \frac{\partial z}{\partial \eta} & \frac{\partial z}{\partial \zeta} \end{bmatrix} \begin{bmatrix} \frac{\partial}{\partial x} \\ \frac{\partial}{\partial y} \\ \frac{\partial}{\partial z} \end{bmatrix} = \begin{bmatrix} \frac{\partial}{\partial \xi} \\ \frac{\partial}{\partial \eta} \\ \frac{\partial}{\partial \zeta} \end{bmatrix}, \tag{159}$$

and

$$\begin{bmatrix} \frac{\partial \xi}{\partial x} & \frac{\partial \xi}{\partial y} & \frac{\partial \xi}{\partial z} \\ \frac{\partial \eta}{\partial x} & \frac{\partial \eta}{\partial y} & \frac{\partial \eta}{\partial z} \\ \frac{\partial \zeta}{\partial x} & \frac{\partial \zeta}{\partial y} & \frac{\partial \zeta}{\partial z} \end{bmatrix} \begin{bmatrix} \frac{\partial}{\partial \xi} \\ \frac{\partial}{\partial \eta} \\ \frac{\partial}{\partial \zeta} \end{bmatrix} = \begin{bmatrix} \frac{\partial}{\partial x} \\ \frac{\partial}{\partial y} \\ \frac{\partial}{\partial z} \end{bmatrix}. \tag{160}$$

The 3×3 matrices on the left hand side of the above two equations are usually referred to as the *Jacobians*. This approach is used to compute spatial derivatives of the flow variables in the physical space (x, y, z) using variables mapped into the computational space (ξ, η, ζ) , thus extending the simulation strategy to any generic grid.

4.8.2 Boundary conditions

Boundary Conditions, or BCs for short, are mathematical constraints enforced at the domain boundaries so that the flow conforms to a desired pattern locally. BCs are often classified into two groups: Dirichlet and Neumann [191], although a mixed combination can also be used, usually referred to as Robin BCs. The purpose of BCs is to provide additional information to the flow variables at domain boundaries, and is required to close the solution procedure of partial differential equations—the Navier-Stokes equations in fluid problems. The most common BCs applied for fluid flow problems can be categorized as inflow, outflow, periodic, no-slip wall or slip wall for the flow variables, and as adiabatic or isothermal for temperature. Furthermore, inflow and outflow BCs can be further classified as subsonic (also referred to as characteristic BC) or supersonic. Additional cells, referred to as “ghost cells,” are created near the boundaries, and BCs are applied to evaluate the values of the flow variables in these cells. Note that these ghost cells are outside the domain of simulation, and do not exist in the physical problem; they are existent only in the mathematical problem. The number of ghost cells required at the boundaries in each direction is related to the order of accuracy of the scheme.

In the current study, supersonic outflow BC, slip and no-slip walls are of interest, and are now summarized.

- Supersonic outflow BC

In supersonic flows, the flow velocity is greater than the local speed of sound, and no characteristic can propagate upstream of the flow. Outflow BCs are imposed using a standard extrapolation method, since information propagates only in one direction. Thus, the properties in the boundary cells can be directly imposed from the interior of the domain. Stated in these terms, a variable U can be extended to the boundaries at index N by the relation (note: $N + \frac{1}{2}$ represents the actual boundary):

$$U_{N+1} = U_N. \quad (161)$$

- Wall BC

No-slip walls are enforced as zero velocity (u, v, w), both in the tangential and normal directions, and with zero pressure (p) and passive scalar (e.g., Y_k) gradients. With respect to temperature (T), a no-slip wall may be implemented as adiabatic ($\frac{dT}{dn} = 0$) or isothermal ($\frac{dT}{dn} \neq 0$); here, n represents the direction normal to the wall. Mathematically, a no-slip wall can be enforced as:

$$u_{N+1} = -u_N; v_{N+1} = -v_N; w_{N+1} = -w_N. \quad (162)$$

Another option for walls is to model them as free-slip walls, also referred to as symmetry BC. This type enforces zero velocity in the direction normal to the wall, but allows slippage of flow in the tangential direction. With respect to temperature, the slip wall enforces an adiabatic condition. For a slip wall with free-slip along the direction of u and w :

$$u_{N+1} = u_N; v_{N+1} = -v_N; w_{N+1} = w_N. \quad (163)$$

Note that for both no-slip as well as slip walls, the pressure (p) and mass fractions (Y_k) obey the relation:

$$p_{N+1} = p_N; Y_{k,N+1} = Y_{k,N}. \quad (164)$$

The temperature (T) BC is enforced as

$$T_{N+1} = T_N \quad (165)$$

for an adiabatic wall, and as

$$T_{N+1} = 2T_{wall} - T_N \quad (166)$$

for an isothermal wall, where T_{wall} denotes the wall temperature known *a priori*.

A widely used BC for subsonic inflows and outflows was proposed by Poinso & Lele [163], based on the use of information from both directions. This BC, typically referred to as “characteristic BC,” is not used in the current study as the interest here is on supersonic flows. The interested reader is referred to [162, 163] for further details.

4.8.3 4^{th} order Runge-Kutta integration for particle phase

The particle phase governing equations summarized in Section 3.2 are integrated using a 4^{th} order Runge-Kutta scheme. Consider for instance the particle position and velocity vector equations:

$$\frac{dx_{p,i}}{dt} = u_{p,i}, \quad (167)$$

$$m_p \frac{du_{p,i}}{dt} = \frac{\pi}{2} r_p^2 C_D \rho_g |u_{g,i} - u_{p,i}| (u_{g,i} - u_{p,i}) - \frac{4}{3} \pi r_p^3 \frac{\partial p_g}{\partial x_i} + m_p A_{c,i}. \quad (168)$$

For integrating these equations from time t to $t + \Delta t$, the following four steps are considered in the Runge-Kutta integration:

Step 1 :

$$\begin{aligned} X_1 &= \Delta t * [u_{p,i}(t)]; \\ U_1 &= \Delta t * \frac{du_{p,i}}{dt}(u_{p,i}(t), \dots), \end{aligned}$$

Step 2 :

$$\begin{aligned} X_2 &= \Delta t * \left[u_{p,i}(t) + \frac{1}{2}U_1 \right]; \\ U_2 &= \Delta t * \frac{du_{p,i}}{dt}\left(u_{p,i}(t) + \frac{1}{2}U_1, \dots\right), \end{aligned}$$

Step 3 :

$$\begin{aligned} X_3 &= \Delta t * \left[u_{p,i}(t) + \frac{1}{2}U_2 \right]; \\ U_3 &= \Delta t * \frac{du_{p,i}}{dt}\left(u_{p,i}(t) + \frac{1}{2}U_2, \dots\right), \end{aligned}$$

Step 4 :

$$\begin{aligned} X_4 &= \Delta t * [u_{p,i}(t) + U_3]; \\ U_4 &= \Delta t * \frac{du_{p,i}}{dt}(u_{p,i}(t) + U_3, \dots). \end{aligned} \tag{169}$$

This is followed by the integration step to obtain the particle position and velocity vectors at the $t + \Delta t$ time step:

$$\begin{aligned} x_{p,i}(t + \Delta t) &= x_{p,i}(t) + \frac{1}{6}X_1 + \frac{1}{3}X_2 + \frac{1}{3}X_3 + \frac{1}{6}X_4; \\ u_{p,i}(t + \Delta t) &= u_{p,i}(t) + \frac{1}{6}U_1 + \frac{1}{3}U_2 + \frac{1}{3}U_3 + \frac{1}{6}U_4. \end{aligned} \tag{170}$$

Similarly, the particle temperature equation is obtained from the four steps:

Step 1 :

$$T_1 = \Delta t * \frac{dT_p}{dt}(T_p(t), \dots),$$

Step 2 :

$$T_2 = \Delta t * \frac{dT_p}{dt}(T_p(t) + \frac{1}{2}T_1, \dots),$$

Step 3 :

$$T_3 = \Delta t * \frac{dT_p}{dt}(T_p(t) + \frac{1}{2}T_2, \dots),$$

Step 4 :

$$T_4 = \Delta t * \frac{dT_p}{dt}(T_p(t) + T_3, \dots), \quad (171)$$

followed by the integration step to obtain the particle temperature at the $t + \Delta t$ time step:

$$T_p(t + \Delta t) = T_p(t) + \frac{1}{6}T_1 + \frac{1}{3}T_2 + \frac{1}{3}T_3 + \frac{1}{6}T_4. \quad (172)$$

A similar procedure is undertaken for evaluating the particle mass, m_p , and is not summarized here for brevity.

4.8.4 Interpolation of gas phase variables to particle location

As mentioned previously, the gas phase variables are computed at the cell center in the finite volume formulation. However, particles are free to evolve within cells, and the local gas properties as ‘seen’ by the particles can be different from the cell centered value. For accurate prediction of the gas phase variables at the location of the particles, it is essential to incorporate an interpolation operation that uses the cell centered gas phase variables from nearby cells to compute the value at the local location of the particle. Two of these approaches are summarized here.

- Trilinear interpolation

For Cartesian grids aligned along the x -, y - and z -directions, Snider [186] and Patankar & Joseph [160] employed a trilinear interpolation approach. Here, a weighting procedure is used in the x -, y - and z -directions to map the gas properties to the location of a particle. A 27-point stencil was used, so that 8 cell centers bound a particle (2 in x - \times 2 in y - \times 2 in z -directions, respectively) and the three-dimensional interpolation operator, S , was obtained as $S = S^x S^y S^z$. For a particle located at (x_p, y_p, z_p) between cell centers i and $i + 1$ (x -direction only), S^x is defined as

$$S^x = \frac{x_{i+1} - x_p}{x_{i+1} - x_i}. \quad (173)$$

Here, x_{i+1} and x_i denote, respectively, the x -coordinates of the cell centers $i + 1$ and i . Similar expressions hold for S^y and S^z , by using the linear interpolation procedure in the y - and z -directions, respectively [160, 186]. 8 such interpolation functions, S_ξ , can be defined (i.e., $\xi = 1 \dots 8$), corresponding to the 8 cell centers that bound the particle. Note that the cell centers that are closest to the particle will have a higher S_ξ , and those that are farther will have smaller values. These S_ξ values are used as weights, and finally, the gas phase variable (U) at the location of the particle (x_p, y_p, z_p) is obtained as:

$$U(x_p, y_p, z_p) = \sum_{\xi=1}^8 S_\xi U_{i,j,k}(\xi), \quad (174)$$

where $U_{i,j,k}(\xi)$ represents the cell centered value, and $U(x_p, y_p, z_p)$ denotes the value at the location of the particle. This interpolation strategy, however, is valid only for grids aligned along the Cartesian directions. For more generic grids, a different weighting procedure is required, and is now discussed.

- $1/d^2$ interpolation

A Taylor series based interpolation scheme was recently proposed by Marchioli et al. [140], applicable for particle tracking in complex domains. Here, the procedure is

similar as above, with the distinction that the weighting operators are different, now based on the actual distance between the location of the particle (x_p, y_p, z_p) and the cell center. [140] considered the nearest 8 cell centers to a particle and average the respective values of the gas phase variables to obtain the final value at the location of the particle. As before, the gas phase variable $U_{i,j,k}$ at cell centers are used to evaluate the value at the particle location as:

$$U(x_p, y_p, z_p) = \sum_{\xi=1}^8 W(\xi) U_{i,j,k}(\xi). \quad (175)$$

[140] define the weights, $W(\xi)$, using an inverse square of distance between the particle and the cell center ξ as follows:

$$W(\xi) = \frac{1/d_\xi^2}{\sum_{\xi=1}^8 1/d_\xi^2}, \quad (176)$$

where d_ξ represents the physical distance between (x_p, y_p, z_p) and (x_ξ, y_ξ, z_ξ) . A higher order interpolation was also proposed in [140], not outlined here for brevity.

In the current study, the $1/d^2$ weighing based averaging is used. This approach has also been tried with a 12 nearest cell centers based averaging. The overall accuracy is improved with the use of a larger number of nearest cell centers. However, for too large a number used for the averaging, the computational cost increases dramatically, and hence the use of 8 or 12 cell centers based averaging is employed in the present study.

CHAPTER V

VALIDATION STUDIES

Before proceeding to the study of explosions, it is customary to validate the computational/numerical simulation strategy developed in Chapter 4. Since the problem under study involves two phases, i.e., gas and solid particles, it is essential to validate the solvers used for both phases. In this chapter, past studies from literature that are pertinent to the current investigation are identified and simulations are carried out with the computational approach described in Chapter 4. The simulation results are compared to these past studies and presented in this chapter, with the primary goal to validate the computational simulation strategy that is currently used.

The gas phase solver is validated in the first half of this chapter with three studies on explosions: (1) explosion from a pressurized sphere; (2) Sedov's point explosion problem; and (3) blast wave from a homogeneous explosive. Study (1) involves comparisons to both experiments as well as numerical results from literature; Study (2) involves comparison with past theoretical results; Study (3) is compared with experiments from literature. In the second half of this chapter, the solid phase solver is validated, both in the dilute as well as the dense limits. In particular, the physics related to inter-particle coupling are assessed with four pertinent studies from literature: (1) particle dispersion in a shock tube; (2) shock propagation through dust-gas suspension; (3) shock propagation through dense gas-particle mixture; (4) shock induced dispersion of acrylic plastic clouds. Simulation results for these studies are compared with experimental data from literature in order to validate the two-phase approach.

Overall, this chapter validates the gas phase and the solid phase solvers for high-speed problems, and the studies undertaken in this chapter will establish the efficacy of the simulation strategy presented in Chapter 4.

5.1 Validation of the Gas Phase Solver

5.1.1 Explosion from a pressurized sphere

- Boyer [33]

In the first study, the focus is on the study of the attenuation of a shock wave from a pressurized sphere. Experimental and numerical investigation of the explosion of pressurized glass spheres was undertaken by Boyer [33], who considered glass spheres of 5.08 cm dia., initially pressurized to 22 atm. To simulate the same, a 1D grid 25.4 cm long with 7500 grid points is considered (other grid sizes have also been tried and the results presented here are grid independent) with geometric source terms to account for the spherical nature of the problem, and the calorically perfect gas model is used. The shock wave Mach number as a function of radial distance, normalized with the initial radius (r_o) is presented in Fig. 13. The shock attenuation rate is also compared to the general attenuation law proposed by Aizik et al. [3] and good agreement is observed. This test study verifies the shock-capturing approach in the hydrocode.

- Vanderstraeten et al. [201]

In this study, the explosion from a 1 m radius sphere of high pressure air is considered, similar to the numerical study of Vanderstraeten et al. [201]. A spherical sector grid 12 m long in the radial (r) direction, 45° in the azimuth (θ) and zenith (ϕ) directions is considered, and is resolved using a $1000 \times 45 \times 45$ grid. Free-slip boundary conditions are applied along the sides of the sector and supersonic outflow in the outermost plane. A spherical source of 10 bar pressure and 300 K temperature air

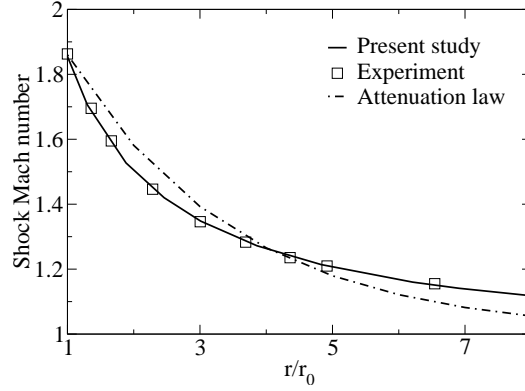


Figure 13: Explosion from a pressurized sphere. Experimental data from [33]; Attenuation law from [3].

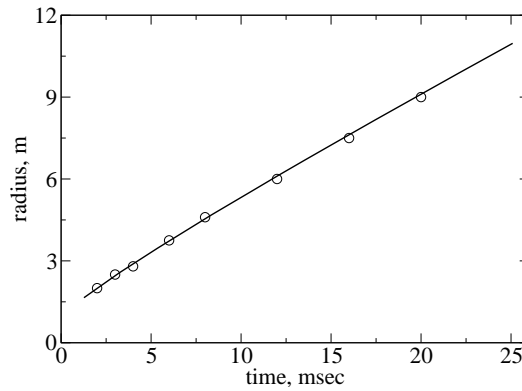


Figure 14: Explosion from a high pressure source. The line denotes the current simulation results; the circles denote the numerical results of [201].

is initialized within 1 m radius from the origin, representing a pressurized charge. Outside of this charge, ambient air is initialized at 1 bar pressure and 300 K temperature. This setup is allowed to run until about 30 msec, and the primary shock wave trajectory is tracked with time, presented in Fig. 14. Also shown in the figure are the simulation results obtained by [201]. As evident, the current simulation results are in good agreement with those of [201], thereby verifying the shock-capturing routines in the current hydrocode, as well as the sector grid approach.

5.1.2 Sedov's point explosion problem

In a seminal work, Sedov [182] demonstrated self-similarity of blast waves from explosions valid under three assumptions: (i) point explosions, i.e., the blast wave must be sufficiently far away that the initial charge can be assumed to be a point; (ii) strong shock limit, i.e., the blast wave is strong enough that the pressure of the gas behind it is significantly larger than that ahead of it; and (iii) perfect gas assumption is valid, i.e., the gas behaves with a constant ratio of specific heats, γ . Stated in these terms, Sedov derived for an explosion conforming to these stated criteria, and with $\gamma = 1.4$, the blast wave radius (r) scales as [182]:

$$r(t) \sim \left(\frac{Et^2}{\rho_o} \right)^{1/(\nu+2)}, \quad (177)$$

where E denotes the energy of the initial charge, t is the time, ρ_o is the ambient density, and ν takes the value 1 for planar, 2 for cylindrical, and 3 for a spherical explosion. In addition, the blast wave overpressure, Δp , is assumed to scale as $\Delta p \sim u^2$, where u denotes the speed of the shock wave, i.e., $u = dr/dt$. Thus, pressure scaling can be represented as

$$\Delta p(t) \sim t^{-2\nu/(\nu+2)}. \quad (178)$$

For a spherical explosion, Sedov's scaling predicts $r \sim t^{0.4}$ and $\Delta p \sim t^{-1.2}$, under the assumption that the aforesaid three criteria are valid, and for a gas with $\gamma = 1.4$.

The problem of a spherical explosion from a high pressure source is simulated in order to verify the ability of the hydrocode to predict Sedov's scaling law. A spherical sector grid 0.256 m in the radial (r) direction, and 45° in the azimuth (θ) and zenith (ϕ) directions is considered, and is resolved using a $1000 \times 45 \times 45$ grid. Free-slip boundary conditions are applied along the sides of the sector, and supersonic outflow in the outermost plane. A high pressure of 1000 Pa is initialized within an initial

radius of 0.005 m centered at the origin of the sector, and a low pressure of 10^{-5} Pa is initialized everywhere outside this high pressure source. Furthermore, the initial density is assumed to be $1 \text{ Kg}/\text{m}^3$ everywhere, with the gas assumed to be air—both in the high and low pressure regions. The blast wave trajectory and overpressure are shown in Fig. 15, including their respective power law curve-fit expressions. The curve-fit expressions conform to $r \sim t^{0.3984}$ and $p \sim t^{-1.1625}$, in good agreement with Sedov’s derivation. This study verifies that the hydrocode can predict Sedov’s self-similar scaling law, and also demonstrates the efficacy of the sector grid approach for the study of spherical explosions.

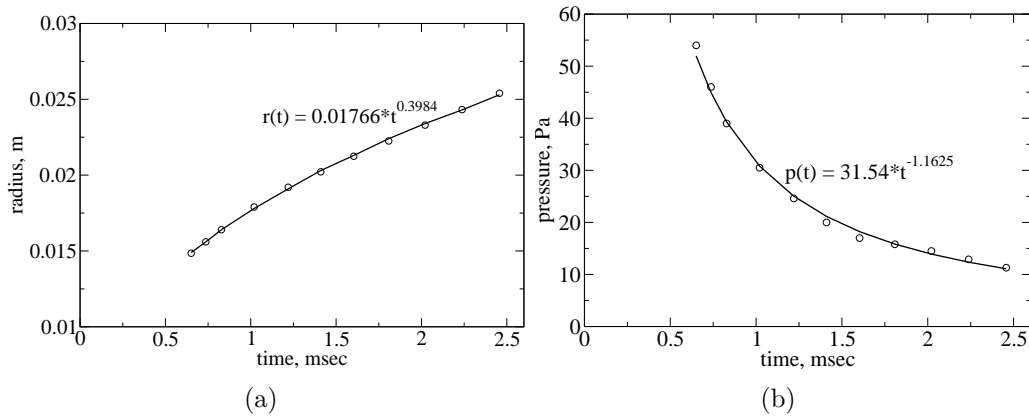


Figure 15: Blast wave trajectory (a) and overpressure (b) profiles for the Sedov point explosion problem. The circles denote the simulation results and the lines denote curve-fits.

5.1.3 Blast wave from a homogeneous explosive

In order to verify the real gas routines implemented in the hydrocode, the blast wave from a homogeneous explosive charge is simulated. A 2.4 m long spherical sector, 20° in the azimuth and zenith directions is considered, with the same boundary conditions as before, and is resolved using a $1000 \times 10 \times 10$ grid. Detonation profiles for a 11.8 cm dia. Nitromethane (NM) charge based on the GISPA method are initialized around the origin of the sector, and ambient air is initialized outside the charge. Experimental

data for the blast wave trajectory and shock overpressure for this charge were reported in Zhang et al. [214], and will be used for validating the simulation results. In Fig. 16, the results are presented, and the blast wave trajectory and shock overpressure are in good agreement with experimental data, thereby verifying the real gas routines in the hydrocode, and the use of the sector grid approach for simulating spherical explosions.

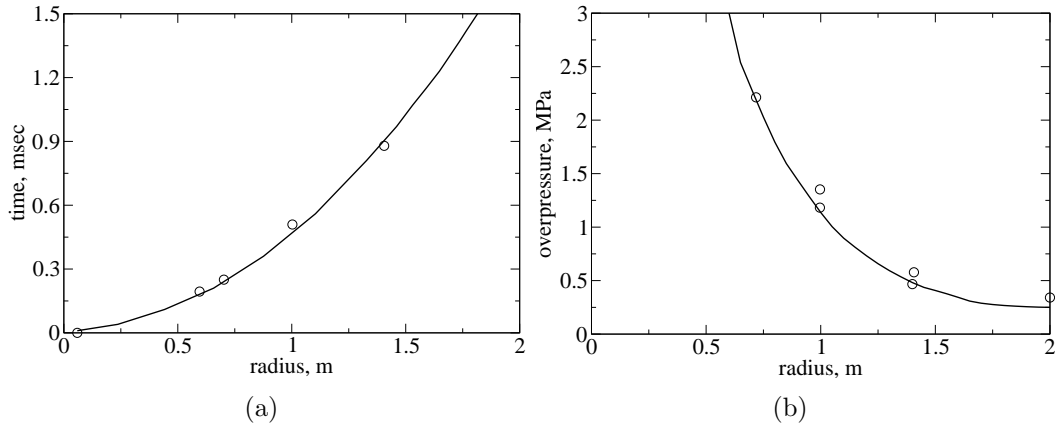


Figure 16: Blast wave trajectory (a) and overpressure (b) profiles for a 11.8 cm dia. Nitromethane charge. Lines denote the simulation results and circles denote the experimental data from Zhang et al. [214].

5.2 Validation of the Solid Phase Solver

5.2.1 Particle dispersion in a shock tube

Particle dispersion due to the passage of a shock wave is a canonical test case to establish the ability of the solver to capture particle motion and dispersion (which requires proper drag modeling) during shock-particle interaction. The dispersion of a nylon particle ($\rho_p = 1170 \text{ Kg}/m^3$) 2 mm dia. subjected to a Mach 1.56 shock is investigated repeating an earlier experimental and numerical study by Devals et al. [54], who concluded that the particle trajectory and the velocity agree with the use of the drag law of Igra & Takayama [102]. In the experiments, a 3.75 m long shock tube with a cross-section of 8 cm \times 8 cm was used, and the initialization was based

on a high pressure region separated from the low pressure region by a diaphragm that was released. The particles were suspended from the ceiling of the shock tube using spider webs, making use of its sticky nature. For the simulation, the same domain size is used and is discretized using a grid of size $375 \times 8 \times 8$, and no-flux boundary conditions are used on the shock tube walls. A high pressure region is initialized in the simulations similar to the experiments, and is used to create the initial shock wave and the flow behind it. The particle trajectory and the velocity evolution with time are shown in Fig. 17, and the present study agrees well with the measured data. Since this shock tube does not have an outlet, the shock reflects from the end wall, which causes the particle velocity to level off at later times (> 3 msec), and the particle trajectory to follow a near-straight line at later times.

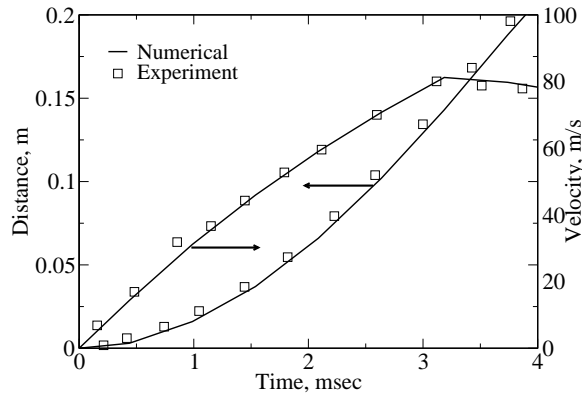


Figure 17: Evolution of particle trajectory (left axis) and velocity (right axis) with time. The experimental data is from [54].

5.2.2 Shock propagation through dust-gas suspension

The attenuation of a shock wave upon its passage through a dilute gas-particle mixture is also studied using a drag law applicable for this regime [45]. This is a well established test case studied earlier using both experiments and numerical modeling [187]. A shock wave of a prescribed Mach number, $M_s = 1.49$ passes through a cloud of glass particles ($27 \mu\text{m}$ dia., $\rho_p = 2500 \text{ Kg/m}^3$) initially occupying a mass loading

ratio, $\eta = 0.63$. The same shock tube geometry [187] is simulated using a no-flux boundary condition in the shock tube walls, and supersonic outflow at the exit plane of the low pressure region. Initialization is achieved by means of a high pressure region that is then allowed to expand. Although the experiments were performed in a circular cross-section shock tube [187], this study uses a square cross-section, which should not affect the results due to the one-dimensionality of the problem. A shock tube 7.81 m long is considered, with a cross section being a square of side 5 cm, and is resolved using a $781 \times 10 \times 10$ grid. The shock wave Mach number as it propagates through the gas-particle mixture is presented in Fig. 18. Due to momentum and energy absorption by the solid particles, the shock wave attenuates as it propagates through the particle cloud. Also shown in the figure are the attenuation rates obtained by Aizik et al. [2], and numerical results obtained by another investigators [41]. The shock wave attenuation predicted by the present hydrocode is in good agreement with other studies, thereby verifying the solid phase solver implemented in the current hydrocode.

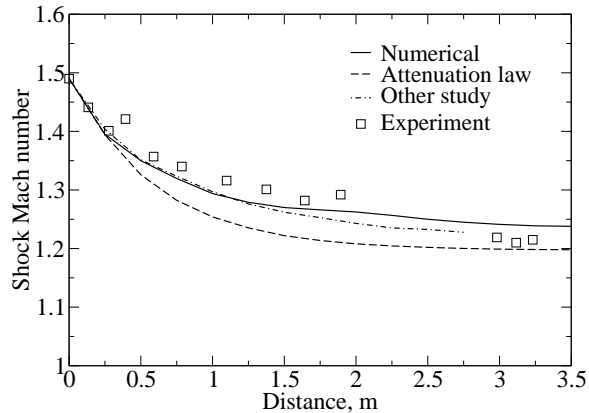


Figure 18: Planar shock wave attenuation in dust-gas suspension. The experimental data is from [187]; the attenuation law is from [2]; the other study is from [41].

5.2.3 Shock propagation through dense gas-particle mixture

In order to validate the Eulerian-Lagrangian DEM approach implemented in the code, the problem of shock wave propagation through a dense gas-particle mixture is investigated and compared to available experimental data [173]. In the experiments, the authors used a 6 m long vertical shock tube with a cross-section of 13 cm \times 13 cm. 1.5 mm dia. glass particles were considered and were initially supported inside the shock tube by a plastic membrane. A diaphragm was used to separate a high pressure region at the bottom of the tube from the low pressure region, and the diaphragm pressure ratio was chosen to give rise to a Mach 1.3 shock. Furthermore, the glass particles initially occupied 65% volume of a 2 cm thick bed on top of the membrane.

The simulations are carried out with the same geometry and initial conditions, and with the use of the drag law of Crowe et al. [51]. No-flux boundary conditions are applied along the side walls of the shock tube, and supersonic outflow in the far extreme of the low pressure region. As before, the initialization for the simulation is based on a high pressure region to generate the shock wave. A grid resolution of 600 \times 13 \times 13 is chosen for the study and is found to be sufficient. The upstream and downstream pressure traces are presented in Fig. 19, and the simulation results are in good agreement with experimental data. Also shown are the results obtained with the DEM turned off, i.e., the simulation carried out without any dense effects accounted (note that this is not physical as the volume occupied by the solid particles is not blocked for the gas). As expected, with the DEM turned off, the upstream pressure is under-predicted and the downstream over-predicted, as without the blockage due to the solid particles, more of the shock energy is transmitted downstream and less upstream; also for the same reason, the transmitted shock arrives at the downstream location about 0.4 msec earlier with the DEM turned off. Blockage effects, if unaccounted for, result in erroneous predictions of the dispersion of particles due to a

shock wave or an explosion. This study validates the DEM methodology and demonstrates the blockage effects in gas-particle flows that have to be accounted for proper modeling of problems of the like.

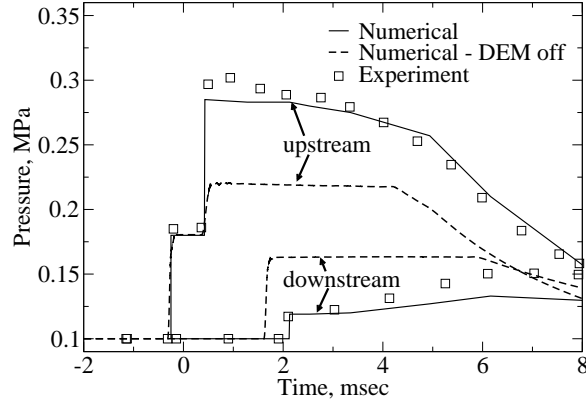


Figure 19: Pressure traces upstream and downstream of a dense particle bed subjected to a shock wave. The experimental data is from [173].

5.2.4 Shock induced dispersion of acrylic plastic clouds

To illustrate the significance of the just mentioned blockage effect and the concomitant available shock energy upstream and downstream of the particle cloud, the problem of the dispersion of a cloud of acrylic plastic cloud due to a Mach 2.8 shock wave in air is considered. Experimental data for this configuration can be obtained from [30] for acrylic plastic clouds containing $300 \mu\text{m}$ dia. particles, with initial volume fractions (i) 0.1% and (ii) 3%, performed in a 6.5 m long shock tube with a $52 \text{ mm} \times 52 \text{ mm}$ cross section. The problem is simulated with a $1250 \times 10 \times 10$ grid using Rankine-Hugoniot conditions to initialize the flow behind the initial Mach 2.8 shock, and the two different volume fractions for the initial acrylic plastic particle cloud are considered. The drag law from the numerical study performed in [30] is used for the current analysis. The trajectory of the left boundary of the cloud as it disperses after interacting with the shock is shown in Fig. 20; simulations are performed with the DEM as well as turning off DEM. As evident, for a 0.1% initial solid volume fraction,

the dense approach is not essential as the trends agree with experimental data, both with and without DEM; on the other hand, for a 3% initial volume fraction, the dispersion characteristics match better with experimental data with the DEM. As seen in the previous test study, with the DEM off, since accurate blockage to the flow of gas by the particle cloud is not accounted for, the transmitted shock and the flow behind it are stronger, thereby the dispersion is faster in relation to the physical case with DEM, i.e., with the blockage accounted for. From this study it is concluded that whereas 0.1% can be treated dilute for simulations, 3% initial volume loading requires the use of a two-phase methodology. It is noted that although 3% may seem low in terms of volume fraction, the passage of the shock compresses the particle cloud resulting in solid volume fractions as high as 10%, thereby necessitating the use of the dense approach. Another observation from Fig. 20 is that the dispersion is more prominent for the 0.1% volume fraction cloud, as this results in lesser blockage and therefore a stronger transmitted gas flow. Overall, this study demonstrates the efficacy of the EL DEM approach.

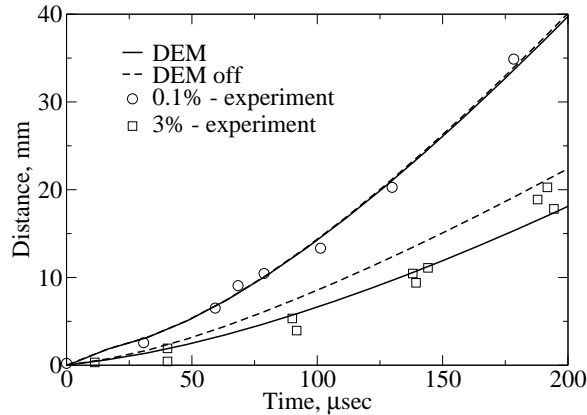


Figure 20: Dispersion of acrylic plastic clouds of initial volume fractions (i) 0.1% and (ii) 3% by a Mach 2.8 shock. The experimental data is from [30].

5.3 Summary

In this chapter, a few past studies from literature are simulated and the results are compared with good agreement. In the first half of this chapter, the gas phase solver was validated by considering three explosion problems: (1) explosion from a pressurized sphere; (2) Sedov's point explosion problem; and (3) blast wave from a homogeneous explosive. These studies validate the efficacy of the developed shock-capturing scheme for applications to explosions.

In the second half of this chapter, the two-phase solver is validated with four past investigations from literature of interest to the current research effort: (1) particle dispersion in a shock tube; (2) shock propagation through dust-gas suspension; (3) shock propagation through dense gas-particle mixture; (4) shock induced dispersion of acrylic plastic clouds. Whereas studies (1) and (2) focus on dilute particle clouds, studies (3) and (4) validate the dense approach developed, in particular the Eulerian-Lagrangian Discrete Equations Method (EL DEM). Furthermore, for the dense two-phase studies, blockage effects are identified to play a significant role in the flow physics of the problem. This exemplifies the necessity of a robust two-phase simulation strategy such as the EL DEM for the investigation of problems of this kind.

Overall, the studies presented in this chapter demonstrate the efficacy of the simulation strategy and validate the hydrocode for application to explosions involving solid particles, in the dilute as well as the dense regimes.

CHAPTER VI

HOMOGENEOUS EXPLOSIVE CHARGES

This chapter focuses on the study of explosions from homogeneous charges, i.e., explosive charges that do not contain metal particles. Past studies [9, 10, 120, 121] have clearly demonstrated that chemical explosions are characterized by hydrodynamic effects such as Rayleigh-Taylor [192] and Richtmyer-Meshkov [169] instabilities. As mentioned in Section 1.2.2, the high density gradients across the contact surface at early times gives rise to the growth of a Rayleigh-Taylor instability. The Rayleigh-Taylor structures grow in size as they expand into outer regions, and are characterized by the presence of surrounding vortex rings due to baroclinic and shear effects [121]. Later, during the outward passage of the secondary shock, its interaction with these structures results in a Richtmyer-Meshkov instability. A mixing layer ensues as these instabilities further grow and mix the inner detonation products and the outer air. Combustion/afterburn effects play a role in the mixing layer subsequent to the detonation, for exothermic heat release due to combustion (afterburn) results in volumetric expansion of the gas, which can change the dynamics in the mixing layer. Thus, the problem of chemical explosions offers a plethora of interesting physics to explore.

Another aspect of interest is the presence of ambient reactive particles, which can perturb the flow field and result in the growth of Rayleigh-Taylor instabilities that can also later result in a mixing layer. Solid particles in the ambient pick up momentum and disperse, pick up heat and ignite. If solid particles are sufficiently large, they disperse only radially and are not influenced by the vortex rings in the mixing layer. On the other hand, if particles are sufficiently small, their response time scales are comparable to the fluid mechanic time scales in the mixing layer, which can result

in clustering of particles around the vortex rings as will be demonstrated later in this chapter. It is of practical relevance to characterize these phenomena, so as to properly understand the underlying physics that play a significant role in the mixing layer ensuing from chemical explosions.

This chapter first considers the flow field subsequent to the detonation of homogeneous explosive charges, with emphasis on estimating the impulsive loading from explosions. Three explosives, i.e., Nitromethane (NM), Trinitrotoluene (TNT) and High-Melting Explosive (HMX)—also referred to as Her Majesty’s Explosive in the Commonwealth countries—are considered for a one-dimensional analysis and the shock overpressure and impulsive loading are assessed. Then, the study is extended to three-dimensions for a TNT charge, and hydrodynamic and afterburn effects are investigated. Here, the effect of afterburn on the impulsive loading is compared to that predicted by the one-dimensional results. Furthermore, the different phases involved in chemical explosions are analyzed, thus laying the groundwork for targeted studies on explosions in multiphase environments.

Later in the chapter, the studies are extended with the consideration of dilute ambient aluminum particle clouds. Subsequent to the detonation event, the ambient particles introduce perturbations on the contact surface, which grows into a Rayleigh-Taylor instability. The effect of particle size, mass loading ratio (defined as the ratio of the mass of solid to mass of gas in a given volume) and initial cloud width are considered, and their effect on the amount of mixing and afterburn are investigated. Furthermore, if small particles are considered, they cluster around the vortex rings in the mixing layer due to smaller response time scales. This phenomena is studied for a range of parameters, and the exact clustering process is elaborately discussed. Overall, this chapter portrays the physics involved in chemical explosions, both into ambient air, as well as into dilute aluminum particle clouds.

6.1 Homogeneous Explosions into Air

The first task is to understand the basic physics of chemical explosions from a one-dimensional sense, i.e., without accounting for hydrodynamic instabilities (no mixing between the detonation products and air is encountered here). To this end, the blast from a 11.8 cm dia. spherical NM charge is simulated using the one-dimensional radial Euler equations. Furthermore, the JWL equation of state is employed in this study to account for real gas effects. Various grids of sizes 3000, 5000, and 7500 are used in the radial direction to simulate a 12 m long domain, and the blast wave trajectory and overpressure are shown in Fig. 21 along with the experimental data of [214]. Grid convergence is achieved for the range of grids, and therefore 5000 grid points are used for all the one-dimensional studies presented here. Also shown in Fig. 21 are the results using the thermally perfect gas model; it is clear that the thermally perfect gas assumption significantly overpredicts the shock speed and the overpressure, thus demonstrating the need to employ a proper real gas equation of state.

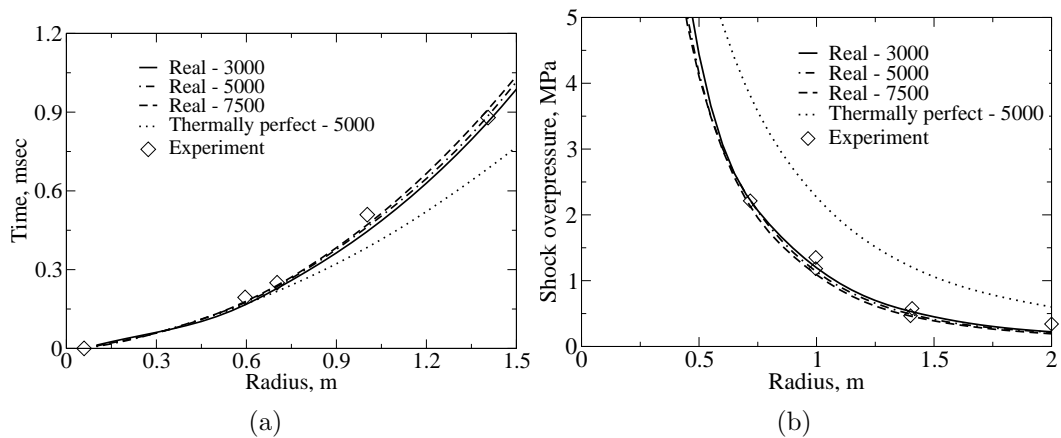


Figure 21: Blast wave from a Nitromethane charge (a) trajectory; (b) overpressure. Experimental data from [214]. The numbers denote the number of grid points used for the one-dimensional grid. Real: real gas assumption; Thermally perfect: thermally perfect gas assumption.

6.1.1 One-dimensional effects only

Here, the three aforementioned explosives, viz. NM, TNT and HMX are studied and their respective shock overpressure and impulsive loading are compared. For the simulations, the one-dimensional approach is used with 5000 grid points in a 12 m long domain, and the detonation profiles are initialized corresponding to a 11.8 cm dia. initial charge. Some relevant detonation characteristics for the various explosives are summarized in Table 3.

Table 3: Properties of the three explosives considered

Explosive	Chemical formula	Chapman-Jouguet pressure (GPa)	Density (Kg/m^3)	Detonation velocity (Km/s)	Detonation energy (MJ/Kg)
NM	CH_3NO_2	12.5	1128	6.28	4.35
TNT	$C_7H_5N_3O_6$	21.0	1630	6.93	4.84
HMX	$C_4H_8N_8O_8$	42.0	1891	9.11	5.86

For these explosives, the primary and secondary shock trajectories and the shock overpressure are shown in Fig. 22. The primary shock is faster for HMX, followed by TNT and lastly, NM, consistent with the order of the mass of the high explosive (and total detonation energy) in each charge. The secondary shock is observed to travel a farther distance during its initial outward movement in the same order for the three explosives, i.e., by 9 cm farther for TNT than NM, and by 5 cm for HMX than TNT. The strength of the primary shock, i.e., the shock overpressure also increases with the total detonation energy. For comparison, the blast overpressure of TNT based on a curve-fit expression from [53] is also shown in the figure, and is observed to be in reasonable agreement with the current prediction, thereby validating the simulation approach.

The total impulsive loading from a homogeneous charge is obtained at different radial locations for the three explosives considered, viz. NM, TNT and HMX. The impulsive loading is estimated on a ‘virtual wall,’ i.e., without the consideration of

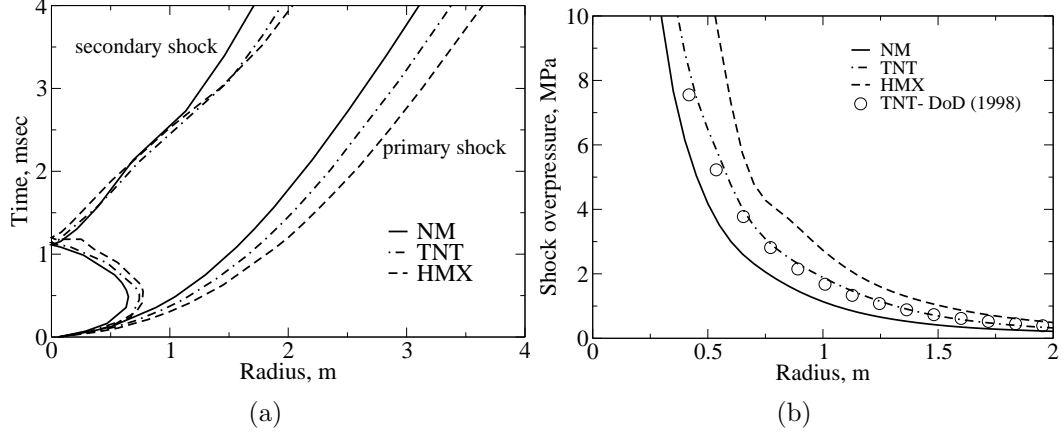


Figure 22: Blast wave from charges containing the same volume of the high explosive (a) primary and secondary shock trajectories; (b) overpressure. DoD (1998) [53].

blast wave reflection/diffraction. Under this assumption, the total deliverable impulse will be due to gas pressure and momentum flux (dynamic pressure). Define the total impulse as

$$I = \int_0^{\infty} (p - p_o)_{p > p_o} dt + \int_0^{\infty} \frac{1}{2} \rho u^2 dt, \quad (179)$$

where p_o denotes the ambient pressure. For a real wall/structure, the drag coefficient between the flow and the wall/structure has to be included in the impulse term due to flow momentum; this, however, is not accounted for in the current study as a simplification. It is emphasized that the impulse estimates presented here correspond only to a virtual wall.

In the past, scaling laws have been generated for the incident positive phase pressure impulse [32, 55, 114], without considering the contribution from subsequent positive pressure phases and from the gas momentum flux. Here, scaling for incident positive phase pressure impulse is considered as well as for the total impulse; for the total impulse, all the positive over-pressure phases are considered, i.e., not only from the phase corresponding to the incident/primary blast wave.

Using the same cube-root scaling law identified earlier [12], the scaled incident

positive phase pressure impulse and the scaled total impulse as a function of the scaled distance are compared in Fig. 23. At scaled radius around $0.3 \text{ m}(\text{Kg})^{-1/3}$, the incident positive phase pressure impulse is lower than at radial distances immediately outwards for the three explosives considered. This is because this region ($\sim 0.3 \text{ m}(\text{Kg})^{-1/3}$) is contained within the distance that the secondary shock moves during its initial outward passage. The secondary shock gives rise to an early termination of the positive phase duration of the pressure, thus explaining the low positive pressure impulse at scaled radius around $0.3 \text{ m}(\text{Kg})^{-1/3}$. At scaled radius around $0.8 \text{ m}(\text{Kg})^{-1/3}$, the incident positive phase pressure impulse is observed to increase slightly for the three explosives considered. As pointed out in [114], the finite size of the explosive charge spreads out the energy, rather than concentrating it as a point source. Thus, the expanding detonation product gases tends to provide slightly increased pressure impulse. This trend in the pressure impulse has also been reported in a different study [32].

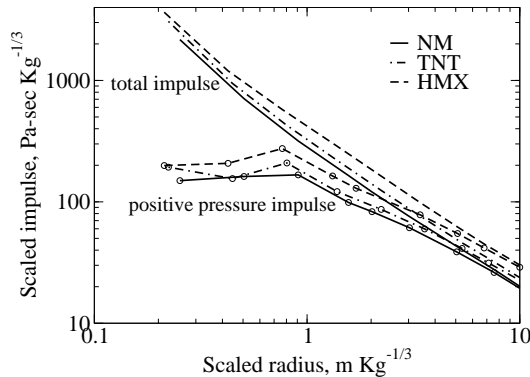


Figure 23: Scaled impulse as a function of the scaled radius for NM, TNT and HMX.

For the three explosives considered, the scaled total impulse decreases monotonically with scaled radius, due to the attenuation of the blast wave as it propagates outwards. The order of scaled impulse is $\text{HMX} > \text{TNT} > \text{NM}$, consistent with the order of their detonation energies. Empirical curve-fit for the shock overpressure, scaled

incident positive phase pressure impulse and scaled total impulse are obtained for the three explosives as a function of the scaled radius. Specifically, curve-fit expressions for overpressure (Δp), scaled incident positive pressure impulse (I_p) and scaled total impulse (I_t) are obtained using the following relations (a similar expression has been used elsewhere [53]):

$$\begin{aligned} \ln(\Delta p) &= A_1 \ln(Z)^4 + B_1 \ln(Z)^3 + C_1 \ln(Z)^2 + D_1 \ln(Z) + E_1, \\ \ln(I_p/W^{1/3}) &= A_2 \ln(Z)^4 + B_2 \ln(Z)^3 + C_2 \ln(Z)^2 + D_2 \ln(Z) + E_2, \\ \ln(I_t/W^{1/3}) &= A_3 \ln(Z)^4 + B_3 \ln(Z)^3 + C_3 \ln(Z)^2 + D_3 \ln(Z) + E_3, \end{aligned} \quad (180)$$

where Δp is expressed in MPa; I_p and I_t in Pa-s, and W in Kg . The variable Z denotes the scaled radius, $r/W^{1/3}$ in $m(Kg)^{-1/3}$. By curve-fitting the overpressure and impulse for the three explosives, the empirical constants in Eqn. (180) are obtained, and are presented in Table 4. In order to ensure the independence of the scaling laws to the initial charge size, different TNT charges comprising of 10, 100, 1000 and 10,000 times the amount of TNT by mass as the baseline 11.8 cm dia charge (the case with 10,000 times corresponds to over 14 tons of TNT) are also considered. These charges correspond to 0.2542, 0.5476, 1.18 and 2.542 m dia., respectively. Identical shock overpressure and scaled impulse are observed for all the TNT charges at the same scaled radius, thereby ensuring a wider applicability of the scaling laws proposed.

Table 4: Overpressure scaling for the three explosives

Explosive	A_1	B_1	C_1	D_1	E_1	Range
NM	0.2656	0.2425	-0.5714	-2.2821	0.1383	$0.25 < Z < 2.5$
	0.1057	-0.7078	1.9499	-4.2259	0.6280	$2.5 < Z < 10$
TNT	0.0749	0.1981	-0.3841	-2.3607	0.3381	$0.25 < Z < 2.5$
	-0.0524	0.2543	-0.1017	-2.4808	0.2762	$2.5 < Z < 10$
HMX	-0.2121	-0.2847	-0.2725	-2.2089	0.5866	$0.25 < Z < 2.5$
	0.0982	-0.6876	2.0007	-4.4864	1.1907	$2.5 < Z < 10$

A generalized empirical scaling law applicable for any explosive can be very useful

in their design. To this end, curve-fits of the coefficients of the scaling laws for each explosive are obtained with their respective detonation energies. Denoting E as the detonation energy of an explosive in MJ/Kg , the coefficients A_1 , B_1 , etc. can be again curve-fit as functions of E as

$$A_1 = \lambda_{A_1} E^2 + \mu_{A_1} E + \delta_{A_1} \text{ etc.} \quad (181)$$

These new curve-fit coefficients (λ , μ , δ) are summarized in Table 5.

Table 5: Empirical scaling law for explosives

Coefficient	0.25<Z<2.5			2.5<Z<10		
	λ	μ	δ	λ	μ	δ
A_1	0.0714	-1.0457	3.4628	0.3114	-3.1841	8.0645
B_1	-0.2534	2.2377	-4.6971	-1.9119	19.5337	-49.5018
C_1	-0.1806	2.0417	-6.0356	4.1378	-42.2129	107.2791
D_1	0.2048	-2.0425	2.7274	-3.6608	37.2042	-96.7928
E_1	-0.1086	1.4059	-3.9221	1.0693	-10.5445	26.2635
A_2	-0.3467	3.6864	-8.8202	-0.0980	1.0888	-2.9745
B_2	-0.1405	1.8144	-4.5817	0.5245	-5.8600	16.1385
C_2	0.6748	-6.8822	16.2307	-0.9927	11.1687	-31.1728
D_2	0.1660	-1.8619	4.1698	0.7793	-8.8246	24.2358
E_2	-0.0619	0.8792	2.3976	-0.2217	2.7346	-3.1971
A_3	-0.0621	0.6813	-1.8305	0.3125	-3.1383	7.6995
B_3	-0.0521	0.5654	-1.5749	-1.9823	19.9721	-49.1849
C_3	0.0345	-0.4329	1.3566	4.4658	-45.1129	111.4637
D_3	0.0246	-0.2093	-0.7844	-4.2205	42.6989	-106.8735
E_3	-0.0256	0.5261	3.8357	1.3814	-13.7146	39.0919

Although detonation energy is chosen as the variable for the curve-fit, other explosive parameters can also be used, for example, detonation velocity or Chapman-Jouguet pressure. More explosives can be considered, and the curve-fit coefficients (λ , μ and δ) can be fine-tuned if needed. To illustrate the significance of the presently obtained scaling law, the blast from a 14.02 ton TNT charge is simulated and the overpressure is compared with the scaling law that is proposed here, and is presented in Fig. 24. The results are in good agreement, thus exemplifying the applicability of the scaling

law for armaments, both kilo- and ton-range alike.

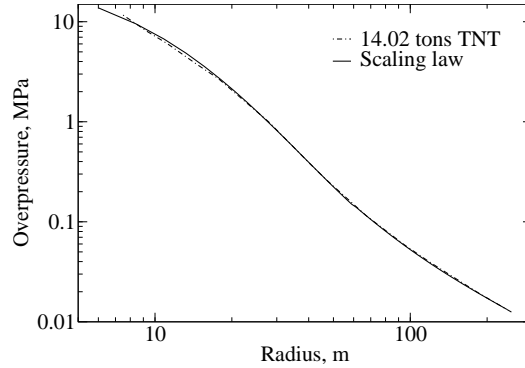


Figure 24: Comparison of a 14.02 ton TNT charge with the scaling law.

6.1.2 Three-dimensional effects included

With the above basic understanding on one-dimensional chemical explosions, the focus is now shifted to the effect of three-dimensional physics on the post-detonation characteristics. In order to study the effect of the growth of hydrodynamic instabilities, a three-dimensional sector grid approach is used. However, to understand the applicability of this approach, a simulation is first undertaken with the three-dimensional sector grid without any hydrodynamic instabilities for the baseline 11.8 cm dia NM charge. A spherical sector 12 m long, and 20° in the azimuth (θ) and zenith (ϕ) directions is considered, and a $5000 \times 10 \times 10$ mesh is used. Free-slip boundary conditions are used along the sides of the sector and supersonic outflow in the outward plane. The initialization uses the same one-dimensional detonation profiles obtained from the GISPA method (Section 4.7, Appendix B).

In Fig. 25 (a), the pressure traces are shown at a radial location 0.9 m from the center of the charge based on the one-dimensional and three-dimensional simulations, and the results are in good agreement. This result demonstrates that the results with the sector grid and the 1D studies agree, which exemplifies the overall applicability of the approach. In Fig. 25 (b), the pressure contour is shown at time 3.34 msec after

the detonation process, and the primary and secondary blast waves are observed to maintain a spherical shape. Other grid sizes and sector angles also show good agreement with the one-dimensional studies. The 20° sector is resolved with 10 grid points, i.e., corresponding to an azimuth/zenith angular cell increment, $\Delta\theta = \Delta\phi = 2^\circ$. For very large sector grid cell increment angles ($\Delta\theta, \Delta\phi > 10^\circ$), slight distortions from the spherical nature of the problem are observed, and thus, necessitates increase in resolution.

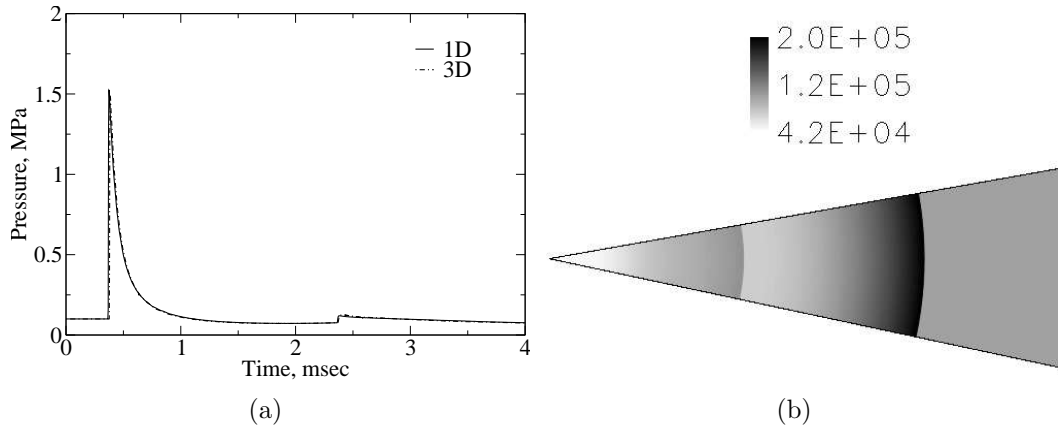


Figure 25: Comparison of one-dimensional and three-dimensional approaches (a) pressure trace; (b) pressure contour.

In order to better understand the effect of hydrodynamic instabilities in explosive blasts, a 11.8 cm dia TNT charge is analyzed. A spherical sector, 2.4 m long and 45° in the azimuth and zenith directions is used, and the one-dimensional detonation profiles (Section 4.7) are used for initializing the explosive charge. Grids of sizes $1000 \times 30 \times 30$ (G1), $1000 \times 45 \times 45$ (G2), $1000 \times 60 \times 60$ (G3), and $1000 \times 75 \times 75$ (G4) are considered. Comparing the time of arrival of the secondary shock, the mixing layer boundaries (to be defined shortly), and the mass-fraction of fuel remaining in the charge, it is observed that the results with G2 only marginally differ from G1, and are in accordance with G3 and G4. Since the focus of this study is on these parameters, it is concluded from these observations that G2 suffices for the remainder

of this study.

To help trigger the growth of instabilities, random fluctuations Gaussian or Laplace in nature, are added to the density (and energy) profiles in a radial sector region $0.9 r_0 \leq r \leq r_0$, where r_0 denotes the initial charge radius. Other investigators [120, 121] used similar perturbation procedures, albeit outside the charge. The source of these instabilities could be assumed to arise either from granular irregularities in the charge surface or from molecular fluctuations.

Figure 26 shows the mixing layer (iso-surface of N_2 mass fraction with value corresponding to mean of N_2 mass fraction in detonation products and ambient air) shape at four different times using the $1000 \times 45 \times 45$ grid and Gaussian initial perturbation. As evident from Fig. 26, four phases are identified: (i) blast wave phase; (ii) implosion phase; (iii) re-shock phase; and (iv) asymptotic mixing phase, consistent with past studies [120, 121]. During the initial blast wave phase, the Rayleigh-Taylor [192] structures grow in time, yet preserve their initial perturbation shape (0.5 msec, Fig. 26 (a)). The mixing layer is created where the detonation products and the shocked air co-exist. Vorticity is created in the mixing layer, leading to entrainment of the surrounding air into these structures, resulting in their spatial growth, and afterburn/combustion between the detonation products (C and CO) and the shocked air. During the implosion phase, the secondary shock, as it implodes inwards, drags along with it the lower end of the mixing layer (1 msec, Fig. 26 (b)). During the re-shock phase, the secondary shock passes through the mixing layer, which is a classic Richtmyer-Meshkov scenario [169, 146], resulting in more vorticity creation due to baroclinic torque effects $(-\nabla(1/\rho) \times \nabla p)$. This results in interaction between contiguous structures, which in turn leads to further mixing enhancement in the layer as is evident from the profiles at 2 msec (Fig. 26 (c)). Subsequently, in the asymptotic phase, contiguous structures begin to merge, thereby giving rise to a more distorted and wrinkled appearance to the mixing layer (8.5 msec, Fig. 26 (d)). This merging

between structures results in loss of memory of the initial perturbation shape. Thus, the problem under study is characterized by these four different phases, each being influenced by distinctly different fluid mechanics.

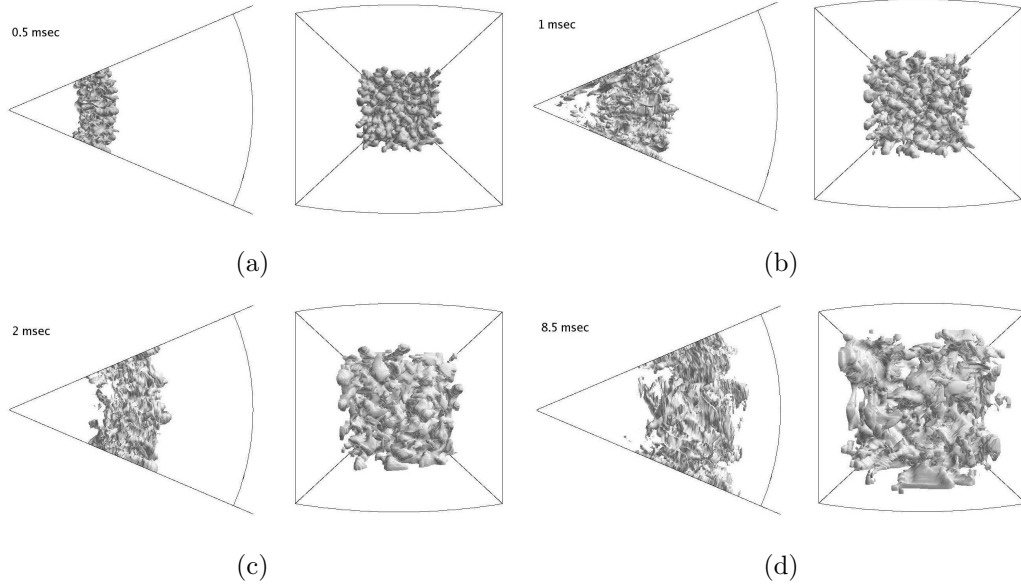


Figure 26: Iso-surface of N_2 mass fraction to illustrate the growth of the mixing layer with time.

In order to quantitatively understand the growth of the mixing layer, the spatially averaged N_2 mass fraction in the azimuth and zenith directions are considered, with the assumption that $1.05Y_{N_2}^i$ and $0.95Y_{N_2}^o$ represent the inner and outer boundaries of the mixing layer, respectively, where $Y_{N_2}^i$ and $Y_{N_2}^o$ denote the nitrogen mass fraction in the detonation products and ambient air, respectively. The locus of the boundaries of the mixing layer are shown in Fig. 27. At early times (~ 0.5 msec), the inner and outer boundaries of the mixing layer are propagated outwards due to the outward motion of the blast wave. During the implosion phase (0.5-1 msec), the secondary shock drags the inner boundary of the mixing layer along with it, resulting in an increase of the mixing layer width (defined as the gap between the outer and inner boundaries). Subsequently, during the re-shock phase (1-2 msec), the outward moving secondary shock drags along with it the inner boundary of the mixing layer, causing its

width to shrink. At around 3 msec, the inward moving tertiary shock causes the inner boundary of the mixing layer to propagate inwards, albeit not as much as observed during the secondary shock's implosion. Furthermore, since the tertiary shock is weak, the contribution to the mixing layer width during its subsequent outward passage is not as pronounced as that of the secondary shock. This is followed by the asymptotic phase (> 5 msec), during which, the overall width of the mixing layer slowly widens and tends to asymptote. Some of these features have also been reported in [120].

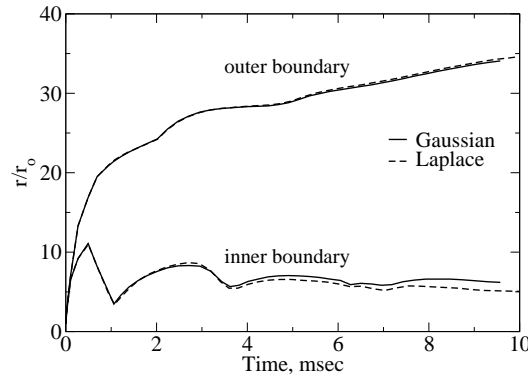


Figure 27: Inner and outer boundaries of the mixing layer for the TNT charge.

The behavior of the mixing layer width (or zone) is useful to analyze for chemical explosions. Upon curve-fitting the mixing layer width with time, during the blast wave phase, the growth is observed to be linear, and given by the expression, $w/r_o = 7.4 (t/W^{1/3})$, where w denotes the mixing layer width based on the above definition, r_o denotes the initial charge radius, t is the time in msec, and W , the mass of the explosive in the charge in *Kg*. For the implosion phase, the mixing layer width is observed to grow non-linear due to the inward stretching of the lower boundary of the mixing layer, and the curve-fit expression is found to be $w/r_o = 19.7(t/W^{1/3})^{1.56}$. These expressions can be used to predict the early stages of the mixing layer growth with time.

Although both Gaussian and Laplace distributions have been used for the initialization, the mixing layer growth is nearly the same for both, as evident from Fig. 27.

In both these scenarios, the initial perturbations grow to much larger sizes quickly, and thus the exact scale of the initial perturbation loses significance. Furthermore, after the re-shock phase, as observed in Fig. 26, contiguous structures interact and merge, thereby resulting in loss of memory. Due to this, the exact initial perturbation does not have a uniqueness to the later development and behavior of the flow field. However, the appearance of the fireball will be different for a different initial perturbation function, as shown in Fig. 28, where the iso-surface of the N_2 mass fraction is shown at 3.2 msec for the Gaussian and Laplace distribution based initial perturbation. As evident from the figure, the final appearance of the structures in the mixing layer is different for the Gaussian and Laplace distribution based initial perturbations. This has implications to real explosive blasts: two different charges of the same size and high explosive, upon detonation, can result in the same afterburn energy, pressure trace and impulsive loading; however the fireball will most certainly look different in photography. The imperfections on two real explosive charges will be different, and this will make their visual appearance different, as the structures evolve non-linearly with time.

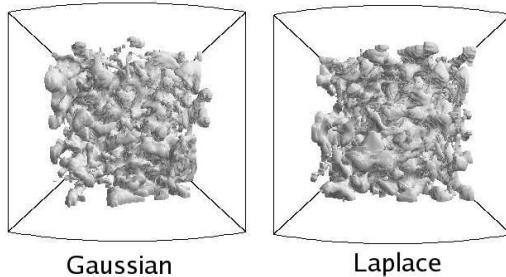


Figure 28: Iso-surface of N_2 mass fraction at 3.2 msec for the random initialization based on Gaussian and Laplace distributions.

As the secondary shock passes through the mixing layer, it interacts with the structures, giving rise to a classical Richtmyer-Meshkov instability [169], which is

characterized by the creation of vorticity due to baroclinic effects. Due to this vorticity, the secondary shock distorts in shape. However, as the secondary shock propagates outside the mixing layer, as there is no more significant baroclinic effects, the secondary shock re-attains its spherical shape outside the mixing layer. To illustrate this fact, the natural logarithm of density (density in Kg/m^3) contours are shown in Fig. 29 at 2.25 and 2.72 msec. At the earlier time, the secondary shock is distorted as it traverses through the mixing layer, due to the presence of vortical structures arising from baroclinic effects. These structures cause spatially varying levels of afterburn/exothermicity, and thus spatially varying speeds of sound, causing the secondary shock to be faster in some regions, and slower in others. This creates the distorted shape of the secondary shock; however, within the next 0.47 msec, the secondary shock re-attains a spherical shape outside the mixing layer, due to transverse pressure waves which tend to equalize pressure in the transverse directions.

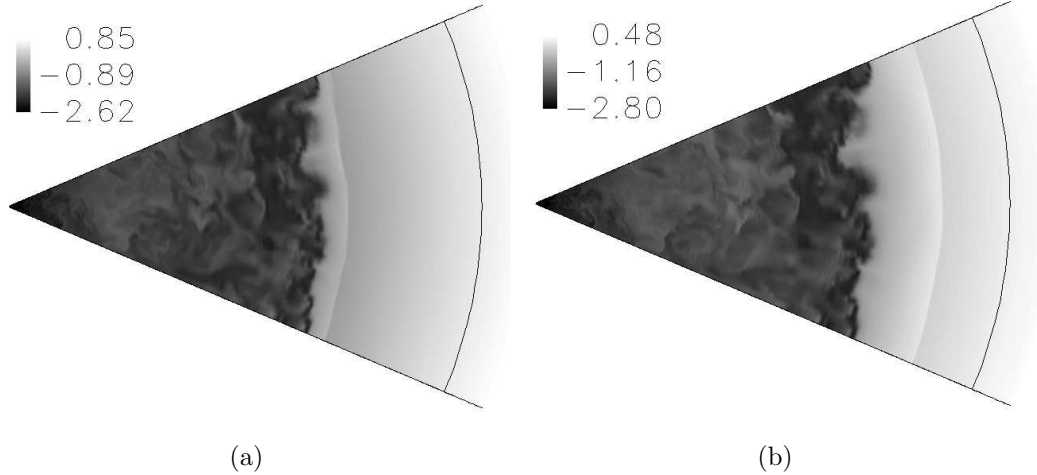


Figure 29: Natural logarithm of density contours at (a) 2.25 msec; (b) 2.72 msec.

To better understand the rate of combustion/afterburn, the time varying mass of CO , C and CO_2 are normalized with the initial charge mass and shown in Fig. 30. Since the chemical kinetic rates are assumed infinitely fast, by rate of combustion, it is referred to the rate at which convective mixing-controlled combustion occurs, i.e.,

not from diffusion or chemical kinetics. The burning rates are sufficiently fast at early times (< 1 msec) as the detonation products and shock compressed oxygen interact for the first time. Subsequently, due to the presence of CO_2 , which acts as a blanket between the detonation products and the shocked oxygen, the burning rate is slowed down. Thus, although more afterburn occurs during the asymptotic phase [121], the burning rate is slower than the corresponding rates at the earlier phases. It is due to this slow afterburning that the primary shock is almost unaffected by the afterburn energy release.

Observations show that at early times (blast wave phase), afterburn occurs primarily along the edges of the Rayleigh-Taylor structures, as these are the regions where the inner detonation products mix with the outer air. Burning occurs more or less along the entire width of the mixing zone during these early times. Later, most of the oxygen in the inner regions of the mixing layer get consumed, transitioning the burning primarily to the outer regions of the mixing layer due to this being closer to the source of oxidizer. However, some pockets of oxidizer still remain trapped inside the mixing layer even until late times (asymptotic mixing phase), owing to the earlier implosion phase, during which the secondary shock drags cavities of air deep into the mixing layer. As these regions of air mix with the inner detonation products, most of the oxygen is consumed, leaving behind some small air pockets where burning sustains along the edges of these pockets. This behavior was also reported in earlier studies [120, 121]. However, as more mixing occurs at later times, these pockets of oxygen get consumed, thereby transitioning the burning to the outer regions of the mixing layer completely.

These burning studies provide useful insights on how fast and how much of the detonation products burn, and the amount of exothermicity involved. Often, one-dimensional studies [6] investigate the blast problem with a parametric energy release, as the exact energy release can only be accurately deduced from three-dimensional

studies. Thus, targeted 3D studies can be used to predict the accurate energy release, and can then be used in parametric one-dimensional studies.

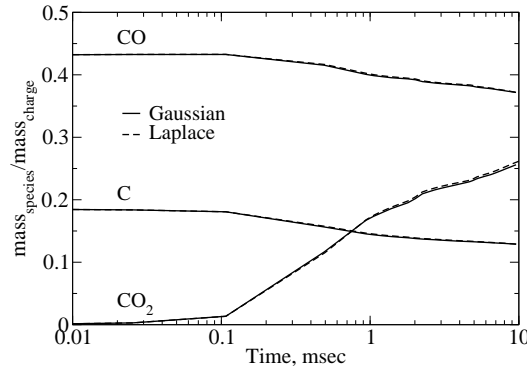


Figure 30: Normalized mass of CO , C and CO_2 variation with time.

To understand the effect of afterburn on the impulsive loading, the pressure traces for the 1D and 3D studies for the same TNT charge are compared in Fig. 31 at 0.9 m from the charge center. The increased mixing and afterburn associated with the three-dimensional case is not observed to affect the primary shock, as the afterburn energy release occurs over a time frame of a few hundred milli-seconds, which is not fast enough to couple with the primary shock. However, the secondary shock is observed to be slightly faster and stronger for the three-dimensional case, due to the increased afterburn energy release, which in turn results in lesser attenuation of the secondary shock as it traverses the mixing region. Another key observation is that the decay rate of the pressure profiles behind the primary shock is substantially different between the 1D and 3D cases. For instance, at around 1 msec, in the case with instabilities and enhanced mixing/afterburn (3D), the pressure decay is less than the corresponding 1D case. It appears that mixing and afterburn energy release are associated with three important features: (1) acceleration of the secondary shock; (2) stronger secondary shock; and (3) lesser decay rate of the pressure behind the primary shock. However, since the primary blast wave is nearly unaffected by the afterburn energy release, 1D studies will suffice for estimating the primary blast wave

overpressure.

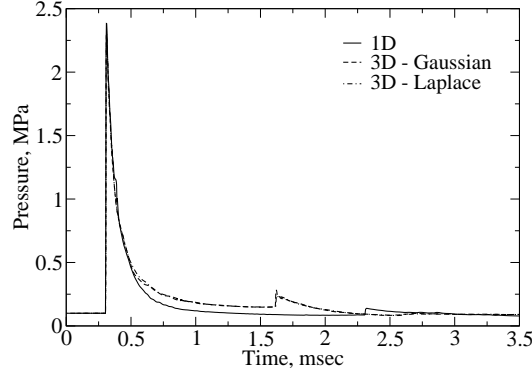


Figure 31: Pressure traces at the 0.9 m radial location for the TNT charge.

The dependence of the pressure on mixing and afterburn has implications in the impulsive loading estimation of explosive charges. The positive phase incident pressure impulse and the total impulse for the 1D and 3D cases are tabulated in Table 6, and a slight increase is observed for the 3D study, due to increased mixing and afterburn energy release. Denote as 3D-11.25° and 3D-22.5°, respectively, the quarter ($\theta = \phi = 11.25^\circ$) and half ($\theta = \phi = 22.5^\circ$) azimuth and zenith locations of the 45° sector. The positive phase pressure impulse and total impulse are higher for the 3D by about 46-60 % and 34-43 %, respectively. While the positive pressure impulse is nearly the same at 3D-11.25° and 3D-22.5° azimuth/zenith locations, the total impulse is slightly different at the 0.80 $mKg^{-1/3}$ location, as this radial location is near the center of the mixing layer, where the presence of vortical structures introduces significant three-dimensionality. Near to the core of the mixing layer, pressure waves can propagate laterally, trying to attain a ‘pressure equilibrium’ in the azimuth and zenith directions, thus explaining the almost same positive pressure impulse at 3D-11.25° and 3D-22.5°. However, near the core of the mixing layer, vortical structures cause significant density gradients, and thus, the total impulse (due to the dynamic pressure term) differs by about 7 % between 3D-11.25° and 3D-22.5° in the mixing layer. The total impulse is observed to be nearly the same for 3D-11.25° and 3D-22.5°

at the $1.38 \text{ mKg}^{-1/3}$ location, as this is near the outer periphery of the mixing layer, where transverse variations are minimal.

Table 6: Scaled impulse for TNT without (1D) and with (3D) mixing

Scaled radius, $\text{mKg}^{-1/3}$	positive pressure impulse, $\text{Pa} - \text{secKg}^{-1/3}$			total impulse, $\text{Pa} - \text{secKg}^{-1/3}$		
	1D	3D-11.25°	3D-22.5°	1D	3D-11.25°	3D-22.5°
0.80	208.9	334.4	335.5	425.9	572.6	611.5
1.38	121.4	177.8	177.5	219.6	296.7	293.0

While 1D results can accurately predict the shock overpressure, 3D studies appear more suited to make accurate impulse estimations. Furthermore, in the blast studies of high explosives, other natural factors such as ambient humidity, density stratifications, and dust content are important parameters that can affect the impulsive loading on structures, and to predict these effects will require 3D simulations. The current methodology appears to have the requisite capability to study some of these significant effects within a single simulation strategy. Also of interest is to determine the effect of the intensity of the initial perturbations on the mixing and afterburn in the post-detonation flow field, and will now be addressed.

6.1.3 Effect of initial perturbations

As previously mentioned, four phases are critical to the problem, i.e., the (1) blast wave phase, (2) implosion phase, (3) re-shock phase and the (4) asymptotic phase [13, 120, 121]. Two sub-cases are considered here, viz. low and high intensity perturbations are added to the initial density (and energy) profiles in the radial region $0.9r_o \leq r \leq r_o$, and the effect of the initial perturbations to the mixing and afterburn characteristics are studied. Specifically, Gaussianly generated random perturbations of intensity (max/min) $\pm 0.1\%$ and $\pm 1\%$, respectively, are added for the low and high intensity perturbation cases, to the density in the said radial band of the initial charge. Furthermore, it was confirmed that the mean of the perturbations is almost

zero, so that the total mass used to simulate the explosive corresponds to the chosen size. Other means of perturbations can also be used, such as by adding velocity perturbations outside the charge, and it is believed that the quantitative results will depend on the choice. Since the goal of this investigation is to understand the ensuing mixing process, the sensitivity to the initial choice (density or velocity, etc.) is considered beyond the scope of this investigation.

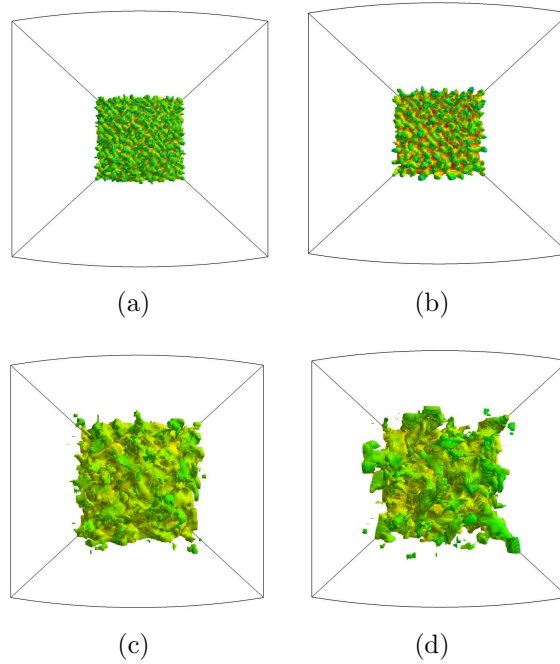


Figure 32: Mixing layer growth at 0.4 msec ((a) & (b)) and 3.5 msec ((c) & (d)) for the low ((a) & (c)) and high ((b) & (d)) intensity initial perturbations. Shown here are the CO isosurface contours shaded with the density.

In this section, the focus is on mixing and hydrodynamic growth due to initial Gaussian perturbations. Figure 32 shows the mixing layer (iso-surface of CO mass fraction) shape at two different times, i.e., Fig. 32 (a) and (b) correspond to 0.4 msec; (c) and (d) to 3.5 msec; (a) and (c) correspond to low intensity initial perturbations; (b) and (d) correspond to high intensity initial perturbations. From Fig. 32 (a) and (b), i.e., at the 0.4 msec time instant, it is observed that the structures are larger but fewer in number for the latter. For the larger initial perturbation intensity,

contiguous structures interact and merge earlier; on the other hand, when the initial perturbations are smaller, since the spacing between contiguous structures is more, they take a longer time to interact and merge. Consequently, the surface area of the structures at 0.4 msec are larger for the case with the larger initial perturbation shape (Fig. 32 (b)), and thus mixing and afterburn are more at 0.4 msec for the larger initial perturbation case. However, at 3.5 msec, comparing Fig. 32 (c) and (d), the scale and the number of structures are nearly similar for the two cases, i.e., the shape of the structures has attained a self-similarity, independent of the initial perturbation intensity. This time instant corresponds to the asymptotic phase, where the secondary shock has already penetrated through the mixing layer and deposited vorticity through baroclinic effects, that causes the merging and mixing of adjacent structures. Thus, at late times, the actual scale of the initial perturbations has lost its significance, and fluid mechanic effects such as entrainment and vorticity induced mixing take over. These observations imply that the early-stage mixing and afterburn rates should depend on the scale of the perturbations, with more mixing and afterburn occurring for larger initial perturbations; however, late time mixing and afterburn rates are nearly self-similar and independent of the scale of the initial perturbation size. The only major difference between Fig. 32 (c) and (d) is that the latter is slightly more radially ‘outside’ than the former.

To better understand the role of afterburn on the profile of the mixing layer, Fig. 33 shows the outer and inner boundaries of the mixing layer, defined here as the radial location where the azimuthally averaged CO mass fraction is $0.1Y_{CO}^i$ and $0.9Y_{CO}^i$, respectively, where Y_{CO}^i represents the mass fraction of CO at the onset of the completion of detonation within the charge, and is assumed uniform within the charge. Note that this definition is *ad hoc*, and is used only to represent the growth of the mixing layer qualitatively. The mixing layer boundaries are normalized with the initial charge radius, r_o . As observed, the mixing layer is wider for the

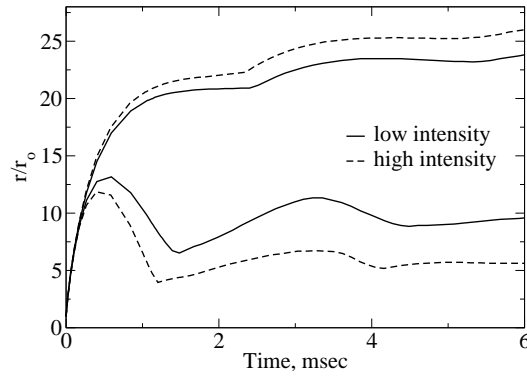


Figure 33: Outer and inner boundaries of the mixing layer with low and high intensity initial perturbations.

high intensity initial perturbation case, as more mixing and afterburn occurs for this case at early times, which expands the gases to a farther radial distance. However, beyond 2 msec, the differences in the mixing layer boundary profiles for the low and high intensity perturbations are nearly maintained, emphasizing self-similarity in the late time mixing layer profiles.

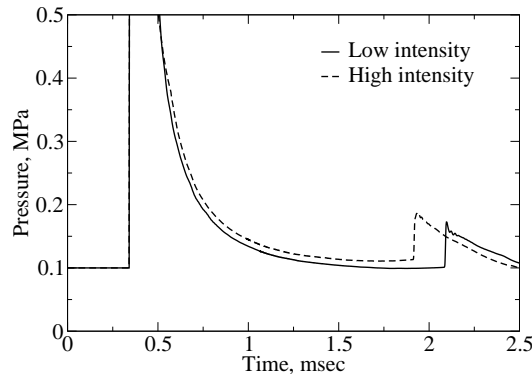


Figure 34: Pressure traces at the 0.9 m radial location for the TNT charge with low and high intensity initial perturbations.

The pressure traces at the radial location 0.9 m from the charge center are plotted as a function of time for the two different initial perturbation cases in Fig. 34. The time of arrival of the primary shock is identical and independent of the initial

perturbations, as the time scale of afterburn energy release is a few orders of magnitude larger than that of the primary blast wave at the 0.9 m location. However, the pressure decay rate behind the primary blast wave is lesser when the initial perturbation intensity is higher (see around 1.25 msec). Moreover, the time of arrival of the secondary shock is earlier for the high intensity perturbation case, due to the higher afterburn energy release at early times associated with the higher initial perturbation intensity. Thus, it is concluded from this study that enhanced initial perturbations inevitably result in higher amounts of mixing and afterburn in the mixing layer, and concomitantly, the flow physics behind the primary shock changes due to this additional exothermic energy release.

Explosions into air have been studied in this section, and the flow physics has been elucidated, in addition to discussions on the gas dynamics of the mixing layer and the afterburn aspects. These studies have laid the groundwork for the investigation of explosions into ambient reactive particles clouds, which forms the crux of the next section.

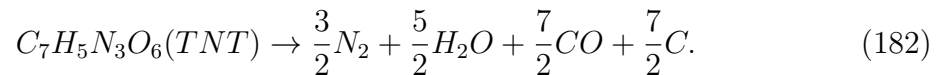
6.2 Homogeneous Explosions into Dilute Aluminum Particle Clouds

The above study of homogeneous explosions into air is hereby extended to investigate explosions into ambient aluminum particle clouds. In this section, focus is laid to explore and understand the role of ambient particles in the mixing and afterburn behind explosions, in particular on the (1) effect of particle size to the mixing characteristics; (2) effect of initial loading ratio (defined as the ratio of the mass of solid aluminum to the mass of gas in a control volume, denoted η hereafter) to the mixing; (3) effect of initial radial extent of the particle distribution; and (4) clustering of small particles.

Based on the dispersion characteristics due to explosions, particles can be classified into two groups, viz. (i) large particle regime and (ii) small particle regime, where the former refers to the scenario where the particles are large enough that their response

time scales are larger than the fluid mechanic time scales of relevance in the mixing layer. Consequently, these particles disperse mostly along the radial direction, without being influenced by the vortex rings in the mixing layer. Small particles, on the other hand, have response time scales comparable to the fluid mechanic time scales, and are thus influenced by the vortex rings in the mixing layer, resulting in the formation of clusters, as will be shown later in this section. First, this section focuses on the large particle regime; then, on the small particle regime.

A 11.8 cm dia. TNT charge is considered for these studies. A spherical sector grid 2.4 m long, and 45° in the azimuth and zenith directions is considered, and is resolved using a $1000 \times 60 \times 60$ grid in the r -, θ - and ϕ -directions, respectively. Grid independence studies have also been carried out, and this resolution is found to suffice to accurately predict the mixing and afterburn characteristics in the mixing layer; in addition, the sector boundary conditions are the same as before (some additional grid independence studies are shown below in Section 6.2.3). The detonation profiles based on the GISPA (Section 4.7, Appendix B) method are initialized within the initial charge radius, and aluminum particles are distributed outside the charge until a specified radius. The TNT detonation products is assumed to comprise of the species: $C(S)$, CO , H_2O and N_2 with the mass fractions assigned based on the following balanced chemical equation:



For thermodynamic closure, the Noble-Abel equation of state is employed (Eqn. (33)), with the constant A determined by trial and error to match the primary blast wave decay with radius, as also done in [181]. The Noble-Abel equation of state is preferred over the use of the JWL equation of state due to its simplicity, especially when aluminum and oxides of aluminum are also involved in the flow field. Focus here, *inter alia*, is on mixing, afterburn and dispersion characteristics.

6.2.1 Perturbation growth and particle dispersion

This discussion applies both to larger as well as small particle regimes. As mentioned in Section 1.2.2, when the detonation wave reaches the outer boundary of the initial charge, a primary shock wave (PS) propagates outwards and a rarefaction wave inwards. The contact surface initially overtakes the particles, and due to the high density gradients across it, is sensitive to perturbations. The particles pick up momentum and heat from the gas, and thereby introduce perturbations on the contact surface. These perturbations subsequently grow into Rayleigh-Taylor [192] hydrodynamic instabilities at multiple transverse scales and wavelengths. Shortly thereafter, the entire particle cloud is engulfed into the detonation products. At the same time, the inward moving rarefaction overexpands the local flow, giving rise to a secondary shock (SS) [34]. This SS is initially weak, is initially a compression wave, and is swept outwards by the outward expanding gases, during which it strengthens. A schematic of the post-detonation flow-field represented in a one-dimensional sense is presented in Fig. 35, showing the primary shock, secondary shock, contact surface and the particle cloud. Note that this representation is in a one-dimensional sense only; in reality, the contact surface will develop into a mixing layer.

For particles sufficiently small, ignition occurs in the cloud early, initially at the leading edge by virtue of it being closer to the source of heat—that due to the afterburn between the inner detonation products and the outer air. Subsequently, the hydrodynamic structures decelerate more than the particles, as the latter have a higher inertia; this results in the leading edge of the particle cloud to catch-up and interact with the structures—the second interaction. Around this time instant, while the leading edge (LE) of the particle cloud is in the mixing layer where the detonation products ($C(S)$, CO , H_2O), air, and afterburn products (CO , CO_2) co-exist, the trailing edge (TE) of the cloud is still engulfed into the detonation products. Furthermore, the SS, which is still a compression wave, penetrates into the TE of the

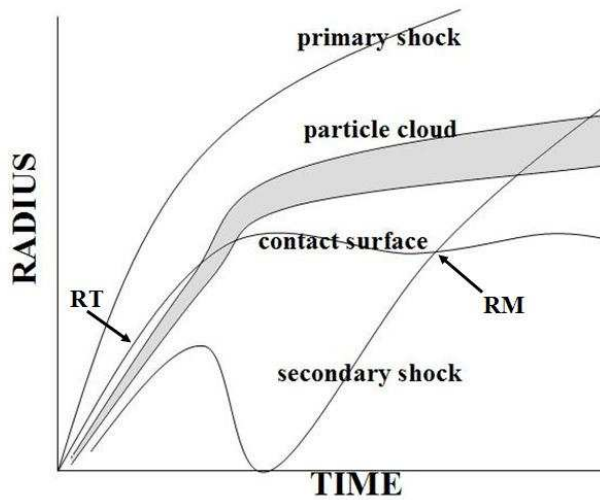


Figure 35: Radius-time diagram of the one-dimensional post-detonation flow-field. Note: this is a schematic only.

cloud, and subsequently strengthens into a shock shortly thereafter; note that this strengthening is not due to the particles, but due to coalescence of pressure pulses arising from the relatively higher pressure immediately behind the PS (see [34] for more discussions on the formation of the SS).

Following this, the SS slows down faster than the particles, as the latter has a higher inertia. Later, the particles are completely engulfed between the PS and SS, and interact with the Rayleigh-Taylor structures that have already started to grow; this growth of the structures in size is due to two reasons: (1) entrainment of the outer air into the structures; and (2) “bubble competition” between contiguous structures [14, 128, 149, 151]. Note that this second interaction between the particle cloud and the contact surface (which by now is essentially a highly perturbed surface due to the growth of the Rayleigh-Taylor structures) lasts for a longer time than their first interaction, as the hydrodynamic structures have grown to a larger transverse scale and width by this time.

Much later, the SS implodes inwards as the pressures have reduced considerably

near the core due to the earlier rarefaction wave. During this implosion phase, the TE of the particle cloud slows down as the local gas velocity reverses—this inevitably widens the particle cloud width. At the same time, the LE of the cloud starts to emerge out of the hydrodynamic structures, whose growth hitherto has ensued in a mixing layer. At this time, the choice of the oxidizer varies across the width of the particle cloud for the aluminum combustion—it is O_2 near the leading edge (aerobic); is H_2O near the TE (anaerobic), and a mixture of possible oxidizers (CO_2, H_2O, O_2) in the middle of the cloud that is currently in the mixing layer. Analysis shows that for the relatively smaller aluminum particles, most of evaporation occurs primarily when the particles are engulfed inside the detonation products.

Vortex rings exist around the hydrodynamic structures [121] due to shear and baroclinic effects, and they introduce transverse velocity components to the otherwise radially dispersing particle cloud. For the large particle regime, due to their larger response time scales, they are not affected by these vortex rings. On the other hand, for the small particle regime, their response time scales are comparable to the time scales of the vortex rings, which in turn results in the transverse dispersion of these smaller particles that leads to their clustering (preferential accumulation) around these vortex rings. Thus, a “foot print” of the Rayleigh-Taylor structures is left on the particle cloud and is preserved even until much later—this phenomena will be revisited later in this chapter. Note that particle structures are referred to as a ‘cluster’, merely to distinguish it from hydrodynamic structures; thus, for the remainder of this study, hydrodynamic fluid structures are referred to simply as ‘structures’, and particle structures as ‘clusters’ to avoid confusion.

At much later times, the particle cloud leaves the mixing layer (refer to Fig. 35), and is quenched shortly thereafter due to the unavailability of heat and the relatively cooler surrounding air (note that quenching essentially refers to the particles not evaporating any longer due to their cooling to temperatures below the ignition

temperature of aluminum). Furthermore, outside the mixing layer, the sources of turbulence and vorticity are not as preponderant as in the mixing layer; thus, the particles disperse mostly along the radial direction once outside the mixing layer, maintaining their clustered shape, i.e., the earlier hydrodynamic induced foot print in the cloud is maintained. Aerodynamic drag slows down the particles and their clustered shape grows in size as they expand outwards into free space.

Meanwhile, the SS that has been imploding, reflects from the origin, and subsequently explodes outwards. During this second outward passage, the SS interacts with the hydrodynamic structures in the mixing layer— giving rise to a Richtmyer-Meshkov instability [169, 146]—this event is also termed as a ‘reshock’ [13, 120]. Here, the pressure gradient across the secondary shock is mis-aligned with the density gradients across the hydrodynamic structures, which results in the creation of vorticity due to baroclinic torque effects ($\dot{\omega} = \frac{1}{\rho^2} \nabla p \times \nabla \rho$). This vorticity sustains afterburn, as it allows for fresh sources of oxygen in the air that was hitherto unreachable to the inner detonation products, to come into contact. Furthermore, during this reshock the mixing layer is compressed [13, 120], due to which the vorticity is able to sustain itself for a slightly longer time, a consequence of the two stretching terms in the vorticity equation [14].

Subsequently, the SS catches-up with the particle cloud and penetrates it, essentially a reshock for the particle cloud, thereby shrinking the width of the cloud. However, the quenched particles do not re-ignite, as their interaction with the SS occurs radially far away, and the latter has already attenuated due to spherical spreading. To illustrate the aforementioned hydrodynamic instabilities behind the blast wave, the isosurface of the mass fraction of CO , shaded with $\ln(\rho)$ are presented in Fig. 36 at times (a) ~ 0.3 msec and (b) ~ 3.8 msec, for $r_p = 5 \mu\text{m}$, $\eta=1$, and initial cloud extending from outside the explosive charge ($r = 5.9$ cm) till $r = 8.68$ cm. As evident, at the earlier time, the hydrodynamic structures are spatially organized and

are mushroom shaped; at the later time, which is after the reshock, the structures are more convoluted/wrinkled owing to the deposited vorticity.

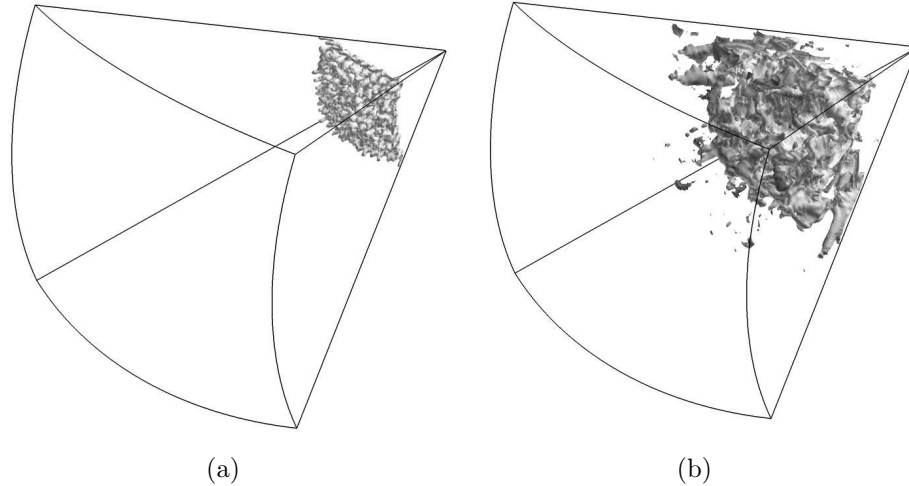


Figure 36: CO isosurface shaded with $\log(\rho)$ at times (a) ~ 0.3 msec; (b) ~ 3.8 msec. Particles are not shown for better clarity.

6.2.2 Large particle regime

The major difference between mixing induced by the inclusion of random perturbations compared to the mixing induced by ambient particles is that in the former, the contact surface is perturbed instantaneously and the ensuing Rayleigh-Taylor instabilities are allowed to grow without any further triggering mechanism; however, in the latter, the triggering of perturbations/instabilities on the contact surface is undertaken for a finite instant of time, viz. the time period required for the contact surface to overtake the particles. If the particles are sufficiently large, by virtue of their inertia, they are not readily set into motion by the blast wave, thus allowing for the contact surface to overtake them initially. During this instant, inter-phase drag and heat transfer comes into play and creates perturbations on the contact surface that subsequently grow into Rayleigh-Taylor instabilities. Higher the density ratio across the contact surface, the more sensitive it is to the interaction with solid particles.

If the particle cloud extends too far radially outwards, the outer particles may not have a significant effect on the triggering of perturbations, since the density ratio across the contact surface decreases as it propagates outwards. Subsequently, the particles encompassed by the contact surface pick up momentum from the gas and are set into motion, catching-up with the contact surface, and interact with it for a second time. If this second interaction occurs too far radially outwards, it may have no significance to the further triggering of perturbations as the density ratio across the contact surface has decreased considerably. Specifically, the interest of this study is on particles of radius 10-100 μm (large particle regime); initial mass loading ratio, $\eta = 1$ and 0.25; and initial cloud width extending from outside the initial charge ($r = 5.9$ cm) till $r = 25$ cm and $r = 8.68$ cm.

The aforementioned physical phenomena are qualitatively presented in Fig. 37 showing the mixing layer and the solid particles at 0.11 and 0.4 msec for the 20 μm particle radius, $\eta = 1$, and an initial particle cloud extending upto 25 cm radial distance. At the earlier time, the particles are seen to interact with the mixing layer, with some particles already being engulfed within the mixing layer; by the later time, the particles have overtaken the mixing layer.

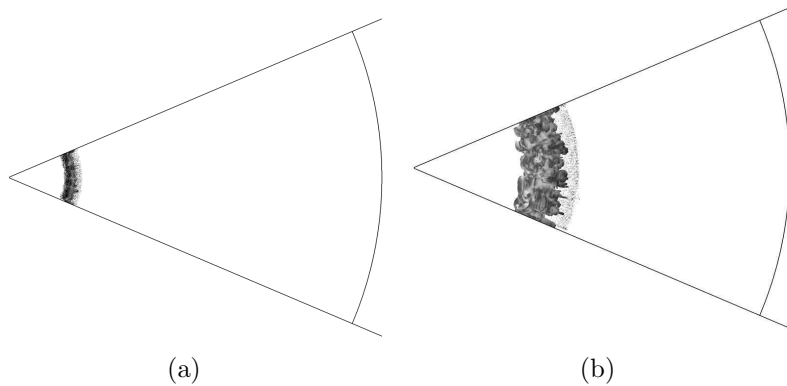


Figure 37: The interaction of solid particles with the mixing layer and their subsequent dispersion at times (a) 0.11 msec; (b) 0.4 msec.

6.2.2.1 *Effect of particle size*

If particles are sufficiently small, by virtue of their lower inertia, a good many of them are set into rapid motion by the blast wave and may not even interact with the contact surface. To study these aspects, a range of particle sizes are considered and their role on the mixing and afterburn process is investigated. First, a loading ratio, $\eta = 1$ is considered, with an initial particle cloud extending from outside the charge radius upto 0.25 m radial distance. Furthermore, the focus here is only on the mixing and afterburn aspects, and not on the dependence of the blast wave overpressure on the particle cloud. The interested reader is referred to [181] for a study of the dependence of the blast wave overpressure on ambient water droplets.

The particle laden cases are compared with the low-intensity Gaussian density perturbations case considered earlier; note that the latter is particle-free and will be the baseline case for the rest of the study. The main distinction between a particle cloud-induced perturbation, and that due to Gaussian perturbation is that in the former, the perturbation event occurs continuously, i.e., the time taken by the contact surface to overtake the particle cloud. In the latter, the perturbation is introduced at a single time instant, and the hydrodynamic structures are allowed to grow thereafter at an un-forced rate. It does not always mean that a continuously perturbed flow encounters more mixing than an instantaneous perturbation, for if the instantaneous perturbation itself is significantly high enough, it can result in more mixing than a continuously perturbed hydrodynamic growth.

The pressure field behind the blast wave at 0.9 m from the center of the charge is shown in Fig. 38 for different particle radii (10-100 μm), along with the baseline case. The pressure decay behind the primary blast wave is less for the cases with particles than the baseline case (see for instance around 1-1.5 msec); furthermore, the secondary shock arrival time is earlier for the particle cases by about 0.25 msec. This is due to the enhanced mixing and afterburn associated with the particle cases in

comparison with the baseline case; the additional energy release lowers the pressure decay rates and accelerates the secondary shock. The enhanced mixing for the particle cases is a direct consequence of the longer triggering/stirring of perturbations on the contact surface for the particle cases, with more (longer) triggering made possible with the presence of more particles. Moreover, enhanced mixing directly contributes to enhanced afterburn energy release, thereby resulting in the observed pressure trends and a faster secondary shock.

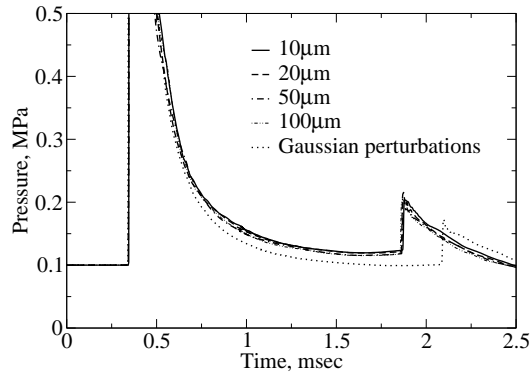


Figure 38: Effect of particle size on the pressure field behind the blast wave.

Another crucial observation from Fig. 38 is that the pressure profiles are nearly similar for the different particle sizes considered. Analysis shows that the early Rayleigh-Taylor instabilities caused by the interaction of the contact surface with the particles starts to grow from a scale comparable to the particle size. At later times, the nonlinear growth of the instability loses memory of the initial conditions regardless of the initial particle size, and all cases for different particle sizes, but with the same initial mass loading and initial radial extent of particles give rise to approximately the same pressure field behind the primary blast wave. Thus, although the instabilities may begin from a scale comparable to the particle size, the later time flow physics (entrainment, baroclinic torque, etc.) dictates subsequent mixing and afterburn. From a practical point of view, this is an important observation, for it suggests that the late stage observation of the flow-field may not directly correlate to

what occurred at the initial stage of explosion in gaseous or particle laden flow-field. This loss of memory of the Rayleigh-Taylor structures has also been pointed out by Youngs [211] based on a two-dimensional simulation, albeit in a low-speed, planar, non-reacting and single phase flow problem.

Another aspect that plays a key role in this loss of memory is “bubble competition,” in which contiguous bubbles ensuing from a multimode initial perturbation interact at early times and merge. Very recently, Leinov et al. [128] undertook an experimental and numerical study of the planar Richtmyer-Meshkov instability and illustrated the significance of the bubble competition process. When multi-wavelength hydrodynamic instabilities co-exist on a surface, a bubble competition ensues as contiguous structures start to grow and interact; large bubbles overtake the volume hitherto occupied by the smaller bubbles. Thus, the average wavelength of the hydrodynamic structures increases faster with time, and the width of the multi-wavelength perturbation grows faster *vis-à-vis* the single-wavelength perturbation.

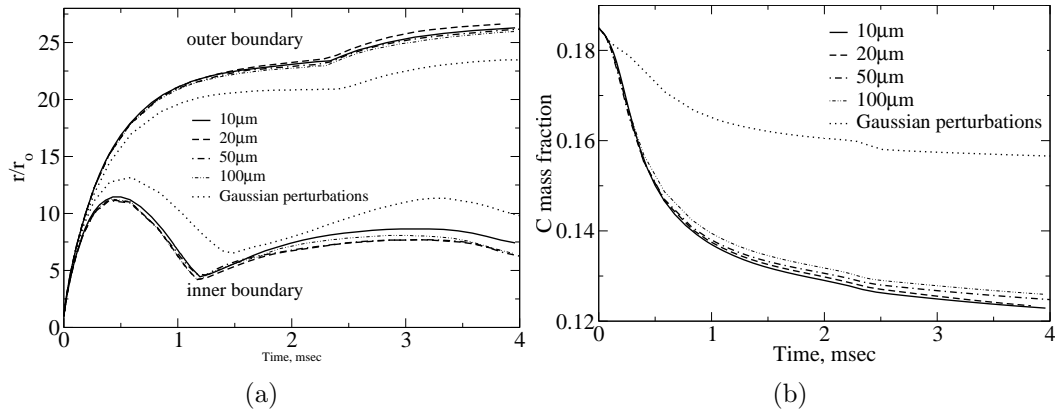


Figure 39: Dependence of mixing and afterburn on particle size: (a) mixing layer boundaries; (b) $C(S)$ mass fractions remaining.

To quantify the mixing and afterburning rates, Fig. 39 shows the (a) mixing layer boundaries and the (b) $C(S)$ mass fraction remaining with time. Here, outer and inner boundaries of the mixing layer are defined as before (radius corresponding to $0.1Y_{CO}^i$ and $0.9Y_{CO}^i$, respectively) and normalized with the initial charge radius, r_0 ;

mass fractions are defined as the mass of the species remaining normalized by the initial charge mass. As observed in Fig. 39 (a), the mixing layer stretches wider for the particle cases as compared with the baseline particle-free case, due to the longer triggering of the initial perturbations in the former. The outer boundary of the mixing layer is independent of the particle size, although slight differences exist for the inner boundary of the mixing layer. Furthermore, the implosion phase is shorter for the particle cases by about 0.25 msec, as identified by the local minima in the inner boundary of the mixing layer in Fig. 39 (a) (1.2 msec for particle cases; 1.45 msec for the baseline case). From Fig. 39 (b), the $C(S)$ consumption rates are faster for the particle cases at early times than the baseline case; however, are nearly parallel to each other beyond about 1.5 msec, maintaining a constant difference. This indicates that once the mixing and afterburn transform to the outer regions of the mixing layer, they attain self-similarity and are thenceforth dictated by entrainment which, at late times, does not depend on the scale at which the very early structures originally grew from (due to memory loss).

Observing the particle evaporation/reaction behavior (not shown here for brevity), it was deduced that large particles ($> 50 \mu\text{m}$ radius) do not ignite due to their large heat transfer time scales. Only intermediate and small particles ignite, and smaller particles subsequently burn longer due to their smaller heat transfer time scales. These conclusions are only valid under the mono-disperse particle size distribution assumption, for in a realistic situation, aluminum particles exist as a distribution of varying sizes. Here, the smaller particles ignite and burn relatively faster, supplying energy to the larger particles, thereby giving rise to the possibility of the ignition of the larger particles. Thus, these conclusions strictly conform to mono-disperse particle clouds only.

6.2.2.2 *Mixing layer/primary blast wave interaction*

Thus far, the growth of perturbations/instabilities and their subsequent role in the mixing and afterburn process has been demonstrated. As these structures propagate radially outward in time, they are decelerated due to aerodynamic drag and spherical spreading. If the deceleration of these structures is lesser than that of the primary blast wave, it is possible for the structures to catch-up with the blast wave, contrary to their behavior as would be predicted by the classical one-dimensional blast wave theory [182]. In particular, if the initial particle distribution causes perturbations sufficiently large, the chances of the ensuing hydrodynamic structures to catch-up with the primary blast wave is higher.

To illustrate this phenomenon, the density contours at six different instants are presented for the case corresponding to the 10 μm particle radius with $\eta=1$ and an initial particle distribution extending from outside the charge surface till $r = 0.25$ m, are presented in Fig. 40; the figures correspond to early times, i.e., in the range 0.11-0.58 msec. At early times, the hydrodynamic structures lag behind the primary blast wave, as observed in Fig. 40 (a). Subsequently, as observed in Fig. 40 (b), one (or more) of the hydrodynamic structures catches-up with the primary blast wave, and creates a ‘bump’ in the latter, more prominently visible in Fig. 40 (c) (as indicated by the arrow). During this instant, the pressure behind the blast wave in the vicinity of the penetrating structure is augmented by about 5 bars, as compared with other regions immediately behind the blast wave that are not affected by the hydrodynamic structures. This ‘bump’ or high pressure spot is created due to the compression of the gas between the outward propagating blast wave and the penetrating structure. Subsequently, the penetrating structure is slowed down more than the blast wave, allowing for the blast wave to re-overtake the structure as observed in Fig. 40 (e). A distorted blast wave is unstable, and pressure waves propagate in the azimuthal directions from the high pressure spot, thereby re-sphericalizing the blast wave, as

observed in Fig. 40 (f). Analysis shows that this early interaction between the hydrodynamic structure and the blast wave does not have any notable long term impacts on the latter. Furthermore, although not verified, it is intuitively believed that this phenomenon of hydrodynamic structure interaction with the blast wave may not be encountered in planar or cylindrical blast waves, as the decay rate of the blast wave would be lesser as compared with the spherical case considered here.

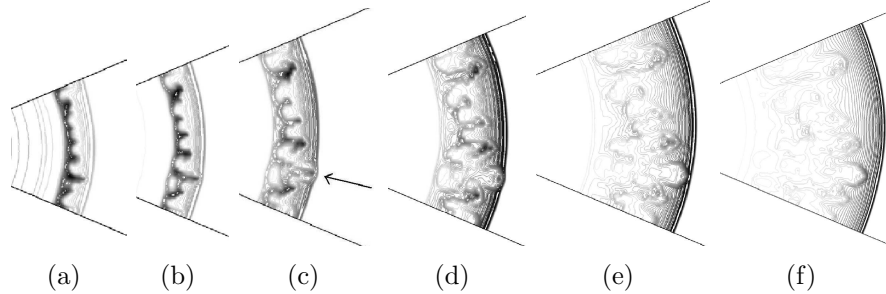


Figure 40: Interaction of the hydrodynamic structures with the primary blast wave: density contours at time instants (a) 0.11 msec; (b) 0.16 msec; (c) 0.22 msec; (d) 0.3 msec; (e) 0.4 msec and (f) 0.58 msec. Note that the figures are shown in different scale for better clarity.

6.2.2.3 Effect of mass loading

The next focus is on the effect of mass loading ratio (η) to the problem under study. The pressure-time traces for particles initially extending from outside the charge radius (5.9 cm) upto 8.68 cm radius, for mass loading ratios $\eta = 0.25$ and 1 are presented in Fig. 41. As observed, the pressure decay rate is lesser, and the secondary shock faster, when the loading ratio is higher, i.e., when more particles are available to perturb the contact surface. The inner and outer boundaries of the mixing layer, as defined before, are shown in Fig. 42, with the plain lines corresponding to $\eta = 1$, and the lines with circles corresponding to $\eta = 0.25$, for the case when the initial particle distribution extends from outside the charge radius till 8.68 cm. As observed, the outer boundary of the mixing layer (Fig. 42 (a)) is radially farther by about one charge radius for the $\eta = 1$ case, and is radially farther for both mass loading ratios

when compared with the baseline particle-free Gaussian perturbations case. The inner boundary of the mixing layer (Fig. 42 (b)) is radially more ‘inside’ for the particle cases than the baseline case due to more mixing. Furthermore, the inner boundary is more ‘inside’ for the $\eta = 0.25$ case than for $\eta = 1$ at late times, presumably due to more obstruction by the particles for the $\eta = 1$ case during the implosion phase (~ 1 msec). However, since the burning transforms to the outer regions of the mixing layer at later times, the inner boundary of the mixing layer loses significance at later times. In summary, this study reveals that the exploding fireball is larger (in terms of outer radius) for the particle cases than the baseline case, indicating that more mixing occurs in the former. Due to this, more afterburn occurs when more ambient particles are available to trigger the early mixing process, as illustrated by the mass fractions of $C(S)$ remaining shown in Fig. 43.

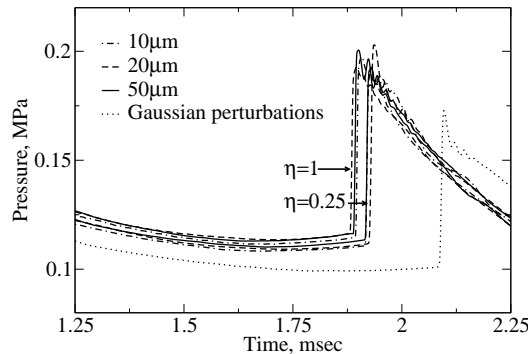


Figure 41: Effect of initial mass loading ratio on the pressure field behind the blast wave.

6.2.2.4 Effect of radial extent of particle distribution

When the initial particle cloud extends radially farther, the contact surface encounters more particles as it propagates outwards. Thus, the triggering mechanism for the early Rayleigh-Taylor structures lasts for a longer time duration for a farther initial extent of the particle cloud. To illustrate this fact, Fig. 44 shows the pressure-time trace at the 0.9 m radial location for two different initial particle cloud extents, i.e.,

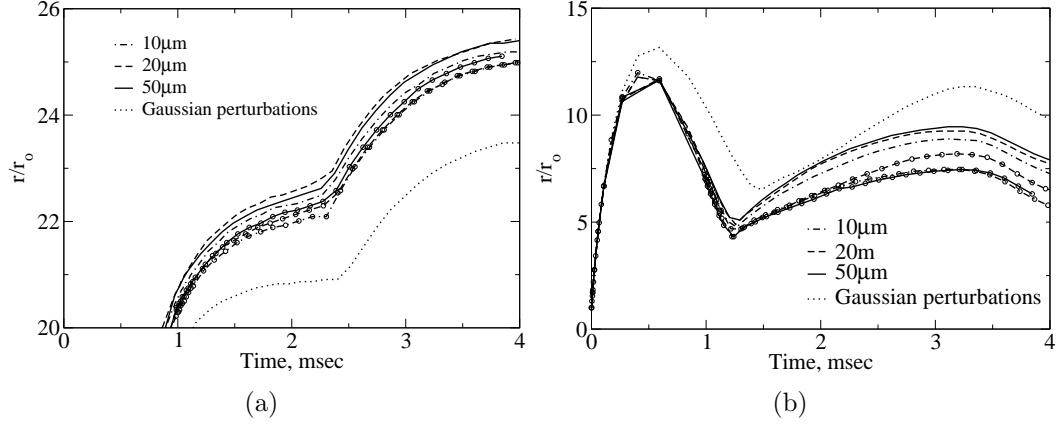


Figure 42: Dependence of mixing layer boundaries on the initial mass loading ratio: (a) outer boundary; (b) inner boundary. The plain lines correspond to $\eta=1$; the lines with circles correspond to $\eta = 0.25$.

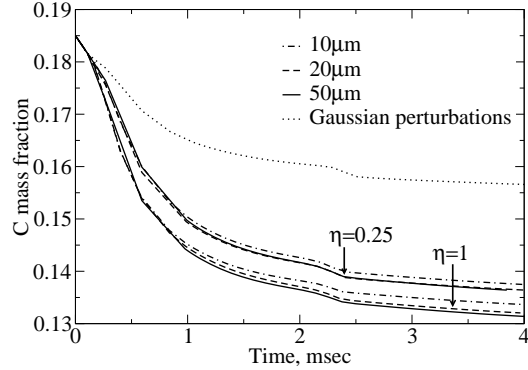


Figure 43: Dependence of afterburn on the initial mass loading ratio: $C(S)$ mass fraction remaining.

from outside the charge radius (5.9 cm) upto (i) 8.68 cm and (ii) 25 cm, for the same mass loading, $\eta = 1$. Particle radii in the range 10-50 μm are considered, and the results are compared with the aforementioned particle-free baseline case. As evident from Fig. 44, the pressure decay rates are lesser when more particles are available to perturb the contact surface, see for instance the time period 1.25-1.5 msec (only 10 and 20 μm size cases are shown here for better clarity). Furthermore, the time of arrival of the secondary shock at this location is earlier by about 0.1 msec for the initial particle extent 5.9-25 cm, in comparison with the 5.9-8.68 cm case; the latter

being 0.4 msec earlier than the baseline case with regard to the time of arrival of the secondary shock.

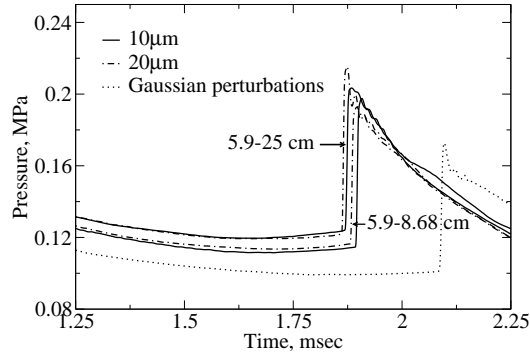


Figure 44: Effect of initial extent of particle distribution on the pressure field behind the blast wave.

To understand the effect on mixing for a farther extent of the initial particle cloud, Fig. 45 shows the (a) outer and (b) inner boundaries of the mixing layer, defined as before. The mixing layer width is clearly wider when more particles are available to trigger the early perturbations. Furthermore, the implosion phase is also shorter when more particles are available, as identified by the local minima in the inner boundary of the mixing layer (see time instant 1.2 msec for 5.9-25 cm; 1.4 msec for 5.9-8.68 cm, and 1.5 msec for the baseline case). Thus, more mixing between the inner detonation products and the outer air occurs when more particles are available to perturb the contact surface earlier. This enhanced mixing also relates to enhanced afterburn, as shown by the trends in the $C(S)$ mass fractions remaining in Fig. 46. It is interesting to observe, as before, the mass fractions remaining at later times to be nearly parallel for the different cases, thus further emphasizing the self-similarity in the afterburn rates at late times.

6.2.2.5 Particle ignition/quenching

Analysis shows that very large particles never reach their ignition temperature for the cases considered in this study, due to their higher mass. On the other hand,

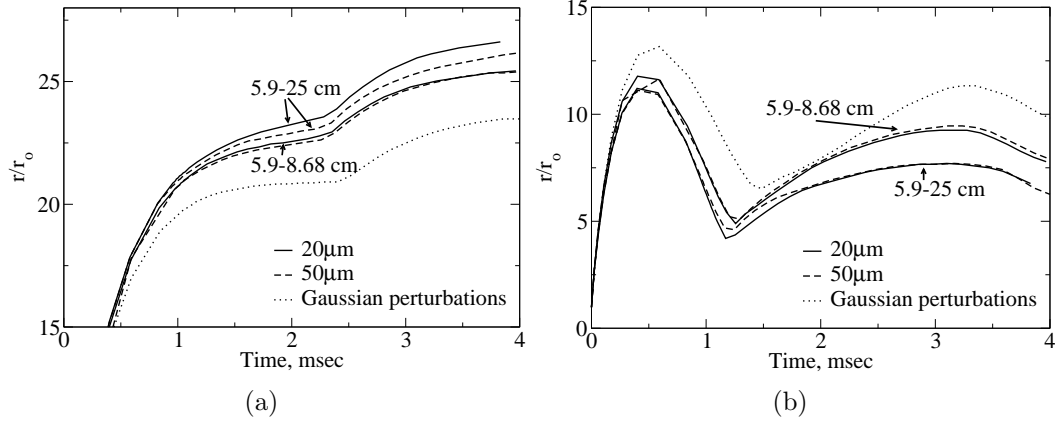


Figure 45: Dependence of mixing layer boundaries on the initial extent of particle distribution: (a) outer boundary; (b) inner boundary.

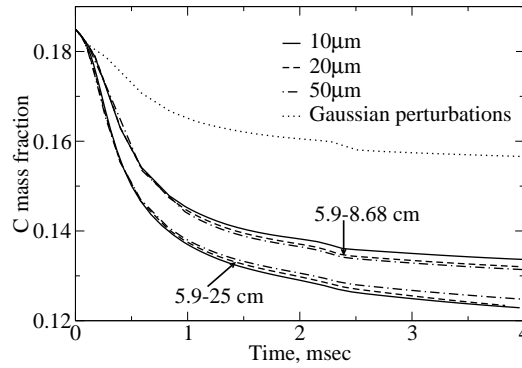


Figure 46: Dependence of afterburn on the initial extent of particle distribution: $C(S)$ mass fraction remaining.

smaller particles readily ignite and burn, anaerobically initially, and aerobically later. However, as they subsequently leave the mixing layer, they encounter regions that are relatively cooler and are thus quenched.

To illustrate the evaporation rates of solid aluminum, the time varying solid aluminum mass remaining for the $10 \mu\text{m}$ particle radius is shown in Fig. 47, normalized with the total initial mass of the aluminum particles. In particular, the focus is on the effect of mass loading, η , and the initial width of the particle cloud extending from outside the charge radius (5.9 cm) upto 25 cm and 8.68 cm. As evident from Fig. 47, about 60% of solid aluminum remains after being quenched for the shorter

initial cloud width, whereas 67% remains with the longer initial cloud. The particles in the outer regions of the longer initial cloud (5.9-25 cm) are set into motion by the leading blast wave and never interact with the afterburning regions of the mixing layer, and thus they evaporate less. On the other hand, shorter initial particle clouds are easily engulfed by the contact surface, and thus spend a longer time in the mixing layer where they can sustain evaporation for a longer time due to availability of heat. Furthermore, it is interesting to note that for the shorter cloud (5.9-8.68 cm), the transient evaporation rates are independent of the mass loading ratio for $\eta = 0.25$ and 1. On the other hand, for the longer cloud (5.9-25 cm), a slightly higher evaporation rate occurs for $\eta=0.25$ in the time interval 0.12-0.6 msec. This is because the blast wave slows down less for $\eta=0.25$ as compared with $\eta=1$, as fewer particles exist in the former, causing higher evaporation rates. However, beyond 0.6 msec, the amount of solid aluminum remaining is identical for both loading ratios ($\sim 67\%$).

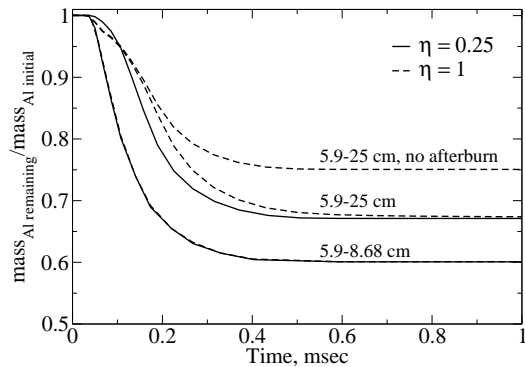


Figure 47: Solid aluminum mass remaining with time.

To illustrate the significance of the afterburn energy release on the evaporation of aluminum, also shown in Fig. 47 is the solid aluminum mass remaining for the $\eta=1$ case, the initial cloud extending upto 25 cm, but with the afterburn of the detonation products and the gaseous aluminum fictitiously turned off. As observed, about 75% of the solid aluminum remains un-evaporated, implying the dependence of the late-time aluminum evaporation on the afterburn energy release. These findings reveal

that ambient solid particles enhance mixing and afterburn of the detonation products, which in turn enhances the evaporation of the particles, i.e., the two phenomena are inter-connected.

Having established these facts, the focus is now shifted to the study of the small particle regime, where the same problem is considered, albeit with 5 and 10 μm particle radius clouds. Recall from earlier discussion, these smaller particles have response time scales comparable to the fluid mechanic time scales in the mixing layer. This, as will be shown now, results in different particle dispersion characteristics, viz. the clustering behavior of the particles upon their dispersal due to chemical explosions.

6.2.3 Small particle regime

Particles sufficiently small have fast response time scales which may be comparable to the fluid mechanic time scales in the mixing layer. This can cause different particle dispersion characteristics and is the focus of the investigation in this sub-section. Before ascertaining the dispersion physics of small particles upon explosive dispersal, it is customary to first demonstrate grid independence. Three different grids are considered: $1000 \times 60 \times 60$, $1000 \times 75 \times 75$ and $1000 \times 90 \times 90$, and some of the primary features are presented in Fig. 48 corresponding to $r_p = 5 \mu\text{m}$ and $t_b = 1 \text{ msec}$. As evident from Fig. 48 (a), the inner and outer boundaries of the mixing layer (defined here based on the CO mass fraction as also done earlier) are in good accordance for the three different grids employed. Furthermore, the mass fraction of $C(S)$ and CO remaining with time is shown in Fig. 48 (b) and the simulation results for the three different grids are identical. The normalized mass of solid aluminum remaining is shown versus time in Fig. 48 (c) and the results for the three grids agree. These studies exemplify that the $1000 \times 60 \times 60$ sector grid suffices to capture the primary mixing and afterburn physics of relevance to the current investigation. For the remainder of this sub-section, the $1000 \times 60 \times 60$ grid is thus employed for the computations.

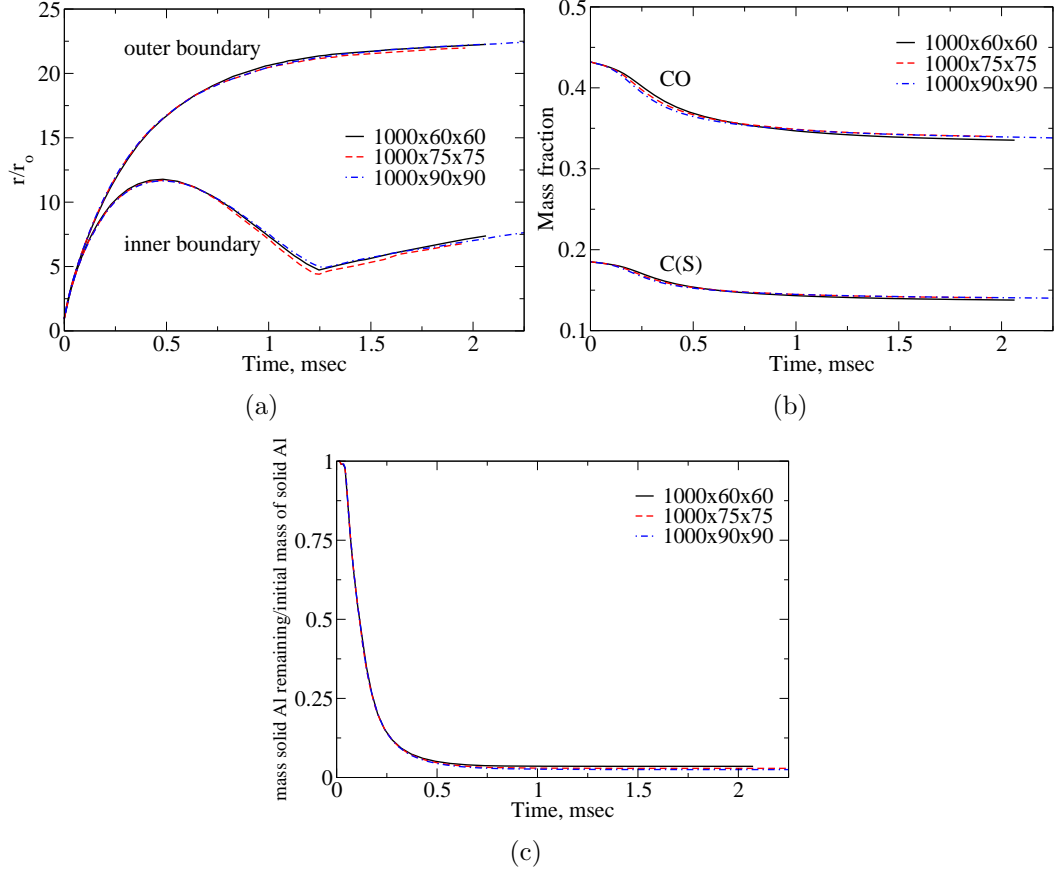


Figure 48: Grid independence study: (a) inner and outer boundaries of the mixing layer; (b) mass fractions of $C(S)$ and CO remaining; (c) normalized mass of solid aluminum remaining.

Simulation of a 5.9 cm radius TNT charge into ambient air comprising of $r_p = 5 \mu\text{m}$ aluminum particles, initially extending from outside the charge radius till $r = 8.68 \text{ cm}$ is undertaken with $t_b = 2 \text{ msec}$ [190]. During the early stages of the explosion, as aforementioned, Rayleigh-Taylor [192] hydrodynamic structures grow as bubbles and spikes, on either sides of the contact surface. This is illustrated in Fig. 49 by presenting the CO mass fraction colored by the local gas density, showing the bubbles in (a) and the spikes in (b). Due to shear and baroclinic effects, vortex rings exist around these structures. Small particles, upon dispersion, interact with these vortex rings in the mixing layer, causing them to also disperse in the transverse direction, and the focus here is to demonstrate and elucidate these phenomena. Since small

particles respond faster to the vortex rings in the mixing layer, unlike their larger counterparts, they have different dispersion characteristics and these differences will now be discussed. It is emphasized that for the remainder of this study, the times are non-dimensionalized using t_o , the time required for detonation completion within the initial charge. As pointed out in Section 1.2.2, explosives are generally scaled using $W^{1/3}$, where W represents the mass of the explosive in the initial charge [12]. Since $W \sim r_o^3$, where r_o denotes the initial charge radius, and $t_o = r_o/D$, where D represents the detonation velocity of the explosive used, the choice of using t_o to scale times is equivalent to the use of $W^{1/3}$. For a 5.9 cm radius TNT charge, the GISPA simulation (described in Appendix B) predicts $t_o = 8.25 \mu\text{sec}$, and this value is used to present the normalized time for the remainder of this analysis.

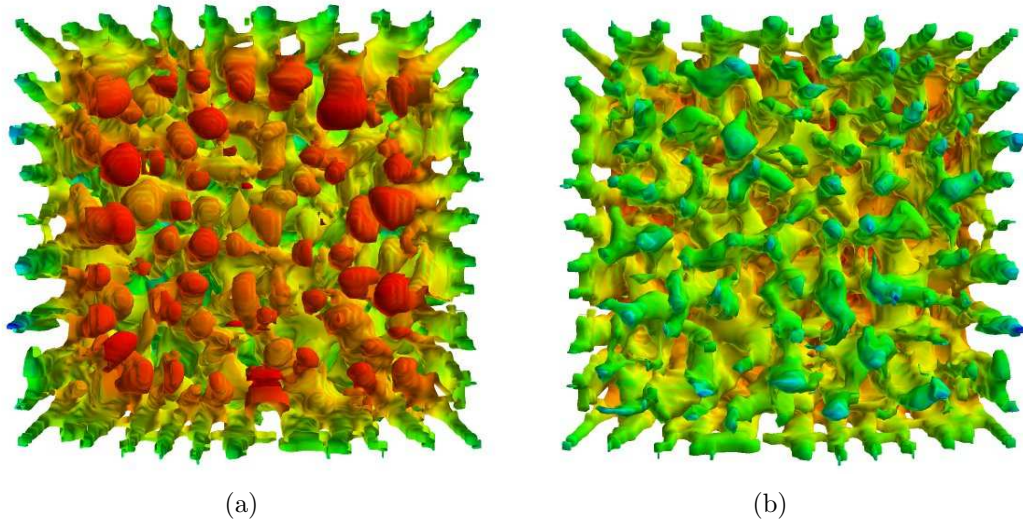


Figure 49: Rayleigh-Taylor hydrodynamic structures in the mixing layer: (a) bubbles; (b) spikes. Shown here are the iso-surfaces of the CO mass fraction, colored by the local gas density.

Vorticity in the mixing layer is primarily concentrated around the Rayleigh-Taylor structures, i.e., at the interface between the two fluids, due to shear and baroclinic effects. In regions between contiguous structures where the fluid is air only, and in the regions inside the structures where the fluid is only the detonation products, vorticity

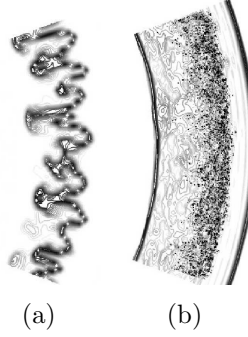


Figure 50: Interaction of the particle cloud with the hydrodynamic structures at $t/t_o \sim 35$: (a) CO_2 mass fraction; (b) $\log(\omega)$ contours and particle locations.

is not as significant. This gives rise to local regions with vorticity (at the tip of the hydrodynamic structures), and those without significant flow rotationality (regions between contiguous structures and inside the structures). The CO_2 mass fraction and vorticity (ω) contours are presented in Fig. 50, along with the particles (shown as black dots) at $t/t_o \sim 35$ —one of the time instants corresponding to the interaction of the particle cloud with the hydrodynamic structures; these profiles are zoomed near the interaction region and presented. The outer and inner bold lines in Fig. 50 (b) represent the primary and secondary shocks, respectively.

Vorticity is accumulated near the product regions, and particles invariably interact with this vorticity, causing them to cluster. The particle cloud is virtually unaffected in the vorticity-free regions, but is inevitably influenced in the regions dominated by the vortices; this, essentially, gives rise to the preferential accumulation (or concentration) of particles. The clustering of solid particles due to isotropic turbulence is well known [188]; however, in the problem under study, the clustering is owing to the interaction of the particle cloud with the hydrodynamic structures in the mixing layer. One main difference is that in isotropic turbulence, the vortices have no directional bias; consequently, no spatial bias for the particle clusters. However, in the present problem, the vortex rings exist only around the Rayleigh-Taylor structures which are spatially aligned along the radial direction. Hence, the clustering shapes

of the particles due to explosion are also spatially biased. For the current problem under study, it has also been verified that clustering of particles occurs even when the sub-grid turbulence model is turned off, i.e., the clustering is not a consequence of the sub-grid modeling aspects, but is physical.

6.2.3.1 Chronology of particle clustering

The chronological illustration of the particle clustering phenomena due to their interaction with the vortex rings is presented in Fig. 51 (the view presented is that as seen from the outermost plane of the sector looking inwards at the origin). At early times (Fig. 51 (a)), the expanding particle cloud is still completely engulfed into the detonation products, and no clustering effects are evident due to the absence of vorticity. Subsequently, particles start to disperse in vortex-dominated regions as they interact with the hydrodynamic structures (Fig. 51 (b)). Later, the dispersion is complete, and the particles are clustered by $t/t_o \sim 50$ (Fig. 51 (c)). The particle cloud front is also corrugated due to the local dispersion of the particles due to the vorticity in the hydrodynamic structures during the interaction event; note that this interaction event is not instantaneous, but lasts for a finite, albeit small period of time. After this, the particles leave the mixing layer, and enter vortex-free regions, thereby preserving their clustered shape, i.e., the hydrodynamic ‘foot print’ (Fig. 51 (e)).

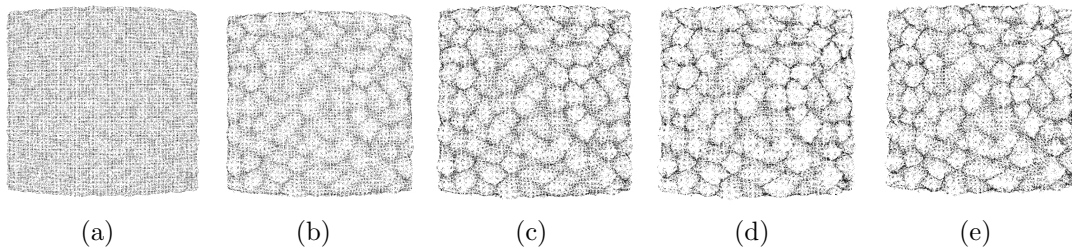


Figure 51: Clustering of particle cloud at times t/t_o (a) 20; (b) 35; (c) 50; (d) 90; (e) 560. The scales of the figures have been adjusted for better clarity.

The dispersion characteristics of particles and the formation of clusters when particle clouds interact with fluid structures is dictated by the Stokes number, St , which is the ratio of the particle’s momentum response time to the flow field time scale, and is given by the expression:

$$St = \frac{\rho_p d_p^2 / 18\mu}{L_o / U_o}, \quad (183)$$

where ρ_p is the particle material density, d_p is the particle diameter, μ is the viscosity of the gas, and L_o and U_o denote, respectively, the flow length and velocity scales (here, L_o can represent the vortex diameter and U_o , the transverse gas velocity in the vortex ring). In previous studies, different dispersion characteristics for different St have been reported [42, 43, 130]. While particles with small St tend to follow the flow, particles with St of the order of unity tend to accumulate near the circumference of fluid structures [130]. Particles with large St , on the other hand, tend to accumulate near the regions of low vorticity and high strain [130]. The clustering patterns observed in Fig. 51 are reminiscent of those presented in [130] (see for instance Fig. 19 of this ref.), where the authors study the particle dispersion characteristics in a three-dimensional temporal mixing layer using direct numerical simulations. In the current study, analysis shows St of the order of unity for the $r_p=5 \mu\text{m}$ particles (which are $r_p=2.5\text{-}3 \mu\text{m}$ during their interaction with the Rayleigh-Taylor structures); and St of the order of 10 for $r_p=10 \mu\text{m}$ particles (which are $r_p=8\text{-}8.5 \mu\text{m}$ during their interaction with the Rayleigh-Taylor structures). Furthermore, the particles are also travelling at speeds in excess of 1 Km/s in the radial direction, and so the time they have to interact with the hydrodynamic structures is limited, indicating that in addition to the particle response time scale, the residence time—time a particle takes to traverse the hydrodynamic structures—is also of significance.

6.2.3.2 Parameters that affect particle clustering

- Particle mass loading ratio

To investigate the effect of mass loading ratio, $\eta=2$ is also considered for the same particle radius ($5 \mu\text{m}$) and initial radial extent of the particle cloud distribution (radial location 5.9-8.68 cm). Recall from earlier in this chapter, more mixing in the gaseous detonation products when the initial particle loading ratio is higher; specifically, the mixing layer width is wider and, consequently, more of the detonation product fuel is consumed, i.e., more afterburn when the initial outer particle cloud mass loading ratio is higher. Note that this enhanced mixing is due to more perturbations introduced to the contact surface during the first interaction event between the particles and the contact surface. These enhanced perturbations later result in stronger/larger vortex rings around the Rayleigh-Taylor structures for the $\eta=2$ case than for $\eta=1$. Consequently, the interaction of the particle cloud with these structures, i.e., the second interaction, is also more prominent when the initial particle loading ratio is higher.

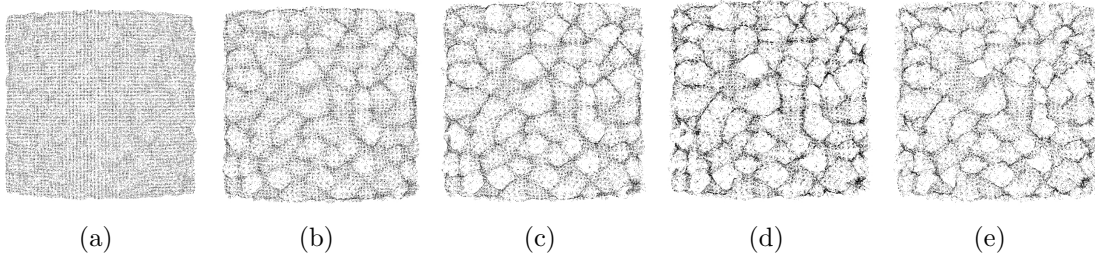


Figure 52: Effect of η on clustering of particle cloud ($\eta=2$): times t/t_o (a) 20; (b) 35; (c) 50; (d) 90; (e) 560. The scales of the figures have been adjusted for better clarity.

The clustering process is chronologically presented in Fig. 52 for $\eta=2$; closer observation reveals, *prima facie*, that due to this larger vortex rings for $\eta=2$, many clusters, albeit not all, appear larger due to more dispersion for $\eta=2$ —a direct consequence of the stronger vortex rings in the ensuing Rayleigh-Taylor structures. Moreover, some

clusters in Fig. 52 appear as a combination of two partial clusters. This formation is owing to the particle cloud having earlier interacted with two merging hydrodynamic structures; recall from Section 1.2.4, the bubble competition process prevalent in the mixing layer that can result in contiguous hydrodynamic structures to interact. Thus, when the particle cloud interacts with two competing hydrodynamic structures, it disperses locally corresponding to this ‘merging shape’, and this shape is preserved even at later times (Fig. 52 (e)). Since $\eta=2$ (Fig. 52) results in more merging shapes of the particle cloud than $\eta=1$ (Fig. 51), it is believed that bubble competition is more significant for $\eta=2$ —due to more perturbations introduced on the contact surface during the first interaction event by the higher loading particle cloud.

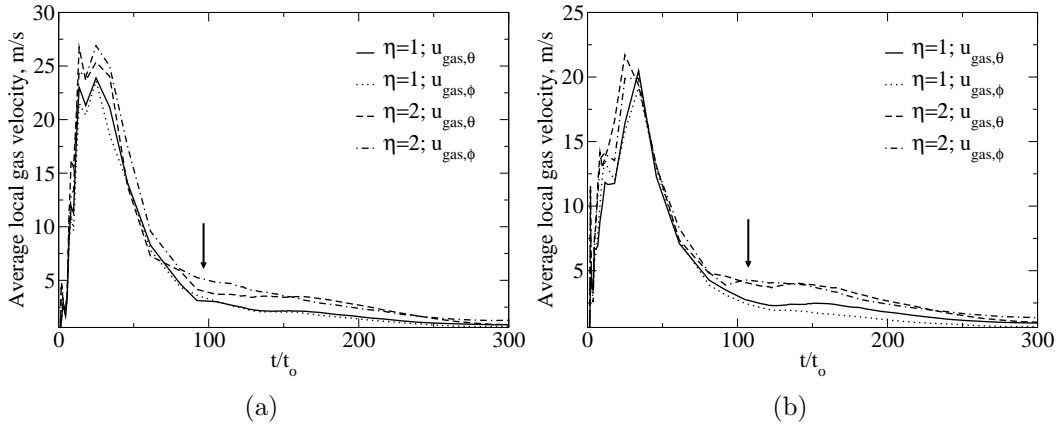


Figure 53: Effect of η on the average local gas velocity seen by the particles for particle group (a) C60; (b) C80.

For a better understanding of the actual clustering process, it is of interest to track the local transverse gas velocities as ‘seen’ by different particles as they disperse. To this end, four groups of particles based on their initial locations in the cloud are considered, and denoted as C60, a collection of 100 randomly chosen particles initially located at radial location $r = (6.0 \pm 0.1)$ cm; as C70, a collection of 100 randomly chosen particles initially located at radial location $r = (7.0 \pm 0.1)$ cm; similarly, C80 corresponding to $r = (8.0 \pm 0.1)$ cm; and C86 corresponding to $r = (8.6 \pm 0.1)$ cm.

Of particular interest here is the average local gas velocity as ‘seen’ by the particles corresponding to each group. Note that for the averaging, absolute values are used, i.e., $|u_{gas,\theta}|$ & $|u_{gas,\phi}|$, so that two particles at diametrically opposite ends of a vortex ring, which ‘see’ local gas velocities equal in magnitude, but opposite in direction, do not cancel out in the averaging.

For the cases corresponding to $r_p=5 \mu\text{m}$, initial cloud extending radially from $r=5.9\text{-}8.68 \text{ cm}$, and $\eta= 1$ & 2 , Fig. 53 presents the average local gas velocity as seen by the particles corresponding to the groups *C60* (Fig. 53 (a)) and *C80* (Fig. 53 (b)) (similar results also hold for *C70* and *C86*, not shown here for brevity). At very early times, the local azimuthal ($u_{gas,\theta}$) and zenith ($u_{gas,\phi}$) velocity components are almost negligible, but rise up fast as the particles pick up momentum from the gas and are set into motion. Around $t/t_o \sim 20$, the particles start to interact with the vortex rings around the hydrodynamic structures, as evident from the peaks in Fig. 53 (a) & (b). Around $t/t_o \sim 30$, the transverse local gas velocities are to the tune of $\sim 20 \text{ m/s}$ —this creates significant enough transverse velocities that clusters the particles around the hydrodynamic structures. Comparing the two different η cases, as evident from Fig. 53, the local average gas transverse velocity components are slightly higher for the $\eta=2$ case during the peak of the second interaction ($t/t_o \sim 30$). Subsequently, the average local azimuthal and zenith gas velocities as seen by the particles are also higher, by a factor of $1.5 - 2$ near the region indicated by the arrow. This sustained higher transverse velocities in the gas for $\eta=2$ results in the slightly more pronounced clustering observed for the higher loading ratio in Fig. 52.

- Particle size and initial distribution

Both 5 and $10 \mu\text{m}$ particle clouds are considered in this study, with $\eta=1$, and the initial cloud extending from outside the charge ($r = 5.9 \text{ cm}$) till $r = 8.68 \text{ cm}$, to illustrate the significance of particle size on the clustering phenomenon. Analysis

shows that the 10 μm radius particles do not form clusters for the chosen conditions, as their ignition is delayed *vis-à-vis* the 5 μm radius particles, due to which the particles are still sufficiently large ($\sim 8\text{-}8.5$ μm radius) during the second interaction event with the hydrodynamic structures. On the other hand, the particles in the 5 μm cloud have already ignited during their engulfment into the detonation products, and are about 2.5-3 μm in radius during the second interaction event. The inter-phase momentum transfer time scales as r_p^2 , where r_p denotes the particle radius; i.e., larger particles take longer to be influenced by the flow. Hence, the particles corresponding to the 10 μm cloud, by virtue of their higher inertia during the second interaction event, are not easily dispersed by the hydrodynamic vortex rings; consequently, the 10 μm particle cloud does not form clusters upon their explosive dispersal for the chosen conditions ($\eta=1$; initial cloud width = 5.9-8.68 cm, etc.). Due to this subdued dispersion of the cloud, even the width of the 10 μm particle cloud is nearly preserved with time, not shown here for brevity.

By considering 10 μm radius particle clouds of the same mass loading ratio ($\eta=1$), but an initial distribution extending from radial location $r=5.9\text{-}12$ cm, significant differences are observed; in Fig. 54, the particle cloud at different times for this case are presented. Comparing this with the aforementioned case with the 5 μm radius particles (Fig. 51), it is evident that although clusters form for the 10 μm radius particle cloud when initially distributed from $r=5.9\text{-}12$ cm, they are much fewer in number and are not prominently visible, i.e., they are more or less degenerate clusters. Furthermore, the clusters are relatively ‘diffuse’ in the sense that the regions of higher particle concentration only gradually change to regions of lower concentration *vis-à-vis* the sharp particle concentration gradients observed for the 5 μm particle radius (Fig. 51). Thus, although more particles (and more mass) are now present for the 10 μm cloud extending initially from 5.9 to 12 cm than the 5 μm cloud extending initially from 5.9 to 8.68 cm, both corresponding to $\eta=1$, the particle clustering effect

is more significant for the latter, due to the shorter momentum transfer time scales during their interaction with the hydrodynamic structures. Hence, the particle size during the second interaction event is critical to the cluster formation.

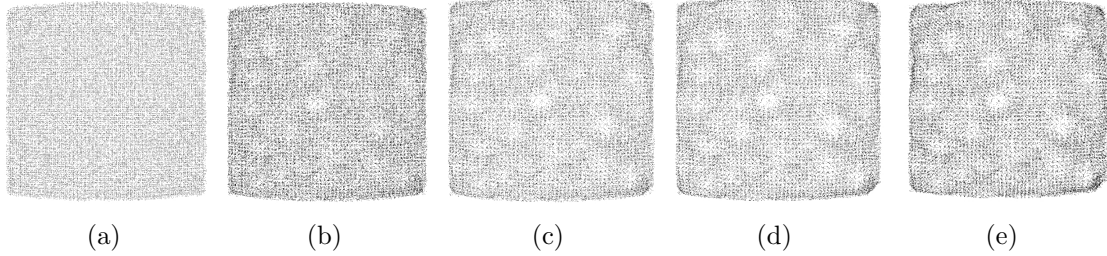


Figure 54: Effect of particle size on clustering of particle cloud ($r_p=10 \mu\text{m}$; initial cloud distribution: 5.9-12 cm; $\eta=1$): times t/t_o (a) 20; (b) 35; (c) 50; (d) 90; (e) 560. The scales of the figures have been adjusted for better clarity.

To illustrate the effect of the local gas velocity in support of the observations made in Fig. 54, the average local gas azimuthal ($u_{gas,\theta}$) and zenith ($u_{gas,\phi}$) velocities as seen by the particle groups $C60$ and $C80$ are presented in Fig. 55 for $r_p=10 \mu\text{m}$, $\eta=1$, and the initial particle cloud extending radially from (1) $r=5.9-8.68 \text{ cm}$ and (2) $r=5.9-12 \text{ cm}$ (the definitions of $C60$ and $C80$ are the same as described previously). As evident from Fig. 55, the average local azimuthal and zenith gas velocities as seen by the particles are higher, when the initial cloud width is wider and, consequently, the clustering is more pronounced. More particles are available to perturb the flow, and the total perturbation time on the contact surface by the particles during the first interaction event is longer for a wider initial cloud width; hence, significantly higher transverse velocities are seen by the particles as they disperse outwards. These differences in the local gas transverse velocities result in the clustering observed for $r_p=10 \mu\text{m}$ when the particles initially extend radially till 12 cm (Fig. 54), but no clustering is observed when initially extending till 8.68 cm. This result could not be verified for $r_p=5 \mu\text{m}$ extending till 12 cm, as this setup requires too many particles to be tracked, stretching computational memory requirements.

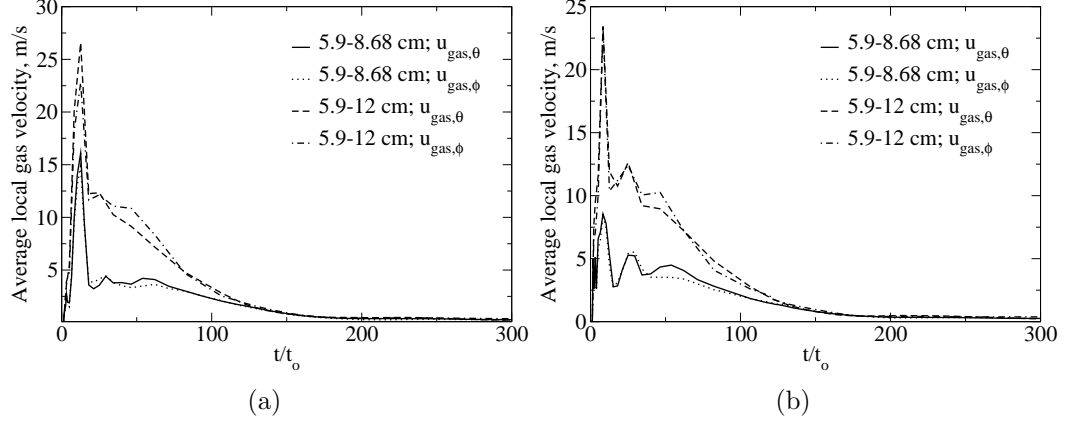


Figure 55: Effect of initial cloud width on the average local gas velocity seen by the particles for particle group (a) *C60*; (b) *C80*.

6.2.3.3 *Mixing layer boundaries and width*

Also of interest for the small particle regime is the quantification of the dynamics of the mixing layer, so as to shed light on the mixing process between the inner detonation products and the outer air. To this end, the mixing layer (*ML*) boundaries are defined based on the mass fraction of *CO*, as also done earlier. The inner and outer boundaries of the *ML* are presented in Fig. 56 (a) for the 5 and 10 μm particle radius cases, corresponding to $\eta=1$, and the initial cloud extending from $r=5.9\text{-}8.68$ cm. The afterburn energy release can also play a central role in the dynamics of the *ML* as this inevitably results in volumetric expansion of the gas in the *ML*; to investigate its significance, another case is considered with 5 μm particle radius, but with the afterburn (of both the detonation products as well as the evaporated aluminum) fictitiously turned off—referred to simply as ‘no afterburn.’ As evident from Fig. 56 (a), the implosion phase ($t/t_0 \sim 125$) is delayed by about $t/t_0 \sim 50$ with the afterburn turned off. Furthermore, the inner and outer boundaries stretch farther outwards without this afterburn during the implosion phase: the outer boundary due to absence of *CO* consumption; the inner boundary due to a weaker secondary shock—a consequence of unavailability of the excess energy. In addition, the weaker

secondary shock also results in a subdued reshock phase ($t/t_o \sim 300$ in Fig. 56 (a)) for the no afterburn case in terms of the distance traversed by the lower boundary of the ML around this time (it traverses from $r/r_o = 5$ to $r/r_o = 9$ with the afterburn energy release on; $r/r_o = 7$ to $r/r_o = 8$, otherwise). At sufficiently late times ($t/t_o \sim 500$), the outer boundary stretches farther outside for the realistic cases than the no afterburn case, for the same reason. Thus, the afterburn exothermic energy release plays a critical role in the dynamics of the ML .

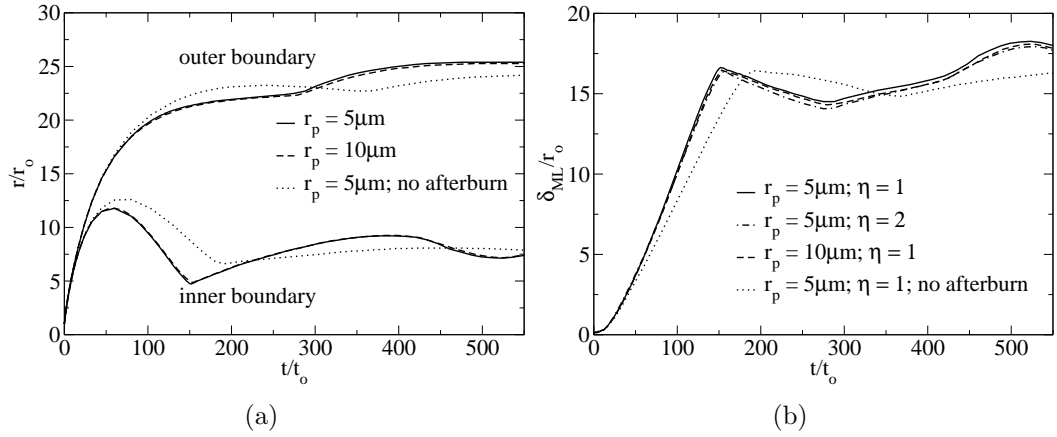


Figure 56: Growth of the mixing layer: (a) outer and inner boundaries of the mixing layer; (b) mixing layer width (δ_{ML}). Both variables are normalized with the initial charge radius, r_o .

In Fig. 56 (b), the ML width (δ_{ML}) for the different cases are presented, normalized with the charge radius, r_o , with the initial cloud extending from $r=5.9$ - 8.68 cm. Here, δ_{ML} is the spatial difference between the outer and inner boundaries of the ML . As evident, δ_{ML} grows slower during the implosion ($t/t_o \sim 125$) without the afterburn energy, due to the delayed and subdued implosion phase (Fig. 56 (a)). During the asymptotic phase ($t/t_o \sim 500$), clearly the afterburning energy release expands the gases in the ML radially further, i.e., the fireball is bigger with the excess energy release, exemplifying the role played by volumetric expansion of the gas in the ML .

6.2.3.4 Particle cloud boundaries and width

An investigation of the boundaries and the width of the particle cloud as it disperses is of interest to understand the exact dispersion process subsequent to the detonation. Since the particle cloud leading (LE) and trailing edges (TE) are corrugated due to clustering effects, it is essential to define the LE and TE of the cloud to investigate their dispersion process. Here, LE ($r_{98\%}$) and TE ($r_{2\%}$) of the particle cloud are defined as the radial location corresponding to which 98% and 2%, respectively, of the total number of particles are contained. Note that this definition is rather *ad hoc*, and is used only to illustrate the dispersion process. Here, the particle cloud width is defined as:

$$\delta_{cloud} = r_{98\%} - r_{2\%}. \quad (184)$$

In Fig. 57 (a), the LE and TE of the cloud are presented for the 5 μm particle radius clouds considered hitherto, normalized with the initial charge radius (r_o). Also shown here are the results corresponding to $t_b=1$ msec, which is close to recent shock tube data [137] for a similar particle size. Five discernable phases of interest are identified in the particle dispersion process: (1) engulfment phase; (2) hydrodynamic instability-interaction phase; (3) first vortex-free dispersion phase; (4) reshock phase; and (5) second vortex-free dispersion phase. As aforementioned, at early times, the particles are engulfed into the detonation products—refer to this phase as the “engulfment phase.” Subsequently, the particles are readily set into motion, and interact with the hydrodynamic instabilities/structures in the *ML*—refer to this phase as the “hydrodynamic instability-interaction phase”; note that this second phase could essentially be also referred to as the “mixing layer phase,” as the particles traverse the *ML* during this time interval. This is the phase where the clustering of particles occurs, owing to the presence of vortex rings in the hydrodynamic instabilities in the *ML*. Then, the particles leave the *ML* and penetrate into the vortex-free outer

region of air. Here, the momentum picked up earlier drives the dispersion and, later the particles slow down; the dispersion during this phase is essentially radial, i.e., free of any significant three-dimensional phenomena like hydrodynamic instabilities, vortices, etc.—hence the name “first vortex-free dispersion phase.” This third phase lasts for a longer time than the earlier two phases.

Subsequently, the secondary shock (SS) penetrates into the particle cloud, compressing it from the inside, as evident from the slight outward acceleration of the TE around $t/t_o \sim 325$. Refer to this phase as the “reshock phase”—not to be confused with the reshock phase pertinent to the gas as well. Observations show that since the reshock phase for the particles occurs outside the ML , baroclinic effects are not significant for the particle reshock phase—note that this is not true for the gas reshock phase. Lastly, after the SS leaves the particle cloud, the LE and TE further disperse radially outwards, preserving their cluster ‘foot print’—refer to this phase as the “second vortex-free dispersion phase.”

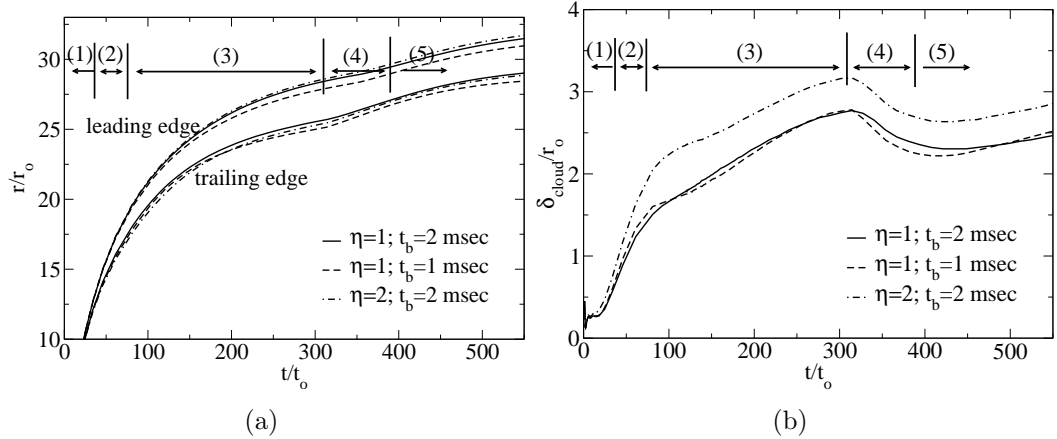


Figure 57: Different phases in the dispersion of the particle cloud: (a) leading and trailing edges of the particle cloud; (b) cloud width. The phases are denoted by (1) engulfment phase; (2) hydrodynamic instability-interaction phase; (3) first vortex-free dispersion phase; (4) reshock phase; and (5) second vortex-free dispersion phase.

In Fig. 57 (b), the cloud width (δ_{cloud}), normalized with the initial charge radius (r_o), is plotted with time, demonstrating the five different phases; three cases based

on η and t_b are presented, self-explanatory by the legend in Fig. 57 (b). As evident, the cloud width grows faster during the hydrodynamic instability-interaction phase *vis-à-vis* the first vortex-free dispersion phase. During the particle reshock phase, δ_{cloud} decreases by about $\frac{1}{2}r_o$ and, subsequently, continues to slowly grow during the second vortex-free dispersion phase, owing to the LE being slightly faster than the TE. Also evident from Fig. 57 (b) is the near-similarity of δ_{cloud} for $\eta=1$ with different t_b , showing independence to the choice of the two different burn times (t_b) used. For $\eta=2$, δ_{cloud} is about $\frac{1}{2}r_o$ greater than for $\eta=1$, and the differences between the two different η s starts to occur even at early times, showing that the concomitant enhanced mixing for a higher η leads to a wider cloud. Hence, the strength of the vortex rings during the hydrodynamic instability-interaction phase plays a critical role in the later time cloud width. Furthermore, starting from the first vortex-free dispersion phase and thereafter, δ_{cloud} for the different η s maintains a more or less uniform difference ($\sim \frac{1}{2}r_o$), showing self-similar behavior.

6.2.3.5 *Scaling laws*

Scaling laws are widely used to model explosives—see the introduction section in [13]. They have also been used to model explosive ML boundaries obtained from computational simulations [13, 120]. Of interest is the variation of the ML width with time, so that the hydrodynamic growth rate of the Rayleigh-Taylor structures can be compared for different parametric test cases. Scaling laws for particle cloud dispersion can also be useful for comparing the cloud dispersion behavior. Stated in these terms, scaling laws for the width of the ML of the explosive fireball are now focused upon, as well as that of the particle cloud (δ_{cloud}). Specifically, consider the ML width (δ_{ML}) for the early blast wave and implosion phases; for the particle phases, scale δ_{cloud} for the hydrodynamic instability-interaction and the first vortex-free dispersion phases. These are modeled using power law curve fits as $\delta_{ML}/r_o = a_{ML} t^m$ and

Table 7: Scaling laws for the mixing layer (δ_{ML}/r_o) and particle cloud (δ_{cloud}/r_o) widths.

η	Phase	a_{ML}	m	a_{cloud}	n
1	blast wave	6.31	1.172		
	implosion	13.07	1.346		
	hydrodynamic instability-interaction			3.315	1.395
	first vortex-free dispersion			1.799	0.487
2	blast wave	6.552	1.171		
	implosion	12.743	1.315		
	hydrodynamic instability-interaction			3.687	1.259
	first vortex-free dispersion			2.33	0.326

$\delta_{cloud}/r_o = a_{cloud}t^n$, respectively, where r_o denotes the initial charge radius. The coefficients obtained from the power law curve fits are summarized in Table 7 (t in msec).

As evident from Table 7, the hydrodynamic structures in the ML grow close to linear ($m \sim 1.17$) during the initial blast wave phase. Past studies [13, 120] have demonstrated linearity during the early blast wave phase, albeit for single-phase explosive charges with an initial perturbation added near the outer periphery of the charge. It is believed that the slight departure from linearity for the current scenario is owing to the continuous nature of the perturbation, i.e., the finite albeit small time span of early interaction of the contact surface with the particle cloud. Thereafter, the growth becomes non-linear ($m \sim 1.31 - 1.35$) during the implosion phase, as the inner boundary of the ML is dragged inwards by the imploding secondary shock. For the particle cloud, the power law index (n) shows a slightly more pronounced dependence on the mass loading ratio (η). Whereas the index $n \sim 1.4$ for $\eta=1$, it is ~ 1.26 for $\eta=2$ during the hydrodynamic instability-interaction phase. Subsequently, during the first vortex-free dispersion phase, the index $n \sim 0.49$ for $\eta=1$, and ~ 0.33 for $\eta=2$. The decrease in the power index n between the two phases is due to the slowing down of the particles outside the ML in the first vortex-free dispersion phase

due to aerodynamic drag.

6.2.3.6 Afterburn of the detonation products

The afterburn of the detonation products is prominent in the *ML*, where they mix with the outer air and form products. The mass of $C(S)$ remaining in the charge, normalized with the initial charge mass, is presented in Fig. 58 for four different cases, self-explanatory from the legend. The $C(S)$ mass fraction decreases rapidly at early times, as it comes in contact with the outer air for the first time; subsequently, the afterburn products (not to be confused with the detonation products) blanket out the inner detonation products and the outer air, and thus the sustenance of burning is limited to where the inner detonation products mix and react with the outer air, which is controlled by vorticity [15, 120, 121].

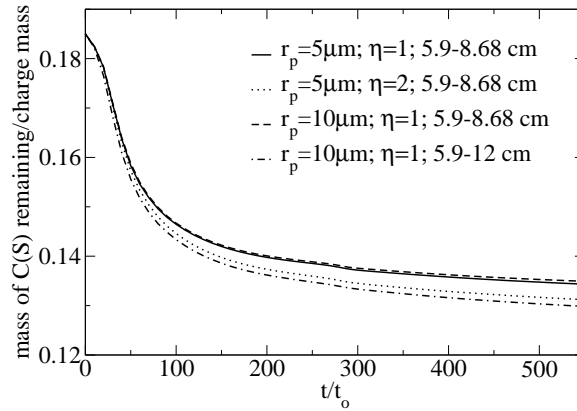


Figure 58: Carbon mass remaining with time, normalized with the initial charge mass.

While Fig. 58 is useful to estimate the carbon mass remaining with time, also of interest is the rate of carbon mass remaining with time, for this illustrates the consumption rate of the fuel. To this end, the rate of mass of carbon remaining, normalized with the initial charge mass, is presented in Fig. 59 for four cases considered hitherto, self-evident from the legend in Fig. 59. As evident, the carbon consumption rates are sufficiently fast at early times ($t/t_0 \sim 30$) as the detonation products and

the air interact for the first time. Subsequently, the afterburn products blanket the inner detonation products and the outer air, thereby subduing the mixing between them—this decreases the carbon consumption rates. Later, during the reshock phase ($t/t_o \sim 275$), the carbon consumption rates are locally enhanced owing to the enhanced mixing rates during the reshock phase—a consequence of the baroclinically generated vorticity. Upon close observation, the carbon consumption rates are nearly similar in time for $r_p=5$ and $10 \mu\text{m}$, showing near-independence to particle size. Also evident at early times is the higher carbon consumption rate for a wider initial particle cloud distribution, i.e., 5.9-12 cm versus 5.9-8.68 cm. These results conform to the observations made earlier for the larger particle regime as well.

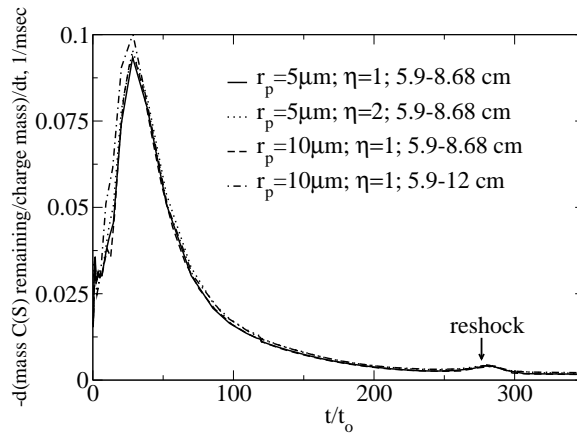


Figure 59: Rate of carbon mass remaining with time.

The afterburn of the detonation products and air is mixing-controlled, and how soon they mix is critical to the afterburn rates encountered. Thus, of preponderant interest here is to quantify the mixing process and investigate its variation with time. To this end, define the quantity, “degree of mixedness,” denoted DM hereafter, similar to the definitions used elsewhere [150, 151], albeit for a binary and non-reacting system in these references. Specifically, define DM as follows:

$$DM = \frac{\left[\frac{\int Y_{CO} (Y_{N_2} - Y_{N_2}^i) dV}{\int dV} \right]}{\left[\frac{\int Y_{CO} dV}{\int dV} \right] \left[\frac{\int (Y_{N_2} - Y_{N_2}^i) dV}{\int dV} \right]}, \quad (185)$$

where Y_{CO} and Y_{N_2} denote the instantaneous mass fractions of CO and N_2 , respectively, and $Y_{N_2}^i$ is the mass fraction of N_2 in the detonation products at the onset of detonation completion, obtained from the chemical balanced equation. Note that the quantity $Y_{N_2} - Y_{N_2}^i$ is used instead of Y_{N_2} , as N_2 is present on both sides of the contact surface (more on the side of the air), and this difference represents only the “excess N_2 ” that belongs to the side of the air. Stated in these terms, the quantity DM will start from zero initially, as the inner CO and the excess N_2 are not yet mixed, and the quantity will increase as they mix subsequently. In Fig. 60 (a), the DM is studied for $r_p=5 \mu\text{m}$, and the initial cloud extending from $r=5.9\text{-}8.68 \text{ cm}$, for $\eta=1$ and $\eta=2$. From Fig. 60 (a), at early times, DM rapidly rises from zero to 0.03 as the species begin to mix. Subsequently, DM slightly decreases near $t/t_o \sim 12$, as the CO is consumed. Then, DM rises again during the implosion phase until about $t/t_o \sim 180$; DM is slightly greater for $\eta=2$ than for $\eta=1$, as more perturbations associated with the higher η result in enhanced hydrodynamic structures induced mixing. DM decreases during the reshock phase as the ML is compressed and, subsequently, increases again during the asymptotic phase at late times as the vorticity deposited in the ML during the reshock sustains the subsequent mixing process. Consequently, DM continues to be superior for the higher η . In Fig. 60 (b), the dependence of DM on particle size and initial width of the cloud are studied—the legend is self-explanatory. Whereas DM is independent of particle size (for $r_p=5$ and $10 \mu\text{m}$), a wider initial cloud width ($r=5.9\text{-}12 \text{ cm}$) results in a superior DM .

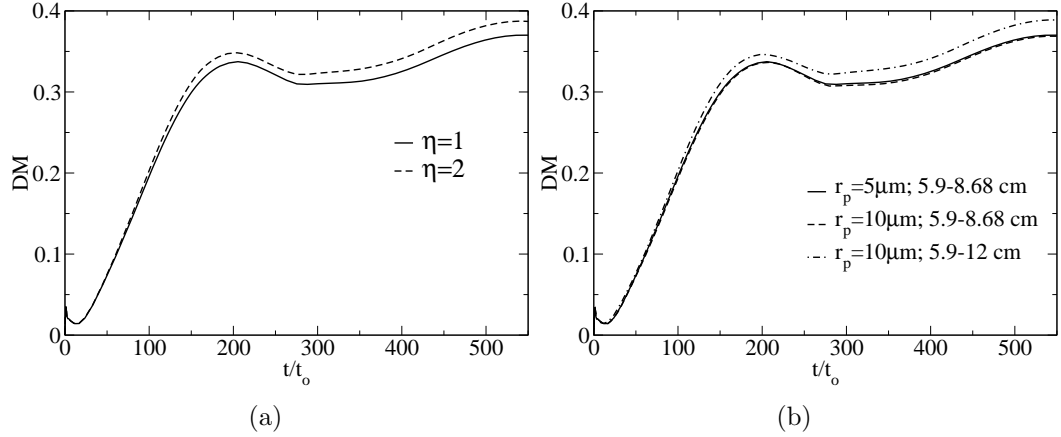


Figure 60: Degree of mixedness (DM): (a) effect of η ; (b) effect of r_p and initial cloud width.

6.2.3.7 Boundaries of aluminum combustion products

Observations show that aluminum particles, owing to their ignition during their engulfment into the detonation products, initially start to burn anaerobically; later, as the leading edge of the particle cloud enters the mixing layer, both aerobic and anaerobic burning concurrently occur; later, after all the particles leave the mixing layer, burning is strictly aerobic; subsequently, the particles quench. This transition between anaerobic to aerobic occurs gradually, and thus the different products of aluminum combustion exist in varying concentrations at different locations. Consequently, the oxides of aluminum (AlO and $Al_2O_3(L)$) exist in an annular region, similar to the aforementioned ML , i.e., they have radial inner and outer boundaries; it is also of interest to investigate the motion of the exact region of this annular region where they exist. To study the region of existence of the aluminum oxides, and their convection with time, the boundaries of the aluminum oxides layer are presented in Fig. 61: inner boundary in Fig. 61 (a) and outer boundary in Fig. 61 (b). Here, define the inner boundary of the aluminum oxide layer as the radial location where the azimuthally averaged mass fraction of AlO or $Al_2O_3(L)$, as the case may be,

transitions from zero to 5% of the instantaneous maximum of the azimuthally averaged mass fraction of the respective aluminum oxide. Likewise, the outer boundary is defined as where the transition is reversed, i.e., from 5% to zero of the respective aluminum oxidizer. Note that this definition is rather *ad hoc*, but does serve useful to portray a qualitative picture of the aluminum oxide layer. Furthermore, note that the region corresponding to AlO will be different from that of $Al_2O_3(L)$. Here, consider the 5 and 10 μm particle radius, with $\eta=1$, and the initial cloud extending from $r=5.9\text{-}8.68$ cm. The radius r (y -axis) is normalized with the initial charge radius, r_o . The profiles of AlO and $Al_2O_3(L)$ region boundaries, from Figs. 61 (a) & (b), look similar qualitatively as the detonation products-air ML presented earlier.

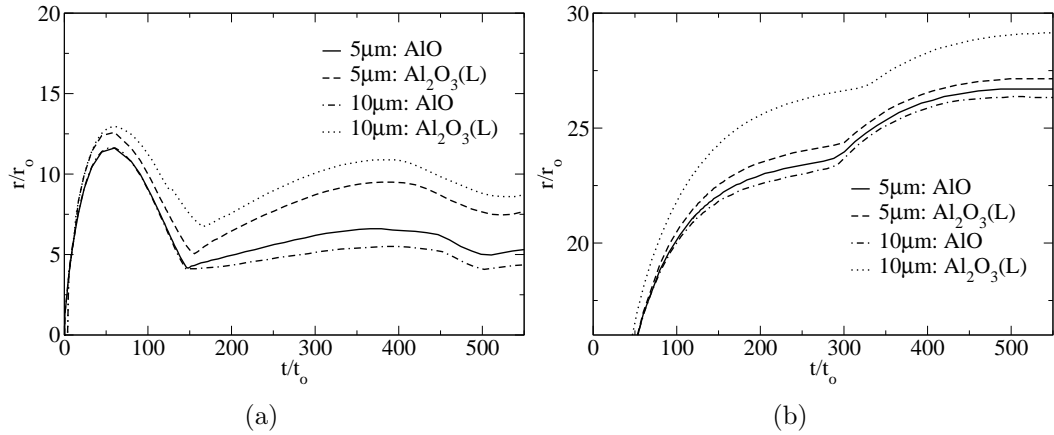


Figure 61: Boundaries of region of aluminum oxides (AlO , $Al_2O_3(L)$): (a) inner boundary; (b) outer boundary. Radius r is normalized with the initial charge radius, r_o .

As evident from Fig. 61 (a), while the inner boundary of the AlO region is radially inside by $\sim 1.5r_o$ for the 10 μm size, it is outside by approximately the same distance for $Al_2O_3(L)$. Since the 10 μm radius particles have a higher inertia than the 5 μm particles, they spend a longer time engulfed into the detonation products. Consequently, when they ignite and burn, anaerobically to begin with, the AlO inner boundary is thus inside for the 10 μm radius particles. Due to the same reason, the 10 μm radius particles take a slightly longer time to reach the ML —the region where

aerobic burning first occurs for the aluminum combustion; consequently, the inner boundary of the $Al_2O_3(L)$ region is also radially outside for the 10 μm particles. Note that once the particles pick up significant amounts of momentum from the gas they are set into motion, and will overtake the aluminum that was evaporated from them at earlier times by virtue of their higher inertia. Observing Fig. 61 (b), whereas the outer boundary of the AlO region is only marginally inside for the 10 μm radius particles, it is significantly outside ($\sim 2r_o$) for the outer boundary of the $Al_2O_3(L)$ region. Thus, for both aluminum oxides, the trends in the inner and outer boundaries conform to the fact that aluminum burning transitions smoothly (in time) from anaerobic to aerobic burning, irrespective of particle size.

6.2.3.8 *Preferential particle combustion*

After the particles ignite during their early engulfment into the detonation products, their sustenance of burning depends on the clustering aspects. The vortex rings around the hydrodynamic structures bring into contact the inner detonation products and the outer air, and thereby sustains the afterburn of the detonation products. Thus, the local gas in the vortex rings are significantly hotter than the vortex-free regions, and so the particles that disperse through these vortex rings pick up more heat than their counterparts that do not. Consequently, preferential combustion of aluminum occurs, with the particles that pass through these vortex rings burning more.

To illustrate this preferential combustion/burning of particles, Fig. 62 presents the particle temperature (Figs. 62 (a) & (b)) and radius (Figs. 62 (c) & (d)) at times $t/t_o \sim 25$ (Figs. 62 (a) & (c)) and $t/t_o \sim 120$ (Figs. 62 (b) & (d)). From Figs. 62 (a), significant particle temperature gradients exist during this burning phase, as evident from the transitions between the red and green regions; this corresponds to the $t/t_o \sim 25$ time instant, when the particles are interacting with the hydrodynamic structures

in the ML —where afterburn occurs in regions dictated by where the inner detonation products and the outer air mix. At $t/t_o \sim 120$ (Fig. 62 (b)), the particles have quenched, but temperature gradients still persist; however, note that after quenching, the range of particle temperatures has narrowed down *vis-à-vis* that during the earlier burning phase. Comparing the particle radii at these times (Figs. 62 (c) & (d)), it is evident that the particles are relatively smaller in the regions where they are hotter, obviously due to the availability of heat from the afterburning regions of the ML . Thus, the burning characteristics of the aluminum particles are mixing-controlled, which is dictated by hydrodynamic instabilities; hence, hydrodynamic instabilities inevitably play a role in the burning of the aluminum particles.

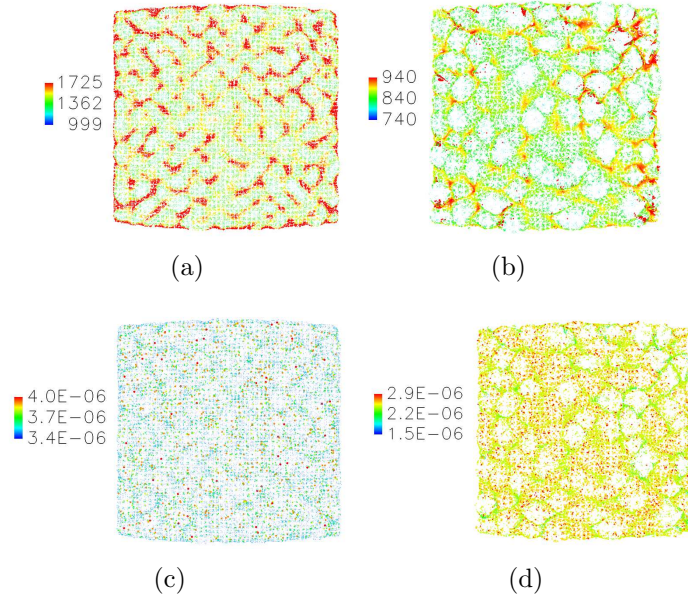


Figure 62: Preferential combustion of aluminum particles: particle temperature ((a) & (b)) and radius ((c) & (d)) at times $t/t_o \sim 25$ ((a) & (c)) and $t/t_o \sim 120$ ((b) & (d)). Temperature is in *Kelvin*, and radius is in *m*. The scales of the figures have been adjusted for better clarity.

6.2.4 Theoretical hydrodynamic considerations

The growth of hydrodynamic instabilities in classical gravity-driven fluid interfaces as well as blast wave driven systems alike, has been studied in the past using many

theoretical models; among these, the Buoyancy-Drag (BD) model is common [56, 152, 158]. In the BD model, the “rise” of bubbles is modeled accounting for buoyancy, drag, and decompression effects. The bubble amplitude (h) is obtained as [152]

$$\frac{d}{dt} \frac{dh(t)}{dt} = \tilde{A}g(t) - \frac{\tilde{C}}{\lambda} u_{inst}(t)^2 + \frac{d}{dt} \omega(t)h(t), \quad (186)$$

where \tilde{A} denotes the post-shock modified Atwood number $\tilde{A} = A(1 + \eta^*)/(C_a + \eta^*)$, where A is the post-shock Atwood number given by $A = (1 - \eta^*)/(1 + \eta^*)$, η^* is the post-shock density ratio, and C_a is the added mass coefficient and equals 2 for 2D and 1 for 3D. Furthermore, $g(t)$ denotes the driving acceleration, and \tilde{C} is the modified drag coefficient, given by the expression $\tilde{C} = C/(C_a + \eta^*)$, with C being the drag coefficient and equals $3 * 2\pi$ for 2D and $\approx 1.22 * 2\pi$ for 3D [152]. In addition, λ represents the perturbation wavelength, u_{inst} is the instability velocity, and $\omega(t)$ is the radial velocity gradient evaluated at the instantaneous interface, given as $\omega(t) = [\frac{\partial u(r,t)}{\partial r}]_{r=r_i(t)}$. Following the approach outlined in [152], the bubble amplitude is obtained as

$$\frac{dh}{dt} = u_{inst}(t) + \omega(t)h(t), \quad (187)$$

where the second term accounts for decompression effects. Substituting this into Eqn. (186), the standard BD equation is obtained:

$$\frac{du_{inst}}{dt} = \tilde{A}g(t) - \frac{\tilde{C}}{\lambda} u_{inst}(t)^2. \quad (188)$$

In the current study, the BD analysis is carried out for the bubbles only, as it is expected that volumetric expansion effects due to chemical reactions, which is not accounted for in the present BD model, will be very significant for spikes as they are smaller (in terms of transverse length scale) than bubbles at the high Atwood numbers encountered in chemical explosions. An ensemble of 10 bubbles are considered from

the simulation corresponding to $r_p=5 \mu\text{m}$, $\eta=1$ case, and the instantaneous amplitude (h) and transverse scale (L) are tracked. The bubble amplitude is a measure of how much the bubble tip grows farther away from the 1D “unperturbed interface,” which is obtained from an additional single-phase, 1D unperturbed simulation. This 1D simulation is also used to evaluate the instantaneous interface radius ($r_i(t)$), $g(t)$ and $\omega(t)$ required for solving the BD equation (Eqn. (188)). Past studies using the BD model assume self-similar growth to obtain an amplitude dependent transverse length scale [149, 152]. In the current investigation, self-similarity is not tacitly assumed; rather, it is demonstrated using the BD model. Furthermore, transverse length scales from the 3D simulations are used as inputs to the BD model to estimate bubble amplitudes, which are then compared with the amplitudes obtained from the 3D simulations. First, the $L(t)$ for the bubble ensemble from the 3D simulations are used to compute $u_{inst}(t)$ from Eqn. (188), and from it $h(t)$ is evaluated using Eqn. (187). This analysis is performed using the initial amplitudes from $t/t_o \sim 12$ —approximately the time required for the contact surface to overtake the initial particle cloud—until $t/t_o \sim 160$ —the time when the secondary shock explodes into the mixing layer during the reshock phase.

Simulation results show that a range of length scales exist for the bubbles, presented in Figs. 63 (a)&(b), including some “runaway” [86] bubbles. Here, a “runaway” bubble is one which has grown significantly larger in size *vis-à-vis* its neighboring counterparts, and often tends to behave very differently than the other bubbles in the vicinity. A wide range of length scales exist for the bubbles, and this needs to be accounted for in the BD analysis. To this end, the ensemble of bubbles are classified into three branches—lower, middle and upper, and three $L(t)$ curve-fits are used for the current analysis (all length scales are normalized with the initial charge radius, r_o). Of preponderant interest here is the self-similarity of bubbles at late times, a topic of wide debate in recent literature for Rayleigh-Taylor instability growth, albeit

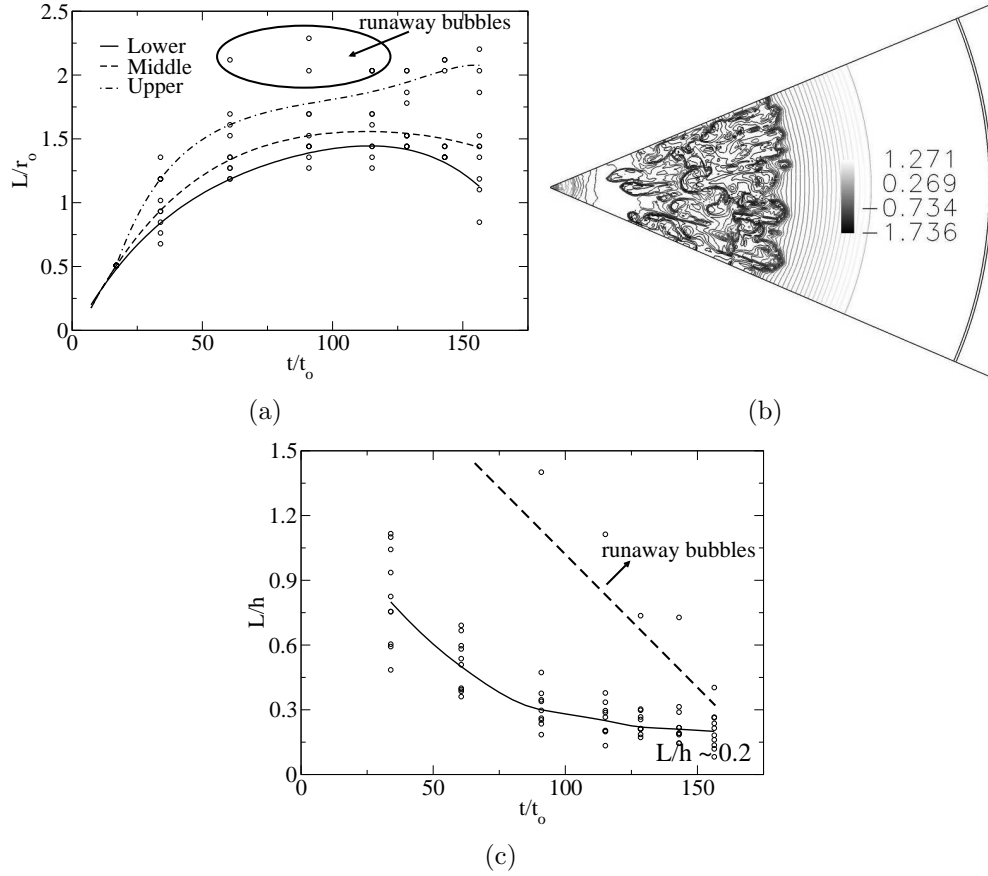


Figure 63: Bubble analysis from the 3D simulation for $\eta=1$, $r_p=5 \mu\text{m}$ and the initial particle cloud extending from $r=5.9\text{-}8.68 \text{ cm}$: (a) L ; (b) $\ln(\rho)$ contours at $t/t_0 \sim 130$ and (c) L/h . The circles in (a)&(c) denote the 3D simulation results.

not previously studied for chemical explosions. By self-similarity, the growth of bubble amplitudes (h) proportional to their transverse scale (L) is implied. Based on 3D simulations, the L/h ratio for the bubbles is presented in Fig. 63 (c), and suggests $L/h \sim 0.8 \pm 0.3$ at early times, but tends to asymptote near $t/t_0 \sim 150$ to 0.2 ± 0.07 . Also, as evident, the “runaway” bubbles shown do not conform to self-similarity.

The asymptote behavior of L/h ratio essentially means that the “bubble competition” process terminates and the bubbles evolve with little or no memory of the initial length scales of the early perturbations. Such studies have been carried out in the past to supernovae and nuclear explosions [149, 151, 152], but not to chemical explosions to the best of the authors’ knowledge. At late times, the bubbles reach

a “freeze-out stage” [149], i.e., no further merging occurs. The mode numbers (m) during this late time freeze-out stage are of preponderant interest; here, mode number is defined as $m = 2\pi r_i(t)/\lambda(t)$, where $r_i(t)$ denotes the instantaneous radial location of the interface. From [149], past simulations of supernovae explosions conform to freeze-out stage $m \sim 16$ -20; X-ray images of Cassiopeia A supernova shows $m \sim 20$; and high altitude nuclear explosions conform to freeze-out stage $m \sim 18$ -36. Current simulations predict freeze-out $m \sim 24$ -44 for the chemical explosions into ambient particle clouds. It is believed that for systems that involve instantaneous perturbation followed by subsequent growth with no further external perturbations, freeze-out stage mode numbers may conform better to the predictions of [149], i.e., m up to 36. However, for chemical explosions into ambient particle clouds, the nature of the initial perturbations is not instantaneous, but rather lasts for a finite albeit small time—the time required for the contact surface to overtake the particle cloud. This prolonged initial forcing inevitably introduces additional perturbations during the first interaction event, which in turn correlates as marginally larger late time freeze-out stage mode numbers, m , up to 44.

The similarity ratio, L/h for the 3D simulation corresponding to $\eta=2$, $r_p=5 \mu\text{m}$ and the initial particle cloud extending from $r=5.9$ -8.68 cm is shown in Fig. 64. As evident, L/h is nearly similar in value to the $\eta=1$ case (Fig. 63 (c)) at early times. However, since more perturbations are introduced for $\eta=2$ during the first interaction event, the late time freeze-out stage L/h asymptotes to 0.27 ± 0.1 , indicating that there is partial retention of memory of the initial conditions at late times, i.e., the freeze-out L/h is not a “universal” value. Recent supernovae simulations also predict partial memory retention of the initial conditions at late times [152]. Furthermore, although there is this weak dependence of the initial conditions, the fact that L/h nearly asymptotes at late times for $\eta=1$ (Fig. 63 (c)) and $\eta=2$ (Fig. 64), indicates that a “quasi-self-similar growth” is possible for chemical explosions, where the transverse

scale of the bubbles grows in proportion to its amplitude. However, this quasi-self-similar regime occurs only for a brief time instant, $t/t_o \sim 120-150$, after which the reshock shrinks the hydrodynamic structures and deposits vorticity (baroclinic effect) which subsequently wrinkles/convolutes the structures.

Due to the partial memory retention, the late time freeze-out stage photography of chemical explosions may contain some useful information on the nature of the initial perturbations. Analysis shows that the reshock phase is faster for the $\eta=2$ case than $\eta=1$ by about $t/t_o \sim 5$; due to this earlier reshock for $\eta=2$, the secondary shock reaches the structures in the mixing layer around $t/t_o \sim 155$ and compresses them. Consequently, h decreases, causing an increase in L/h beyond $t/t_o > 150$, which is of no interest in the present study.

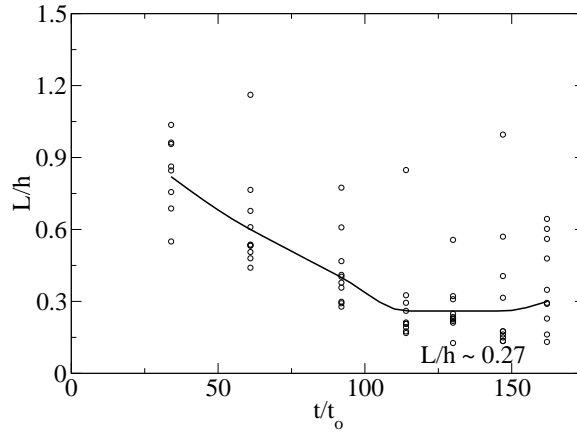


Figure 64: Bubble similarity from the 3D simulation for $\eta=2$, $r_p=5 \mu\text{m}$ and the initial particle cloud extending from $r=5.9-8.68 \text{ cm}$.

The BD model is applied for the ensemble of bubbles with the transverse length scale as input, and the amplitude growths with time are predicted. Critical to the BD model calculations is the definition of λ ; $\lambda=L$ has been used by some researchers [56], as well as $\lambda=2L$ by others [158]. To be precise, λ should be the ratio of the volume to cross-sectional area for the bubbles, which can be different for different bubbles depending on their shape. For instance, a “hemi-ellipsoidal bubble” can have

a higher volume to cross-sectional area ratio than hemispherical bubbles. Both $\lambda=L$ and $\lambda=2L$ are used in the current analysis and the amplitudes (h) obtained from the BD model are presented in Fig. 65 for the lower, middle and upper branches, along with the 3D simulation results. As evident, $\lambda=2L$ is in better accordance with higher amplitude bubbles, while $\lambda=L$ conforms to the smaller amplitude bubbles. During the implosion phase, 3D simulation results show that small bubbles, albeit not all, implode deep into the core—increasing their amplitude, as shown in Fig. 63 (b). These small bubbles have lesser drag and thus “rise” higher (higher is actually deeper by convention), resulting in more oblong shapes that have high volume-to-area ratio; thus, as expected, the BD model predicts a higher amplitude for $\lambda=2L$. Larger bubbles, on the other hand, have a higher drag, which slows them as they try to “rise” away from the interface; thus, these bubbles have relatively smaller amplitudes, as also predicted by the BD model results. It is believed that to properly characterize bubbles using the BD model, it is necessary to appropriately define bubble wavelengths (λ) based on their shapes. There is, however, limited work in literature on theoretical models with bubble shape-dependent wavelengths.

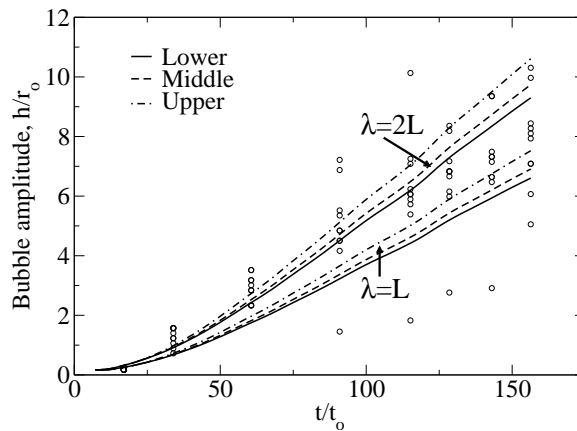


Figure 65: Bubble amplitudes obtained from the BD model for the case corresponding to $\eta=1$, $r_p=5 \mu\text{m}$ and initial cloud extending from $r=5.9\text{-}8.68 \text{ cm}$. The circles denote the 3D simulation results.

CHAPTER VII

HETEROGENEOUS EXPLOSIVE CHARGES

This chapter focuses on the study of heterogeneous explosive charges, i.e., charges comprising of a high explosive and solid metal particles. Heterogeneous explosive charges are of recent interest, both from a research standpoint as well as military application. Experiments have been carried out for a combination of charges containing Nitromethane (NM) and steel particles, demonstrating that particles pick up significant amounts of momentum from the gas, resulting in shock overpressure deficit [214]. Later, another experimental study from the same research group, backed with one-dimensional numerical analysis, investigated the impulsive loading from a combination of heterogeneous explosive charges [75] and showed that the impulsive loading contribution from the solid particles is significantly larger in the near field, thus exemplifying the usefulness of such charges for application, especially to the near-field impulse deliverance. These studies, however, did not address three-dimensional effects such as hydrodynamic instabilities, for photographic evidence from the same research group [74] clearly demonstrate that the mixing layer ensuing from the detonation of heterogeneous explosive charges is inevitably prone to hydrodynamic instabilities. In addition, the dispersion and burning characteristics of particles from dense, aluminized explosions are also of interest, and will also be investigated in this chapter.

To explore these plethora of interesting physical phenomena, this chapter discusses the post-detonation behavior of heterogeneous explosive charges, and considers three sections to it. In the first part of this chapter, only one-dimensional effects are considered, with the twin goal of demonstrating the efficacy of the currently developed ELD-DEM formulation, as well as to understand the impulsive loading deliverance from

heterogeneous explosions corresponding to inert steel particles, for a wide range of operating parameters such as particle size and initial solid volume fraction. Here, although a three-dimensional grid is employed for the calculations, the grid is poorly resolved in the azimuthal directions, as the primary focus of these studies are on the variations of flow features in the radial direction, without any significant hydrodynamic instabilities. Moreover, these one-dimensional studies have quick turn-around times, enabling parametric studies by varying the different operating parameters to study the effects of the same on the deliverable impulsive loading. In the second part of this chapter, three-dimensional effects are accounted for by considering a larger simulation domain and finely resolved sector grid. The mixing layer ensuing from the detonation of heterogeneous explosive charges containing inert steel particles are investigated, and the mean and rms profiles of the flow are discussed. Then, a comparison is made between the mixing layers of the heterogeneous and homogeneous explosive charges, and for different particle sizes. Finally, in the third part of this chapter, dense aluminized high explosive charges are investigated, focusing on the effects of particle size and initial volume fraction to the afterburn and dispersion characteristics of the particle clouds.

7.1 One-Dimensional Effects Only

7.1.1 Detonation in a heterogeneous explosive

In order to verify the simulation strategy, it is customary to compare the simulation results with experimental data available in literature. To this end, detonation studies from the experiments of Zhang et al. [214] are considered, involving a heterogeneous charge of 11.8 cm dia. containing nitromethane and steel particles. For the initial study, steel particles of 463 μm dia., randomly distributed and occupying 62% of the total charge volume is simulated using a spherical sector grid 2.4 m long along the radial direction (r), and 20° in the azimuth (θ) and zenith (ϕ) directions, and

is resolved using a $1000 \times 10 \times 10$ grid. Due to the consideration of one-dimensional effects only, the grid resolutions are coarse in the azimuthal and zenith directions; three-dimensional effects will be investigated later in this chapter employing much finer grids. As before, free-slip boundary conditions are used along the azimuth (θ) and zenith (ϕ) directions of the sector, and a supersonic outflow at the outermost plane. Thermodynamic closure is obtained with the use of the JWL equation of state (Eqn. (27)).

The current investigation involves solid particles of very high solid volume fractions ($\sim 62\%$) at early times, necessitating the use of volume fraction dependent drag and heat transfer laws. To this end, the drag law and Nusselt number correlations of Akhatov & Vainshtein [4] are considered, mainly due to the authors of this reference having demonstrated its applicability to a detonation problem involving dense, two-phase flow fields. This drag law predicts a drag coefficient (C_D) dependent on the solid volume fraction (α_p) and Reynolds number (Re), and the current computations show that C_D is as high as 4 for the particles in the near-field owing to the dense nature of the flow, and decreases to 0.42 – 0.5 in the far-field as the flow transitions to the dilute regime for the problem considered by Zhang et al. [214]. The Snider’s model [160, 186] coefficient, P_s , is chosen as 500 MPa, based on an order of magnitude analysis comparing collision and drag forces on a particle (see further discussions below). For the solid volume fraction range applicable to the current study, the chosen value of P_s (500 MPa) results in inter-granular stresses lower than the ultimate strength of steel, i.e., the maximum stress that steel can withstand before rupturing. Moreover, the inter-granular stress predicted by this model for the problem is in the range obtained by material researchers [157], who measured the inter-granular stress by tensile straining carbon steels. The parameters $\beta = 3$ [160] and $\alpha_{cs} = 0.9$ are chosen for the collision model.

The blast wave, the particle front trajectory, and the shock overpressure are shown

in Fig. 66, and the results are in good agreement with experimental data. Also shown is the overpressure obtained from a homogeneous charge (NM) containing the same amount of high explosive as this heterogeneous charge (NM/Fe). As observed, the momentum and energy transfer to the particles results in a decrease in the overpressure for the heterogeneous charge. It is observed that the particles at the leading edge of the cloud attain a velocity of around 1300 m/s in about 0.1 msec, and subsequently maintain a constant terminal velocity. At around 0.9 m and 0.6 msec, the particle cloud front is observed to overtake the shock wave, and subsequently the leading particles slow down. The radius of the particle front is defined as the radius within which 98% of the particles are contained as the average particle cloud front.

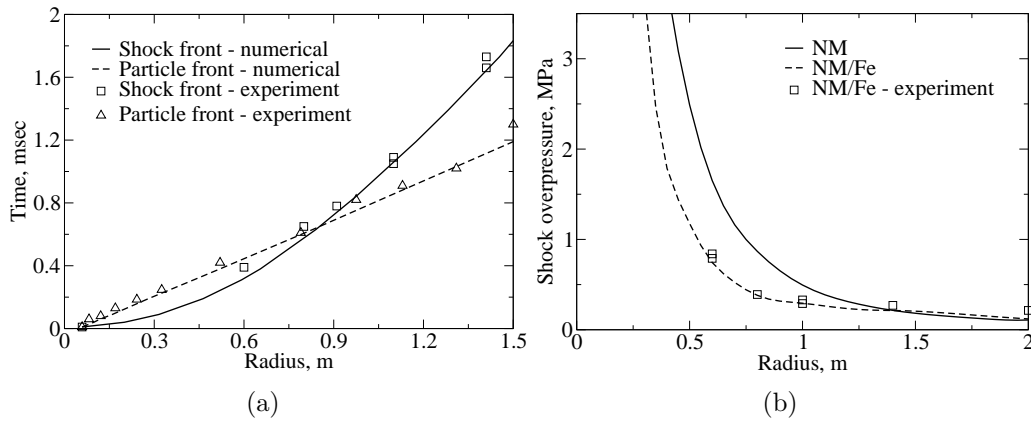


Figure 66: Detonation of a 11.8 cm diameter Nitromethane charge with a dense loading of steel particles: (a) trajectory and (b) shock overpressure. The experimental data is obtained from [214].

To illustrate the flow topography, the sector grid showing the gas pressure contour and the location of the particles at 0.38 and 0.98 msec are shown in Fig. 67. The particles lag behind the blast wave at the earlier time, but some of them have overtaken the blast wave at the latter time. The front of the particle cloud is not a sharp interface due to the initial random distribution of the particles. The minor “perturbations” observed closer to the leading edge of the particle cloud in Fig. 67 (b) are presumably due to the initial random distribution of the particles. Moreover,

post-detonation photography from [214] for the 463 μm particle size clearly indicates that the particle cloud for this heterogeneous explosive combination is nearly spherically-symmetric.

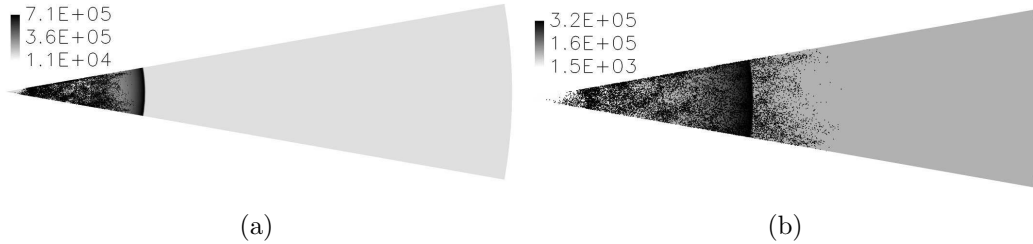


Figure 67: Flow topography at (a) 0.38 msec and (b) 0.98 msec. The legend denotes the pressure field in Pa.

The flow physics as observed from the simulation is now described, with many aspects being similar to the homogeneous charge considered earlier. When an explosive charge is detonated, a detonation wave propagates radially outwards within the charge. As this detonation wave reaches the charge surface, a blast wave propagates outwards and an expansion wave inwards. The outward moving blast wave decelerates and attenuates as it expands radially outwards. The inward moving expansion accelerates the flow outwards. For the heterogeneous explosion, this process is accompanied by inter-phase drag (viscous and pressure) effects, resulting in acceleration of the particle cloud outwards. During this process, the dense nature of the solid particle cloud creates inter-particle collisions/contact, resulting in further outward acceleration of the particles. This is due to the nature of the inter-particle forces trying to lower the bulk density of the packed solid particles within the explosive charge, which is accomplished only by a radially outward acceleration of the solid particles. After the particle front has propagated a distance of about 3-4 charge diameters, the volume fraction decreases to the dilute limit, and the inter-particle collision force becomes negligible. Furthermore, as the particles propagate outwards, the momentum transfer time scale increases due to three reasons: (1) decrease in the

solid volume fraction results in a decrease of the drag coefficient; (2) decrease in the gas velocity results in a smaller velocity difference between the gas and the particles; and (3) decrease in the gas density. Due to inertia, the particles attain a terminal velocity, which remains nearly constant for a significant time, as observed by the near straight line trajectory of the particle front in Fig. 66 (a).

It is of interest to study the magnitude of the forces acting on the particles at early times, viz. the forces due to viscous drag (C_D), pressure drag (gas pressure gradient, $\frac{\partial p_g}{\partial x_i}$), and inter-particle collision/contact ($A_{c,i}$). To this end, Fig. 68 presents the magnitude of the average acceleration/deceleration on all the particles due to these three forces. As evident, the average total acceleration on the particles is $\sim 5 \times 10^7 \text{ m/s}^2$ at very early times ($\sim 0.01 \text{ msec}$), with that due to viscous and pressure drag being about 3-4 times that due to inter-particle collision/contact. Subsequently, the acceleration due to pressure drag decreases faster, as the gas pressure gradients decrease due to flow expansion. By $\sim 0.15 \text{ msec}$, the collision/contact forces become less significant in magnitude *vis-à-vis* the pressure drag, and both these forces are about one order of magnitude smaller than the viscous drag forces; beyond $\sim 0.175 \text{ msec}$, the collision/contact forces are two orders of magnitude smaller than the viscous drag; after $\sim 0.2 \text{ msec}$, the viscous drag forces emerge as the only significant force on the particles, with the acceleration/deceleration being about 10^4 m/s^2 . Thus, although the collision/contact forces are significant only for the first $\sim 0.1 \text{ msec}$, these forces play a vital role in the initial distribution of particles, in particular near the leading edge of the expanding particle cloud where the collision/contact forces are more significant due to the higher solid volume fraction gradient.

The leading particles catch-up with the primary blast wave, as the latter has attenuated and slowed down owing to its spherical spreading. The particles at the front of the cloud overtake the primary blast wave and, subsequently, the momentum transfer time scale decreases slightly as the velocity difference between the particles

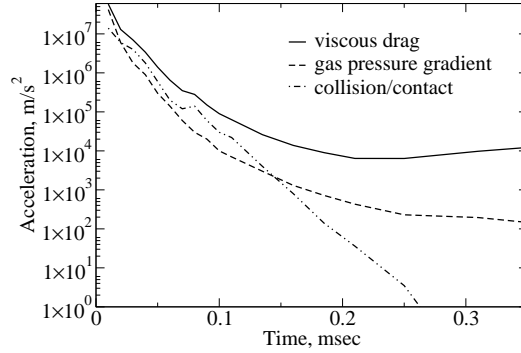


Figure 68: Average acceleration/deceleration due to viscous drag, pressure drag (gas pressure gradient) and inter-particle collision/contact.

and the gas is suddenly enhanced, due to the ambient air being at rest. Thus, the particles that penetrate the blast wave are slowed down due to aerodynamic drag, allowing for the blast wave to again catch-up and overtake the solid particle front, as also reported in [214]; however, the current simulation domain is not radially long enough to capture this event. At the same time, the inward moving rarefaction over-expands the flow, giving rise to a secondary shock. This secondary shock is initially weak, and is swept outwards by the expanding detonation products and solid particles. During this initial outward passage, the strength of the secondary shock is augmented, as it propagates into regions of higher pressure. Subsequently, the secondary shock implodes inwards, as the pressure near the core has decreased considerably by the rarefaction wave. After its reflection from the origin, the secondary shock propagates outwards for the second time, and trails behind the primary shock.

More physics on the formation and propagation of the secondary shock is given in [34], albeit for a homogeneous charge. The wave diagram comparing the primary and secondary shock trajectories for homogeneous (NM) and heterogeneous (NM/Fe) charges containing the same amount of high explosive is shown in Fig. 69. The primary and secondary shocks are slower for the heterogeneous charge, due to the momentum and energy transfer to the particles. Furthermore, as the secondary shock

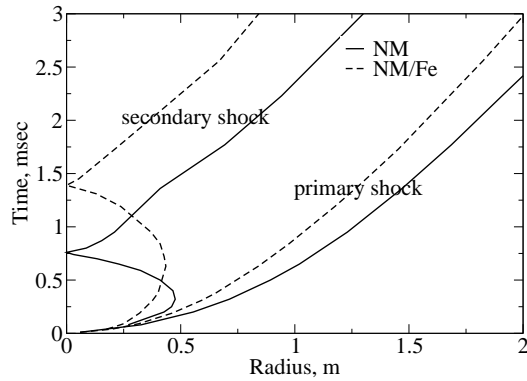


Figure 69: Wave diagram comparing the primary and secondary shock trajectories for homogeneous (NM) and heterogeneous (NM/Fe) charges containing the same amount of high explosive.

implodes inwards, the particles act as an obstruction and slow it down further. Thus, the secondary shock reaches the origin about 0.6 msec later for the heterogeneous charge.

7.1.2 Impulsive loading

7.1.2.1 Gas and particle momentum flux

It has been shown that the presence of particles results in impulse augmentation due to momentum transfer [75]. To demonstrate this phenomenon, the pressure and the momentum flux profiles at 0.9 m and 1.55 m are compared for the homogeneous (NM) and heterogeneous (NM/Fe) charges containing the same amount of high explosive in Fig. 70. The pressure is lower for the NM/Fe charge when compared to NM (Fig. 70 (a)). With the addition of solid particles, momentum and heat transfer from the detonation products to the solid particles results in a slower blast wave for the NM/Fe charge, and a corresponding lower pressure trace. The same argument holds for gas momentum flux profiles in Fig. 70 (b) & (c). It is observed that the solid momentum flux has a slightly higher peak than the gas momentum flux at the 0.9 m and 1.55 m locations, contrary to the numerical predictions of [75]. This is owing to an increased distribution of solid particles closer to the leading edge of the particle cloud due to

the gas pressure gradient term in the solid momentum equation, and will be revisited later. Furthermore, the solid momentum flux lasts for a longer time duration than the gas due to its inertia, as also reported in [75]. In the current Eulerian-Lagrangian (EL) approach, the absence of continuum modeling of the solid phase results in a “noisy” solid momentum flux profile.

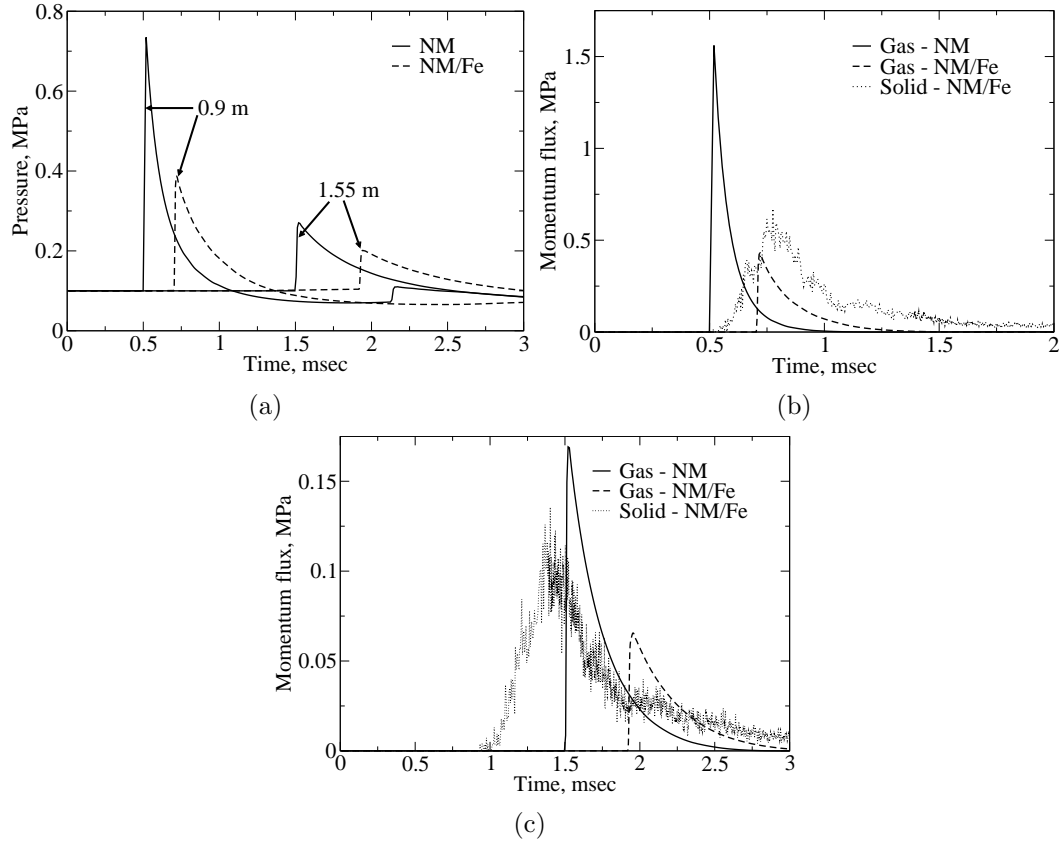


Figure 70: Pressure (a) and momentum flux (b & c) profiles for NM and NM/Fe charges at 0.9 m (a & b) and 1.55 m (a & c).

In order to better understand the transfer of momentum from the gas to the particles, four different groups of particles are considered. 100 particles initially occupying radial locations between (0.058 ± 0.001) m are randomly chosen, and this group is named C58. Similar groups of 100 particles each are considered, initially occupying radial locations between (0.048 ± 0.001) m, (0.038 ± 0.001) m and (0.028 ± 0.001) m and named C48, C38 and C28, respectively. The average velocity of all the 100 solid

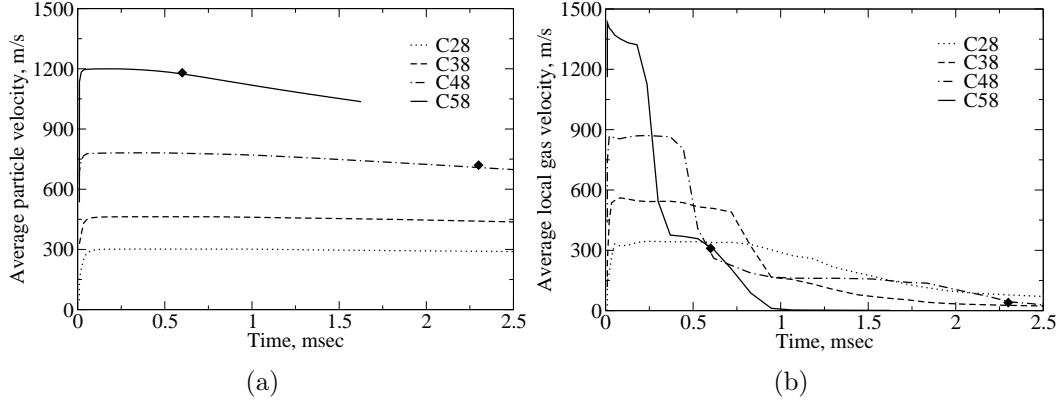


Figure 71: Flow field behind the blast wave: (a) average particle velocity and (b) average local gas velocity for different groups of particles. The diamond symbols indicate the times at which half the number of particles belonging to the corresponding group have penetrated the shock front.

particles belonging to each group, and the average local gas velocity as seen by each group are plotted in Fig. 71. It is seen that the terminal velocities can be arranged as $C58 > C48 > C38 > C28$, with the differences narrowing down between adjacent groups at smaller initial radial locations. This is due to an outer group being more free to move outwards than an inner one, the latter being constrained by the dense cloud of surrounding particles. The terminal velocity is reached within about 0.1 msec for all the groups, indicating the preponderance of the inter-particle interaction force, which is dominant at early times. Another reason for the rapid attainment of the terminal velocity is because the drag coefficient (and drag force) on the particles is higher in a denser cloud.

In Fig. 71, the diamond symbols indicate the times at which half the number of particles belonging to the corresponding group have penetrated the shock front. As evident from the figure, the average particle velocity of C58 and C48 groups start to decrease after penetrating the shock front. C38 and C28 are not observed to penetrate the shock front in the time duration of study. From the average local gas velocity seen by each group, it can be concluded that each group initially encounters different average local gas velocities in the order $C58 > C48 > C38 > C28$. Particles

closer to the outer surface of the charge encounter higher local gas velocities due to the rapidly expanding gas, caused by the inward moving rarefaction wave. After an initial plateau, it is observed that the local gas velocities fall off, earlier (≈ 0.25 msec) for C58, but slightly later for the other groups, due to the faster travelling C58. For C58, C48 and C38, a second plateau is observed in the average local gas velocity as they approach the blast wave, but the two plateaus are coupled into one for C28. This second plateau lasts only for a short duration (≈ 0.25 msec) for C58, as the particles by virtue of being faster, catch-up with the leading blast wave earlier. For the chosen size of the simulation domain, the leading blast wave reaches the outer boundary before C38 and C28 groups, and thus, it could not be ascertained whether or not these inner groups penetrate the leading blast wave.

7.1.2.2 *Impulsive loading estimation*

The total deliverable impulse from a heterogeneous charge can be estimated from the simulation data and typically, will be due to three components, i.e., pressure, gas and particle momentum fluxes. These quantities can be integrated in time to obtain the total deliverable impulse. Some investigators [103, 119] have considered the impulse due to excess gas pressure and particle momentum only, while others have considered the bending of a cantilever rod to quantify impulse [75]. Here, the impulse deliverable to a “virtual wall” is considered since the physical wall is not included in the current simulation. Define the total impulse (I) as:

$$I = \int_0^{\infty} (p_g - p_o)_{p_g > p_o} dt + \int_0^{\infty} \frac{1}{2} \rho_g \alpha_g u_g^2 dt + \int_0^{\infty} \frac{1}{2} \rho_p \alpha_p u_p^2 dt, \quad (189)$$

where p_0 denotes the ambient pressure. The impulse due to pressure, gas and particle momentum fluxes are denoted as I_p , I_{gm} and I_{pm} , respectively. I_{pm} is computed as a summation over all the particles present in a small control volume around the radial distance of interest. The total impulse and its three components are shown in Fig. 72

(a), along with the ratio, I_{pm}/I_{gm} . The expansion of the gas and particle phases with radius causes the total impulse to decrease. I_{pm} is larger than I_{gm} at all radius, by a factor of about 3.5-4.75. Similar trends have been reported by other investigators [75]. In Fig. 72 (b), the impulse between the NM and NM/Fe charges containing the same amount of high explosive are compared at different radial locations along with the ratio of the impulses for NM/Fe and NM. As evident from the figure, impulse augmentation for the NM/Fe charge over the NM charge decreases from a factor of 2 in the near-field (~ 4 charge dia.) to about 1.1 in the far-field (~ 20 charge dia.). Thus, the advantage of adding solid particles to an explosive charge is more pronounced in the near-field, and asymptotes towards unity in the far-field. At farther distances from the charges, the significant slowing of the solid particles negates any impulse augmentations, thereby tending the behavior of a heterogeneous charge to that of a point source homogeneous charge.

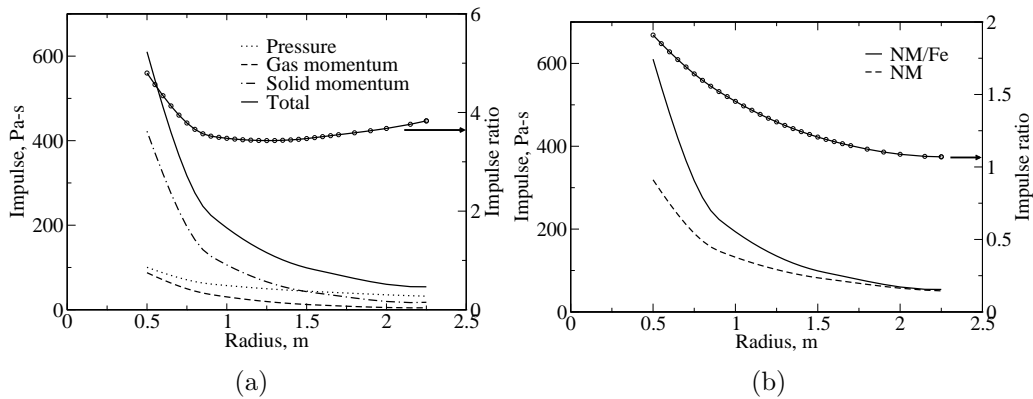


Figure 72: Impulsive loading of a heterogeneous explosive: (a) total impulse and its components and (b) comparison between NM and NM/Fe charges. In (a), the line with the circles represents the ratio between the solid and gas momentum impulses and corresponds to the right y -scale; in (b), the line with the circles represents the ratio of the total impulses due to NM/Fe and NM and corresponds to the right y -scale.

7.1.2.3 *Transient impulsive loading*

The impulse estimate in Fig. 72 are the final impulsive loading delivered, i.e., obtained by integrating Eqn. (189) up to a large time. It does not represent the transient behavior, i.e., whether the impulsive loading felt by an imaginary structure is sudden or gradual. To quantify this, the transient impulsive loading is presented at 0.5 m and 2.25 m in Fig. 73, obtained by performing the integrations in Eqn. (189) up to a certain time instant. The total impulse, as well as its individual components converge earlier at 0.5 m than at 2.25 m. At farther distances, the gas and particle phases are slower, and hence take a longer time to pass a given point, thereby resulting in a longer time duration for the impulse convergence. Since the blast wave arrives earlier than the particles at the 0.5 m location, only the impulse due to gas pressure and gas momentum contribute initially; subsequently, after the particles arrive, their contribution takes over as the dominant component. At this location, the passage of the primary blast wave raises the pressure, but subsequently falls to sub-atmospheric levels and low gas velocities, and thus all the pressure and gas momentum impulse are delivered in a very short time (within ~ 0.6 msec). On the other hand, the intermediate velocity particles take a longer time to pass the 0.5 m location, and thus the impulse due to solid momentum converges later (~ 2 msec).

At the 2.25 m location, the reverse is observed for the early contribution to the total impulse. Since the particles reach this location earlier than the blast wave, they are the dominant early contributors; beyond about 3.5 msec, with the arrival of the blast wave, the pressure impulse takes over as the dominant contributor. Moreover, at this location the convergence of the impulse due to pressure and gas momentum occur almost at the same time (~ 4.75 msec), but that due to the particles is delayed until ~ 7 msec. Due to the shifts of the solid and gas phases as the primary contributor, the transient total impulse at the 2.25 m location occurs in two phases, resulting in a sudden slope change observed in the total impulse, indicated by the arrow in Fig. 73

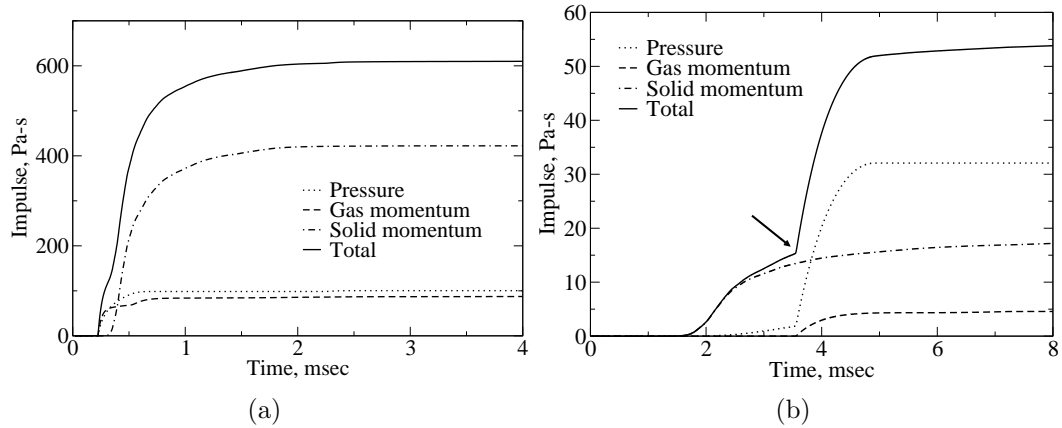


Figure 73: Transient impulse and its components for a heterogeneous explosive at radial locations: (a) 0.5 m and (b) 2.25 m.

(b). Thus, while an imaginary structure at the 0.5 m location may destruct/deform gradually, its response will occur in two phases at the 2.25 m location. While most civil engineering structures may have a slow response, solid propellants/explosives have faster responses to the impulsive loading [143]. For instance, if the heterogeneous explosive charge under study is used as an igniter of a larger solid propellant/explosive, the transient nature of the impulse can be very critical in its ignition. Here, ignition is achieved by a combination of mechanical and thermal stresses. For these studies, transient impulsive response can be very critical in the ignition event.

Another observation from Fig. 73 (b) at the 2.25 m location is that the pressure impulse starts to rise even before the onset of the blast wave, i.e., in the time interval 2.5-3.5 msec. This rise, albeit small, is due to the leading particles which, upon penetration into the ambient air, perturb the local flow-field. The impulsive loading predictions for the NM/Fe charge that have been hitherto studied can be used for damage assessment, albeit in a crude sense. The impulse predictions considered here do not account for other physical phenomena such as blast wave reflection and diffraction, and particle collision with a structure. Thus, simulations such as these can be used as a first approximation for damage assessment.

7.1.3 Parametric studies

7.1.3.1 Sensitivity to collision model coefficient

For the heterogeneous blast wave simulations performed hitherto, the collision model coefficient, P_s was chosen as 500 MPa, based on an order of magnitude analysis of the drag and collision/contact forces on a particle. In order to better elucidate the sensitivity of the results to the collision model coefficient, four other studies are carried out: (1) $P_s = 0$ MPa, (2) $P_s = 100$ MPa, (3) $P_s = 250$ MPa and (4) $P_s = 1500$ MPa. Fig. 74 shows the primary blast wave and the particle front trajectories for different values of P_s so chosen, along with $P_s = 500$ MPa used hitherto. The blast wave trajectory is nearly unaffected by the choice of the collision/contact model coefficient, P_s for values in the range 0-500 MPa. For P_s in the same range (0-500 MPa), the particle front trajectory is observed to be only slightly faster for the higher collision model coefficient, albeit not to a significant extent.

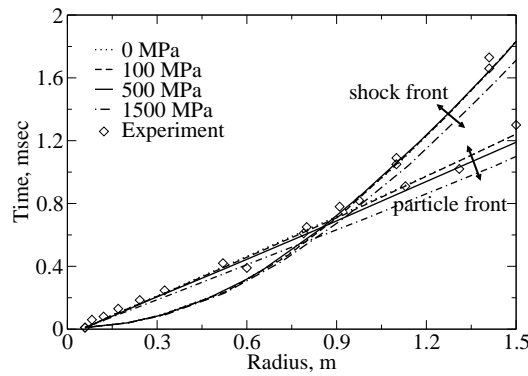


Figure 74: Effect of collision model: shock and particle front trajectories for different collision/contact model coefficients (P_s) (the results for the 0 MPa case are nearly coincident with the 100 MPa case, and thus the former is not clearly visible).

The authors of [214] showed numerically that with the “solid pressure” term turned off (analogous to $P_s = 0$ in the current study), the particle front trajectory is considerably slower, although the current simulations show that the particle front is only marginally slower (Fig. 74) for $P_s = 0$ MPa. These differences are attributed to the choice of

the initialization used. The authors of [214] used a constant volume initialization, i.e., a high pressure source, and thus, the particles are still at rest when the blast wave breaks out of the initial charge. On the other hand, this study uses a more realistic GISPA method, in which the particles attain significant velocities during the detonation wave crossing within the initial charge. From Fig. 103 (b) in Appendix B, it is deduced that the maximum particle velocity as the detonation wave reaches the outer boundary of the charge is about 750 m/s, which is more than 50% of terminal velocity the leading particles will subsequently attain. Due to the initial head start with the use of the GISPA method for the particle velocities, the particle front trajectory from the current simulation for $P_s = 0$ MPa is significantly faster than that numerically predicted by [214] without the “solid pressure” term. However, the particle front trajectory predicted by the physical simulations ($P_s = 500$ MPa in this study, and with the “solid pressure” turned on in [214]) in both studies are in good agreement with the experimental data of [214].

From Fig. 74, for $P_s = 1500$ MPa, both the blast wave and particle front trajectories are significantly faster. A value of $P_s = 1500$ MPa is unphysically high and causes the particles to travel much faster, as well as more concentrated towards the leading edge of the cloud, due to the associated higher collision/contact forces at early times (0-0.1 msec). Furthermore, $P_s = 1500$ MPa results in inter-granular stresses larger than the ultimate strength of steel, that can result in the rupture of the particles, unaccounted for in this study. Since the particle cloud is initially lagging behind, the blast wave trajectory for the case with $P_s = 1500$ MPa matches with the other cases until about 0.6 msec, as the particles have no influence on the blast wave until this time. However, beyond 0.6 msec, as the leading particles get closer to the blast wave, they compress the gas, which decreases the decay rate of the primary blast wave. Due to the unphysically high particle speeds and concentration, this compression effect is strong for the case with $P_s = 1500$ MPa. Indeed, a second

compression wave is observed (not to be confused with the secondary shock) in front of the particle cloud as they catch-up with the blast wave, not shown here for brevity. The presence of this compression wave is more pronounced for $P_s = 1500$ MPa than for the other lower values considered due to the unphysically high speeds and higher leading concentration of the particle cloud.

High values of the collision model coefficient (P_s) not only cause higher particle speeds, but higher particle concentration near the outer boundary of the particle cloud. At early times (0-0.1 msec), the ensuing particle collisions tend to force the particles outward in the radial direction. That is to say, near the center of the charge, inter-particle collisions are equally likely in all directions; but for particles near the cloud boundary, collisions are biased to force the particles outwards. Subsequently, as the particles reach farther radial distances, the solid volume fraction approaches the dilute limit, and the collision/contact force becomes negligible. However, since a few more particles are concentrated closer to the outer boundary of the cloud at early times, this distribution of particles is maintained even long after the collision/contact force becomes negligible.

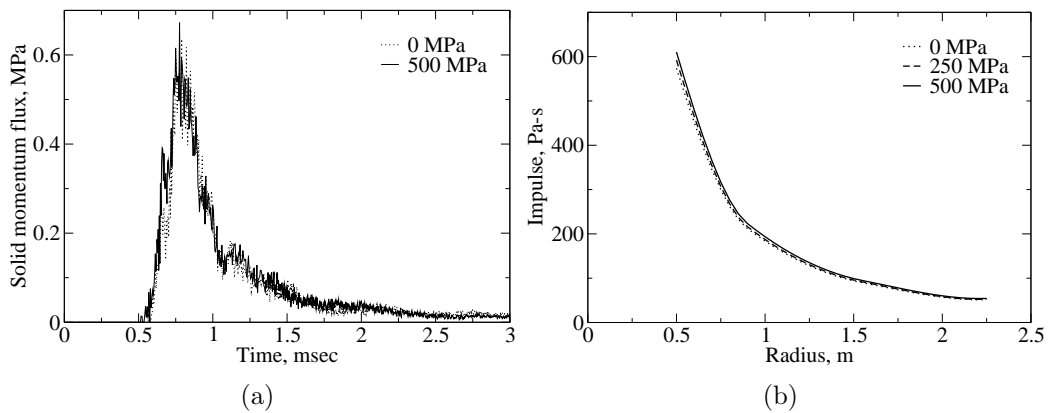


Figure 75: Effect of collision model on the (a) solid momentum flux and (b) total impulse.

To understand the effect of the initial solid particle collisions, the solid momentum flux profile is shown in Fig. 75 (a) at the 0.9 radial location for $P_s = 0$ and 500 MPa.

For both cases, although the solid momentum flux begins to rise around 0.6 msec at the 0.9 m location, the peak is marginally higher when $P_s = 500$ MPa due to a greater particle concentration near the cloud's outer edge. Fig. 75 (b) shows the total impulse obtained from the same NM/Fe charge for $P_s = 0, 250$ and 500 MPa. The total impulse is about 6% higher for $P_s = 500$ MPa than with $P_s = 0$ MPa, primarily due to more particles accumulated closer to the leading edge of the particle cloud.

In summary, the shock and particle front trajectories are not significantly affected by the collision/contact model coefficient, P_s in the range 0-500 MPa. For $P_s = 1500$ MPa, both the blast wave and particle front trajectories are unphysically faster due to the compression in front of the particle curtain as they catch-up with the blast wave. Furthermore, for a higher P_s , due to more particles being concentrated closer to the front of the cloud, a marginally higher peak solid momentum flux is observed, resulting in a slightly higher impulse.

7.1.3.2 Effect of particle size

The baseline numerical solution for this study is computed for steel particles $463 \mu\text{m}$ in diameter, corresponding to a particle volume fraction of 62%. To better understand the effect of particle size on the impulse characteristics of heterogeneous explosive charges, steel particles with diameters 50, 100, 275, 925 and $1500 \mu\text{m}$ are also considered, for the same charge diameter and initial particle volume fraction. The attendant numerical solutions are compared with those for the baseline charge. Figure 76 shows the shock and particle front trajectories for this selection of particle diameters. As observed, the shock front is unaffected by the solid particle size, but the particle front is observed to be slightly faster for smaller particles. For instance, the trajectory of the leading edge for the $275 \mu\text{m}$ particles is observed to be 100-150 m/s faster than that for $925 \mu\text{m}$ particles, correlating to a distance of 0.1-0.15 m over a time frame of 1 msec or about one charge diameter distance. Although the authors

of [214] concluded that the particle front trajectory is insensitive to the particle size beyond $275\ \mu\text{m}$, based on current numerical results, it is deduced that the differences although small, are distinctive enough to conclude that smaller particles travel faster than larger particles. At a radial distance of 12 charge diameters, smaller particles will propagate about one charge diameter farther.

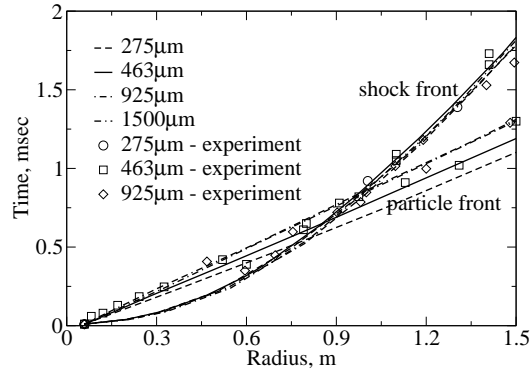


Figure 76: Effect of particle size on the primary blast wave and particle front trajectories. Experimental data is from [214]; experimental particle front for the $275\ \mu\text{m}$ size not available in [214].

Figure 77 shows the solid momentum flux profiles at the $0.9\ \text{m}$ radial location for charges containing 463 and $925\ \mu\text{m}$ particle sizes. Since the $463\ \mu\text{m}$ particles are slightly faster than the $925\ \mu\text{m}$ particles, the solid momentum flux starts to rise earlier for the former. However, the peak solid momentum flux is $\sim 15\%$ higher for the $925\ \mu\text{m}$ particles, as these are slower and hence, slightly more concentrated in space. Nevertheless, the impulse due to solid momentum is nearly identical for the two particle sizes. Thus, larger particles are characterized by a higher peak momentum flux of shorter duration than for smaller particles, yet both provide nearly the same contribution to the total impulse. Another observation is that the “noise” in the solid momentum flux is more pronounced for the larger particle size, as these violate the continuum to a greater extent than their smaller counterparts.

The total impulse for charges with different particle sizes in the range 50 - $1500\ \mu\text{m}$ are shown in Fig. 78 (a). Particle sizes above $275\ \mu\text{m}$ are observed to result in the

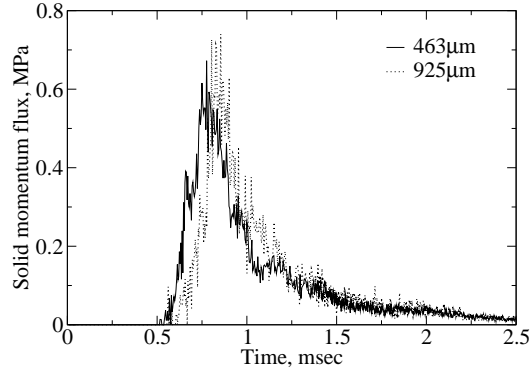


Figure 77: Effect of particle size on the solid momentum flux profiles at 0.9 m.

same total impulse, thus indicating insensitivity of the total impulse to particle size beyond $275 \mu\text{m}$. This emphasizes that the total impulse is directly related to the total mass of metal in the charge for charges with particle sizes in the range $275\text{-}1500 \mu\text{m}$. For the 50 & $100 \mu\text{m}$ size, the total impulse is $\sim 8\%$ higher than the larger particle sizes, as these small particles pick up significant amounts of momentum from the gas, and are more concentrated closer to the leading edge of the exploding particle cloud. After these smaller particles penetrate the leading blast wave, they surrender most of their momentum back to the gas, as they have lesser inertia compared to the larger particles; however, by virtue of being more concentrated closer to the leading edge of the particle cloud, the total impulse is still superior for the 50 & $100 \mu\text{m}$ particles.

In Fig. 78 (b), the three components of the total impulse, i.e., due to pressure, gas momentum and solid momentum, as percentage of the total impulse are shown at the 0.9 and 1.55 m locations. The percentage of the pressure impulse is observed to increase for all particle sizes from 0.9 m to 1.55 m, while the percentage of the gas and solid momentum are observed to decrease between these two radial locations. As the gas expands out farther, it slows down, and thus contributes less from its momentum to the total impulse. As the solid particle cloud expands radially outwards, its concentration decreases as it disperses into more free space, and thus also contributes less from its momentum at farther distances. The pressure impulse is $\sim 28\%$ of the total

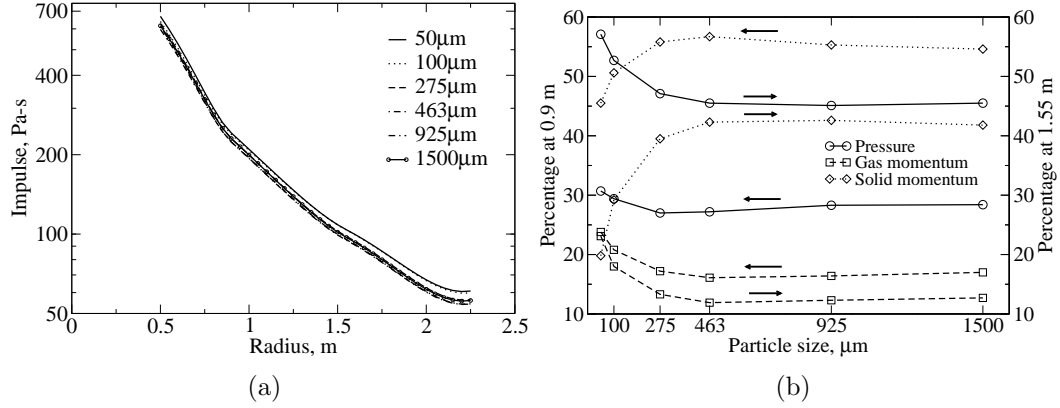


Figure 78: Effect of particle size: (a) total impulse; (b) components of total impulse expressed as a percentage of the total. The arrows in (b) denote the left or right y -scale to which each curve corresponds.

impulse for particle sizes larger than $275 \mu\text{m}$ at the 0.9 m location, and decreases at the 1.55 m location from 57% for $50 \mu\text{m}$ to 45% for $1500 \mu\text{m}$ particles. Furthermore, the solid momentum flux contribution increases with particle size at both locations, i.e., from 45% to 55% at 0.9 m , and from 20% to 42% at 1.55 m , as the particle size is increased from $50 \mu\text{m}$ to $1500 \mu\text{m}$. Owing to a higher inertia, larger particles contribute more to the total impulse from solid momentum than their smaller counterparts. Due to this reason, the contribution from gas momentum flux decreases at both locations with increasing particle size. Furthermore, it is interesting to note the rapid changes in the individual contributions of the different impulse components below the $275 \mu\text{m}$ particle size due to the significant slowing of these smaller particles at farther distances. This clearly illustrates that the faster response time scales of the particles smaller than $275 \mu\text{m}$ results in the different impulse predictions for the particles smaller than this cutoff value. However, particles equal to or larger than $275 \mu\text{m}$ tend to attain an ‘equilibrium’ with the local gas, thereby delivering the same impulse (and impulse components) at a given radius.

7.1.3.3 *Effect of gas pressure gradient*

The gas pressure gradients can be steep enough at early times, and can result in pressure drag forces on the particles comparable to the viscous drag forces and/or inter-particle collision forces (refer to Eqn. (64) for their mathematical forms). In the numerical simulations of [214], this term was not included in the particle motion. To better understand the effect of the pressure drag on the exploding particle front, another simulation was carried out with the gas pressure gradient term ($\frac{\partial p_g}{\partial x_i}$) excluded in the solid particle momentum equation and inter-phase coupling terms (but accounted in the gas momentum equations); this approach is widely used in many Eulerian-Lagrangian based studies [41, 117, 118, 144]. Observations show that at early times, the pressure drag on the particles is comparable to the viscous drag; but the overall particle front trajectory is nearly unaffected with and without this term, not shown here for brevity. However, the gas pressure gradients play a critical role in the distribution of the solid particles in the exploding particle cloud. Without this gas pressure gradient term in the solid momentum equation (and coupling terms), fewer particles are concentrated closer to the leading edge of the particle cloud, thereby resulting in a lower peak solid momentum flux, as shown in Fig. 79. Here, at the 0.9 m radial location, the peak solid momentum flux is about 25% lower with the gas pressure gradient unaccounted in the particle motion. Thus, the inclusion of the pressure gradient term in the solid phase momentum equation and the coupling terms is essential for the problem under study.

7.1.3.4 *Effect of initial volume fraction*

In this section, the effect of the initial volume fraction is studied in the explosive charge. When fewer solid particles occupy the same size charge, more volume is available to the high explosive, and hence higher is the explosive mass (and detonation energy). Thus, with a decreased initial solid volume fraction, more explosive

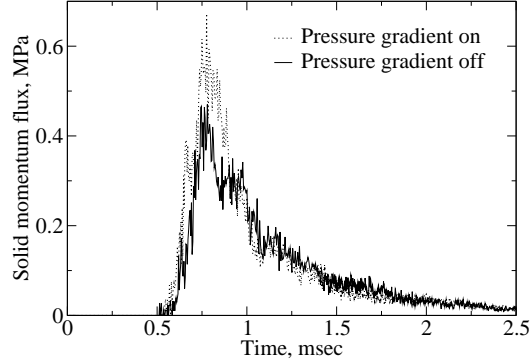


Figure 79: Effect of gas pressure gradient on the solid momentum flux at the 0.9 m location.

energy is available to drive fewer solid particles. To illustrate the dependence of the initial solid volume fraction, the same 11.8 cm dia. charge with 463 μm dia. steel particles is considered, with the same collision model coefficient $P_s=500$ MPa, but with an initial solid volume fraction $\alpha_{p,initial}=0.3$, and is compared with the baseline $\alpha_{p,initial}=0.62$ charge. The trajectories of the leading blast wave and the particle front for these two charges are shown in Fig. 80 (a), along with the experimental data for $\alpha_{p,initial}=0.62$ from [214]. As evident, the leading blast wave and the particle front are significantly faster for the decreased initial solid volume fraction $\alpha_{p,initial}=0.3$, due to the higher explosive energy available to drive fewer solid particles. However, the distance required for the particle front to overtake the leading blast wave is higher by $\sim 30\%$ for $\alpha_{p,initial}=0.3$, contrary to the numerical predictions of [214]. These differences are attributed to the different initial conditions used in the current research effort; furthermore, experimental data for $\alpha_{p,initial}=0.3$ is not available in literature, and thus the overtaking distance is not verifiable for the decreased initial solid volume fraction.

The current study also shows that the peak pressure and gas momentum flux profiles at a radial location are higher for $\alpha_{p,initial}=0.3$ *vis-à-vis* $\alpha_{p,initial}=0.62$, as more explosive mass is available for the former; however, the peak solid momentum flux at

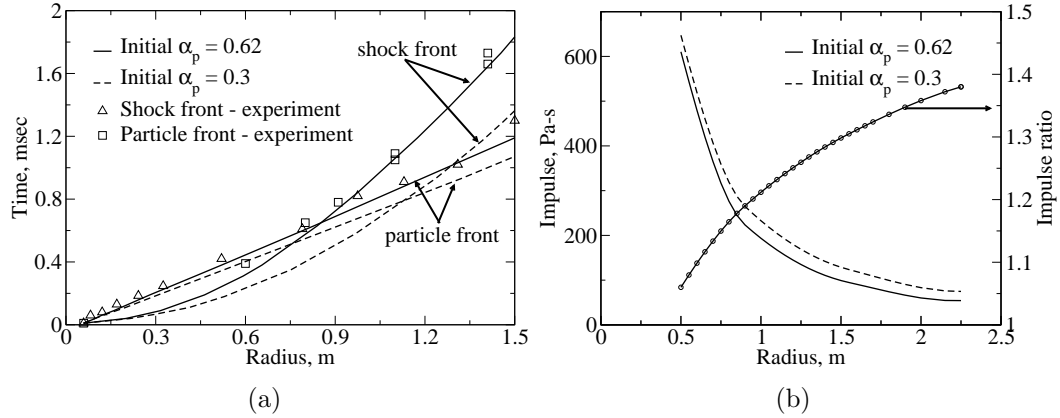


Figure 80: Effect of initial volume fraction: (a) blast wave and particle front trajectories; (b) total impulse. In (b), the ratio of the total impulse values computed at $\alpha_{p,initial}=0.3$ and $\alpha_{p,initial}=0.62$ is represented by the curve annotated with circles.

a radial location is higher for the latter, as more particles are available for the same (these results are not presented here for brevity). Since this investigation is primarily focused on impulsive loading aspects of heterogeneous explosives, the total impulses of the two said initial volume fraction charges are presented in Fig. 80 (b), along with their ratio. As evident, the total impulse is only 6% higher at the 0.5 m radial location for $\alpha_{p,initial}=0.3$, but is 38% higher for the same charge at the 2.25 m radial location. This suggests that in the near-field, the impulse augmentation by adding more solid particles to the charge can be easily compensated by otherwise having more high explosive. However, in the far-field, significant impulse augmentation is achieved by substituting part of the solid volume in the charge with the high explosive, as this excess gas phase energy enhances the far-field impulsive loading.

7.2 Three-Dimensional Effects Included

The above studies of heterogeneous charges are extended with the inclusion of three-dimensional effects, viz. hydrodynamic instability growth, mixing and afterburn effects in the mixing layer. Recalling, the initial heterogeneous explosive charge is 5.9 cm in radius, and consists of 463 μm steel particles occupying 62% of the volume of

the charge. The same sector grid approach is employed; however, this time with the sector being 2.4 m long, and 45° in the azimuth and zenith directions. The particles are randomly distributed within the charge with velocities based on the aforementioned one-dimensional detonation simulation using the GISPA method (Section 4.7, Appendix B).

In order to resolve the small scales of relevance in the mixing layer, it is essential to use a fine enough grid that can accurately capture the same. For the present study, three different grids are tried: $1000 \times 45 \times 45$, $1000 \times 60 \times 60$ and $1000 \times 75 \times 75$, and the results now to be presented demonstrate that the latter two grids are sufficient resolutions to predict the shear instabilities and turbulent features in the mixing layer. To compare results obtained with different grids, or different explosive charges, it is customary to use a normalized spatial co-ordinate consistent with the definition of the mixing layer boundaries. To this end, the concept of a scaled distance (χ) is introduced, defined as

$$\chi = \frac{r - r_{0.5}}{r_{0.05} - r_{0.95}}, \quad (190)$$

where $r_{0.5}$, $r_{0.05}$ and $r_{0.95}$ denote respectively, the radial distance at which the azimuthally averaged Y_{CO} is 0.5, 0.05 and 0.95 times the Y_{CO} in the detonation products after the completion of the detonation ($=0.459$ in this study, obtained from the balanced chemical reaction $CH_3NO_2 \rightarrow CO + H_2O + \frac{1}{2}H_2 + \frac{1}{2}N_2$). A similar scaled distance concept was used by Kuhl [120]. Here, the denominator of Eqn. (190) is used as a measure of the mixing layer width (δ).

To demonstrate grid independence, Fig. 81 shows the azimuthally averaged (a) rms velocity components and (b) resolved KE at the 4 msec time instant for the $1000 \times 60 \times 60$ and $1000 \times 75 \times 75$ grids (Note: the $1000 \times 75 \times 75$ grid has 56.25% more grid points than $1000 \times 60 \times 60$ grid). Here, u_r , u_θ and u_ϕ denote, respectively, the radial (r), the azimuthal (θ) and the zenith (ϕ) velocity components, normalized

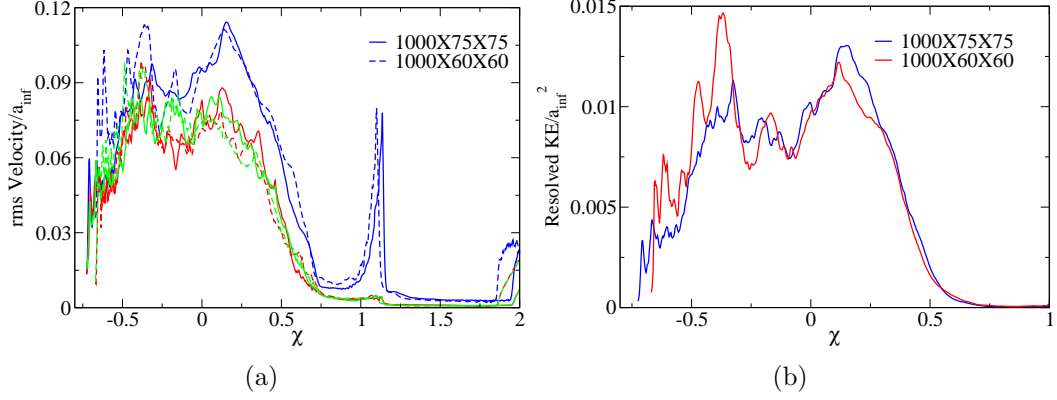


Figure 81: Grid independence. Profiles at 4 msec: (a) rms of velocity profiles (blue: u_r , red: u_θ , green: u_ϕ); (b) resolved turbulent KE.

with the ambient speed of sound (a_{inf}); furthermore, the resolved KE is normalized by a_{inf}^2 (note that this is only a normalization and does not represent the local Mach number, since the speed of sound in the ambient is used instead of the local value). As evident from the figure, reasonable matching is attained for both the rms and KE profiles, thus exemplifying the choice of the grid used ($1000 \times 75 \times 75$) and its accuracy. Some small discrepancies exist in the inner regions, especially near $\chi \sim -0.4$, and this is presumably due to the particle size being comparable to the grid size in the inner regions of the sector grid. However, the discrepancies are small considering that the problem is inherently transient in nature. The turbulence predictions in the outer regions of the mixing layer—in particular, the turbulence decay in the $0.25 \leq \chi \leq 0.6$ (Fig. 81 (b)) region is accurately predicted for both grids. Even the mixing layer boundaries are in reasonable agreement for the $1000 \times 60 \times 60$ and $1000 \times 75 \times 75$ grids, not shown for brevity.

Having demonstrated grid independence, the results from the $1000 \times 75 \times 75$ grid are used for the remainder of this study. The current study confirms that the particle front is spherically symmetric, i.e., not influenced by the three-dimensional effects in the mixing layer for the chosen particle size ($463 \mu\text{m}$ dia.). This is consistent with the experimental observations [214], and is owing to the large size of the particles

chosen ($463 \mu m$), and the high material density of steel, due to which the particles are almost unaffected by the hydrodynamic instabilities.

7.2.1 Mixing layer characteristics

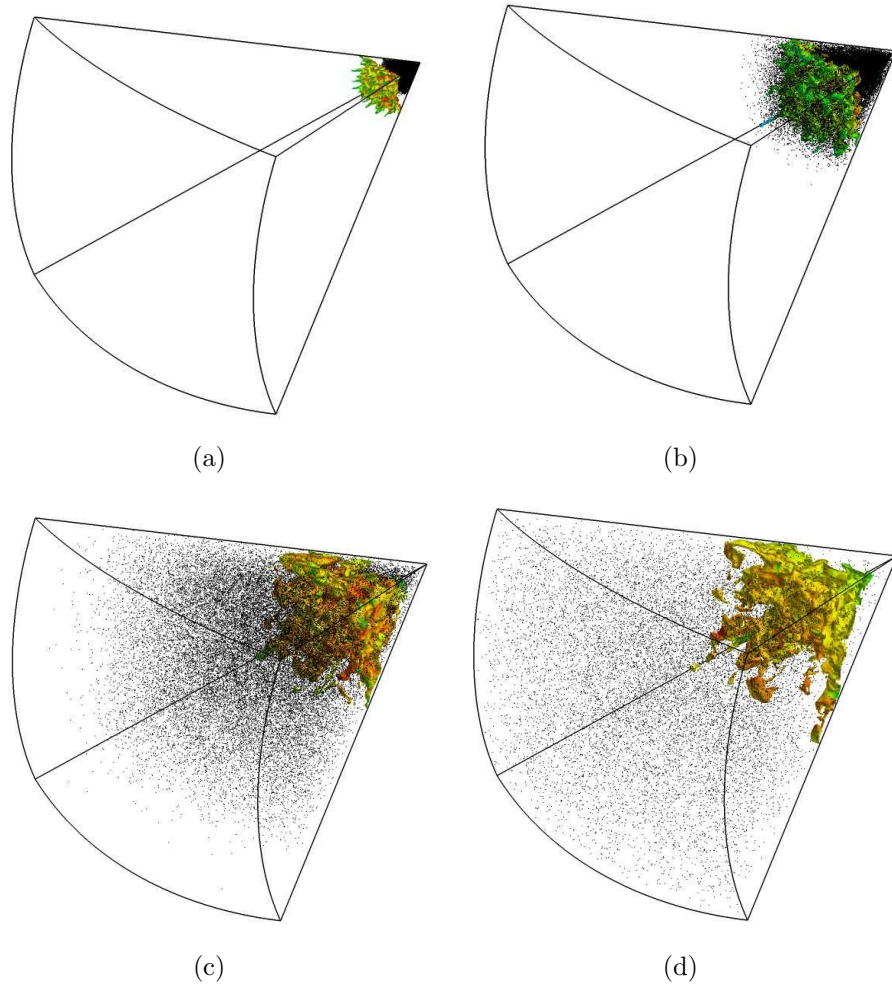


Figure 82: Mixing layer profiles shown at different times: (a) 0.13 msec, (b) 0.58 msec, (c) 1.52 msec, and (d) 4.02 msec.

Here, the dynamics of the mixing layer ensuing from the detonation of the heterogeneous explosive are investigated to detail. The mixing layer at four different times are shown in Fig. 82. It is interesting to note that at early times, i.e., at 0.13 msec (Fig. 82 (a)), the initial Rayleigh-Taylor structures are formed even before the particles overtake the contact surface. This phenomena has been reported in

experimental photography by Frost et al. [74], and is explained as follows: after the onset of the detonation inside the explosive charge, the high-density detonation products expand outward with velocities faster than that of the solid particles, thereby overtaking them. During this process, the expanding detonation products have to encounter the leading particles of the cloud which, by virtue of their random spatial distribution, enforce a non-spherical flow to the expanding gases. In other words, the flow-field between the leading edge of the particle cloud and the contact surface is non-spherically symmetric, with finite, albeit small azimuthal and zenith velocity components induced by the random particle distribution. This non-spherically symmetric flow upon subsequent interaction with the decelerating contact surface, gives rise to the source of the initial perturbations in the latter as shown in Fig. 82 (a). Subsequently, at 0.58 msec (Fig. 82 (b)), the solid particles are seen to overtake the contact surface, during which they further enhance the growth of perturbations in the mixing layer by interacting with the gas in the mixing layer through momentum, heat and work transfer. By 1.52 msec (Fig. 82 (c)), the secondary shock propagates inwards, thereby dragging along with it the lower boundary of the mixing layer, and widening it. Subsequently, the secondary shock reflects from the origin and propagates outwards, and in so doing, interacts with the hydrodynamic structures in the mixing layer during the re-shock phase, a typical Richtmyer-Meshkov instability [169, 146]. This is characterized by the creation of vorticity due to baroclinic torque effects, i.e., mis-aligned pressure and density gradients. This vorticity creation subsequently distorts/wrinkles the flame (Fig. 82 (d)), thereby sustaining the mixing process, and resulting in a loss of memory of the shape of the structures in the mixing layer at late times. In the following sub-sections, these physical phenomena and their consequence to the mixing layer dynamics will be studied in detail.

Figure 83 shows the mass-fractions of CO_2 (Y_{CO_2} , Fig. 83 (a)) and CO (Y_{CO} , Fig. 83 (c)), and the temperature (T , Fig. 83 (b)) field along a slice of the sector

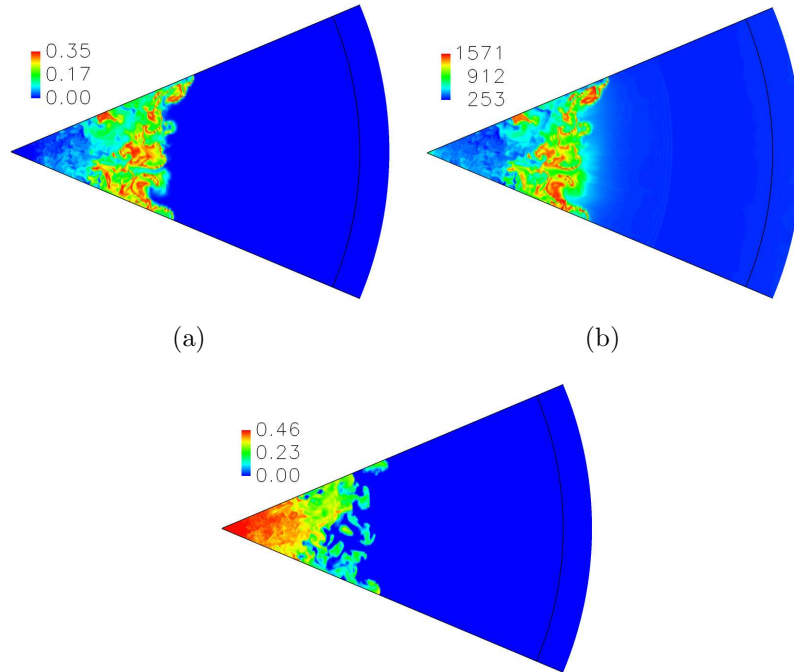


Figure 83: (a) Y_{CO_2} ; (b) Temperature (K); (c) Y_{CO} contours in the mixing layer at 4 msec. In order to illustrate the structure of the mixing layer, the solid particles are not shown.

at the 4 msec time instant; the solid particles are not shown for more clarity of the mixing layer. As evident, the maximas of Y_{CO_2} and T are nearly similar, indicating the obvious exothermicity associated with the burning regions. Furthermore, the T at the core of the sector is significantly ‘cold’, due to the absence of O_2 in these regions, and hence no afterburn occurs at late times in the inner regions of the mixing layer. It is emphasized that if ‘anaerobic’ burning is considered, i.e., combustion of CO with H_2O in the detonation products, the inner regions of the mixing layer would not be ‘cold’; however, no data exists on the kinetics of these reactions behind an explosion, and hence the problem has been reduced to a mixing-controlled combustion and not a kinetic-controlled process. Observing Y_{CO} , mushroom-like structures are evident, and significant concentration fluctuations persist in the mixing layer.

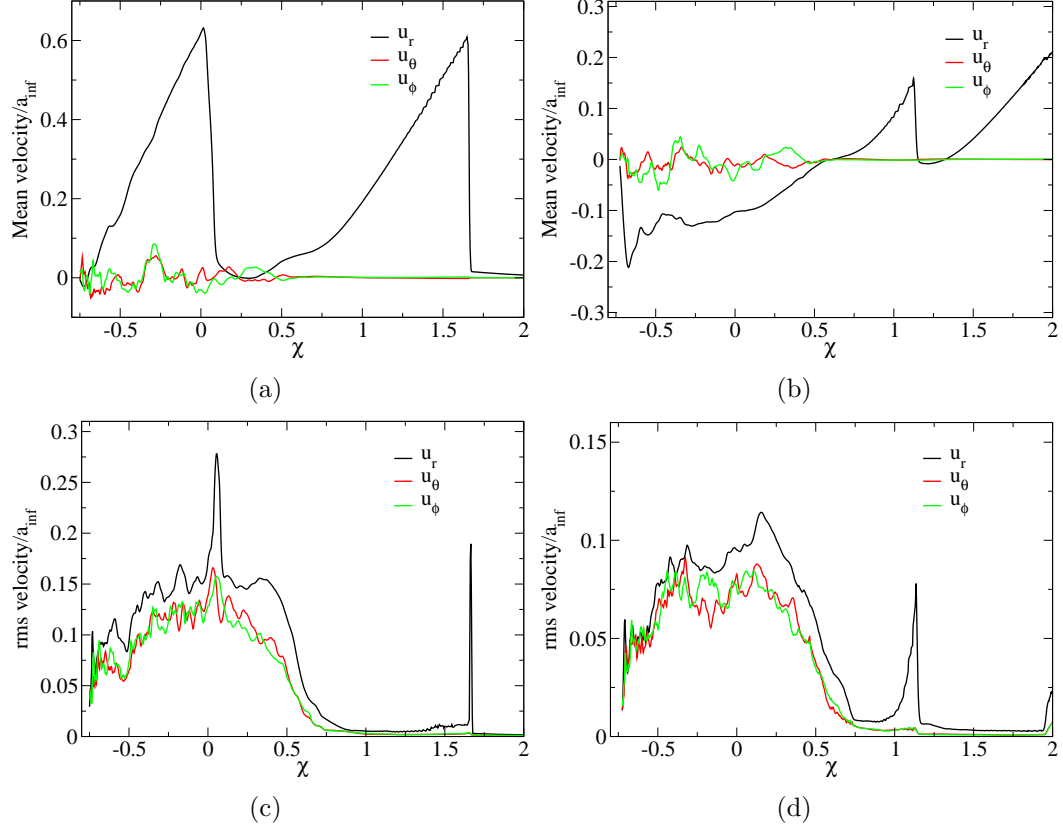


Figure 84: Mixing layer mean ((a) & (b)) and rms ((c) & (d)) velocity profiles shown at 2.2 msec ((a) & (c)) and 4 msec ((b) & (d)).

7.2.1.1 Mean and rms profiles

To get a better understanding of the velocity profiles, Fig. 84 shows the mean (Fig. 84 (a) & (b)) and rms (Fig. 84 (c) & (d)) at times 2.2 and 4 msec, normalized by the ambient speed of sound (a_{inf}). As before, the x -axis denotes the non-dimensional scaled distance (χ), defined as in Eqn. (190). From Fig. 84, both the mean and the rms velocity magnitudes are observed to decrease with time due to the expansion of the flow, and the spikes observed in the radial velocity profiles represent the primary and the secondary shocks. Moreover, as expected, the mean u_θ and u_ϕ fluctuate about zero in Figs. 84 (a) & (b), and are of a similar magnitude. In Figs. 84 (c) & (d), the rms of u_r is about 25% higher than that of u_θ and u_ϕ in the mixing layer, a consequence of the flow being preponderantly biased in the radial direction.

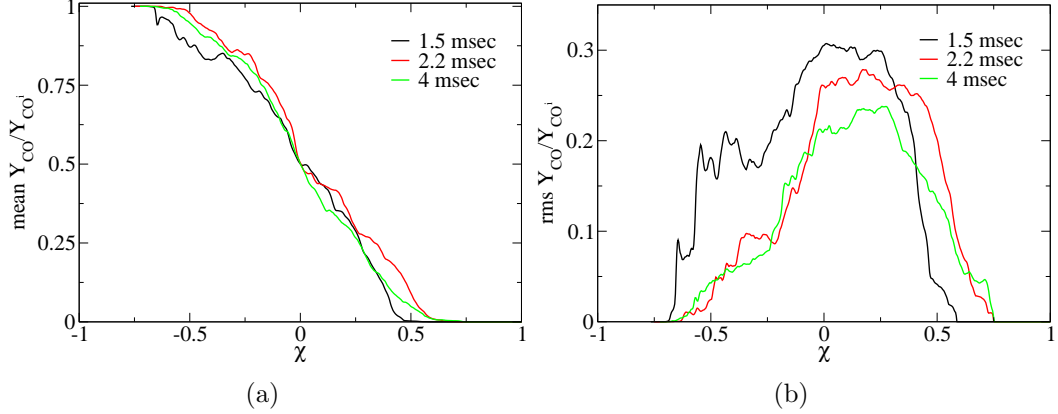


Figure 85: Y_{CO} profiles in the mixing layer normalized with the initial CO mass fraction in the detonation products, Y_{CO}^i : (a) mean; (b) rms.

In order to understand the concentration patterns in the mixing layer, the mean and rms of Y_{CO} are presented at different times, normalized with $Y_{CO}^i = 0.459$, the value of Y_{CO} in the detonation products at the completion of the detonation, in Fig. 85. As before, the x -axis denotes the scaled distance (χ) defined as in Eqn. (190). The mean concentration profiles (Fig. 85 (a)) are self-similar, suggesting that the scaling procedure that has been used is valid. The rms concentration profiles (Fig. 85 (b)) are similar in shape, and the peaks are about 23-30% in intensity; the peak rms concentration decreases in time as a consequence of the decreasing perturbation intensities in the mixing layer.

7.2.1.2 Turbulent kinetic energy and baroclinic torque

The role of perturbations/instabilities is best illustrated with an investigation of the resolved and sub-grid turbulent kinetic energy (KE), as shown in Fig. 86, normalized with a_{inf}^2 . As evident, the resolved and sub-grid KE decay in time owing to the decrease of the velocity magnitudes due to the expansion of the gas. The sub-grid KE is observed to be about 3-4% of the resolved, indicating that most of the turbulent KE is resolved with the $1000 \times 75 \times 75$ grid. Although the contribution of k^{sgs} to the total kinetic energy is minimal, it is essential to capture the finer scales, which would

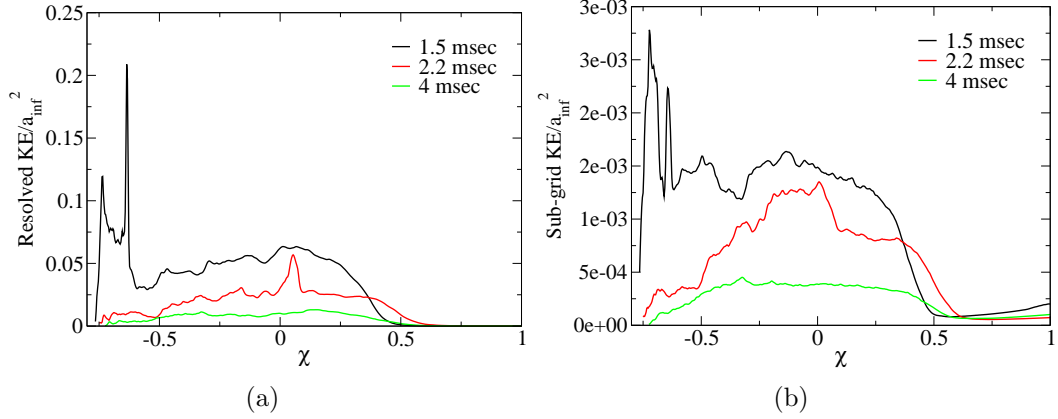


Figure 86: Turbulent kinetic energy profiles: (a) resolved; (b) sub-grid.

otherwise not be accounted for. At 1.5 msec, the peak observed near $\chi = -0.6$ is a consequence of the secondary shock, which enhances the perturbation intensity locally through the baroclinic mechanism. At 2.2 msec, the same peak is observed near $\chi = 0$, albeit of a lower magnitude due to the decay in the strength of the secondary shock as it propagates outwards. The mechanism of turbulence generation is explained with the baroclinic torque effect, i.e., vorticity creation due to mis-alignment of pressure and density gradients, which is prominent inside the mixing layer during the re-shock phase. Of preponderant interest is the role played by vorticity in the dynamics of the flame that exists in the outer regions of the mixing layer during the re-shock phase. Note that since infinite chemistry has been assumed, the flame location is dictated by where and how fast the CO in the inner detonation products mix with the O_2 in the outer air. The effect of the vorticity created during the re-shock phase on the flame will now be studied to detail.

During the re-shock phase, the secondary shock (denoted SS hereafter) deposits vorticity in the mixing layer due to baroclinic effects, as reported in other studies albeit for a homogeneous explosive [13, 120, 121]. This vorticity plays a prominent role in the subsequent wrinkling of the flame, the dynamics of which will now be investigated. Figure 87 shows the temperature and reaction rate of CO ($\log(\exp(-2)-$

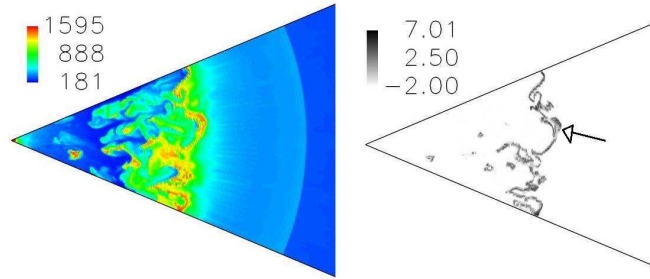
$\dot{\omega}_{CO}$)), with the temperature in K and $\dot{\omega}_{CO}$ in $Kg/m^3/sec$, at different times starting from just before the re-shock phase until a short while later. Since infinitely fast chemistry has been assumed, by reaction rate, it is referred to a mixing-controlled reaction rate, and not kinetically- (temperature) controlled. Thus, the reaction rate refers to how fast CO and O_2 meet/mix so as to react. In Fig. 87 (a), the SS is propagating outwards after reflection from the origin, but before its interaction with the structures in the mixing layer. The thin braid-shaped flame is seen as large-scale structures with smaller-scale corrugations. Subsequently, at 2.21 msec (Fig. 87 (b)), the SS interacts with the flame, across which density gradients exist; this generates vorticity due to baroclinic effects. Arrows are drawn in Figs. 87 (a)-(c) to illustrate a location of interest used to elucidate the role played by vorticity on the flame dynamics. By 4.02 msec (Fig. 87 (c)), the SS has traversed the entire region of the flame, and is outside the mixing layer. In the vicinity of the arrow in Fig. 87 (c), the flame has started to convolute/wrinkle, a consequence of the vorticity deposited by the SS. This phenomenon enhances the effective surface area of the flame, due to which fresh sources of O_2 , which was hitherto unreachable to the inner CO , is now made available for reaction and for sustaining the flame. At the same time, smaller pockets of air that were earlier driven inwards during the implosion phase, get trapped inside the core detonation products and are also being slowly consumed; these pocket flames are also seen in the inner regions at later times (Fig. 87 (c)). Subsequently, these pocket flames will get extinguished after all the O_2 in the inner regions of the detonation products get consumed. In summary, the shape of the main outer flame at the late time (Fig. 87 (c)) is very different from that at the early time (Fig. 87 (a)), due to the significant wrinkling/convolution of the flame during and after the re-shock phase.

7.2.1.3 Concentration gradients

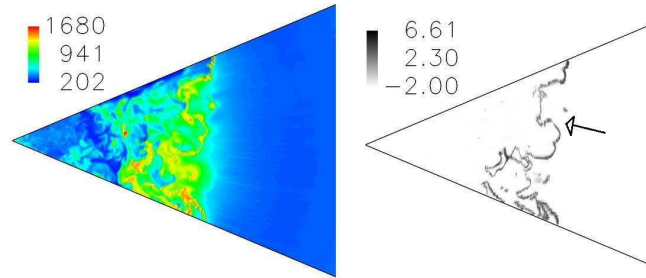
The mixing layer under study is characterized by deep intrusions of the inner detonation product gases into the outer ambient air and vice versa, a typical characteristic of Rayleigh-Taylor instabilities. The study of concentration gradients is an indicative measure of the mixing process in any mixing layer, as has also been studied by Freund et al. [70] for a turbulent annular mixing layer. In the mixing layer under study presently, the behavior of concentration gradients is complicated due to the spherical nature of the problem and the presence of a re-shock, when compared to planar and annular mixing layers. The CO mass fraction gradients are presented at different times in Fig. 88 ($\log(\exp(-2) + |\nabla Y_{CO}|)$); the *prima facie* observations that can be deduced from this figure are: at very early times (Fig. 88 (a)), thin braid-like structures of high CO concentration gradients exist, typical of Rayleigh-Taylor instabilities. These gradients are initially aligned along the radial direction, with C-shaped ‘caps’ connecting them outside and inside—the outer ones are the spikes and the inner ones are the bubbles (Note: radial braids represent azimuthal/zenith concentration gradients, and ‘caps’ represent radial concentration gradients). These caps correspond to the bubbles and spikes, while the gradients along the radial direction correspond to the stem of the Rayleigh-Taylor instability that connects the bubbles and spikes.

Subsequently, due to the spherical nature of the problem, the behavior of these concentration gradients differs from planar and annular mixing layers that have been studied in the past. As the flow convects outwards, the concentration gradients are radially stretched, causing the concentration gradients across the radially aligned braids to decrease in magnitude as the surrounding air is entrained into them. The concentration gradients across the ‘caps’ also decrease, but to a much lower degree when compared to the radial braids, as seen in Fig. 88 (b). This indicates that mixing due to flow entrainment decreases the concentration gradients faster across

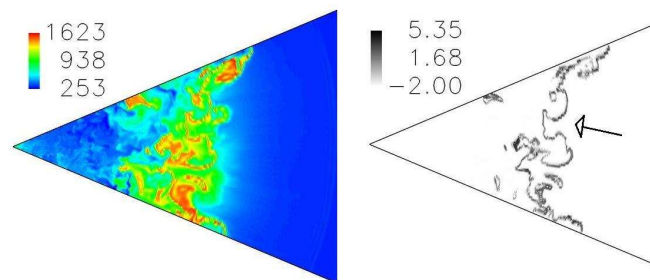
the radial braids, than across the inner and outer ‘caps’. Analysis suggests that this feature is due to the higher surface area of the radial braids than the caps and, consequently, a higher entrainment of the ambient air through the radial braids than through the inner and outer caps. During the implosion phase (Fig. 88 (c)), the inner ‘caps’ are imploded inwards, still preserving their ‘cap’-like curved shape. However, subsequently, after the re-shock phase, these concentration gradients (or ‘caps’) flatten out, a phenomenon known as ‘phase inversion’ [219]. At late times (Fig. 88 (d)), the regions of steep CO concentration gradients are more or less flat, and start to lose their preferential alignment.



(a)



(b)



(c)

Figure 87: Flame dynamics in the mixing layer: Temperature (K) and $\dot{\omega}_{CO}$ ($\log(\exp(-2) - \dot{\omega}_{CO})$) profiles at times (a) 1.42 msec; (b) 2.21 msec; (c) 4.02 msec. Temperature on the left and $\log(\exp(-2) - \dot{\omega}_{CO})$ on the right.

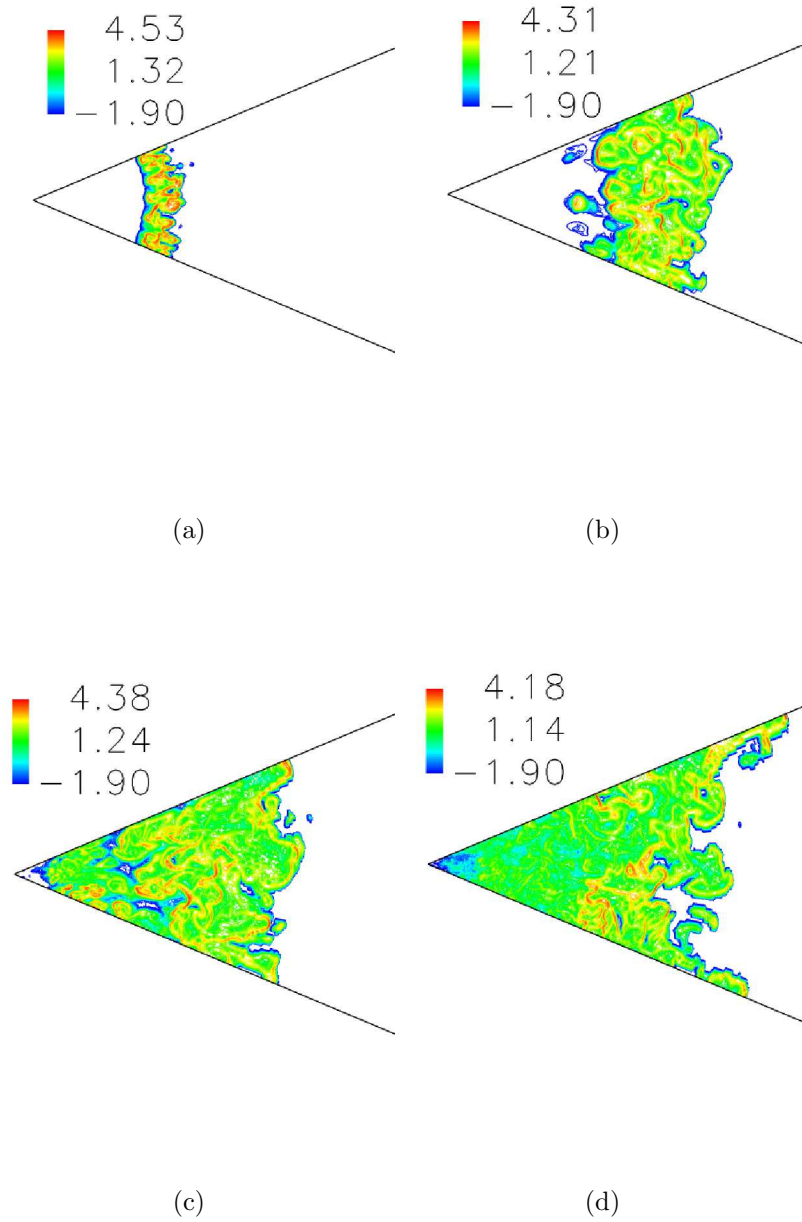


Figure 88: *CO* mass fraction gradient in the mixing layer at times (a) 0.22 msec; (b) 1.04 msec; (c) 1.62 msec; (d) 4.02 msec. The quantity $\log(\exp(-2) + |\nabla Y_{CO}|)$ is presented.

7.2.2 Some parametric studies

7.2.2.1 Comparison to a homogeneous explosive charge

To illustrate the role played by the particles in the mixing and perturbations/instabilities in the mixing layer of the heterogeneous explosive, the heterogeneous explosive charge (NM/Fe) is compared with a homogeneous explosive (NM) containing the same amount of the high explosive, but, instead, Gaussian random perturbations are added in the outer vicinity of the charge to serve as a source of the initial perturbations. This approach of adding perturbations has been used before [13, 120, 121]. One of the major differences between the mixing layers for the NM and NM/Fe charges is that, for the former, the perturbations are added at the initial time instant, and then allowed to grow at its own ‘un-forced’ rate. On the other hand, for the mixing layer of the NM/Fe charge, the perturbations are constantly ‘forced’ due to the presence of the particles; thus, the mixing layers for NM and NM/Fe charges differ in the underlying physics.

In Fig. 89, the (a) rms of velocity and (b) rms of Y_{CO} are compared between the NM/Fe and NM charges at the 4 msec time instant. As evident, the rms of velocity and concentrations are higher for the NM/Fe charge than the NM charge by about 25-40%, illustrating that the former has higher perturbation levels in the mixing layer. Since the perturbations in the mixing layer are constantly forced for the NM/Fe charge owing to the presence of the particles, the perturbation levels are concomitantly higher. Furthermore, due to the presence of particles for the NM/Fe charge, the implosion and re-shock phases are delayed (to be discussed shortly) as a part of the momentum and energy from the gas are absorbed by the particles. Consequently, the baroclinic torque effect, which plays an important role in re-energizing the turbulence levels in the mixing layer is also delayed, implying that the perturbation intensity persists longer for the heterogeneous charge, as also confirmed in the turbulent KE profiles (Fig. 89 (c)).

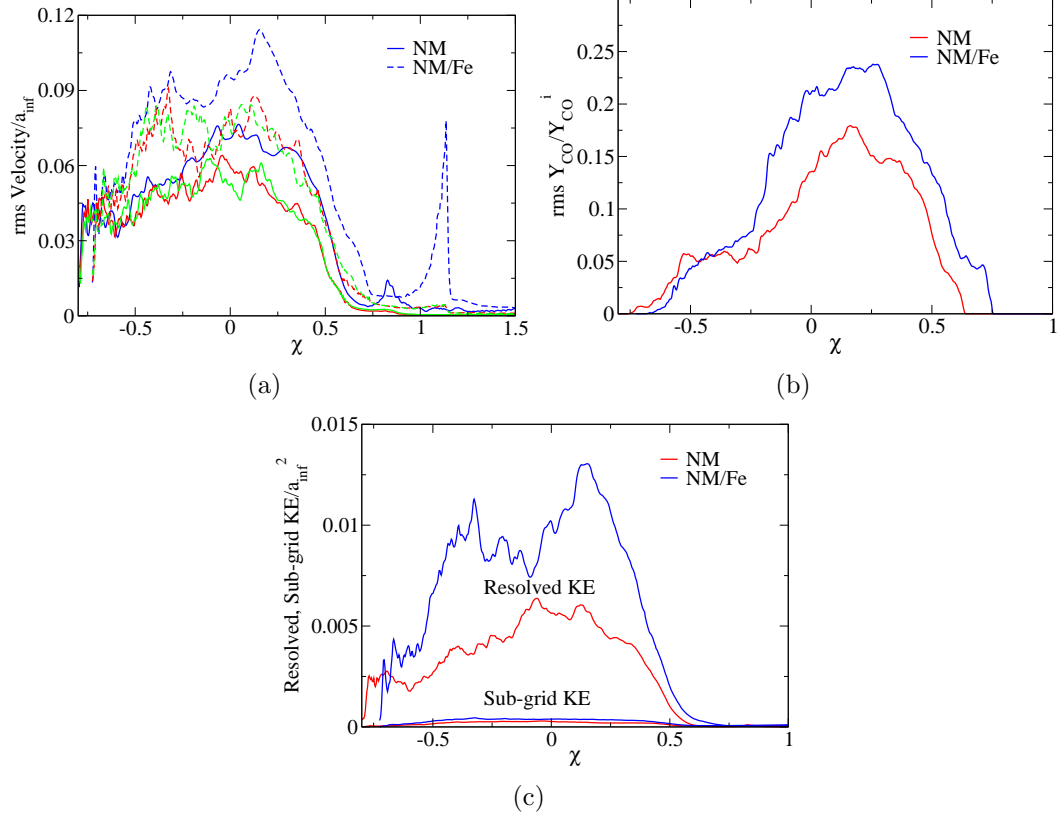


Figure 89: Comparison of homogeneous (NM) and heterogeneous (NM/Fe) explosives at 4 msec: (a) rms of velocity profiles (blue: u_r , red: u_θ , green: u_ϕ); (b) rms of Y_{CO} ; (c) resolved and sub-grid turbulent KE.

Figure 90 presents the (a) the mixing layer boundaries for the NM and NM/Fe charges and (b) the mixing layer width (δ). Here, the inner and outer boundaries are defined as the locus of the azimuthally averaged Y_{CO} being equal to $0.95Y_{CO}^i$ and $0.05Y_{CO}^i$, respectively, where Y_{CO}^i denotes the mass fraction of CO at the completion of the detonation (assumed 0.459 in this study from a simple balanced equation). Furthermore, the mixing layer width is defined as $\delta = r_{0.05} - r_{0.95}$, where $r_{0.05}$ and $r_{0.95}$ represent, respectively, the outer and inner boundaries of the mixing layer as just defined; the subscripts 0.05 and 0.95 are used in accordance with their respective mass-fraction value based definitions. Although this definition of the mixing layer boundaries is rather *ad hoc*, it gives a reasonable measure of the mixing layer width. As evident from Fig. 90 (a), the implosion phase terminates later for the NM/Fe

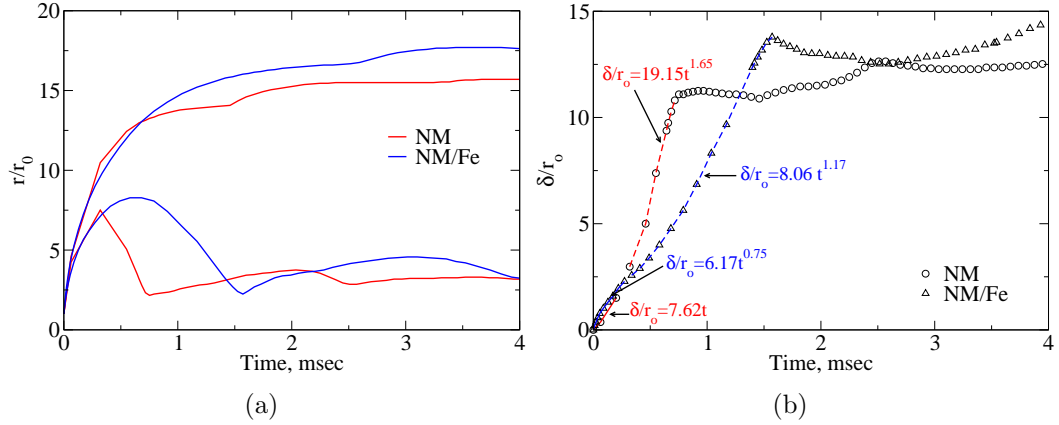


Figure 90: Comparison of the homogeneous (NM) and heterogeneous (NM/Fe) explosive charges containing the same amount of the high explosive: (a) mixing layer boundaries; (b) mixing layer width (δ). For the curve-fit expressions in (b), t is computed in msec.

charge (0.75 msec for NM, 1.5 msec for NM/Fe). This is due to the absorption of momentum and energy from the gas by the particles, and thereby ‘obstructing’ its passage during both its outward and inward passages; this delays the implosion phase for the NM/Fe charge. Furthermore, since perturbations and mixing levels are higher for the NM/Fe charge at the same time instant, as aforementioned, the outer boundary of the mixing layer extends farther by about 2.5 charge radii for the NM/Fe charge as more mixing results in more afterburn energy release—a driving force for the outer boundary.

To compare the dependence of the mixing layer widths on the perturbation/instability effects, δ , normalized with the charge radius (r_o) is plotted in Fig. 90 (b) for the NM and NM/Fe charges; also shown are the curve-fit expressions for δ/r_o as functions of time (t in msec). During the early blast wave phase, δ grows linearly with time ($\sim t$) for NM, but non-linearly for NM/Fe ($\sim t^{0.75}$), and is wider for the latter at the same time instant during these early times (note that for small t , $t^{0.75}$ is a faster growth than t^1). While the linear trend has also been reported in other studies [13, 120] for homogeneous explosive charges, the non-linear growth for the heterogeneous charge

is presumably due to the continuously forced perturbations introduced to the flow in the mixing layer by the particles. At early times, small perturbations begin to grow linearly—first predicted by Richtmyer [169]—until the perturbation grows to large enough sizes, after which non-linear growth ensues. This theory is presumably not valid for NM/Fe explosions due to the continuous forcing introduced by the particles. For the NM charge, the Gaussian random perturbations added grow at their own ‘un-forced’ rate, while for the NM/Fe charge, the continuous perturbation of the flow due to the particles causes the mixing layer to grow at a ‘forced’ rate. As reported earlier, the perturbations form even before the particles overtake the mixing layer, suggesting that the early perturbations in the mixing layer for the NM/Fe charge must be significantly high in order to cause the departure from linearity. This is supportive of observations stated previously with reference to Fig. 89. Subsequently, since the implosion phase starts earlier for the NM charge (see Fig. 90 (a)), δ grows faster for NM, overtaking that for the NM/Fe charge near 0.35 msec (see Fig. 90 (b)).

During this implosion phase, the growth rate of δ scales as $\sim t^{1.65}$ for NM, and $\sim t^{1.17}$ for NM/Fe, suggesting that particles subdue the rate of implosion of the inner boundary of the mixing layer *vis-a-vis* the un-obstructed passage permissible for the NM charge. This claim is further substantiated by observing the inner boundary of the mixing layer during the implosion phase in Fig. 90 (a), from which it is evident that the inner boundary implodes to about $2.5 r_o$ for both charges, albeit about 0.8 msec later for NM/Fe charge. Thus, since the particles absorb momentum and energy from the gas, the rate of growth of the mixing layer during the implosion phase is subdued due to the lesser momentum and energy available to drive the secondary shock inwards. Due to this delay, the outer boundary stretches farther for NM/Fe (see Fig. 90 (a)), and concomitantly, the mixing layer width is also wider by about $2.5 r_o$ at the completion of the implosion phases for both the charges. Subsequently, the mixing layer stays wider for the NM/Fe charge, as evident from Fig. 90 (b).

7.2.2.2 Effect of particle size

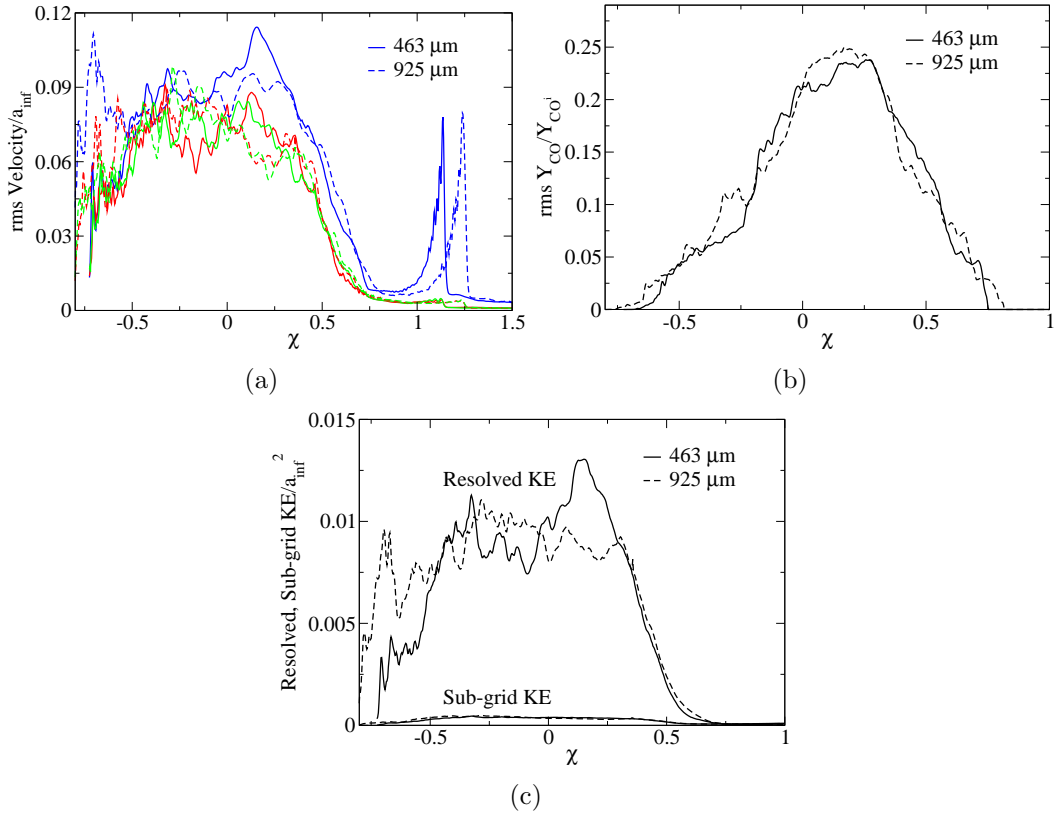


Figure 91: Comparison of 463 μm and 925 μm particle sizes at 4 msec: (a) rms of velocity profiles (blue: u_r , red: u_θ , green: u_ϕ); (b) rms of Y_{CO} ; (c) resolved and sub-grid turbulent KE.

Since the mixing layer turbulence characteristics are influenced by the particles, it is also of interest to consider the effect of particle size. To this end, another simulation is carried out for a 11.8 cm dia. heterogeneous explosive charge containing NM and steel, with the same initial volume fraction of solid particles as before (62%), but with 925 μm steel particles; experimental data for this choice also exists [214]. The rms of velocity and Y_{CO} are shown in Figs. 91 (a) & (b), respectively, at the 4 msec time instant, and compared with those corresponding to the 463 μm particle size used hitherto. As evident from Fig. 91 (a), the velocity trends are nearly similar in shape for the two particle sizes, although some minor differences do exist in the

turbulence intensities—near $\chi \sim 0.25$, the intensities are about 10% higher for the 463 μm particle charge; this reverses near $\chi \sim -0.75$, i.e., near to the core of the charge, with the intensities being higher for the 925 μm charge. However, note that the 925 μm particle size is comparable to the grid size in the core regions—the point particle assumption is over-stretched in these regions. Despite this minor discrepancy, the dense multiphase approach used in the current study is able to simulate and predict most of the flow-physics of relevance to the problem. From Fig. 91 (b), observing the trend of rms of Y_{CO} , the profiles are similar, showing independence to the choice of the particle size; this demonstrates that the mixing-controlled reaction time scales are much faster than the particle-gas interaction time scales, due to the large size of the particles, 463 μm and 925 μm alike. In Fig. 91 (c), the resolved and the sub-grid kinetic energies (KE) are presented; as evident from the figure, the profiles are similar, with slightly enhanced turbulence levels near $\chi \sim 0.25$ with the 463 μm particles, and a trend reversal near $\chi \sim -0.75$, consistent with the findings from Fig. 91 (a). However, note that these differences are minimal.

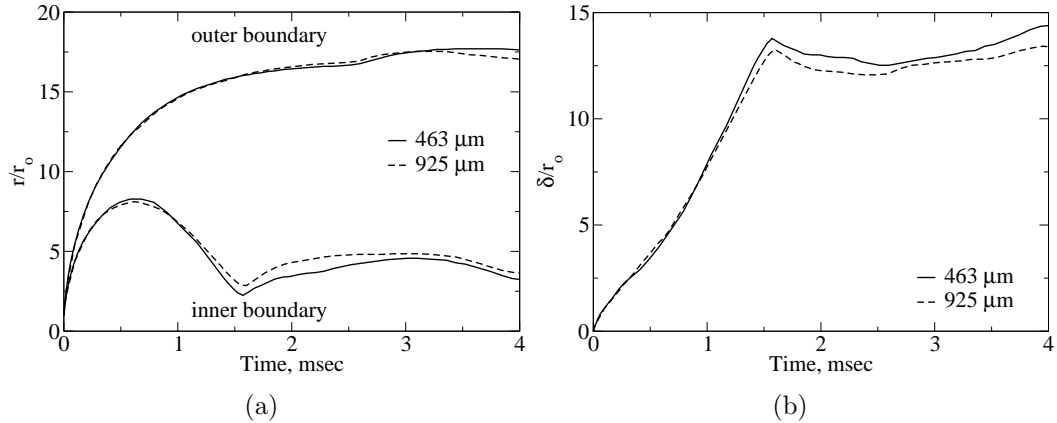


Figure 92: Comparison of the 463 μm and 925 μm particle sizes: (a) mixing layer boundaries; (b) mixing layer width (δ).

Also of interest are the mixing layer boundaries and the width for the two explosive charges with different particle sizes, viz. 463 and 925 μm . To this end, the outer and

inner boundaries of the mixing layer are presented in Fig. 92 (a), normalized with the initial charge radius, r_o . The profiles are nearly similar, except for some minor differences in the inner boundary subsequent to the reshock phase (~ 1.5 msec). The inner boundary of the mixing layer for the 463 μm charge is slightly more inside, by about $\frac{1}{2}r_o$, presumably due to the relatively shorter momentum transfer time scales of the 463 μm particles relative to their 925 μm counterparts. This results in a slightly wider mixing layer width from Fig. 92 (b) for the charge corresponding to the 463 μm particles. However, note that the ‘fireball’ as seen by an observer from outside the charge will nevertheless be the same, as is evidenced by the outer boundary of the mixing layer in Fig. 92 (a). In summary, from Figs. 91 and 92, the mixing layer characteristics do not differ significantly for the 463 and 925 μm particle sizes.

7.2.3 Concluding remarks

Thus far in this chapter, the problem of heterogeneous explosive charges was discussed, both from a one-dimensional and three-dimensional sense. The one-dimensional study demonstrates the efficacy of the EL DEM formulation for investigating similar problems, and has demonstrated the use of this approach as a tool to study impulsive loading from heterogeneous explosive charges for a wide range of operating parameters. In the second part, three-dimensional effects such as hydrodynamic instabilities are observed to play a prominent role in the mixing layer. Furthermore, the study demonstrates that inert particles perturb the mixing layer, causing higher perturbation/instability levels at the same time instant, and concomitantly, higher mixing and afterburn than the corresponding homogeneous explosive charge containing the same amount of the high explosive. Thus, the mixing layer characteristics subsequent to the detonation of a heterogeneous explosive are significantly different from that of a homogeneous explosive charge containing the same amount of the high explosive. For a heterogeneous explosive charge comprising of particles with twice the size as the

baseline charge, the mixing layer characteristics are not very different, emphasizing that particle size does not play a role in the mixing process for heterogeneous explosive charges of the kind explored in this study. Overall, these studies have demonstrated the efficacy of the EL DEM approach, and have provided useful insights to characterize the perturbations/instabilities in the mixing layer ensuing from heterogeneous explosions.

7.3 Aluminized Explosive Charges

Reactive metal particles are very commonly added to high explosive charges due to their high energy content, thereby providing energy release in addition to that from the detonation and afterburn of the high explosive. Aluminum (Al), magnesium (Mg) and zirconium (Zr) are the usual candidates for the choice of the metal added to explosives, as these metal particles absorb heat from the gas, ignite and burn, and release significant amounts of energy. The study of explosive charges containing solid aluminum particles has been undertaken in the past, see for instance [72, 190, 197, 216, 218] and the references therein. Despite these studies, three-dimensional simulations of these explosives, with focus on the aluminum burning characteristics, and its effects on the fire-ball are still in its infancy.

Explosive charges containing inert steel particles have been considered hitherto in the current research effort; building on this foundation, the simulation is extended to the study of explosive charges containing a dense loading of solid aluminum particles. Recall from before, whereas explosive charges containing large inert steel particles find their application as an heterogeneous explosive charge by delivering additional impulsive loading from bombardment on to a structure by the solid particles, the role of aluminum particles when present in explosives is to deliver additional impulse by afterburning and releasing additional energy. Here, the afterburn characteristics of aluminized explosive charges are considered, with TNT as the high explosive. Of

particular interest here is the ignition and burning characteristics of the aluminum particles—necessitating the use of small size particles. It is emphasized that the Lagrangian tracking approach used here does not enable the simulation of cm-size explosive charges (corresponding to Kg-range high explosive by mass) with $\sim 5\text{--}10\ \mu\text{m}$ particles due to limited computational memory. Thus, mm-size charges corresponding to gram-range high explosive by mass is considered with small aluminum particles. The goal here is not to directly compare these gram-range charges with their counterpart Kg-range charges that have been hitherto studied; rather, the goal here is to demonstrate the efficacy of the currently developed EL-DEM for dense aluminized explosive charges, and shed light on the physics of this kind of explosives, albeit in the gram-range initial charge mass.

The simulation strategy employed before is used here, and the initial explosive charge comprising of TNT and aluminum is 5 mm in radius. This is simulated using a 0.256 m long, 45° sector, which is resolved using a $1000\times 60\times 60$ grid. Grid independence has been checked, and this chosen resolution is found to suffice to capture the relevant scales in the mixing layer. The aforementioned one-equation eddy viscosity sub-grid closure is used to compute the effect of the sub-grid scales on the resolved scales. This study is divided into three subsections to address the (i) effect of particle size; (ii) effect of initial solid volume fraction in the charge; and (iii) effect of the choice of burn time used for the aluminum evaporation model. These studies are now elaborated, focusing on the transient burning of aluminum particles, particle front trajectory, mass-weighted average particle temperature and velocity, afterburn of detonation products and the radius of the ensuing fire-ball. Particle radius (r_p) in the range $2.5\text{--}10\ \mu\text{m}$, and initial solid volume fractions in the range 10-40 % are considered for the present investigation. The simulations are stopped at approximately 0.25 msec for each of the cases considered here.

For the TNT-Al charge comprising of $r_p = 2.5\ \mu\text{m}$ Al particles, initially occupying

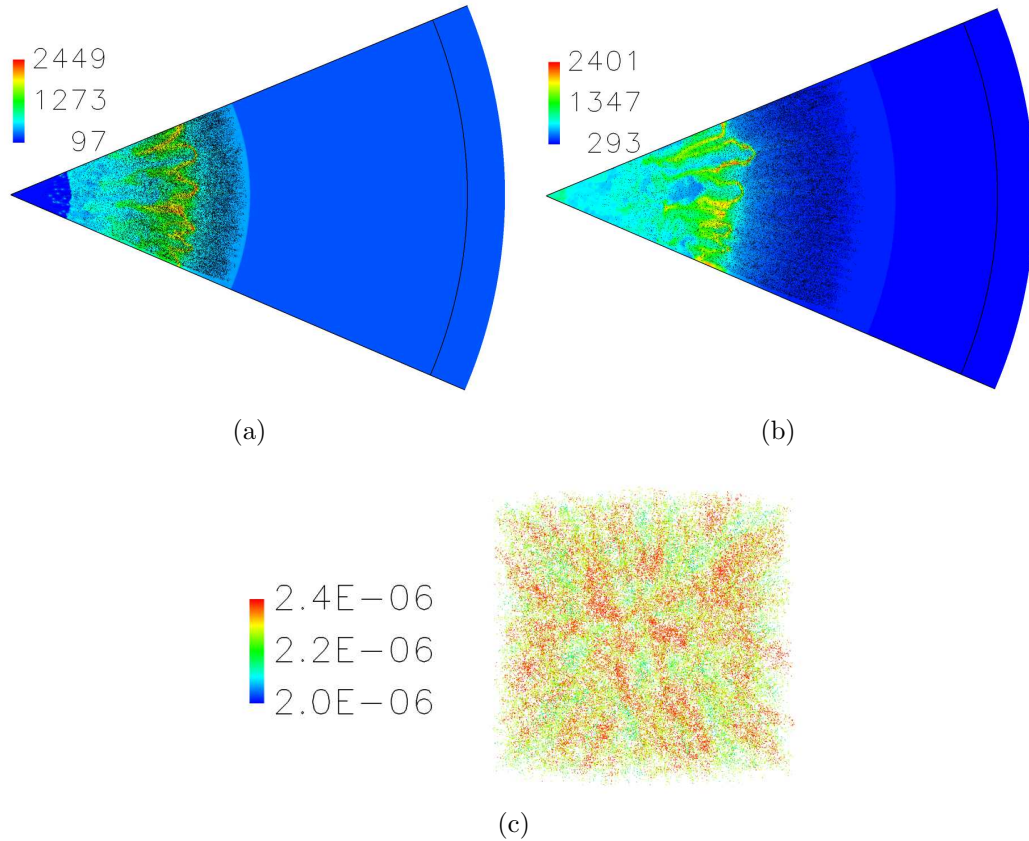


Figure 93: Aluminized explosive charges ($r_p = 2.5 \mu\text{m}$; 40 % initial solid volume fraction): gas temperature (in K) and particle locations at (a) 0.1 msec, (b) 0.215 msec; (c) particle radius in μm at 0.215 msec (only leading particles shown).

a 40 % solid volume fraction, the gas temperature (in K) and particle locations are shown for illustration in Fig. 93 at (a) 0.1 msec and (b) 0.215 msec. At the earlier time, the particle cloud is observed to just trail behind the leading blast wave; at the later time, the leading particles are observed to have slowed down further, thereby widening the gap between the particle front and the leading blast wave. To demonstrate preferential combustion of aluminum particles, Fig. 93 (c) shows the particle locations colored with their respective temperatures (only the leading particles are shown for better clarity) at 0.215 msec, and, as evident, slightly different burning characteristics are observed for different particles, with some particles burning more than their neighboring counterparts, owing to some particles having gone through

enhanced afterburning regions of the mixing layer. The observed particle distribution and temperature patterns are different when compared to the clustering presented earlier for dilute aluminum particle clouds when present outside the explosive charge.

7.3.1 Effect of particle size

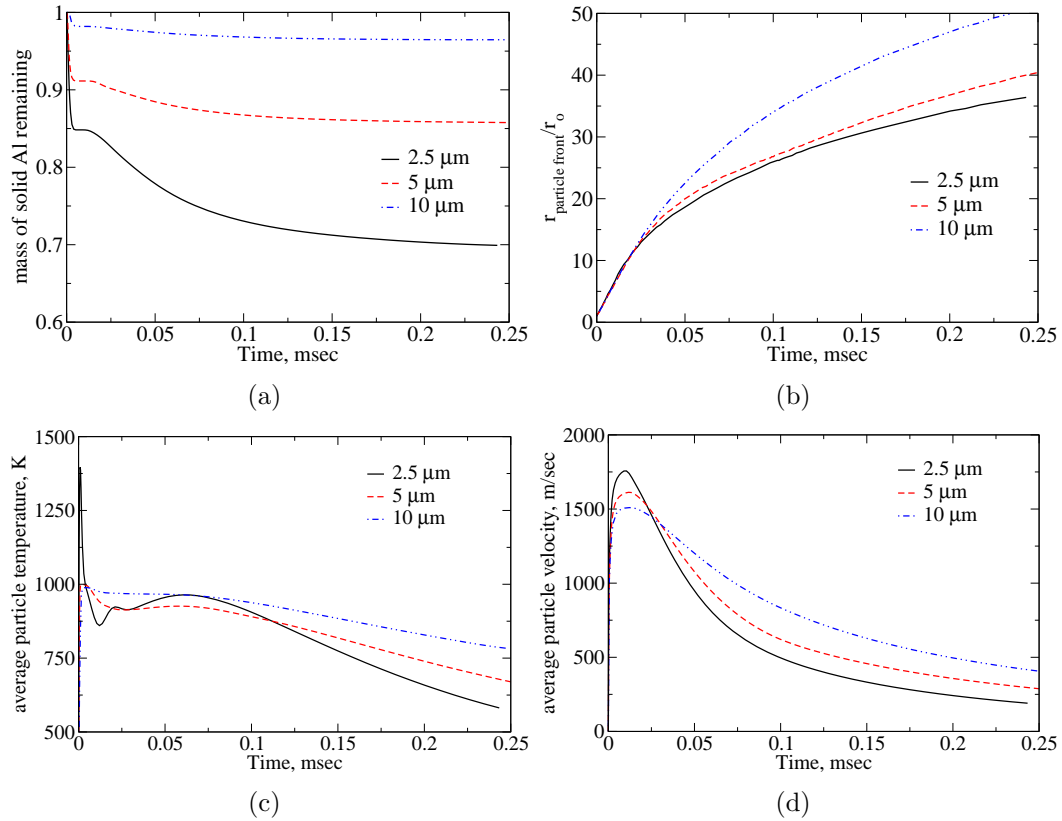


Figure 94: Effect of particle size on aluminumized explosive charges: (a) normalized mass of solid Al remaining; (b) particle front trajectory; (c) average particle temperature; (d) average particle velocity.

The effect of particle size is illustrated in Fig. 94 for a TNT-Al charge corresponding to 20 % initial solid volume fraction, for charges with $r_p = 2.5, 5$ or $10 \mu\text{m}$ Al particles, with the amount of solid Al remaining with time, normalized with the initial mass of solid Al, presented in Fig. 94 (a). As evident, the particles quickly ignite and then burn for a short while ($\sim 5 \mu\text{sec}$), with the rarefaction wave quenching

them. Subsequently, as the leading particles enter the mixing zone, the afterburn energy release, viz. from the afterburn of the inner detonation products with the outer air, re-ignites the particles, and sustains the burning for a longer time than the first aluminum burning phase. As more particles enter the mixing zone and ignite, more solid aluminum by mass evaporates. Later, as the particles leave the mixing zone, they quench, with 96 % solid Al by mass still unevaporated for $r_p = 10 \mu\text{m}$; 86 % for $r_p = 5 \mu\text{m}$; and 70 % for $r_p = 2.5 \mu\text{m}$. In Fig. 94 (b), the particle front trajectory (defined here as the radius within which 98% of the total particles are contained) is presented for the three different sizes and, as evident, the larger particles by virtue of their higher inertia travel a farther distance than their smaller counterparts.

The mass-weighted average particle temperature is presented in Fig. 94 (c); it is observed that the initial temperature rises rapidly as the particles pick up energy from the gas; the particles then cool-off fast due to the rarefaction, and then the temperature more-or-less flattens out near 0.07 msec, only to constantly decrease much later as the particles leave the mixing zone. It is interesting to note that the $r_p = 2.5 \mu\text{m}$ particles actually show a temperature increase around 0.07 msec, as these particles have faster response times and therefore pick up significant amounts of heat as they traverse the mixing zone; it is also interesting to note that the smaller $r_p = 2.5 \mu\text{m}$ particles not only heat up more during the heating phase, but also cool down more during the cooling phase (~ 0.01 msec)—when they interact with the rarefaction wave.

The mass-weighted average particle velocity is shown in Fig. 94 (d) and, as evident, the smaller particle size not only accelerates more during the early acceleration phase, but also decelerates more during the later deceleration phase—exemplifying that inertia plays a role in the particle velocities. The afterburn of the detonation products is of interest, and the normalized C(S) mass fraction is presented in Fig. 95 (a). As observed, more of the detonation products are consumed for $r_p = 10 \mu\text{m}$,

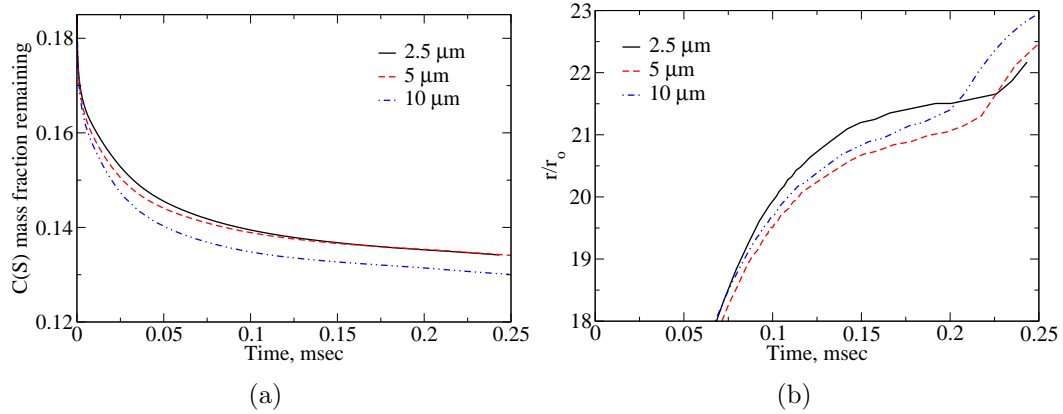


Figure 95: Effect of particle size on afterburn effects of aluminized explosive charges: (a) mass fraction of C(S) remaining; and (b) fire-ball radius.

as these large particles introduce significant amounts of early perturbations on the contact surface, which later grows into wider Rayleigh-Taylor structures, thereby resulting in more afterburn. Observing Fig. 95 (b), the fire-ball radius (defined here as the radius corresponding to where the azimuthally averaged CO mass fraction corresponds to 5 % of the CO mass-fraction at the onset of detonation completion within the initial charge) grows faster for the smaller particle size, but is later overtaken for the larger particle size. It is also evident that the re-shock is delayed for the smaller particle size, as the amount of afterburn of the detonation products is less (even though more aluminum burns for the smaller particle size).

7.3.2 Effect of volume fraction

The focus here is to understand the effect of volume fraction to the parameters of interest in the afterburn phase. Both $r_p = 5 \mu\text{m}$ and $r_p = 2.5 \mu\text{m}$ are considered so as to investigate whether particle size plays a role in the trends observed; the initial solid volume fraction is varied in the range 10-40 %. First, the results for $r_p = 5 \mu\text{m}$ are presented in Fig. 96. From Fig. 96 (a) (normalized mass of solid Al remaining with time), more solid Al is consumed when the initial solid volume fraction is lower. This is evident because a lower solid volume fraction corresponds to a scenario where

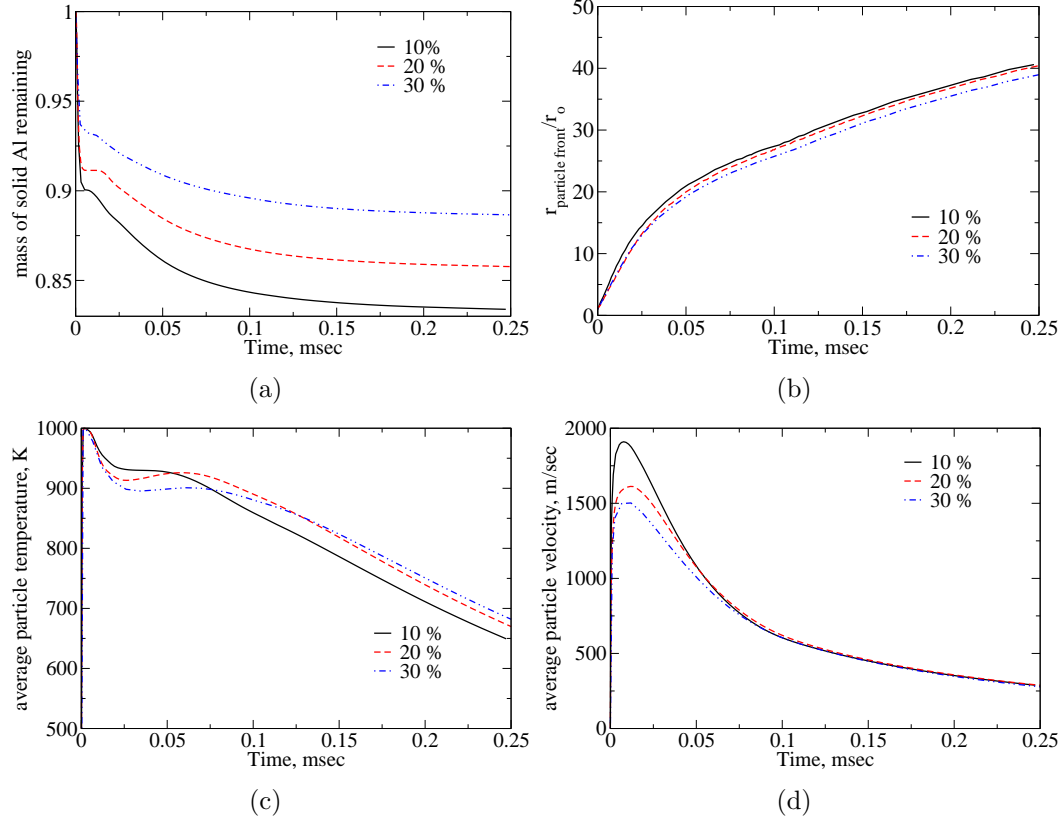


Figure 96: Effect of initial solid volume fraction on aluminized explosive charges containing $r_p = 5 \mu\text{m}$ particles: (a) mass of solid Al remaining; (b) particle front trajectory; (c) average particle temperature; (d) average particle velocity.

more high explosive by mass is present to ignite and drive fewer Al particles. Hence, even the particle front travels a farther distance when the initial solid volume fraction is lower, as presented in Fig. 96 (b). Observing the mass-weighted average particle temperature in Fig. 96 (c), it is evident that when fewer particles (and more high explosive) are present, the early time particle temperatures are higher (~ 0.05 msec) due to more explosive energy available; however, at late times, the average particle temperature decreases more when the initial volume fraction is lower, maintaining a more-or-less constant difference with the other initial solid volume fraction cases considered.

Observing the mass-weighted average particle velocity in Fig. 96 (d), it is evident that smaller initial solid volume fractions result in faster particle velocities as

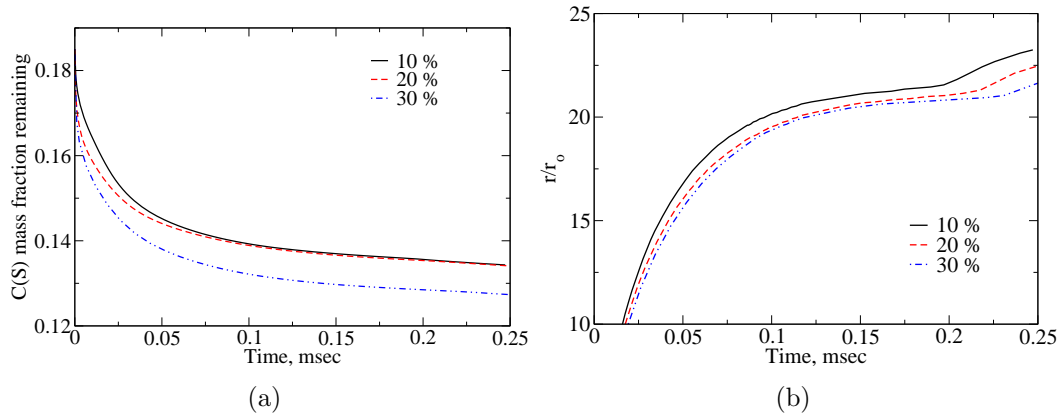


Figure 97: Effect of initial solid volume fraction on the afterburn effects of aluminized explosive charges containing $r_p = 5 \mu\text{m}$ particles: (a) mass fraction of C(S) remaining; (b) fire-ball radius.

more explosive energy is available to drive fewer solid particles; at later times, it is interesting to note that the solid particles decelerate to velocities independent of the initial explosive energy content—emphasizing that the drag effects at late times do not depend on the early time particle acceleration phase behavior. It is also of interest to investigate the afterburn effects in the fireball, and these aspects are presented in Fig. 97. Observing the C(S) mass fraction remaining with time in Fig. 97 (a), it is evident that more particles when present in the initial charge result in more perturbations on the contact surface, and therefore more afterburn of the detonation products. Observing the fire-ball radius from Fig. 97 (b), fewer solid particles when present in the initial charge (smaller initial solid volume fraction)—correspondingly, more high explosive by mass—result in larger fire-balls at late times owing to the higher volume of detonation product gases produced in the explosion event. These trends and discussions also hold for $r_p = 2.5 \mu\text{m}$, as observed from the counterpart figures presented in Figs. 98 and 99.

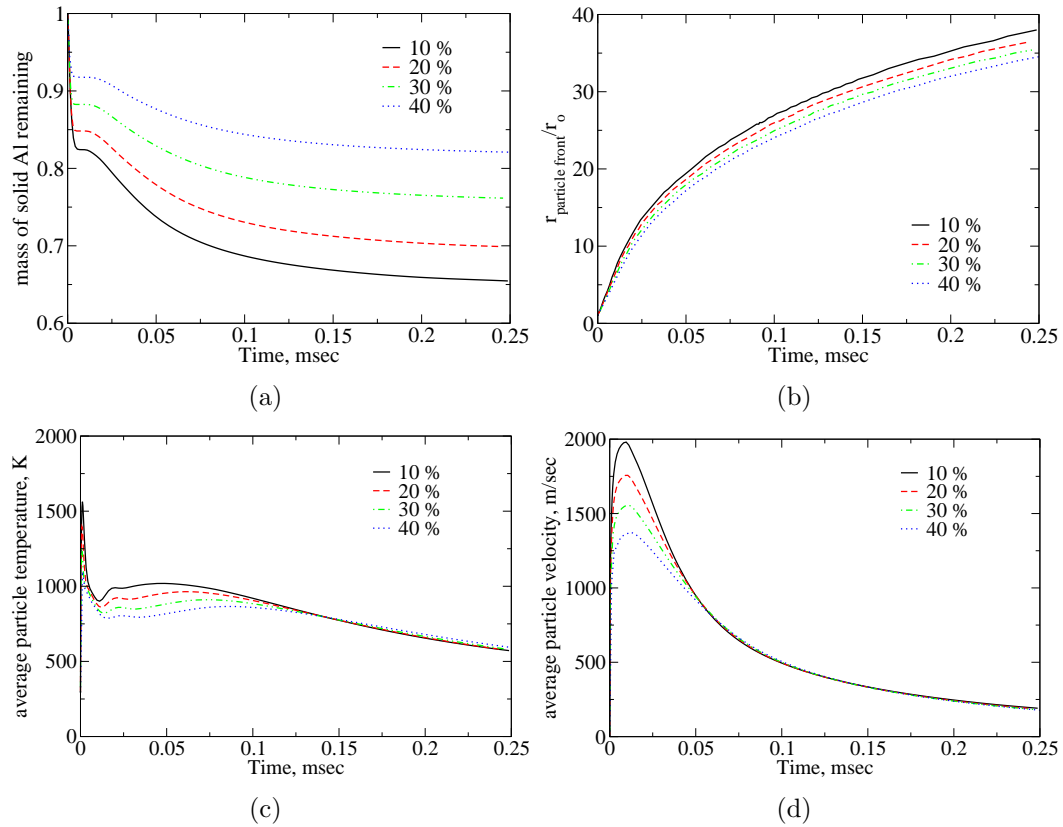


Figure 98: Effect of initial solid volume fraction on aluminumized explosive charges containing $r_p = 2.5 \mu\text{m}$ particles: (a) mass of solid Al remaining; (b) particle front trajectory; (c) average particle temperature; (d) average particle velocity.

7.3.3 Effect of burn time

The choice of burn time used in the aluminum evaporation model is critical to the analysis, and this study analyses the same for the 5 mm radius TNT-Al heterogeneous explosive charge currently under investigation. To this end, burn times of 1 and 2 msec have been considered for the initial charge corresponding to 20 % initial solid volume fraction, and $r_p = 5 \mu\text{m}$. The normalized mass of solid Al remaining with time is presented in Fig. 100 (a), and as evident burntime only has a minor role in predicting the amount of solid aluminum that remains with time. Also shown are the results obtained for a hypothetical case with the afterburn effects turned off, and lesser solid Al evaporates for this case—demonstrating the significance of

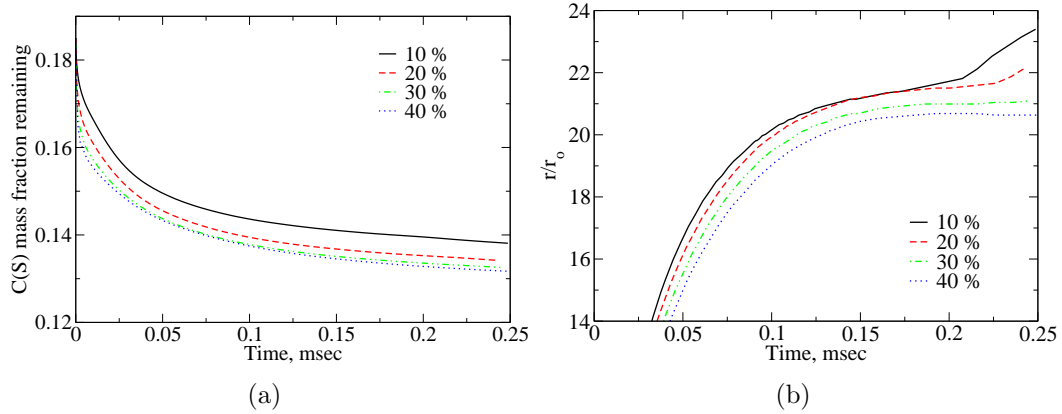


Figure 99: Effect of initial solid volume fraction on the afterburn effects of aluminized explosive charges containing $r_p = 2.5 \mu\text{m}$ particles: (a) mass fraction of C(S) remaining; (b) fire-ball radius.

the afterburn energy release. It is, however, interesting to note that at early times, more Al is evaporated (~ 0.04 msec) for this hypothetical case with the afterburn turned off (‘no afterburn’)—the absence of energy release slows down the inward moving rarefaction wave *vis-à-vis* that otherwise predicted for the realistic cases. Consequently, the rarefaction wave for this hypothetical ‘no afterburn’ case interacts with the solid particles much later, allowing for additional time for their evaporation. The particle front trajectory is presented in Fig. 100 (b) and it is observed to be nearly insensitive to the choice of the burn time used.

The mass-weighted average particle temperature is presented in Fig. 100 (c), and as evident, is also insensitive to the choice of burn time, especially at late times; the case with afterburn turned off (legend: ‘no afterburn’) predicts lower average particle temperature as expected. The mass-weighted average particle velocity is presented in Fig. 100 (d), and is insensitive to the choice of burn time at late times; however, at early times during the acceleration phase, the average particle velocity for the case with afterburn turned off actually predicts a slightly faster average particle velocity ($\sim 12 \mu\text{sec}$). The fire-ball radius (based on CO mass fraction) is shown in Fig. 100 (e), and is observed to be larger at early times for the case with afterburn turned off,

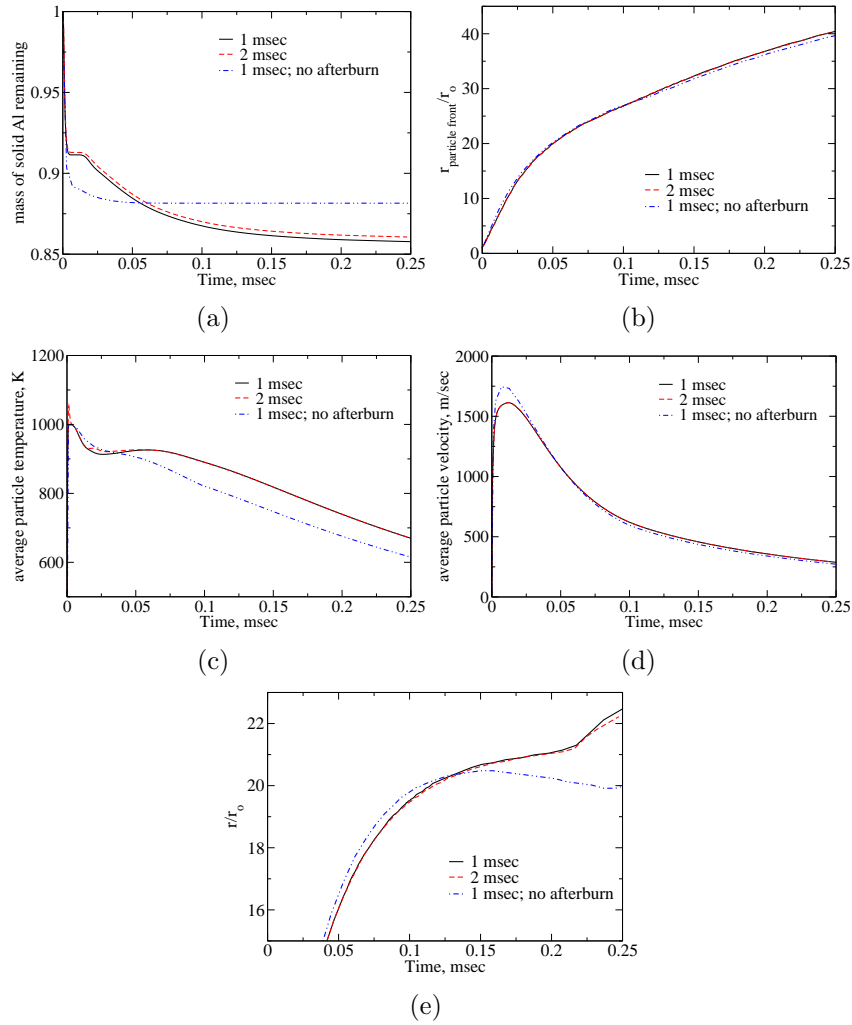


Figure 100: Effect of burn time on aluminized explosive charges: (a) mass of solid Al remaining; (b) particle front trajectory; (c) average particle temperature; (d) average particle velocity; (e) fire-ball radius.

as no CO is consumed for this hypothetical case; however, as expected, at later times the fireball is larger for the real cases *vis-à-vis* the no afterburn case, owing to the volumetric expansion of the exploding gases due to the afterburn energy release.

CHAPTER VIII

CONCLUSIONS AND RECOMMENDATIONS

8.1 Conclusions

To meet the objectives of this research effort that were identified in Chapter 2, a solid phase solver is developed, modeled along the lines of the existing liquid phase solver, with appropriate empirical models to account for the inter-phase mass, momentum, and energy transfer, and is coupled to the gas phase solver in the hydrocode. Due to the study focusing on explosions, the perfect gas equation of state is not valid, necessitating the implementation of a real gas model; to this end, the Jones-Wilkins-Lee (JWL) and the Noble-Abel equations of state are considered in the current study. Furthermore, a new Eulerian-gas Lagrangian-solid dense approach (termed EL DEM) is developed based on the Discrete Equations Method (DEM) [1], to account for dense/blockage effects encountered in flow fields involving high solid volume fractions. In addition, an empirical inter-particle collision/contact model is implemented to account for interactions between particles—critical for dense flow fields. The gas and particle solvers, under both dense and dilute loading conditions, are validated using experimental data from literature for shock/blast problems involving solid particles, and good agreement is achieved. The investigation is classified into two studies: (i) post-detonation flow field of homogeneous explosives into ambient air without and with aluminum particle clouds; (ii) post-detonation flow field of heterogeneous explosive charges comprising of inert steel or reactive aluminum particles into ambient air.

The first study involves the investigation of homogeneous explosive charges with

two primary classifications. The post-detonation flow field of homogeneous explosions into ambient air is investigated with real gas effects accounted, focusing on the growth of hydrodynamic instabilities such as Rayleigh-Taylor and Richtmyer-Meshkov, hydrodynamic mixing, and afterburn effects. The impulsive loading with such three-dimensional effects included are found to be higher than that otherwise predicted from one-dimensional simulations, due to the excess energy release from afterburn. Furthermore, for explosions involving higher intensity initial perturbations, enhanced mixing and afterburn are observed in the fireball at late times. This study meets the first objective proposed in Chapter 2.

The investigation is then extended to homogeneous explosions into ambient aluminum particle clouds, and it is observed that whereas the particle size does not play a significant role in the amount of mixing and afterburn in the mixing layer, the initial particle cloud loading and width does play a role, with higher mixing and afterburn observed when more particles are present in the initial cloud. Furthermore, sufficiently small particles are observed to cluster around the vortex rings in the mixing layer, which is observed to result in preferential ignition and combustion of the particles. The clustering patterns observed here are similar to past numerical studies of two-phase mixing layers reported in literature, and demonstrates that the Stokes number plays a crucial role in the clustering of particles as they traverse the mixing layer. Five different phases with respect to particle dispersion are identified: (1) engulfment phase; (2) hydrodynamic instability-interaction phase; (3) first vortex-free dispersion phase; (4) reshock phase; and (5) second vortex-free dispersion phase. Scaling laws for the growth rates of the widths of the mixing layer as well as that of the exploding particle cloud are obtained, and it is revealed that the scaling power index is more dependent on the mass loading ratio for the particles than for the gas. Furthermore, since the particle induced perturbations are multi-mode, the “bubbles” in the mixing layer compete at early times, resulting in their amalgamation

and growth in size; later, the bubbles grow in a quasi-self-similar manner and reach a freeze-out stage with partial memory retention of the initial perturbing conditions. The ratio of the transverse scale to amplitude of the bubbles is found to reach an asymptotic value around 0.2–0.27 during the freeze-out stage. Overall, these studies satisfy the requirements for the second objective identified in Chapter 2.

Building on the accomplishments of the studies on homogeneous explosions, the investigation extends to the post-detonation flow field of heterogeneous explosive charges, focusing first on the charge combinations used in the experiments undertaken by Zhang et al. [214]. This study is explored with two primary classifications. First, the post-detonation flow field of heterogeneous explosive charges are investigated from a one-dimensional sense, i.e., without accounting for three-dimensional effects such as hydrodynamic instabilities and turbulent mixing. The total deliverable impulsive loading from the detonation of heterogeneous explosive charges are estimated for a range of operating parameters, and it is shown that particles make a significant contribution to the near-field impulsive loading, demonstrating the efficacy of heterogeneous explosive charges for near-field applications. The impulse due to particle momentum is found to be about 3.5–4.75 times that due to the gas momentum, emphasizing that particles deliver a higher near-field impulsive loading. The total deliverable impulsive loading is found to be insensitive to the particle size for particles equal to or larger than 275 μm , even though the individual impulse components show differences. The near-field impulse from heterogeneous explosions are about twice as large as that from counterpart homogeneous explosions; however, these impulse augmentations decline in the far-field as the particle surrender their momentum back to the gas. Overall, these studies demonstrate that heterogeneous explosive charges can be efficiently used to deliver impulsive loading within radial distances of about 10 charge diameters away from the center of the charge.

In the second part, three-dimensional phenomena such as hydrodynamic instabilities are investigated for heterogeneous explosions, and the fluctuating intensities in the mixing layer are observed to be $\sim 25\text{-}40\%$ higher than that for counterpart homogeneous explosive charges, demonstrating that solid particles play a critical role in augmenting the perturbation intensities in the mixing layer. Furthermore, with twice as large a particle size in the initial heterogeneous explosive charge, the primary hydrodynamic/perturbation features in the mixing layer are observed to be nearly similar. The growth rate trends of the mixing layer widths are significantly different for heterogeneous explosions compared to counterpart homogeneous explosions, thereby demonstrating that particles play a vital role in altering the flow field. This study exemplifies the efficacy of the dense approach used to study two-phase explosions, and meets the said requirements of the third objective in Chapter 2.

Finally, the investigation is extended to the simulation and study of aluminized high explosive charges comprising of dense solid loading. Focus is laid on characterizing the dispersion, heating, ignition and afterburn of the aluminum particles, and the dynamics of the fireball. It is found that smaller particles heat up more during the early time heating phase, and also cool down more during the late time cooling phase. Furthermore, smaller particles accelerate more during the early time acceleration phase, and also decelerate more during the late time deceleration phase. In addition, it is found that the initial volume fraction in the explosive charge although plays a role in the early time particle velocities acquired, however does not play a significant role in the late time velocities during the deceleration phase, as the particles tend to achieve an equilibrium with the local gas. The choice of the burn time used in the evaporation model employed in the study is not observed to play a prominent role in the overall gas dynamics of the problem. This study fulfills the requirements for the fourth and final objective proposed in Chapter 2.

Overall, the twin studies (homogeneous and heterogeneous explosions) demonstrate the efficiency of the two-phase approach used, both in the dilute and dense regimes, for two-phase, reacting, high-speed flows. Several fluid mechanic and gas dynamic effects of relevance to the problem of two-phase explosions have been addressed. In short, the groundwork is laid to investigate a whole new class of engineering problems that are, from a numerical simulation standpoint, still in their infancy.

8.2 Recommendations for Future Work

Apropos of the presently developed simulation approach and the problem of explosions in two-phase flows, several additional investigations, physical and numerical alike, are recommended for future studies. Some of the major ones are summarized:

- From a physical standpoint, high temperature effects such as ionization/plasma can be considered. If ionization is considered, presumably the temperatures predicted behind blast waves may be lesser than that otherwise predicted. This can have a direct impact on particle ignition (if present) and hydrodynamic instability growth rates.
- Another useful direction for two-phase explosions could be the consideration of the kinetic regime of aluminum combustion, which recent shock tube data predict is more relevant for high-speed flow fields. This will require modifications to the presently developed solid phase solver to also include combustion effects, i.e., not only evaporation as currently done.
- The role of turbulence can be investigated in the mixing layer ensuing from explosions. The hydrodynamic instabilities that have been investigated in the present study will eventually transition to turbulence, and so a measure of the

turbulent kinetic energies at late times can shed light on the turbulence production and dissipation mechanisms in the mixing layer ensuing from chemical explosions.

- Particle agglomeration can also be considered, for it is well known from literature that aluminum particles tend to agglomerate when present in clouds and exposed to high temperature surrounding gases. This, however, will need modifications to the drag law to account for neighboring particles.
- The problem of two-phase explosions involves the interaction of strong shocks with solid particles, which can also result in particle fragmentation/break-up effects that can be accounted for in future studies. Although the macroscale quantities such as shock and particle front trajectories, shock overpressure, etc. agree with experiments even without the consideration of particle fragmentation in this study, the local quantities such as perturbation intensities, hydrodynamic instabilities, etc., may depend on the same. Since energy from the gas is expended to fragment particles, the mixing and hydrodynamic instability growth rates in the fireball may be subdued. Furthermore, fragmentation results in smaller particles which have faster response time scales, and can therefore affect the flow physics. These aspects need further research.
- Due to the very high accelerations encountered upon explosive dispersal, the particles can also deform to non-spherical shapes and this may affect the drag coefficient (C_D). This can play a significant role in the inter-phase momentum transfer and therefore also impulsive loading.
- From a numerical standpoint, the EL DEM can be extended to include compressible solid particles as well. This will enable the study of compaction waves in particle clouds, which may be critical to the study of Deflagration-to-Detonation Transition (DDT) in dense, two-phase flows. Also, the study of

Shock Dispersed Fuel (SDF) charges may require both phases, viz. gas and solid to be treated as compressible, since these compaction waves may perhaps play a crucial role in the ignition and burning of the particles subsequently.

- Another addition can be the implementation of local Adaptive Mesh Refinement (AMR) to complement the present developments, which will enable the resolution of finer hydrodynamic scales in the mixing layer.
- The use of a stochastic approach to model the dispersion of particles can be very handy, especially when a cloud of very small particles in the micron and sub-micron range are considered. This will enable the study of dense clouds of very small particles like aerosols, when present in sufficiently large sized clouds. Furthermore, for very small particles, Brownian motion can also be included to complement the current developments.

APPENDIX A

PARTICLE DRAG LAWS AND NUSSELT NUMBER CORRELATIONS

Some of the widely used drag laws and Nusselt number correlations from literature are summarized. The application to which the author(s) originally used them are also mentioned for each correlation presented.

A.1 Drag coefficient correlations

Akhatov & Vainshtein [4]

Application: Deflagration-to-Detonation Transition (DDT) in two-phase explosives.

$$\begin{aligned} C_D &= C_1 = \frac{24}{Re} + \frac{4.4}{Re^{0.5}} + 0.42, \alpha_s \leq 0.08 \\ C_D &= C_2 = \frac{4}{3\alpha_g} \left(1.75 + \frac{150\alpha_s}{\alpha_g Re} \right), \alpha_s \geq 0.45 \\ C_D &= \frac{(\alpha_s - 0.08) C_2 + (0.45 - \alpha_s) C_1}{0.37}, 0.08 < \alpha_s < 0.45 \end{aligned}$$

Carlson & Hoglund [37]

Application: Rocket motor flows.

$$C_D = \frac{24}{Re} \left[\frac{(1 + 0.15Re^{0.687}) \left(1 + e^{-0.427/M^{4.63} - 3/Re^{0.88}} \right)}{1 + M/Re (3.82 + 1.28e^{-1.25Re/M})} \right]$$

Clift [45]

Application: unknown.

$$C_D = \frac{24}{Re} (1 + 0.15Re^{0.687}) + \frac{0.42}{1 + 42500Re^{-1.16}}$$

Crowe [51]

Application: unknown.

$$C_D = \frac{24}{Re} \left(8.33 \frac{\alpha_s}{\alpha_g} + 0.0972 Re \right)$$

Fedorov [64]

Application: Shock-particle interaction.

$$C_D = \frac{24}{Re} + \frac{4.4}{Re^{0.5}} + 0.42$$

Gidaspow [81]

Application: Dense gas-particle fluidized beds.

$$C_D = \frac{24}{Re} (1 + 0.15 Re^{0.687}) \alpha_g^{-1.8}, Re < 1000$$

$$C_D = 0.44 \alpha_g^{-1.8}, Re \geq 1000$$

Igra & Takayama [102]

Application: Shock-particle interaction.

$$\log_{10}(C_D) = 7.8231 - 5.8137 \log_{10}(Re) + 1.4129 [\log_{10}(Re)]^2 - 0.1146 [\log_{10}(Re)]^3$$

Schiller & Naumann [180]

Application: unknown.

$$C_D = \frac{24}{Re} (1 + 0.15 Re^{0.687})$$

A.2 Nusselt number correlations

Akhatov & Vainshtein [4]

Application: Deflagration-to-Detonation Transition (DDT) in two-phase explosives.

$$Nu = 2 + 0.106 Re Pr^{0.33}, Re \leq 200$$

$$Nu = 2.274 + 0.6 Re^{0.67} Pr^{0.33}, Re > 200$$

Drake [58]

Application: Water flow past a sphere.

$$Nu = 2 + 0.459 Pr^{0.33} Re^{0.55}$$

Whitaker [207]

Application: Flow in pipes, past flat plates, single cylinders, single spheres, packed beds and tube bundles.

$$Nu = 2 + (0.4Re^{0.5} + 0.06Re^{0.667}) Pr^{0.4}$$

White [208]

Application: unknown.

$$Nu = 2 + 0.3 Pr^{0.33} Re^{0.6}$$

Yuen & Chen [213]

Application: Evaporating liquid droplets.

$$Nu = 2 + 0.6 Re^{0.5} Pr^{0.33}$$

APPENDIX B

INITIAL DETONATION PROFILE (GISPA METHOD)

The initial detonation profiles are obtained based on a one-dimensional simulation employing the Gas-Interpolated-solid-Stewart-Prasad-Asay (GISPA) method for the detonation process [209]. Here, the one-dimensional radial Euler equations are solved using a mixture equation of state to account for the condensed explosive and the detonation product gases [209]. These simulations were carried out by *Dr. Douglas V. Nance* of the Eglin Air Force Base, FL.

The initialization of the detonation profile within the initial charge is critical to the problem under study. Two approaches are proposed to take into account the effect of the particles on the detonation wave in a two-phase explosive charge: (i) based upon the limited availability of data, the pure explosive detonation conditions may be scaled by appropriate factors, especially for the particles, or (ii) the detonation energy may be scaled based upon the ratio of the mass of energetic material to metal mass. The former method tends to work well if there is a sufficient body of data; the latter method is robust and more generally applicable. Since there is very little data available for heterogeneous explosives at the onset of detonation, this study incorporates method (ii).

In the GISPA method, a single reaction progress variable, λ , which determines the degree of the detonation, is used. The reaction rate expression for the detonation process is non-specific, since it takes on different forms for different explosives. Proper equations of state for both the condensed explosive (liquid or solid) and the detonation products (gases) must be included to solve the governing equations [209]. In the current study, the Hayes equation of state is used for the condensed explosive [96]

and the JWL equation of state for the product gases [220]. The GISPA method utilizes mixture-based quantities [210], and the mixture equation of state is defined as:

$$e(\rho, p, \lambda) = (1 - \lambda) e(\rho_s, p) + \lambda e(\rho_g, p) \quad (191)$$

(the subscript s is used to denote the condensed explosive). The governing equations are solved by flux-difference splitting using the Glaister's version of the Roe scheme for equations of state of the form $e = e(\rho, p, \lambda)$ with the exact calculation of pressure derivatives [83]. The MUSCL extrapolation is applied to the primitive variables and a non-linear limiter is employed to restore monotonicity to the extrapolated variables [194].

Extensive studies have been performed to verify the efficacy of the GISPA approach, and a representative case is discussed here. A basic detonation problem used for validation applies the detonation equations of state to a calorically perfect gas [209]. The specific internal energy for the detonation products has the form:

$$e(\rho, p) = \frac{p}{\rho(\gamma - 1)} - Q. \quad (192)$$

Here, Q denotes the detonation energy release. For this equation of state, the detonation Hugoniot is well behaved, and the computed solution can be compared to an exact solution. Based upon the initial conditions provided in Xu et al. [209], the predicted solutions for pressure and gas velocity are shown in Fig. 101, and the agreement between the numerical and the exact solutions is quite good. Both the speed and the shape of the detonation, and the Taylor waves are captured accurately, thereby verifying the GISPA method.

In addition to the above, the detonation algorithm can also be validated for condensed explosive materials that possess equation of state and reaction rate data. Of particular interest in this study is the liquid explosive Nitromethane (NM) used in

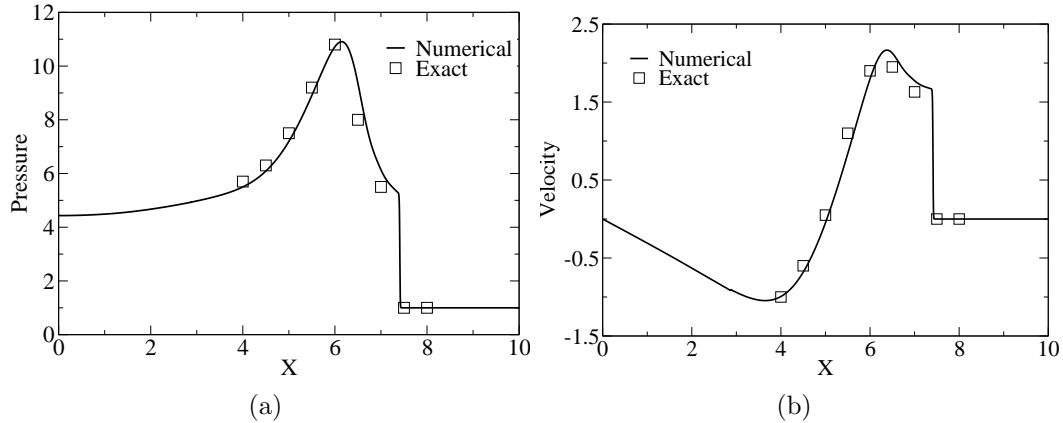


Figure 101: Detonation wave profile (a) pressure (non-dimensional) and (b) velocity (non-dimensional) for the calorically perfect gas equation of state.

Table 8: Detonation programming validation data for nitromethane: P_{CJ} - CJ pressure, u_{CJ} - CJ velocity, D - detonation velocity

Property	Numerical	Empirical	% Difference
P_{CJ} (Pa)	0.138×10^{11}	0.125×10^{11}	10.4
u_{CJ} (m/s)	2030	1765	15.0
D (m/s)	6337	6280	-0.9

the experiments performed by Zhang et al. [214]. Data for both Hayes and JWL equations of state for NM, and a suitable reaction rate expression are available [57]. For verification, the macroscopic parameters such as the Chapman-Jouguet (CJ) conditions and detonation velocity [57] are compared, and the validation is based on the plane wave detonation solution. It is necessary to estimate the location of the end of the reaction zone in order to fix the CJ point and its properties. The computed CJ parameters (pressure, gas velocity, and detonation wave speed) for NM are provided in Table 8 along with the empirical values. The comparisons with experimental data are good, especially when considering the level of variation in the measurement procedures.

For NM and other explosives, e.g., TNT, and HMX, the detonation pressure and

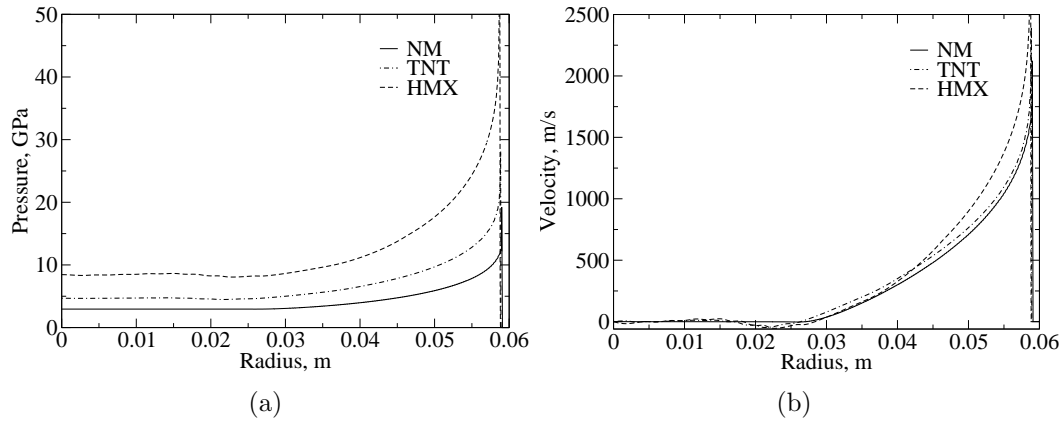


Figure 102: Initial profiles for the homogeneous 11.8 cm dia NM/TNT/HMX charges: (a) pressure; (b) velocity.

velocity profiles as the detonation wave reaches the outer end of a 11.8 cm dia. charge are shown in Fig. 102, and are used as an initial profile for homogeneous explosive charges in this study.

The detonation initialization based on the GISPA method differs from other ways of initialization, such as “programmed burn” [19], and constant volume explosion [214]. In a programmed burn, the detonation wave speed must be known *a priori*, which may not always be the case. In the constant volume explosion initialization, the pressure field is assumed constant, and so the early momentum transfer from the gas to the particles can be erroneous. On the other hand, the GISPA algorithm is based on first principles and, therefore, the initialization is expected to be more realistic.

The initial detonation profiles as predicted by the GISPA algorithm, corresponding to a 11.8 cm diameter heterogeneous explosive charge comprised of Nitromethane (NM) and 463 μm steel particles, initially occupying 62% by volume of the charge (as used in [214]) is shown in Fig. 103 as the detonation wave reaches the outer periphery of the charge. Also shown are the profiles for a homogeneous 11.8 cm diameter NM charge for comparison. As observed, the pressure and velocity profiles for the

heterogeneous charge (NM/Fe) show a deficit as compared with the homogeneous charge (NM), due to the absorption of momentum and energy by the particles in the former. Furthermore, the particles are also observed to attain a significant velocity, albeit lower than the gas. These profiles are used as initialization for the NM/Fe heterogeneous explosive charge simulations reported in Chapter 7.

Based on a numerical study presented by Ripley et al. [171], the velocity transmission factor (defined as the ratio of the particle to gas velocities as the detonation wave crosses the particle) is about 0.42 when the particle size is comparable to the reaction zone, and is about 0.34 when the particle size is much larger, both corresponding to a volume fraction of 62%. Interestingly, from Fig. 103, the ratio of the peak solid particle velocity as predicted by the GISPA algorithm to the gas velocity at the Chapman-Jouguet (CJ) point is in this range.

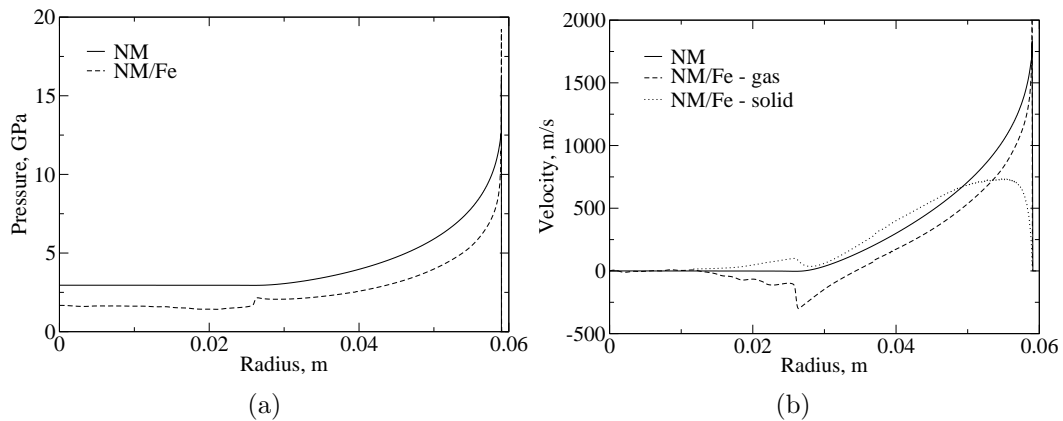


Figure 103: Initialization for the detonation simulations involving homogeneous (NM) and heterogeneous (NM/Fe) explosive charges: (a) pressure and (b) velocity.

The GISPA method discussed here is a promising initialization approach for both homogeneous and heterogeneous explosive charges alike. In the current study, the one-dimensional GISPA solution is extrapolated to a three-dimensional spherical sector grid as the initial condition to investigate the flow field subsequent to the detonation process. More details on the numerical implementation of the GISPA method can be

found in [209, 210].

REFERENCES

- [1] ABGRALL, R. and SAUREL, R., “Discrete equations for physical and numerical compressible multiphase mixture,” *Journal of Computational Physics*, Vol. 186, pp. 361–396, 2003.
- [2] AIZIK, F., BEN-DOR, G., ELPERIN, T., IGRA, O., MOND, M., and GRONIG, H., “Attenuation law of planar shock waves propagating through dust-gas suspensions,” *AIAA Journal*, Vol. 33, No. 5, pp. 953–955, 1995.
- [3] AIZIK, F., BEN-DOR, G., ELPERIN, T., IGRA, O., “General attenuation laws for spherical shock waves in pure and dusty gases,” *AIAA Journal*, Vol. 39, pp. 969–971, 2001.
- [4] AKHATOV, I. S. and VAINSHTEIN, P. B., “Transition of porous explosive combustion into detonation,” *Combustion, Explosion and Shock Waves*, Vol. 20, No. 1, pp. 63–69, 1984.
- [5] ALON, U., SHVARTS, D., and MUKAMEL, D., “Scale-invariant regime in Rayleigh-Taylor bubble-front dynamics,” *Physical Review E*, Vol. 48, No. 2, pp. 1008–1014, 1993.
- [6] AMES, R. G., DROTAR, J. T., SILBER, J., and SAMBROOK, J., “Quantitative distinction between detonation and afterburn energy deposition using pressure-time histories in enclosed explosions,” *Thirteenth International Detonation Symposium, Norfolk, VA*, 2006.
- [7] ANDERSON, J. D., *Computational Fluid Dynamics: The Basics with Applications*. McGraw Hill, 1994.
- [8] ANDREWS, M. J. and O’ROURKE, P. J., “The multiphase particle-in-cell (MP-PIC) method for dense particulate flows,” *International J. Multiphase Flow*, Vol. 22, No. 2, pp. 379–402, 1996.
- [9] ANISIMOV, S. I. and ZELDOVICH, Y. B., “Rayleigh-Taylor instability of boundary between detonation products and gas in spherical explosion,” *Pisma Zh. Eksp. Teor. Fiz.*, Vol. 3, pp. 1081–1084, 1977.
- [10] ANISIMOV, S. I., ZELDOVICH, Y. B., INOGAMOV, M. A., and IVANOV, M. F., “The Taylor instability of contact boundary between expanding detonation products and a surrounding gas,” *Progress in Astronautics and Aeronautics*, Vol. 87, pp. 218–227, 1983.

- [11] BAER, M. R. and NUNZIATO, J. W., “A two-phase mixture theory for the deflagration-to-detonation-transition (ddt) in reactive granular materials,” *International Journal of Multiphase Flow*, Vol. 12, No. 6, pp. 861–889, 1986.
- [12] BAKER, W. E., ed., *Explosions in Air*. University of Texas Press, 1973.
- [13] BALAKRISHNAN, K., GENIN, F., NANCE, D. V., and MENON, S., “Numerical study of blast characteristics from detonation of homogeneous explosives,” *Shock Waves*, Vol. 20, pp. 147–162, 2010.
- [14] BALAKRISHNAN, K. and MENON, S., “On the role of ambient reactive particles in the mixing and afterburn behind explosive blast waves,” *Combustion Science and Technology*, Vol. 182, No. 2, pp. 186–214, 2010.
- [15] BALAKRISHNAN, K., NANCE, D. V., and MENON, S., “Simulation of impulse effects from explosive charges containing metal particles,” *Accepted for publication in Shock Waves*, DOI: 10.1007/s00193-010-0249-z, 2010.
- [16] BALAKRISHNAN, K. and MENON, S., “Mixing layer characterization due to the impulsive dispersion of dense solid particle clouds,” *45th AIAA/ASME/SAE/ASEE Joint Propulsion Conference & Exhibit*, AIAA Paper 2009-5056, Denver, CO, 2009.
- [17] BATTEN, P., CLARKE, N., LAMBERT, C., and CAUSON, D. M., “On the choice of wavespeeds for the HLLC Riemann solver,” *SIAM Journal of Scientific Computing*, Vol. 18, No. 6, pp. 1553–1570, 1997.
- [18] BAZYN, T., KRIER, H., and GLUMAC, N., “Evidence of the transition from the diffusion-limit in aluminum particle combustion,” *Proc. Combust. Instit.*, Vol. 31, pp. 2021–2028, 2007.
- [19] BDZIL, J. B., STEWART, D. S., and JACKSON, T. L., “Program burn algorithms based on detonation shock dynamics: Discrete approximations of detonation flows with discontinuous front models,” *Journal of Computational Physics*, Vol. 174, pp. 870–902, 2001.
- [20] BDZIL, J. B., MENIKOFF, R., SON, S. F., KAPILA, A. K., and STEWART, D. S., “Two-phase modeling of a deflagration-to-detonation transition in granular materials: a critical examination of modeling issues,” *Physics of Fluids*, Vol. 11, No. 2, pp. 378–402, 1999.
- [21] BECKSTEAD, M. W., “A summary of aluminum combustion,” *RTO/VKI Special Course on Internal Aerodynamics in Solid Rocket Propulsion*, Rhode-Saint-Genese, Belgium, 27-31 May, 2002.
- [22] BECKSTEAD, M. W., LIANG, Y., and PUDDUPPAKKAM, K., “Numerical simulation of single aluminum particle combustion (review),” *Combustion, Explosion, and Shock Waves*, Vol. 41, No. 6, pp. 622-638, 2005.

- [23] BELYAEV, A. F., FROLOV, YU. V., and KOROTKOV, A. I., “Combustion and ignition of particles of finely dispersed aluminum,” *Combustion, Explosion & Shock Waves*, Vol. 4, No. 3, pp. 323–329, 1968.
- [24] BENKIEWICZ, K. and HAYASHI, A. K., “Aluminum dust ignition behind reflected shock wave: two-dimensional simulations,” *Fluid Dynamics Research*, Vol. 30, pp. 269–292, 2002.
- [25] BENKIEWICZ, K. and HAYASHI, A. K., “Two-dimensional numerical simulations of multi-headed detonations in oxygen-aluminum mixtures using an adaptive mesh refinement,” *Shock Waves*, Vol. 13, pp. 385–402, 2003.
- [26] BENKIEWICZ, K. and HAYASHI, A. K., “Parametric studies of aluminum combustion model for simulations of detonation waves,” *AIAA J.*, Vol. 44, No. 3, pp. 608–619, 2006.
- [27] VAN DEN BERG, A. C., “BLAST: A compilation of codes for the numerical simulation of the gas dynamics of explosions,” *J. of Loss Prevention in the Process Industries*, Vol. 22, pp. 271–278, 2009.
- [28] BESHARA, F. B. A., “Modeling of blast loading on aboveground structures - i. general phenomenology and external blast,” *Computers and Structures*, Vol. 51, No. 5, pp. 585–596, 1994.
- [29] BOIKO, V. M., LOTOV, V. V., and PAPYRIN, A. N., “Ignition of gas suspension of metal powders in reflected shock waves,” *Combustion, Explosion, and Shock Waves*, Vol. 2, pp. 193–199, 1989.
- [30] BOIKO, V. M., KISELEV, V. P., KISELEV, S. P., PAPYRIN, A. N., POPLAVSKY, S. V., and FOMIN, V. M., “Shock wave interaction with a cloud of particles,” *Shock Waves*, Vol. 7, pp. 275–285, 1997.
- [31] BOIKO, V. M. and POPLAVSKI, S. V., “Self-ignition and ignition of aluminum powders in shock waves,” *Shock Waves*, Vol. 11, pp. 289–295, 2002.
- [32] BORGERS, J. B. W. and VANTOMME, J., “Towards a parametric model of a planar blast wave created with detonation cord,” *19th International Symposium on the Military Aspects of Blast and Shock*, Calgary, Canada, 2006.
- [33] BOYER, D. W., “An experimental study of the explosion generated by a pressurized sphere,” *Journal of Fluid Mechanics*, Vol. 9, pp. 401–429, 1960.
- [34] BRODE, H. L., “Blast wave from a spherical charge,” *The Physics of Fluids*, Vol. 2, pp. 217–229, 1959.
- [35] BROUILLETTE, M., “The Richtmyer-Meshkov instability,” *Annual Review of Fluid Mechanics*, Vol. 34, pp. 445–468, 2002.

- [36] BRZUSTOWSKI, T. A. and GLASSMAN, I., “Spectroscopic investigation of metal combustion,” *Heterogeneous Combustion*, Academic, New York, 1964.
- [37] CARLSON, D. J. and HOGGLUND, R. F., “Particle drag and heat transfer in rocket nozzles,” *AIAA Journal*, Vol. 2, pp. 1980–1984, 1964.
- [38] CHANDRASEKHAR, S., *Hydrodynamic and Hydromagnetic Stability*. Oxford University Press, Oxford, 1961.
- [39] CHANG, C. H. and LIOU, M. S., “A conservative compressible multifluid model for multiphase flow: Shock-interface interaction problems,” *17th AIAA Computational Fluid Dynamics Conference*, AIAA Paper 2005-5344, June 6-9, Toronto, ON, 2005.
- [40] CHANG, C. H. and LIOU, M. S., “A robust and accurate approach to computing compressible multiphase flow: Stratified flow model and $AUSM^+$ -up scheme,” *Journal of Computational Physics*, Vol. 225, pp. 840–873, 2007.
- [41] CHANG, E. J. and KAILASANATH, K., “Shock wave interactions with particles and liquid fuel droplets,” *Shock Waves*, Vol. 12, pp. 333–341, 2003.
- [42] CHEIN, R. and CHUNG, J. N., “Effects of vortex pairing on particle dispersion in turbulent shear flows,” *Int. J. Multiphase Flow*, Vol. 13, No. 6, pp. 785–802, 1987.
- [43] CHEIN, R. and CHUNG, J. N., “Simulation of particle dispersion in a two-dimensional mixing layer,” *AIChE J.*, Vol. 34, pp. 946–954, 1998.
- [44] CHINNAYYA, A., DANIEL, E., and SAUREL, R., “Modelling detonation waves in heterogeneous energetic materials,” *Journal of Computational Physics*, Vol. 196, pp. 490–538, 2004.
- [45] CLIFT, R., GRACE, J. R., and WEBER, M. E., *Bubbles, Drops and Particles*. Academic, New York, 1978.
- [46] CLUTTER, J. K., MATHIS, J. T., and STAHL, M. W., “Modeling environmental effects in the simulation of explosion events,” *International Journal of Impact Engineering*, Vol. 34, pp. 973–989, 2007.
- [47] COLELLA, P. and WOODWARD, P., “The piecewise-parabolic method for hydrodynamics,” *Journal of Computational Physics*, Vol. 54, pp. 174–201, 1984.
- [48] COOK, A. and DIMOTAKIS, P. E., “Transition stages of Rayleigh-Taylor instability between miscible fluids,” *Journal of Fluid Mechanics*, Vol. 443, pp. 69–99, 2001.
- [49] COURANT, R., ISAACSON, E., and REEVES, M., “On the solution of nonlinear hyperbolic differential equations by finite differences,” *Comm. Pure and Applied Mathematics*, Vol. 5, pp. 243–255, 1952.

- [50] COWPERTHWAIT, M., “Significance of some equations of state obtained from shock-wave data,” *American Journal of Physics*, Vol. 34, No. 11, pp. 1025–1030, 1966.
- [51] CROWE, C., SOMMERFELD, M., and TSUJI, Y., *Multiphase flows with droplets and particles*. CRC Press, 1998.
- [52] DAVIS, S. F., “Simplified second-order Godunov-type methods,” *SIAM Journal on Scientific and Statistical Computing*, Vol. 9, pp. 445–473, 1988.
- [53] “Department of defense ammunition and explosives hazard classification procedures,” DoD Publication TB 700-2 NAVSEAINST 8020.8B TO 11A-1-47 DLAR 8220.1, Department of Defense, 1998.
- [54] DEVALS, C., JOURDAN, G., ESTIVALEZES, J. L., MESHKOV, E. E., and HOUAS, L., “Shock tube spherical particle accelerating study for drag coefficient determination,” *Shock Waves*, Vol. 12, pp. 325–331, 2003.
- [55] DE YONG, L. V. and CAMPANELLA, G., “A study of blast characteristics of several primary explosives and pyrotechnic compositions,” *Journal of Hazardous Materials*, Vol. 21, pp. 125–133, 1989.
- [56] DIMONTE, G. and SCHNEIDER, M. B., “Turbulent Rayleigh-Taylor instability experiments with variable acceleration,” *Phys. Rev. E*, Vol. 54, pp. 3740–3743, 1996.
- [57] DOBRATZ, B. M., “LLNL handbook of explosives,” *LLNL Publication UCRL-52997*, Lawrence Livermore National Laboratory, 1985.
- [58] DRAKE, R. M., “Discussion on the paper entitled “Forced convection heat transfer from an isothermal sphere to water” by G. C. Violet and G. Leppert,” *ASME Journal of Heat Transfer*, Vol. 83, No. 2, pp. 170–179, 1961.
- [59] DREW, D. A., “Mathematical modeling of two-phase flow,” *Annual Review of Fluid Mechanics*, Vol. 15, pp. 261–291, 1983.
- [60] DREW, D. A. and PASSMAN, S. L., *Theory of Multicomponent Fluids*. Springer, 1999.
- [61] EINFELDT, B., “On Godunov-type methods for gas dynamics,” *SIAM J. Numer. Anal.*, Vol. 25, No. 2, pp. 294–318, 1988.
- [62] EINFELDT, B., MUNZ, C. D., ROE, P. L., and SJOGREEN, B., “On Godunov-type methods near low densities,” *Journal of Computational Physics*, Vol. 92, pp. 273–295, 1991.
- [63] ERLEBACHER, G., HUSSAINI, M. Y., SPEZIALE, C. G., and ZANG, T. A., “Toward the large-eddy simulation of compressible turbulent flows,” *Journal of Fluid Mechanics*, Vol. 238, pp. 155–185, 1992.

- [64] GOSTEEV, YU. A. and FEDOROV, A. V., “Calculation of dust lifting by a transient shock wave,” *Combustion, Explosion, and Shock Waves*, Vol. 38, No. 3, pp. 322–326, 2002.
- [65] FEDOROV, A. V. and KHARLAMOVA, YU. V., “Ignition of an aluminum particle,” *Combustion, Explosion, and Shock Waves*, Vol. 39, No. 5, pp. 544–547, 2003.
- [66] FEDOROV, A. V. and KHMEL, T. A., “Numerical simulation of formation of cellular heterogeneous detonation of aluminum particles in oxygen,” *Combustion, Explosion, and Shock Waves*, Vol. 41, No. 4, pp. 435–448, 2005.
- [67] FEDOROV, A. V., FOMIN, V. M., and KHMEL, T. A., “Theoretical and numerical study of detonation processes in gas suspensions with aluminum particles,” *Combustion, Explosion, and Shock Waves*, Vol. 42, No. 6, pp. 735–745, 2006.
- [68] FICKETT, W. and DAVIS, W. C. *Detonation Theory and Experiment*. University of California Press, Berkeley, CA, 1979.
- [69] FORMBY, S. A. and WHARTON, R. K., “Blast characteristics and TNT equivalence values for some commercial explosives detonated at ground level,” *Journal of Hazardous Materials*, Vol. 50, pp. 183–198, 1996.
- [70] FREUND, J. B., MOIN, P., and LELE, S. K., “Compressibility effects in an annular compressible mixing layer part 2: Mixing of a passive scalar,” *Journal of Fluid Mechanics*, Vol. 421, pp. 269–292, 2000.
- [71] FROLOV, YU. V., POKHIL, P. F., and LOGACHEV, V. S., “Ignition and combustion of powdered aluminum in high-temperature gaseous media and in a composition of heterogeneous condensed systems,” *Combustion, Explosion, and Shock Waves*, Vol. 8, No. 2, pp. 168–187, 1972.
- [72] FROST, D. L., ZHANG, F., MURRAY, S. B., and MCCAHAN, S., “Critical conditions for ignition of metal particles in a condensed explosive,” *12th Symposium on Detonation*, San Diego, CA, August 11–16, 2002.
- [73] FROST, D. L. and ZHANG, F. “Nonideal blast waves from heterogeneous explosives,” *Materials Science Forum*, Vols. 465–466, pp. 421–426, 2004.
- [74] FROST, D. L., ZAREI, Z., and ZHANG, F., “Instability of combustion products interface from detonation of heterogeneous explosives,” *Twentieth International Colloquium on the Dynamics of Explosions and Reactive Systems*, Montreal, Canada, 2005.
- [75] FROST, D. L., ORNTHANALAI, C., ZAREI, Z., TANGUAY, V., and ZHANG, F., “Particle momentum effects from the detonation of heterogeneous explosives,” *Journal of Applied Physics*, Vol. 101, No. 113529, 2007.

- [76] FRYXELL, B. and MENON, S., “Hybrid simulations of Richtmyer-Meshkov instability,” *43rd AIAA Aerospace Sciences Meeting*, AIAA Paper 05-0314, Reno, NV, 2005.
- [77] FUREBY, C. and MOLLER, S. I., “Large-eddy simulations of reacting flows applied to bluff-body stabilized flames,” *AIAA Journal*, Vol. 33, pp. 2339–2347, 1995.
- [78] GÉNIN, F., *Study of Compressible Turbulent Flows in Supersonic Environment by Large-Eddy Simulation*. PhD thesis, Georgia Institute of Technology, Atlanta, GA, 2009.
- [79] GÉNIN, F. and MENON, S., “Studies of shock / turbulent shear layer interaction using large-eddy simulation,” *Computers and Fluids*, Vol. 39, pp. 800–819, 2010.
- [80] GEORGE, E. and GLIMM, J., “Self-similarity of Rayleigh-Taylor mixing rates,” *Physics of Fluids*, Vol. 17, pp. 054101, 2005.
- [81] GIDASPOW, D., *Multiphase Flow and Fluidization Continuum and Kinetic Theory Description*. Academic Press, Boston, 1994.
- [82] GILEV, S. D. and ANISICHKIN, V. F., “Interaction of aluminum with detonation products,” *Combustion, Explosion, and Shock Waves*, Vol. 42, No. 1, pp. 107–115, 2006.
- [83] GLAISTER, P., “An approximate linearized riemann solver for the euler equations for real gases,” *Journal of Computational Physics*, Vol. 74, pp. 383–408, 1988.
- [84] GLASSMAN, I., *Metal Combustion Processes*. American Rocket Society Preprint 938-59, New York, 1959.
- [85] GLASSMAN, I., MELLOR, A. M., SULLIVAN, H. F., and LAURENDEAU, N. M., “A review of metal ignition and flame models,” *AGARD Conference Proceedings*, No. 52, pp. 19-1–19-30, 1970.
- [86] GLIMM, J., MCBRYAN, O., MENIKOFF, R., and SHARP, D. H., “Stable and runaway bubble merger in a model for Rayleigh-Taylor unstable interfaces,” *Phys. Letters A*, Vol. 123, pp. 289–292, 1987.
- [87] GLIMM, J., LI, X. L., MENIKOFF, D. H., SHARP, D. H., and ZHANG, Q., “A numerical study of bubble interactions in Rayleigh-Taylor instability for compressible fluids,” *Physics of Fluids A*, Vol. 2, pp. 2046–2054, 1990.
- [88] GODUNOV, S. K., “A difference method for numerical calculation of discontinuous solutions of the equations of hydrodynamics,” *Math. Sbornik.*, Vol. 47, pp. 271–306, 1959.

- [89] GOKHALE, S. S. and KRIER, H., “Modeling of unsteady two-phase reactive flows in porous propellants,” *Progress in Energy and Combustion Science*, Vol. 8, pp. 1–39, 1982.
- [90] GONOR, A., HOOTON, I., and NARAYAN, S., “Steady-state model of heterogeneous detonation with reactive metallic particles,” *12th International Detonation Symposium*, San Diego, CA, August 11–16, 2002.
- [91] GONTHIER, K. A. and POWERS, J. M., “A high-resolution numerical method for a two-phase model of deflagration-to-detonation transition,” *Journal of Computational Physics*, Vol. 163, pp. 376–433, 2000.
- [92] GORDON, S. and MCBRIDE, B. J., “Computer program for calculation of complex chemical equilibrium compositions and applications,” *NASA Reference Publication 1311*, NASA, 1994.
- [93] HARGATHER, M. J. and SETTLES, G. S., “Optical measurement and scaling of blasts from gram-range explosive charges,” *Shock Waves*, Vol. 17, pp. 215–223, 2007.
- [94] HARTEN, A., LAX, P. D., and VAN LEER, B., “On upstream differencing and Godunov-type schemes for hyperbolic conservation laws,” *SIAM Review*, Vol. 25, pp. 35–61, 1983.
- [95] HARTEN, A. and ZWAS, G., “Self-adjusting hybrid schemes for shock computations,” *Journal of Computational Physics*, Vol. 9, pp. 568–583, 1972.
- [96] HAYES, D. B., “A P^nt detonation criterion from thermal explosion theory,” *Sixth International Symposium on Detonation, Pasadena, CA*, 1976.
- [97] HECHT, J., ALON, U., and SHVARTS, D., “Potential flow models of Rayleigh-Taylor and Richtmyer-Meshkov bubble fronts,” *Physics of Fluids*, Vol. 6, No. 12, pp. 4019–4030, 1994.
- [98] HILL, D. J., PANTANO, C., and PULLIN, D. I., “Large-eddy simulation and multiscale modelling of a Richtmyer-Meshkov instability with reshock,” *Journal of Fluid Mechanics*, Vol. 557, pp. 29–61, 2006.
- [99] HILL, T. L., *An Introduction to Statistical Thermo-dynamics*. Addison-Wesley, Reading, Massachusetts, 1960.
- [100] HIRSCH, C., *Numerical computation of internal and external flows*, Vol. 2. John-Wiley and Sons, Inc., 1997.
- [101] HOU, T. Y. and LE FLOCH, P., “Why non-conservative schemes converge to the wrong solution: error analysis,” *Math. Comp.*, Vol. 62, pp. 497–530, 1994.
- [102] IGRA, O. and TAKAYAMA, K., “Shock tube study of the drag coefficient of a sphere in a non-stationary flow,” *Proc. Royal Society of London A*, Vol. 442, pp. 231–247, 1993.

- [103] IVANDAIEV, A. I. and KUTUSHEV, A. G., “Influence of screening gas-suspension layers on shock wave reflection,” *Journal of Applied Mechanics and Technical Physics*, Vol. 26, pp. 103–109, 1985.
- [104] JOHNSTON, I. A., “The noble-abel equation of state: Thermodynamic derivations for ballistics modelling,” *DSTO Publication DSTO-TN-0670*, Defence Science and Technology Organisation, 2005.
- [105] JONES, M. A. and JACOBS, J. W., “A membraneless experiment for the study of Richtmyer-Meshkov instability of a shock-accelerated gas interface,” *Physics of Fluids*, Vol. 9, pp. 3078–3085, 1997.
- [106] KAPILA, A. K., MENIKOFF, R., BDZIL, J. B., SON, S. F., and STEWART, D. S., “Two-phase modeling of deflagration-to-detonation transition in granular materials: Reduced equations,” *Physics of Fluids*, Vol. 13, No. 10, pp. 3002–3024, 2001.
- [107] KARTOON, D., ORON, D., ARAZI, L., and SHVARTS, D., “Three-dimensional multimode Rayleigh-Taylor and Richtmyer-Meshkov instabilities at all density ratios,” *Laser and Particle Beams*, Vol. 21, pp. 327–334, 2003.
- [108] KHASAINOV, B. A. and Veysiere, B., “Steady, plane, double-front detonations in gaseous detonable mixtures containing a suspension of aluminum particles,” *Dynamics of Explosions, Prog. in Astro. and Aero.*, Vol. 114, pp. 284–298, 1988.
- [109] KHASAINOV, B. A. and Veysiere, B., “Initiation of detonation regimes in hybrid two-phase mixtures,” *Shock Waves*, Vol. 6, pp. 9–15, 1996.
- [110] KHMEL, T. A. and Fedorov, A. V., “Interaction of a shock wave with a cloud of aluminum particles in a channel,” *Combustion, Explosion, and Shock Waves*, Vol. 38, No. 2, pp. 206–214, 2002.
- [111] KIM, W.-W., *A New Dynamic Subgrid-Scale Model for Large-Eddy Simulation of Turbulent Flows*. PhD thesis, Georgia Institute of Technology, Atlanta, GA, September 1996.
- [112] KIM, W.-W., MENON, S., and MONGIA, H. C., “Large eddy simulations of a gas turbine combustor flow,” *Combustion Science and Technology*, Vol. 143, pp. 25–62, 1999.
- [113] KINGERY, C. N. and BULMASH, G., “Airblast parameters from spherical air burst and hemispherical surface burst,” *US Army Armament Research and Development Center*, Technical Report, ARBRL-TR-02555, 1984.
- [114] KINNEY, G. F. and GRAHAM, K. J., *Explosive Shocks in Air*. Springer-Verlag, New York, 1985.
- [115] KOLMOGOROV, A. N., “Dissipation of energy in locally isotropic turbulence,” *Proceedings of the USSR Academy of Sciences*, Vol. 32, pp. 16–18, 1941.

- [116] KOLMOGOROV, A. N., “The local structure of turbulence in incompressible viscous fluid for very large reynolds numbers,” *Proceedings of the USSR Academy of Sciences*, Vol. 30, pp. 299–303, 1941.
- [117] KOSINSKI, P., HOFFMANN, A. C., and KLEMENS, R., “Dust lifting behind shock waves: comparison of two modelling techniques,” *Chemical Engineering Science*, Vol. 60, pp. 5219–5230, 2005.
- [118] KOSINSKI, P., “Numerical investigation of explosion suppression by inert particles in straight ducts,” *Journal of Hazardous Materials*, Vol. 154, pp. 981–991, 2008.
- [119] KRUGLIKOV, B. S. and KUTUSHEV, A. G., “Attenuation of air shock waves by layers of dusty gas and lattices,” *Journal of Applied Mechanics and Technical Physics*, Vol. 29, pp. 48–53, 1988.
- [120] KUHL, A. L., “Spherical mixing layers in explosions,” in *Dynamics of Exothermicity* (BOWEN, J. R., ed.), pp. 291–320, Gordon and Breach Publishers, 1996.
- [121] KUHL, A. L., FERGUSON, R. E., and OPPENHEIM, A. K., “Gasdynamic model of turbulent exothermic fields in explosions,” *Progress in Astronautics and Aeronautics*, Vol. 173, pp. 251–261, 1997.
- [122] LANOVETS, V. S., LEVICH, V. A., ROGOV, N. K., TUNIK, Y. V., and SHAM-SHEV, K. N., “Dispersion of the detonation products of a condensed explosive with solid inclusions,” *Combustion, Explosion, and Shock Waves*, Vol. 29, No. 5, pp. 638–641, 1993.
- [123] LATINI, M., SCHILLING, O., and DON, W. S., “Effects of WENO flux reconstruction order and spatial resolution on reshocked two-dimensional Richtmyer-Meshkov instability,” *Journal of Computational Physics*, Vol. 221, pp. 805–836, 2007.
- [124] LAYZER, D., “On the instability of superposed fluids in a gravitational field,” *The Astrophysical Journal*, Vol. 122, No. 1, pp. 1–12, 1955.
- [125] LE METAYER, O., MASSONI, J., and SAUREL, R., “Modelling evaporation fronts with reactive riemann solvers,” *Journal of Computational Physics*, Vol. 205, pp. 567–610, 2005.
- [126] LEE, J. J., BROUILLETTE, M., FROST, D. L., and LEE, J. H. S., “Effect of diethylenetriamine sensitization on detonation of nitromethane in porous media,” *Combustion and Flame*, Vol. 100, pp. 292–300, 1995.
- [127] LEE, H., JIN, H., YU, Y., and GLIMM, J., “On validation of turbulent mixing simulations for Rayleigh-Taylor instability,” *Physics of Fluids*, Vol. 20, pp. 012102, 2008.

- [128] LEINOV, E., MALAMUD, G., ELBAZ, Y., LEVIN, L. A., BEN-DOR, G., SHVARTS, D., and SADOT, O., “Experimental and numerical investigation of the Richtmyer-Meshkov instability under re-shock conditions,” *Journal of Fluid Mechanics*, Vol. 626, pp. 449–475, 2009.
- [129] LEVEQUE, R. J., *Finite Volume Methods for Hyperbolic Problems*. Cambridge University Press, 2002.
- [130] LING, W., CHUNG, J. N., TROUTT, T. R., and CROWE, C. T., “Direct numerical simulation of a three-dimensional temporal mixing layer with particle dispersion,” *Journal of Fluid Mechanics*, Vol. 358, pp. 61–85, 1998.
- [131] LISKA, R. and WENDROFF, B., “Comparison of several difference schemes on 1D and 2D test problems for the Euler equations,” *SIAM Journal of Scientific Computing*, Vol. 28, No. 3, pp. 995–1017, 2003.
- [132] LIU, X. D, OSHER, S., and CHAN, T., “Weighted essentially nonoscillatory schemes,” *Journal of Computational Physics*, Vol. 115, No. 1, pp. 200–212, 1994.
- [133] LOMBARDINI, M. and PULLIN, D. I., “Startup process in the Richtmyer-Meshkov instability,” *Physics of Fluids*, Vol. 21, pp. 044104, 2009.
- [134] LOMBARDINI, M. and PULLIN, D. I., “Small-amplitude perturbations in the three-dimensional cylindrical Richtmyer-Meshkov instability,” *Physics of Fluids*, Vol. 21, pp. 114103, 2009.
- [135] LOMBARDINI, M., *Richtmyer-Meshkov instability in converging geometries*. PhD thesis, California Institute of Technology, Pasadena, CA, 2008.
- [136] LYNCH, P., KRIER, H., and GLUMAC, N., “A correlation for burn time of aluminum particles in the transition regime,” *Proc. Combust. Instit.*, Vol. 32, pp. 1887–1893, 2009.
- [137] LYNCH, P., KRIER, H., and GLUMAC, N., “Size distribution effects in heterogeneous shock tube burntime experiments,” *45th AIAA/ASME/SAE/ASEE Joint Propulsion Conference & Exhibit*, AIAA Paper 2009-5053, Denver, CO, 2009.
- [138] MACCORMACK, R. W., “The effect of viscosity in hypervelocity impact cratering,” *AIAA Hypervelocity Impact Conference*, AIAA Paper 69-354, Cincinnati, OH, Apr 30-May 2, 1969.
- [139] MACCORMACK, R. W., “An efficient numerical method for solving the time-dependent compressible Navier-Stokes equations at high Reynolds number,” *Tech. Rep. NASA Technical Memorandum X-73*, National Aeronautics and Space Administration, 1976.

- [140] MARCHIOLI, C., ARMENIO, V., and SOLDATI, A., “Simple and accurate scheme for fluid velocity interpolation for Eulerian-Lagrangian computation of dispersed flows in 3D curvilinear grids,” *Computers and Fluids*, Vol. 36, pp. 1187–1198, 2007.
- [141] MASSONI, J., SAUREL, R., LEFRANCOIS, A., and BAUDIN, G., “Modeling spherical explosions with aluminized energetic materials,” *Shock Waves*, Vol. 16, No. 1, pp. 75–92, 2006.
- [142] MAXEY, M. R. and RILEY, J. J., “Equation of motion for a small rigid sphere in a nonuniform flow,” *Physics of Fluids*, Vol. 26, No. 4, pp. 883–889, 1983.
- [143] MENIKOFF, R., “Detonation waves in PBX 9501,” *Combustion Theory and Modeling*, Vol. 10, No. 6, pp. 1003–1021, 2006.
- [144] MENON, S. and PATEL, N., “Subgrid modeling for simulation of spray combustion in large-scale combustors,” *AIAA Journal*, Vol. 44, No. 4, pp. 709–723, 2006.
- [145] MENON, S., YEUNG, P.-K., and KIM, W.-W., “Effect of subgrid models on the computed interscale energy transfer in isotropic turbulence,” *Computers and Fluids*, Vol. 25, No. 2, pp. 165–180, 1996.
- [146] MESHKOV, E. E., “Instability of the interface of two gases accelerated by a shock wave,” *Fluid Dynamics*, Vol. 4, No. 5, pp. 101–104, 1969.
- [147] MESHKOV, E. E., NEVMERZHITSKY, N. V., ZMUSHKO, V. V., “On possibilities of investigating hydrodynamic instabilities and turbulent mixing development in spherical geometry,” *The Physics of Compressible Turbulent Mixing*, pp. 343–347, Marseille: Impr. Caractere, 1997.
- [148] MEYER, K. A and BLEWETT, P. J., “Numerical investigation of the stability of a shock accelerated interface between two fluids,” *Physics of Fluids*, Vol. 15, pp. 753–759, 1972.
- [149] MILES, A. R, “Bubble merger model for the nonlinear Rayleigh-Taylor instability driven by a strong blast wave,” *Phys. of Plasmas*, Vol. 11, No. 11, pp. 5140–5155, 2004.
- [150] MILES, A. R, EDWARDS, M. J., and GREENOUGH, J. A., “Effect of initial conditions on two-dimensional Rayleigh-Taylor instability and transition to turbulence in planar blast-wave-driven systems,” *Phys. of Plasmas*, Vol. 11, No. 11, pp. 5278–5296, 2004.
- [151] MILES, A. R., ET AL., “Transition to turbulence and effect of initial conditions on three-dimensional compressible mixing in planar blast-wave-driven systems”, *Phys. of Plasmas*, Vol. 12, No. 5, pp. 056317-056317-10, 2005.

- [152] MILES, A. R., “The blast-wave-driven instability as a vehicle for understanding supernova explosion structure”, *The Astrophysical Journal*, Vol. 696, pp. 498–514, 2009.
- [153] MILNE, A. M., “Detonation in heterogeneous mixtures of liquids and particles,” *Shock Waves*, Vol. 10, pp. 351–362, 2000.
- [154] MUNKEJORD, S. T. and PAPIN, M., “The effect of interfacial pressure in the discrete-equation multiphase model,” *Computers and Fluids*, Vol. 36, pp. 742–757, 2007.
- [155] NELSON, C. C., *Simulations of spatially evolving compressible turbulence using a local dynamic subgrid model*. PhD thesis, Georgia Institute of Technology, Atlanta, GA, 1997.
- [156] OEFELEIN, J. C., “Large eddy simulation of turbulent combustion processes in propulsion and power systems,” *Progress in Aerospace Sciences*, Vol. 42, pp. 2–37, 2006.
- [157] OLIVER, E. C., DAYMOND, M. R., and WITHERS, P. J., “Interphase and intergranular stress generation in carbon steels,” *Acta Materialia*, Vol. 52, pp. 1937–1951, 2004.
- [158] ORON, D., ARAZI, L., KARTOON, D., RIKANATI, A., ALON, U., and SHVARTS, D., “Dimensionality dependence of the Rayleigh-Taylor and Richtmyer-Meshkov instability late-time scaling laws,” *Physics of Plasmas*, Vol. 8, No. 6, pp. 2883–2889, 2001.
- [159] OSHER, S. and SETHIAN, J., “Fronts propagating with curvature-dependent speed: Algorithms based on Hamilton-Jacobi formulations,” *Journal of Computational Physics*, Vol. 79, pp. 12–49, 1988.
- [160] PATANKAR, N. A. and JOSEPH, D. D., “Modeling and numerical simulation of particulate flows by the eulerian-lagrangian approach,” *International Journal of Multiphase Flow*, Vol. 27, pp. 1659–1684, 2001.
- [161] PATEL, N., *Simulation of Hydrodynamic Fragmentation from a Fundamental and an Engineering Perspective*. PhD thesis, Georgia Institute of Technology, Atlanta, GA, 2007.
- [162] POINSOT, T. and VEYNANTE, D., *Theoretical and Numerical Combustion*. Edwards, Inc., 2001.
- [163] POINSOT, T. J. and LELE, S. K., “Boundary conditions for direct simulations of compressible viscous flows,” *Journal of computational physics*, Vol. 101, No. 1, pp. 104–129, 1992.

- [164] POKHIL, P. F., BELYAYEV, A. F., FROLOV, YU. V., LOGACHEV, V. S., and KOROTKOV, A. I., “Combustion of powdered metals in active media,” *Nauka*, FTD-MT-24-551-73, 1972.
- [165] POPE, S. B., *Turbulent Flows*. Cambridge University Press, 2000.
- [166] QUIRK, J. J., “A contribution to the great Riemann solver debate,” *International Journal for Numerical Methods in Fluids*, Vol. 18, pp. 555–574, 1994.
- [167] READ, K. I., “Experimental investigation of turbulent mixing by Rayleigh-Taylor instability,” *Physica D*, Vol. 12, pp. 45–58, 1984.
- [168] READ, K. I. and YOUNGS, D. L., “Experimental investigation of turbulent mixing by Rayleigh-Taylor instability,” *AWRE Report 011/83*, Atomic Weapons Research Establishment, United Kingdom, 1983.
- [169] RICHTMYER, R. D., “Taylor instability in a shock acceleration of compressible fluids,” *Communications in Pure and Applied Mathematics*, Vol. 13, pp. 297–319, 1960.
- [170] RIKANATI, A., ORON, D., SADOT, O., and SHVARTS, D., “High initial amplitude and high Mach number effects on the evolution of the single-mode Richtmyer-Meshkov instability,” *Physical Review E*, Vol. 67, Issue. 2, pp. 026307, 2003.
- [171] RIPLEY, R., ZHANG, F., and LIEN, F. S., “Detonation interaction with metal particles in explosives,” *Proc. 13th International Detonation Symposium, July 23-28, Norfolk, Virginia, USA*, 2006.
- [172] ROE, P. L., “Approximate Riemann solvers, parameter vectors and difference schemes,” *Journal of Computational Physics*, Vol. 43, pp. 357–372, 1981.
- [173] ROGUE, X., RODRIGUEZ, G., HAAS, J. F., and SAUREL, R., “Experimental and numerical investigation of the shock-induced fluidization of a particles bed,” *Shock Waves*, Vol. 8, pp. 29–45, 1998.
- [174] SAINSAULIEU, L., “Travelling-wave solutions of convection-diffusion systems in nonconservation form,” *SIAM Journal of Math. Anal.*, Vol. 27, No. 5. pp. 1286–1310, 1996.
- [175] SAUREL, R. and ABGRALL, R., “A multiphase Godunov method for compressible multifluid and multiphase flows,” *Journal of Computational Physics*, Vol. 150, pp. 425–467, 1999.
- [176] SAUREL, R., COCCHI, J. P., and BUTLER, P. B., “A numerical study of the cavitation effects in the wake of a hypervelocity underwater projectile,” *AIAA J. Propulsion and Power*, Vol. 15, No. 4, pp. 513–522, 1999.

- [177] SAUREL, R. and LEMETAYER, O., “A multiphase model for interfaces, shock, detonation waves and cavitation,” *Journal of Fluid Mechanics*, Vol. 431, pp. 239–271, 2001.
- [178] SAUREL, R. *Private Communication*, 2007.
- [179] SAUREL, R., PETITPAS, F., and BERRY, R. A., “Simple and efficient relaxation methods for interfaces separating compressible fluids, cavitating flows and shocks in multiphase mixtures,” *Journal of Computational Physics*, Vol. 228, pp. 1678–1712, 2009.
- [180] SCHILLER, L. and NAUMANN, A., “A drag coefficient correlation,” *V.D.I. Zeitung*, Vol. 77, pp. 318–320, 1935.
- [181] SCHWER, D. A. and KAILASANATH, K., “Numerical simulation of the mitigation of unconfined explosions using water-mist,” *Proc. Combust. Instit.*, Vol. 31, pp. 2361–2369, 2007.
- [182] SEDOV, L. I., *Similarity and Dimensional Methods in Mechanics*. Academic Press, 1959.
- [183] SHARP, D. H., “An overview of Rayleigh-Taylor instability,” *Physica D: Non-linear Phenomena*, Vol. 12, pp. 3–10, 1984.
- [184] SHOSHIN, Y. and DREIZIN, E., “Particle combustion rates in premixed flames of polydisperse metal-air aerosols,” *Combustion and Flame*, Vol. 133, pp. 275–287, 2003.
- [185] SNIDER, D. M., O’ROURKE, P. J., and ANDREWS, M. J., “Sediment flow in inclined vessels calculated using a multiphase particle-in-cell model for dense particle flows,” *International Journal of Multiphase Flow*, Vol. 24, pp. 1359–1382, 1998.
- [186] SNIDER, D. M., “An incompressible three-dimensional multiphase particle-in-cell model for dense particle flows,” *Journal of Computational Physics*, Vol. 170, pp. 523–549, 2001.
- [187] SOMMERFELD, M., “The unsteadiness of shock waves propagating through gas-particle mixtures,” *Experiments in Fluids*, Vol. 3, pp. 197–206, 1985.
- [188] SQUIRES, K. D. and EATON, J. K., “Preferential concentration of particles by turbulence,” *Phys. Fluids A*, Vol. 3, No. 5, 1169–1178, 1991.
- [189] SREBRO, Y., ELBAZ, Y., SADOT, O., ARAZI, L., and SHVARTS, D., “A general buoyancy-drag model for the evolution of the Rayleigh-Taylor and Richtmyer-Meshkov instabilities,” *Laser and Particle Beams*, Vol. 21, pp. 347–353, 2003.

- [190] TANGUAY, V., GOROSHIN, S., HIGGINS, A. J., and ZHANG, F., “Aluminum particle combustion in high-speed detonation products,” *Combustion Science and Technology*, Vol. 181, pp. 670–693, 2009.
- [191] TANNEHILL, J. C., ANDERSON, D. A., and PLETCHER, R. H., *Computational Fluid Mechanics and Heat Transfer*. Taylor & Francis, 1997.
- [192] TAYLOR, G. I., “The instability of liquid surfaces when accelerated in a direction perpendicular to their planes,” *Proc. of the Royal Society of London. Series A, Mathematical and Physical Sciences*, Vol. 201, No. 1065, pp. 192–196, 1950.
- [193] TORO, E. F., “A fast Riemann solver with constant covolume applied to the random choice method,” *International Journal for Numerical Methods in Fluids*, Vol. 9, pp. 1145–1164, 1989.
- [194] TORO, E. F., *Riemann Solvers and Numerical Methods for Fluid Dynamics*. Springer, 1999.
- [195] TORO, E. F., SPRUCE, M., and SPEARES, W., “Restoration of the contact surface in the HLL Riemann solver,” *Shock Waves*, Vol. 4, pp. 25–34, 1994.
- [196] TRUNOV, M. A., SCHOENITZ, M., and DREIZIN, E. L., “Ignition of aluminum powders under different experimental conditions,” *Propellants, Explosives and Pyrotechnics*, Vol. 30, No. 1, pp. 36–43, 2005.
- [197] TRZCINSKI, W. A., CUDZILO, S., and PASZULA, J., “Studies of free and confined explosions of aluminum enriched RDX compositions,” *Propellants, Explosives and Pyrotechnics*, Vol. 32, No. 6, pp. 502–508, 2007.
- [198] UKAI, S., GENIN, F., SRINIVASAN, S., and MENON, S., “Large eddy simulation of re-shocked Richtmyer-Meshkov instability,” *47th AIAA Aerospace Sciences Meeting Including The New Horizons Forum and Aerospace Exposition*, AIAA Paper 2009-944, Jan. 5-8, Orlando, FL, 2009.
- [199] VAN LEER, B., “Towards the ultimate conservative difference scheme I. the quest for monotonicity,” *Lecture Notes in Physics*, Vol. 18, pp. 163–168, 1973.
- [200] VAN LEER, B., “Towards the ultimate conservative difference scheme V. A second order sequel to Godunov’s method,” *Journal of Computational Physics*, Vol. 32, pp. 101–136, 1979.
- [201] VANDERSTRAETEN, B., LEFEBVRE, M., and BERGHMANS, J., “A simple blast wave model for bursting spheres based on numerical simulation,” *Journal of Hazardous Materials*, Vol. 46, pp. 145–157, 1996.
- [202] VETTER, M. and STURTEVANT, B., “Experiments on the Richtmyer-Meshkov instability of an air/SF6 interface,” *Shock Waves*, Vol. 4, No. 5. pp. 247–252, 1995.

- [203] VEYSSIERE, B. and KHASAINOV, B. A., “A model for steady, plane, Double-Front Detonations (DFD) in gaseous explosive mixtures with aluminum particles in suspension,” *Combustion and Flame*, Vol. 85, pp. 241–253, 1991.
- [204] VEYSSIERE, B. and KHASAINOV, B. A., “Structure and multiplicity of detonation regimes in heterogeneous hybrid mixtures,” *Shock Waves*, Vol. 4, pp. 171–186, 1995.
- [205] VULIS, L. A., *Thermal Regimes of Combustion*. McGraw-Hill, 1961.
- [206] WHARTON, R. K., FORMBY, S. A., and MERRIFIELD, R., “Air-blast tnt equivalence for a range of commercial blasting explosives,” *Journal of Hazardous Materials*, Vol. 79, pp. 31–39, 2000.
- [207] WHITAKER, S., “Forced convection heat transfer correlations for flow in pipes, past flat plates, single cylinders, single spheres, and for flow in packed beds and tube bundles,” *AIChE Journal*, Vol. 18, pp. 361–371, 1972.
- [208] WHITE, F. M., *Viscous Fluid Flow, Second Edition*. McGraw-Hill, 1991.
- [209] XU, S., ASLAM, T., and STEWART, D. S., “High resolution numerical simulation of ideal and non-ideal compressible reacting flows with embedded internal boundaries,” *Combustion Theory and Modeling*, Vol. 1, pp. 113–142, 1997.
- [210] XU, S. and STEWART, D. S., “Deflagration-to-detonation transition in porous energetic materials: a comparative model study,” *Journal of Engineering Mathematics*, Vol. 31, pp. 143–172, 1997.
- [211] YOUNGS, D. L., “Numerical simulation of turbulent mixing by rayleigh-taylor instability,” *Physica*, Vol. 12, pp. 32–44, 1984.
- [212] YOUNGS, D. L. and WILLIAMS, R., “Turbulent mixing in spherical implosions,” *International Journal for Numerical Methods in Fluids*, Vol. 56, pp. 1597–1603, 2008.
- [213] YUEN, M. C. and CHEN, L. W., “Heat-transfer measurements of evaporating liquid droplets,” *International Journal of Heat and Mass Transfer*, Vol. 21, pp. 537–542, 1978.
- [214] ZHANG, F., FROST, F. D., THIBAUT, P. A., and MURRAY, S. B., “Explosive dispersal of solid particles,” *Shock Waves*, Vol. 10, pp. 431–443, 2001.
- [215] ZHANG, F., THIBAUT, P. A., and LINK, R., “Shock interaction with solid particles in condensed matter and related momentum transfer,” *Proceedings: Mathematical, Physical and Engineering Sciences*, Vol. 459, No. 2031, pp. 705–726, 2003.

- [216] ZHANG, F. and FROST, D. L., “Dense solid particle-fluid detonation flow,” *Minsk International Colloquium on Physics of Shock Waves, Combustion, Detonation and Non-Equilibrium Processes*, MIC 2005, Minsk, November 14–19, 2005.
- [217] ZHANG, F., MURRAY, S. B., and GERRARD, K. B., “Aluminum particles-air detonation at elevated pressures,” *Shock Waves*, Vol. 15, pp. 313–324, 2006.
- [218] ZHANG, F., ANDERSON, J., and YOSHINAKA, A., “Post-detonation energy release from TNT-aluminum explosives,” *AIP Shock Compr. Cond. Matter*, Waikoloa, Hawaii, 2007.
- [219] ZHANG, Q. and GRAHAM, M. J., “Numerical study of Richtmyer-Meshkov instability driven by cylindrical shocks,” *Physics of Fluids*, Vol. 10, No. 4, pp. 974–992, 1998.
- [220] ZUKAS, J. A. and WALTERS, W. P., *Explosive Effects and Applications*. Springer, 1998.